SOLID STATE NMR STUDIES OF STRUCTURE AND DYNAMICS OF MEMBRANE ASSOCIATED INFLUENZA FUSION PEPTIDE

By

Ujjayini Ghosh

A DISSERTATION

Submitted to
Michigan State University
in partial fulfillment of the requirements
for the degree of

Chemistry—Doctor of Philosophy

2016

ABSTRACT

SOLID STATE NMR STUDIES OF STRUCTURE AND DYNAMICS OF MEMBRANE ASSOCIATED INFLUENZA FUSION PEPTIDE

By

Ujjayini Ghosh

This work seeks to delineate the role of influenza fusion peptide in the process of membrane fusion. Influenza fusion peptide is represented by the ~ 23 N-terminal residues of the HA2 subunit of the hemagglutinin (HA) protein. The influenza fusion peptide plays an important role in the membrane fusion between the host viral and the host cell endosomal membrane and has pH dependence. The influenza fusion peptide is the most conserved sequence in the in the influenza genome such that a modest mutation can arrest the fusion activity. It was shown that in detergents the structure of the 20 residue and the 23 residue influenza fusion peptide have different structures. However, influenza fusion peptide is a membrane peptide and induces fusion the lipid vesicles and not between the detergent micelles.

In this work, solid state NMR was used to study the structure of the influenza fusion peptide in membranes and its correlation to the vesicle fusion. The influenza peptide was chemically synthesized chemically and was used as a model system to study the membrane fusion process. In PC:PG membranes, the influenza fusion peptide adopts closed and semiclosed structure. Both the closed and the semiclosed structure have a helix/turn/helix structure with an interhelical angle of ~ 158° and ~146° respectively. Unlike detergents, the structures of the 20 residue and the 23 residue are very similar in membranes with some minor differences. At low pH or the fusogenic pH, there is a higher fraction of the semiclosed fraction for both the influenza peptide constructs. For the longer peptide, higher fractions of the closed structures were determined. Vesicle fusion assays served as a surrogate for the virus/endosome fusion. Our data supported a

strong positive correlation between the vesicle fusion and the hydrophobic surface area. Based on these data we proposed that the hydrophobic interaction between HAfp and the membrane is an important factor in HAfp-catalyzed fusion.

Solid state NMR has been applied to study the structure and dynamics of lipid molecules in membrane with fusion peptide but the solid-state NMR data are typically the sum over all lipid molecules with only a small fraction of these molecules next to the fusion peptide. My second project primarily utilized ^{2}H NMR to study the dynamics of the influenza fusion peptide in membranes. This work describes the development and application of the cross polarization with solid or quadrupolar echo. The main idea of the work is to probe the motions of the lipids adjacent/close to the peptide. This method is applied to two different peptides, HIV-fusion peptide and influenza fusion peptide in presence of membranes. By comparing the conventional solid-echo experiment and the newly developed cross polarization with quadrupolar echo, I have seen differences in the lipid dynamics.

To my Mom, Dad and Anirban

ACKNOWLEDGEMENTS

I take this opportunity to thank my advisor, Professor David Weliky for accepting me into his lab and not strangling me when I probably deserved it. I thank him for inspiring me, and for the many countless one-to-one hour discussion in his office for the past five years. Professor Weliky has greatly influenced my interest and understanding of NMR spectroscopy and its biological applications. His optimism has helped me to get through many frustrating days. If it wasn't the valuable discussions in his office I wouldn't have made it this far.

I also thank my committee members Professor Daniel Jones, Professor John McCracken, and Professor Robert Cukier, for their valuable inputs, guidance and taking the time to attend the meetings, providing valuable feedbacks and criticism.

The Max T Rogers NMR facility staff at the Michigan State has been extremely helpful for the last five years of my graduate school experience. I thank Dr. Dan Holmes for helping me countless times with any NMR issues throughout my graduate school. I also thank Dr. Li Xie for always being around when I needed help with various things and for being a friend. In addition, Dan's and Li's willingness to devote time to conversations about my research, and NMR in general, are much appreciated.

I am also grateful for the support and help from the former and current Weliky group members, Dr. Charles Gabrys, Dr. Punsisi Ratnayake, Shuang Liang, Lihui Jia, Robert Wolfe and Ahinsa Ranaweera. They have been very helpful not only in research but also in non-Chemistry interactions.

I would also like to thank my friends at Michigan State. Their wonderful company has made my past five years truly enjoyable. Thank you all for your support and best wishes.

I thank my parents, for their encouragement and for always being there for me throughout my life. Words cannot express how grateful I am to my parents and because of their unconditional love, support and encouragement I have made this far. My sister has also been extremely supportive during my graduate studies. She has always been protective of me and I am truly thankful for her sisterly love. A special thanks to my parents-in law for the support and best wishes.

At the end, I would like to express my appreciation to my beloved husband Anirban. My wonderful and loving husband, Anirban, has stuck with me through some of my hardest times in graduate school. He was always there for me when I needed encouragement and inspires me every day. Finally, Anirban has, as ever, kept my computer working and borne my bad tempers with patience and even a little humor.

TABLE OF CONTENTS

LIST OF TABLES xi

LIST OF FIGURES xiii

KEY TO SYMBOLS AND ABBREVIATIONS xxiv

Chapter 1 Introduction 1
1.1 NMR Introduction 1
1.1.1 Zeeman interaction 2
1.1.2 The effect of radiofrequency (rf) pulses 5
1.1.3 Zeeman truncation 8
1.1.4 Density operator and magnetization 9
1.1.5 Rotating frame of reference 11
1.1.6 Important NMR interactions 12
1.1.6.1 Dipolar coupling interaction 14
1.1.6.2 Quadrupolar interaction 16
1.1.6.3 Isotropic and anisotropic chemical shift interactions 19
1.2 NMR Methods 24
1.2.1 Magic Angle Spinning (MAS) 24
1.2.2 Cross Polarization (CP) 26
1.2.3 Rotational Echo Double Resonance (REDOR) 30
1.2.4 Quadrupolar Echo (QUECHO) 37
1.3 Introduction to the Influenza 39
1.3.1 Influenza virus 40
1.3.2 Cell biology of influenza virus 43
1.3.3 Proposed mechanism of membrane fusion 45
1.3.4 Structural studies of hemagglutinin protein 48
REFERENCES 51

Chapter 2 Materials and Method 55
2.1 Materials 55
2.2 Peptide sequences, preparation and purification 55
2.3 Vesicle preparation 57
2.4 Membrane sample preparation for MAS and static solid state NMR 57
2.5 Vesicle fusion assay 58
2.6 Solid state NMR 59
2.6.1 MAS solid state NMR spectroscopy 59
2.6.2 Static solid state NMR spectroscopy 61
REFERENCES 63

Chapter 3 Structural Studies of Membrane Associated Influenza Fusion Peptide 65
3.1 Introduction 65
3.2 Results 74
3.2.1 ^{13}C Chemical shifts 74
3.2.2 Calculation of $(\Delta S/S_0)^{lab}$ 85
3.2.3 Intermolecular vs intramolecular G16^{13}CO - F9^{15}N proximity 90
3.2.3.1 Derivation of $(\Delta S/S_0)^{inter}$ 90
3.2.3.2 Derivation of $(\Delta S/S_0)^{intra}$ 92
3.2.4 Fitting of the $^{13}CO - ^{15}N$ REDOR data 95
3.2.5 Alternate fitting models 99
3.3 Discussion 106
REFERENCES 109

Chapter 4 Structure - Function Correlation and Modeling of Membrane Associated Influenza Fusion Peptide 113
4.1 Introduction 113
4.2 Modeling of the closed structure 114
4.3 Modeling of the semiclosed structure 118
4.4 Linewidth analysis 125
4.5 Insertion of Phe-9 in the semiclosed structure and the stabilization of the semiclosed structure 127
4.6 Correlation of the structure of HAfp with vesicle fusion 131
4.7 Discussion 135
REFERENCES 142

Chapter 5 Development of Cross-Polarization with Quadrupolar Echo (cpquecho) and ^2H NMR Studies of Protein Dynamics 146
5.1 Introduction 146
5.1.1 Relaxation measurements 153
5.2 Probe design 154
5.2.1 Tuning of a NMR probe 157
5.3 Pulse sequence programming 159
5.3.1 Phase cycling 160
5.4 Setup compound(s) 162
5.5 Pulse sequence optimization 164
5.5.1 ^2H 90° pulse optimization 164
5.5.2 Transmitter frequency setup 165
5.5.3 CP optimization 168
5.6 Testing a new pulse sequence 171
5.7 Experimental conditions 174
5.8 Results 177
5.8.1 Secondary structure of HFP and HAfp in DMPC-d54 177
5.8.2 Solid echo or quecho experimental results 178
5.8.2.1 Variable temperature ^2H NMR 178
5.8.2.2 Segmental order parameters 183
5.8.2.3 Transverse relaxation studies 189

5.8.3 Cpquecho experimental results..... 199
5.8.3.1 DMPC-d54 cpquecho spectra..... 199
5.8.3.2 HFP/DMPC-d54 cpquecho spectra..... 204
5.8.3.3 HAfp/DMPC-d54 cpquecho spectra..... 204
5.8.3.4 Quadrupolar splitting..... 207
5.8.3.5 Transverse relaxation studies..... 208
5.9 Discussion..... 216
5.9.1 HFP and HAfp disrupts acyl chain packing..... 216
5.9.2 Insertion of the peptides into the hydrophobic core of the membrane..... 220
5.9.3 Spin-spin relaxation studies..... 224
5.9.4 Alternative fitting method..... 225
APPENDICES..... 229
APPENDIX A NMR File Location..... 230
APPENDIX B Solid Phase Peptide Synthesis (SPPS)..... 235
APPENDIX C HPLC Program and Mass Spectra of the Purified Peptide..... 241
APPENDIX D Mathematica Algorithm for the Global Fitting of the $^{13}CO - ^{15}N$ REDOR Data..... 250
APPENDIX E Computer Program of the Cpquecho Experiment..... 269
REFERENCES..... 275

Chapter 6 Summary and Future Work..... 278
6.1 Summary..... 278
6.2 Future work..... 280
6.3 Studies of the dynamics of HAfp and HFP..... 281
6.4 Mutational studies of HAfp..... 281
APPENDIX..... 283
REFERENCES..... 286

LIST OF TABLES

Table 2.1. Labeling scheme of HAfps..... 56

Table 3.1. Interhelical distances of HA3fp20 at pH 5 in the open structure and HA1fp23 in the closed structure based on the previously observed solution NMR data. The distances were measured in PYMOL..... 72

Table 3.2. Linewidths of membrane associated HAfp at τ = 2 ms and τ = 40 ms. The line broadening used for each spectrum during processing was 20 Hz..... 82

Table 3.3. CO_k– F9 N distances.[a]..... 87

Table 3.4. ($\Delta S/S_0$) values for the G16 ^{13}CO / F9 ^{15}N samples.[a] The uncertainties are in parenthesis..... 88

Table 3.5. ($\Delta S/S_0$) values for the A5 ^{13}CO / M17 ^{15}N samples.[a] The uncertainties are in parenthesis..... 89

Table 3.6. S_0 expressions for intermolecular and intramolecular models[a]..... 93

Table 3.7. Best-fit parameters of the closed/semi-closed model[a,b]..... 97

Table 3.8. Best-fit parameters of the models used to fit the G16/F9 SSNMR REDOR data..... 101

Table 3.9. ($\Delta S/S_0$) values for d = 51.7 Hz [a]..... 105

Table 4.1. Interhelical distances of HAfp in membranes and in detergents..... 113

Table 4.2. φ/ψ angles in degrees of residues Gly-1 to Gly-23 for closed and semiclosed structure of HAfp. φ/ψ angles in degrees of residues Gly-1 to Gly-20 for open structure of HA3fp20 in detergents at pH 5. Standard deviations are given in parenthesis.[2]..... 122

Table 4.3. φ/ψ angles in degrees of residues Gly-1 to Gly-20 for semiclosed structure of HAfp after YASARA energy minimization..... 123

Table 4.4. Typical linewidths of the HAfp spectra labeled at Gly-16 and Ala-5..... 125

Table 4.5. Average hydrophobic surface areas of HAfp and extent of vesicle fusion. Uncertainties are given in parenthesis and were obtained by repeating the experiments twice 134

Table 4.6. Ratio of the hydrophobic to the hydrophilic surface areas..... 140

Table 5.1. Phase cycling of the cpquecho experiment..... 161

Table 5.2. Best-fit ^2H T_2 (μs) measured using quecho experiment. The uncertainties are in parenthesis and is given by standard error. The T_2 values obtained by fitting the $–CD_2$ intensity are listed in the column intensity..... 198

Table 5.3. ^2H quadrupolar splitting of DMPC-d54 with and without peptide at different temperatures. The numbers in italics represent the quadropolar splitting determined from the quecho experiment. Below the phase transition temperature, the quadrupolar splitting was not determined because of the lack of the well resolved $–CD_2$ resonances..... 207

Table 5.4. Best-fit ^2H T_2 values in μs of DMPC-d54 lipid with and without peptide. The uncertainties are given in parenthesis. The T_2 values are obtained by fitting the $–CD_2$ intensities..... 215

Table 5.5. Best-fit T_2 (μs) values at different temperatures. Uncertainties are in parenthesis 224

Table 5.6. Best-fit T_2 (μs) values at different temperatures obtained by fitting the tip of the echo as a function of 2τ. Uncertainties are in parenthesis..... 225

LIST OF FIGURES

Figure 1.1.(a)The figure illustrates the magnitude of μ and the projection of μ on the z-axis. For spin ½ nuclei, $\mu_z = ½$ and $\mu = (\sqrt{3})/2$ ($\hbar$ is dropped in both the cases). (b) Precession of μ_α about the external magnetic field $\mathbf{B}_0$. The two Zeeman states of spin ½ nucleus in the presence of $\mathbf{B_0}$. The $\vec{B}_0$ field is in the z-direction. In this figure, μ_α and μ_β are precessing around the $\mathbf{B}_0$ field with an angular frequency $\omega_0 = \gamma B_0$. This precession is known as Larmor precession and the corresponding frequency is called Larmor frequency.....4

Figure 1.2. Rabi precession of **M** around the $\mathbf{B_1}$ field of (a) 90_x pulse and (b) 180_x pulse..... ...7

Figure 1.3. Definition of r and θ. 'r' is the distance between the nucleus I and S. θ is the angle between the internuclear vector and the external magnetic field $\mathbf{B_0}$ along z-axis..... 15

Figure 1.4. Charge distribution in a quadrupolar nucleus. (a) prolate and (b) oblate charge distribution.[6]..... 17

Figure 1.5. Stick diagram showing the orientation dependence of the ^2H spectra for C – ^2H bond. θ is the angle between the C – ^2H bond and $\mathbf{B_0}$ field. (a) θ = 0°, (b) θ = 54.7°, (c) θ = 90°. (d) The form of a quadrupolar powder pattern. The doublet nature of the pattern is due to there being two allowed spin transitions (m = +1 → m = 0, and m = 0 → m = -1). [6]..... 20

Figure 1.6. (a) PAF and shielding tensor (red). θ is the angle between $\mathbf{B_0}$ and the z-axis of PAF. ϕ is the angle between the x-axis of PAF and the projection of $\mathbf{B_0}$ in the xy-plane of PAF. (b) The principal values associated with PAF are σ_{xx}, σ_{yy} and σ_{zz} which also correspond to three principal values of chemical shifts in the powder pattern. (c) Definition of Euler angles, α, β, and γ with respect to $\mathbf{B_0}$ field. [6]..... ...22

Figure 1.7. (a) Structure of peptide plane in a protein. The grey ellipsoid shows the CSA tensor of ^{13}CO. (b) The PAF of ^{13}CO in protein backbone. The x^{PAF} and y^{PAF} are in the C -CO- N plane whereas the z^{PAF} is perpendicular to the C-CO-N plane. (c) CSA powder pattern of ^{13}CO. σ_{xx} = 247 ppm, σ_{yy} = 176 ppm and σ_{zz} = 99 ppm corresponds to three chemical shifts. Note that the most shielded component σ_{zz} appears at lower chemical shift (upfield) and the least shielded component σ_{xx} is at higher chemical shift (downfield)..... 23

Figure 1.8. Schematic representation of the geometry of the ^{13}C – ^{15}N vector in solid state NMR sample under MAS. The sample is spun rapidly in a cylindrical rotor about a spinning axis oriented at the magic angle (α = 54.7°) with respect to $\mathbf{B_0}$..... ...25

Figure 1.9. The effect of slow rate of MAS. A set of spinning sidebands appears with the isotropic shift. The spinning sidebands are spaced at the spinning frequency. [1].....25

Figure 1.10. The CP pulse sequence. The effect of the CP pulse sequence is to transfer magnetization from the abundant spins (^{1}H) to the rare spins, X (eg. ^{13}C) via the heteronuclear dipolar coupling between the ^{1}H and X spins..... ..27

Figure 1.11. A typical REDOR NMR pulse sequence. In this case, the observed spin is ^{13}C and the dephased spin is ^{15}N..... ..32

Figure 1.12. Evolution of dipolar coupling as a function of rotor period in S_0 experiment. Rotor synchronized ^{13}C π-pulses does not interfere with the MAS averaging of the heteronuclear dipolar interaction..... ..34

Figure 1.13. Evolution of dipolar coupling as a function of rotor period in S_1 experiment. Rotor-synchronized ^{15}N π-pulses prevent MAS averaging of the heteronuclear dipolar coupling..... ..35

Figure 1.14. Solid echo pulse sequence. The quecho pulse sequence is used for ^{2}H T_2 measurements. Theoretically $\tau_1 = \tau_1$ and the total time is $2\tau_1$..... .37

Figure 1.15. Schematic represention of the structure of influenza virus. [30] The single stranded genome is constituted of eight segments which are complexed with nucleoprotein. The nucleocapsid segments are surrounded by the envelope containing three membrane proteins. ..... .42

Figure 1.16. Life cycle of influenza virus. [34] (1) Binding of the virus to the sialic acid containing glycolipids; (2) - (3) Entry of the virus inside the cell by the process of endocytosis; (4) Fusion of the viral membrane and the endosomal membrane in acidic pH of the endosomes. (5) Transport of the viral RNAs to the nucleus. Influenza contains negative stranded RNA. First a positive stranded RNA or mRNA is transcribed from the negative sense RNA and the process is aided by the RNA polymerase initially present in the virus. (6) Next the mRNAs exit the nucleus. Synthesis of the viral protein components in the cytosol and endoplasmic reticulum. (7) The newly synthesized viral RNAs and the viral proteins proceed towards the host cell plasma membrane. Finally, assembly and the budding of the progeny virus occur..... ..44

Figure 1.17. Proposed mechanism of membrane fusion. (A) In the prefusion state, the protein is attached to the viral membrane by a C-terminal transmembrane domain. (*B*) Low pH (pH ~ 5) triggers a conformational change in which the fusion peptide projects toward the target membrane, forming an extended intermediate that bridges the two membranes. (*C*) The intermediate collapses. (*D*) The collapse pulls the two membranes together, leading to formation of a hemifusion stalk. (*E*) A fusion pore opens up, and snapping into place of the membrane-proximal and transmembrane segments of the protein completes the conformational transition and stabilizes the fusion pore..... ..46

Figure 1.18. Pre- and post-fusion structures of HA. (a) HA ectodomain (Protein Data bank entries 1RD8 [25] and 1QU1 [32] for pre- and post-fusion forms of the ectodomain, respectively).HA1 chains in shades of red/gold and HA2 chains in shades of blue (paired as red-blue, gold-cyan, and dark red-marine blue). The N-terminus of HA1 and the C-terminus of the HA2 ectodomain are labeled. Blue arrow: position of fusion peptides inserted near three fold axis in pre-fusion form. (b) Crystal structure of HA2 at pH 5. Only HA2 is shown. The N-terminus

(green arrow; Note: the fusion peptide is not part of the structure shown) and C-terminus of the cyan-colored subunit is indicated..... ..47

Figure 2.1. ^{13}C – ^{15}N REDOR pulse sequence. Each sequence starts with a CP from ^{1}H to the observed ^{13}C nucleus to enhance the intensity of ^{13}C signal followed by a dephasing and acquisition period. TPPM ^{1}H decoupling was applied during the dephasing and the acquisition time..... ..60

Figure 2.2. "Quecho" pulse sequence used to measure ^{2}H T_2. The phase of the second 90° pulse is always 90° out of phase with respect to the first 90° pulse. Theoretically $\tau = \tau_1$. However, experimentally $\tau_1 < \tau$..... .62

Figure 3.1. Structures of HAfp in DPC micelles; (a) HA3fp20 at pH 5, (b) HA3fp20 at pH 7.4, and [13](c) HA1fp23 at both pH 4 and pH 7.4. [14] The structure (a) and (c) are refered to as open boomerang and closed structure respectively. (d) Ribbon diagram of the closed structure of HA1fp23 showing the orientation of Gly residues and side chains of Ala-5, Ile-6 and Ile-18. Helix/turn/helix structure of HA3fp20 in PC/PG membranes at (e) pH 5, and (f) pH 7.4. [19] (g) Closed, extended and L-shaped N-helix/turn/C-helix structure of HA1fp23-G8A mutant at pH 7.[16]..... .70

Figure 3.2. ^{13}C detect / ^{15}N - dephase REDOR S_0 (colored) and S_1 (black) experimental spectra of membrane - associated HAfp at τ = 40 ms. Each spectrum is the sum of ~ 50000 scans and processed with 100 Hz Gaussian line broadening and polynomial baseline correction. (a) HA3fp20, pH 5 G16c-F9n, (b) HA1fp23, pH7 G16c –F9n, (c) HA3fp20, pH 7 A5c-M17n, and (d) HA1fp23, pH 5 A5c-M17n. The observed chemical shifts for Gly-16 and Ala-5 are consistent with α - helical conformation of HAfp in membranes. The spectra were taken with samples containing 1 μmole of either HA1fp23 or HA3fp20 and membranes composed of 20 μmole of DTPC and 5 μmole of DTPG. The cooling gas temperature was ~ -50 °C and the sample temperature was ~ -30 °C..... ..77

Figure 3.3. Experimental ^{13}CO Ala-5 REDOR S_0 spectra of both the HAfp constructs at pH 5 for A5c-M17n labeling scheme at 2 ms and 40 ms dephasing times. Each spectrum was processed with 20 Hz Gaussian line broadening and baseline polynomial correction of the order 5. The typical ^{13}CO chemical shift was 179.6 ppm which correlates with the alpha helical secondary structure..... .78

Figure 3.4. Experimental ^{13}CO Ala-5 REDOR S_0 spectra of both the HAfp constructs at pH 7 for A5c-M17n labeling scheme at two different dephasing times. Each spectrum was processed with 20 Hz Gaussian line broadening and baseline polynomial correction of the order 5. The typical ^{13}CO chemical shift was 179.6 ppm which correlates with the alpha helical structure.....79

Figure 3.5. Experimental ^{13}CO Gly-16 REDOR S_0 spectra of both the HAfp constructs at pH 5 for G16c-F9n labeling scheme. Each spectrum was processed with 20 Hz Gaussian line broadening and baseline polynomial correction of the order 5. The typical ^{13}CO chemical shift for each spectrum was 177 ppm which correlates with the alpha helical structure.....80

Figure 3.6. Experimental ^{13}CO Gly- 16 REDOR S_0 spectra of both the HAfp constructs at pH 7 for G16c-F9n labeling scheme. Each spectrum was processed with 20 Hz Gaussian line broadening and baseline polynomial correction of the order 5. The typical ^{13}CO chemical shift was ~ 177.1 ppm which correlates with the alpha helical structure..... 81

Figure 3.7. (a) ^{13}C detect / ^{15}N - dephase REDOR S_0 (colored) and S_1 (black) experimental spectra of membrane - associated HA1fp23 at τ = 40 ms at 0°C. the pH of the sample was 7. (b) ^{13}CO - ^{15}N $(\Delta S/S_0)^{exp}$ buildups with sample temperatures of ~ -30 and ~ 0°C (cooling gas temperatures of -50 and -20 °C, respectively). The signal-per scan at 0 °C is about half that at -30 °C..... .. 83

Figure 3.8. Experimental REDOR dephasing buildup of $(\Delta S/S_0)$ vs τ. (a) G16 ^{13}CO – F9 ^{15}N, and (b) A5 ^{13}CO – M17 ^{15}N. The typical uncertainty in $(\Delta S/S_0)$ is 0.03 based on the standard deviation of the integrals of 12 different spectral regions of the noise..... ...84

Figure 3.9. Antisymmetric dimer configurations of the HAfp. Each arrow represents either N- or C- terminal helices. Labeled HAfp is a red dashed line and unlabeled HAfp is a black line.....93

Figure 3.10. $(\Delta S/S_0)^{exp}$ buildups for pH 5 samples with either 2 µmole G16 ^{13}CO/F9 ^{15}N labeled HA3fp20 or 1 µmole labeled and 1 µmole unlabeled HA3fp20. The calculated $(\Delta S/S_0)^{intra}$ and $(\Delta S/S_0)^{inter}$ for the mixed sample are also displayed. The blue up triangles (▲) and red down triangles (▼) were calculated according to the equations 3.20 and 3.27 respectively. The HAfp: lipid ratio was 1:25 in all the NMR samples. The lipids were composed of DTPC/DTPG in 4:1 ratio. 94

Figure 3.11. Simulated ^{13}C-^{15}N REDOR dephasing curves of $(\Delta S/S_0)$ vs τ for (a) G16^{13}CO-F9^{15}N and (b) A5^{13}CO-M17^{15}N. (a) The F9n-G16c distance in the closed structure of HA1fp23 and the open structure of HA3fp20 are 3.9 and 11.5 Å respectively. (b) The A5c-M17n distance in the closed and the open structures are 5.5 and 11.9 Å respectively. Natural abundance corrected $(\Delta S/S_0)^{lab}$ vs τ for (c) G16^{13}CO-F9^{15}N and (d) A5^{13}CO-M17^{15}N. The uncertainties are represented by the error bars and are typically ± 0.03 – 0.04. Color coding: HA3fp20 pH 5, HA3fp20 pH 7, HA1fp23 pH 5, and HA1fp23 pH 7..... 96

Figure 3.12. Plots of the experimental $(\Delta S/S_0)^{lab}$ and the best-fit $(\Delta S/S_0)^{sim}$ for the closed/semiclosed model. The colored and the black points represent the experimental $(\Delta S/S_0)^{lab}$ and the $(\Delta S/S_0)^{sim}$ from the closed/semiclosed model. The f_c and f_s represent the fraction of the closed and the semiclosed population. The best-fit closed distance for the G16c-F9n (r_{cG}) = 3.9 Å and A5c-M17n (r_{cA}) = 5.4 Å common to all four samples. The best-fit semiclosed distance for r_{sG} = 5.4 Å and r_{sA} = 8.2 Å common to all four samples. The χ^2_{min} = 52 and is close to the degrees of freedom = 48. Table 3.6 lists all the best-fit parameters for the closed/semiclosed model used for the global fitting for all four samples..... 98

Figure 3.13. Plots of experimental G16c-F9n and best-fit $(\Delta S/S_0)$ from the closed/semiclosed model. The top, HA3fp20 and the bottom, HA1fp23 data are fitted separately. The best-fit closed and the semiclosed fractions for (a) f_{c1} = 0.33, f_{s1} = 0.67; (b) f_{c2} = 0.53, f_{s2} = 0.47; (c) f_{c3} = 0.51, f_{s3} = 0.49 and (d) f_{c4} = 0.66, f_{s4}= 0.34. The best-fit closed and semiclosed distances for a/b are 3.78 Å and 5.33 Å and for c/d are 3.82 Å and 5.29 Å respectively 102

Figure 3.14. Plots of the experimental G16c-F9n and the best-fit ($\Delta S/S_0$) from the closed/open model using r_c = 4 Å..... 103

Figure 3.15. Plots of experimentally-derived $(\Delta S/S_0)^{lab}$ and best-fit ($\Delta S/S_0$) from the closed/semi-closed/open model using (top) $d_o(r_o)$ = 2.0 Hz (11.5 Å) and (bottom) $d_o(r_o)$ = 8.2 Hz (7.2 Å). The d_c and d_s are fixed..... ...104

Figure 4.1. Example of .ang file 116

Figure 4.2. Superimposed backbone closed structures of HA1fp23 obtained by the method described in the section 4.1 (green) and the PDB coordinates of the 2KXA (cyan), fitting from Gly-1 to Gly-23. The RMSD is 0.40 Å. Here the alignment was done only for C-alpha atoms 117

Figure 4.3. Heavy atom backbone structural models of membrane associated HA1fp23 from the residues Gly-1 to Gly-23. The amino terminus is marked as N. Longitudinal view of the (a) closed and (b) the semiclosed structure. C-atoms are represented by green vertices, N-atoms by blue vertices and the O-atoms by red vertices. (a) The interhelical angle between the helix A (residues 2-12) and helix B (residues 14-22) is 158°. (b) The interhelical angle between the helix A (residues 2-11) and helix B (residues 14-22) is 146°..... 121

Figure 4.4. Structure of membrane associated HAfp from the residues Gly-1 to Gly-20. Lateral view of the (a) closed structure of HA1fp20 and (b) the semiclosed structure of HA3fp20. Hydrophobic side chains are represented in yellow, polar side chains in green and acidic side chains in red. Cartoon structures showing the orientation of the Gly residues in the (c) closed and the (d) semiclosed structures. (c) Gly-4, Gly-8, Gly-16 and Gly-20 in the closed structure are present at the inner faces of the N- and C-terminal helices. (d) Position of the Gly residues in the semiclosed structure..... ...124

Figure 4.5. Insertion model of Phe-9 ring in the semiclosed structure. The ^{1}H's of the Phe-9 are replaced by ^{2}H's and are shown in black..... ...128

Figure 4.6. ^{13}C detect ^{2}H dephased REDOR spectra of membrane-associated HA3fp20 at 40 ms dephasing time. S_0 (color) and S_1 (black) spectra of HA3fp20 in DTPC:DTPG at (a) pH 5, and (b) pH 7. The chemical shift of Gly-16^{13}CO is 177 ppm which correlates with a helical structure. (c) Experimental dephasing building for HA3fp20 samples with G16^{13}CO/F9 ring ^{2}H labeling. The typical uncertainty is 0.02. (d) ^{13}CO-^{2}H $(\Delta S/S_0)^{exp}$ and best-fit [0.65 x $(\Delta S/S_0)^{exp}$] buildups with d_{sD} = 19 Hz..... 129

Figure 4.7. View of the Met-17 S – Phe-9 ring hydrophobic interaction in the energy minimized HA3fp20 structure..... ... 130

Figure 4.8. HAfp induced vesicle fusion for 1:50 peptide to lipid mole ratio in DTPC:DTPG (4:1) membrane at 37°C..... 131

Figure 4.9. Models of the location of the closed structure of the HA1fp23 in detergent micelles and membranes. Dashed lines represent the hydrophobic core..... 132

Figure 4.10. (a) Schematic representation of a hemifusion stalk. (b) Schematic representation

showing the hexagonal phase (H_{II}) of the lipid. The lipids with a small polar head group also induces a negative curvature strain and favor the organization of the membrane into inverted micelle (H_{II}) structures..... ... 138

Figure 4.11. Top row shows different membrane curvature (a) zero, (b) positive and (c) negative curvature. Space-filling representation of (d) the semiclosed and (e) the closed structures with the hydrophobic (yellow), hydrophilic (red) and basic amino (blue) groups. (f) HAfp can introduce an amphipathic helical structure into one leaflet of the membrane. This "inverted wedge" displaces lipids and can cause the membrane to bend towards itself thereby creating a negative curvature. This mechanism is referred to as wedging mechanism..... 139

Figure 5.1. Chemical structure of DMPC-d54 lipid..... ...147

Figure 5.2. (a) Energy level diagram of ^{2}H. The Zeeman Hamiltonian ($\hat{H}_z$) is perturbed in presence of the quadrupolar Hamiltonian ($\hat{H}_Q$). Due to the quadrupolar interaction, the two spin energy levels are no longer equal. (b) Due to the two spin transitions, doublets of resonances are observed in the ^{2}H spectrum separated by the quadrupolar splitting $\Delta\nu_Q$..... 147

Figure 5.3. (a) Representative ^{2}H NMR powder spectrum of unoriented powdered plexiglass, PMMA-d8.The contributions of methyl and methylene groups are shown in the figure, and the methyl group undergoes threefold motion. (b) Different frames used in S_{CD} analysis. L represents the laboratory frame and is defined by the $\mathbf{B_0}$ field, N represents the bilayer normal frame, I designate the internal frame and P represents the principal axis frame. The L is parallel to N for a 0° oriented bilayer sample. For methylene groups, the z-axis of the internal frame, I, is perpendicular to the D-C-D plane..... ...148

Figure 5.4. ^{2}H NMR spectrum of a multilamellar dispersion of 50 wt % [$^2H_{31}$] 16:0 – 18:1 PC at 22°C. (a) Powder spectrum, and (b) de-Paked spectrum..... ...150

Figure 5.5. (a) Solid state NMR bprobe. (b) Tuning tube and tuning rods. (c) Series plug-ins (left) and traps (right) used in solid state NMR probes..... 156

Figure 5.6. Schematic representation for the cable connections used for low power tuning.....158

Figure 5.7. The response on the oscilloscope when the probe is connected to the sweep generator for a well tuned and well matched probe. The tune rod changes the frequency while the match adjusts the depth of the peak. The horizontal axis position of the dip indicates the resonance frequency of the coil; the depth of the dip is a measure of the match between the impedance of the circuit and the 50 Ohm load..... 158

Figure 5.8. Pulse sequence of cpquecho. The effect of the CP pulse is to transfer the magnetization from the rare (^{1}H) spins to the abundant (^{2}H) spins followed by ^{2}H detection. Here ramped CP is used to increase the efficiency of the matching conditions..... ...160

Figure 5.9. ^{2}H spectra of D_2O static sample at 25°C. pw90X arrayed from 1.0 μs to 10.5 μs with an increment of 0.5 μs, aXrf ampl = 0.7, number of scans = 8. The best optimized pw90X is $\frac{pw360X}{4}$..... 165

Figure 5.10. ^{2}H spectra of DMPC-d54 with HAfp in the ratio 25:1 at pH 7. The delay between the two 90° pulses in the solid echo experiment are arrayed from τ_1 = 30 μs, τ_1 = 11 μs to τ_1 = 415 μs, τ_1 = 396 μs for static sample at temperature 35°C. In the above figure, we can see that the decay is not fully exponential but there is an echo at some other frequency ~ 3 kHz..... ...166

Figure 5.11. ^{2}H spectra of DMPC-d54 lipid with HIV-fusion peptide in the ratio 25:1. The spectra were recorded with the transmitter frequency of 61.204 MHz. As we can see from the above figure that the echo point changed and the resonance offset is ~ 2 kHz. So, the transmitter frequency is changed by 2 kHz..... ...167

Figure 5.12. ^{2}H-spectra of DMPC-d54 lipid with HIV fusion peptide acquired with the corrected transmitter frequency. The transmitter frequency for ^{2}H was 61.5207824 MHz was used for all the ^{2}H-NMR experiments..... ...167

Figure 5.13. ^{2}H spectra of DMPC-d54 for pw90H array from 3 μs to 11.8 μs with an increment of 0.8 μs, for 360 scans, aHrf ampl = 0.65, static sample, temperature = 35°C..... ...169

Figure 5.14. ^{2}H spectra of DMPC-d54 at 30°C. Contact time is arrayed from 1 ms to 10.5 ms with 0.5 ms increment, number of scans is 2000, pw90H = 3.8 μs, aHrf ampl = 0.8, aHcp = 0.9, pw90X = 1.6 μs, aXrf ampl = 0.56, aXcp = 0.25, aXcpmod = 0.1, dwell time = 2 μs..... ...170

Figure 5.15. Voltage response in the oscilloscope due to the application of the pulse in the spectrometer. The first signal shows the ramped spin-locked pulse and the last component represents the ^{2}H 90° pulse..... 171

Figure 5.16. ^{2}H spectra of Gly-d2 for pw90H array from 3.0 μs to 13.4 μs with 0.8 μs increament at 23°C, static sample, 360 scans..... 172

Figure 5.17. ^{2}H FID of Gly-d2 for **(a)** aHcp = 0, and (b) aHcp = 0.9 at 23°C for static sample. The number of scans in case of (a) is 250 and in (b) is 350. Comparison of the above two figure shows that the there is no ^{2}H sgnal when the ^{1}H contact pulse is turned off.....173

Figure 5.18. (a) pulse sequence of quecho experiment, and (b) cpquecho experiment..... 174

Figure 5.19. "cpquecho" ^{2}H NMR spectrum of Glycine-d_2 under static condition at 23°C. The first, second and third panel shows the cpquecho ^{2}H spectra acquired when ^{1}H decoupling = 0, ^{1}H decoupling = ~ 15 kHz and ^{1}H decoupling = ~ 30 kHz respectively. Each spectrum was processed with 500 Hz line broadening, -19 data shift. The number of scans for each spectrum was 360..... 176

Figure 5.20. Ala-5 ^{13}CO NMR spectrum of HAfp in DMPC-d54 in the ratio 1:25 at pH 7. The spectrum was acquired using a ramped cross polarization pulse sequence. Experimental conditions include: 3000 scans, 8 kHz MAS and -50°C. 5. The chemical shift of Ala-^{13}CO is 180.3 ppm which confirms that HAfp is helical in DMPC-d54 lipid..... ..177

Figure 5.21. ^{2}H NMR spectra of DMPC-d54 taken at different temperatures..... ...179

Figure 5.22. ^{2}H NMR spectra as a function of temperature of DMPC-d54 with HFP..... 180

Figure 5.23. ^{2}H NMR spectra of DMPC-d54 with HAfp at pH 5 taken at different temperatures. 181

Figure 5.24. ^{2}H NMR spectra of DMPC-d54 with HAfp at pH 7 taken at different temperatures. 182

Figure 5.25. ^{2}H NMR spectra of DMPC-d54 with and without peptide at 35°C..... 184

Figure 5.26a. de-Paked spectra of DMPC-d54 (bottom) and DMPC-d54 containing HAfp (top) at pH 5. The $\Delta\nu_Q$ in case of the lipid containing HAfp is smaller than the neat lipid..... 185

Figure 5.26b. de-Paked spectra of DMPC-d54 (bottom) and DMPC-d54 containing HAfp (top) at pH 7. The $\Delta\nu_Q$ in case of the lipid containing HAfp is larger than the neat lipid..... 186

Figure 5.26c. de-Paked spectra of DMPC-d54 (bottom) and DMPC-d54 containing HFP (top) at pH 7. The $\Delta\nu_Q$ in case of the lipid containing HFP is smaller than the neat lipid..... 187

Figure 5.27. Effect of HFP and HAfp on the order parameters profile of DMPC-d54 at 35°C. HFP and HAfp at pH 5 decreases the order parameters along the acyl chain of the lipid compared to the pure DMPC-d54 lipid. In contrast, HAfp at pH 7 increases the order parameters compared to pure lipid..... ...188

Figure 5.28. ^{2}H-NMR spectrum of LM3-DMPC dac sample. Measurement of the outer feature or the $-CD_2$ intensity. The outer component is measured between the outer $-CD_2$ peaks of the Pake doublet and the spectrum baseline..... 190

Figure 5.29. Representative stacked plots DMPC-d54 at 10°C (top) and 25°C (bottom). The ^{2}H spectra were obtained by varying τ and τ_1. For each τ and τ_1, the number of scans was 500. All spectra were processed with 500 Hz line broadening, data shift = -11, and baseline correction of the order 5..... 191

Figure 5.30. Representative stacked plots of HFP in DMPC-d54 in the ratio 1:25 at 20°C (top) and 35°C (bottom). The ^{2}H stacked plots were obtained by varying τ and τ_1. For each τ and τ_1, the number of scans was 200. All spectra were processed with 500 Hz line broadening, data shift = -11, and baseline correction of the order 3..... 192

Figure 5.31. Representative stacked plots of HAfp in DMPC-d54 in the ratio 1:25 at 25°C (top, pH 5) and 35°C (bottom, pH 7). The ^{2}H spectra were obtained by varying τ and τ_1. For each τ and τ_1, the number of scans was 1000 (top) and 400 (bottom). All spectra were processed with 500 Hz line broadening, data shift = -11, and baseline correction of the order 3..... 193

Figure 5.32. Quecho experimental (colored squares) and best fit (red lines) plots of $-CD_2$ intensity vs 2τ under static conditions for DMPC-d54 lipid at different temperatures. The fitting equation is $I(2\tau)=I(0)\times\exp(-2\tau/T_2)$ 194

Figure 5.33. Quecho experimental (colored squares) and best fit (red lines) plots of -CD_2 intensity vs 2τ under static conditions for HFP in DMPC-d54 in the ratio 1:25 at different temperatures. The fitting equation is $I(2\tau)=I(0)\times\exp(-2\tau/T)$.....195

Figure 5.34. Quecho experimental (colored squares) and best fit (red lines) plots of -CD_2 intensity vs 2τ under static conditions for HAfp in DMPC-d54 in the ratio 1:25 at different temperatures. The fitting equation is $I_2(2\tau)=I(0)\times\exp(-2\tau/T)$ The pH of the NMR sample was 5.....196

Figure 5.35. Quecho experimental (colored squares) and best fit (red lines) plots of -CD_2 intensity vs 2τ under static conditions for HAfp in DMPC-d54 in the ratio 1:25 at different temperatures. The fitting equation is $I_2(2\tau)=I(0)\times\exp(-2\tau/T)$ The pH of the NMR sample was 7..... 197

Figure 5.36. "cpquecho" experiments of DMPC-d54 at variable temperature under static conditions for 3000 scans. Top: ^{2}H FID for τ = 30 μs and τ_1 = 12 μs at 30°C. Bottom: ^{2}H cpquecho spectra for τ = 30 μs and τ_1 = 12 μs. Each spectrum was processed with 2000 Hz Gaussian line broadening, and -10 data shift..... 200

Figure 5.37. "cpquecho" experiments of HFP with DMPC-d54 (1:25 ratio) at variable temperature under static conditions. Top: ^{2}H FID for τ = 30 μs and τ_1 = 12 μs at 30°C. Bottom: ^{2}H cpquecho spectra for τ = 30 μs and τ_1 = 12 μs. Each spectrum was processed with 2000 Hz Gaussian line broadening, -10 data shift. The number of scans for each spectrum was 6000..... 201

Figure 5.38. "cpquecho" experiments of HAfp with DMPC-d54 (1:25 ratio) at variable temperature under static conditions at pH 5. Top: ^{2}H FID for τ = 30 μs and τ_1 = 12 μs at 30°C. Bottom: ^{2}H cpquecho spectra for τ = 30 μs and τ_1 = 12 μs. Each spectrum was processed with 2000 Hz Gaussian line broadening, -10 data shift. The number of scans for each spectrum was 3000..... 202

Figure 5.39. "cpquecho" experiments of HAfp with DMPC-d54 (1:25 ratio) at variable temperature under static conditions at pH 7. Top: ^{2}H FID for τ = 30 μs and τ_1 = 12 μs at 30°C. Bottom: ^{2}H cpquecho spectra for τ = 30 μs and τ_1 = 12 μs. Each spectrum was processed with 2000 Hz Gaussian line broadening, -10 data shift. The number of scans for each spectrum was 3000..... 203

Figure 5.40. Comparison of the ^{2}H NMR spectrum of HFP/DMPC-d54 for cpquecho (top) and quecho (bottom) experiment at 10°C. Each spectrum was processed with -10 data shift and polynomial baseline correction of the order 5. The top and the bottom spectra were processed with 2000 and 500 Hz Gaussian line broadening..... 205

Figure 5.41. Comparison of the ^{2}H NMR spectrum of HFP/DMPC-d54 for cpquecho (top) and quecho (bottom) experiment at 30°C. The processing parameters are similar to the ones as described in figure 5.31. The 2τ for the top and bottom spectrum is 64 μs..... .206

Figure 5.42. Representative "cpquecho" stacked plots DMPC-d54 at 35°C (top) and HFP/DMPC-d54 at 30°C (bottom). The ^{2}H spectra were obtained by varying τ and τ_1. For each τ and τ_1, the number of scans was ~ 4000. All spectra were processed with 1000 Hz line broadening, data shift = -11, and baseline correction of the order 5..... 209

Figure 5.43. Representative "cpquecho" stacked plots HAfp/DMPC-d54-pH 5 sample at 35°C (top) and HAfp/DMPC-d54-pH 7 at 30°C (bottom). The ^{2}H spectra were obtained by varying τ and τ_1. For each τ and τ_1, the number of scans was ~ 2000. All spectra were processed with 1000 Hz line broadening, data shift = -11, and baseline correction of the order 5..... 210

Figure 5.44. "cpquecho" experimental (colored squares) and best fit (red lines) plots of -CD_2 intensity vs 2τ under static conditions for DMPC-d54 lipid at different temperatures. The fitting equation is $I(2\tau)=I(0)\times\exp(-2\tau/T_2)$ 211

Figure 5.45. "cpquecho" experimental (colored squares) and best fit (red lines) plots of -CD_2 intensity vs 2τ under static conditions for HFP/DMPC-d54 lipid at different temperatures. The pH of the sample was 7. The fitting equation is $I(2\tau)=I(0)\times\exp(-2\tau/T_2)$ 212

Figure 5.46. "cpquecho" experimental (colored squares) and best fit (red lines) plots of -CD_2 intensity vs 2τ under static conditions for HAfp in DMPC-d54 in the ratio 1:25 at different temperatures. The fitting equation is $I(2\tau)=I(0)\times\exp(-2\tau/T_2)$ The pH of the NMR sample was 5.....213

Figure 5.47. "cpquecho" experimental (colored squares) and best fit (red lines) plots of -CD_2 intensity vs 2τ under static conditions for HAfp in DMPC-d54 in the ratio 1:25 at different temperatures. The fitting equation is $I(2\tau)=I(0)\times\exp(-2\tau/T_2)$ The pH of the NMR sample was 7..... 214

Figure 5.48. Effect of the peptide concentration on quadrupolar splitting. ^{2}H quecho NMR spectra of HFP/DMPC at 35°C..... 218

Figure 5.49. ^{2}H quecho NMR spectra of HAfp/DMPC at 35°C. (a) at pH 5 and (b) at pH 7. In case of pH 5, at higher peptide concentration the quadrupolar splitting gets narrower. In contrast, at pH 7, the quadrupolar splitting at higher and lower peptide concentration are similar..... 219

Figure 5.50. Normalized order parameter profiles of DMPC-d54 after the addition of the 0.04 mole % peptides. The normalized order parameter profiles are calculated at 35°C. The plot shows the fractional change in the order parameters at each acyl chain position. The positive value indicates an increase in the disorder and a negative value indicates an increase in the order of the acyl chain..... 221

Figure 5.51. "cpquecho" ^{2}H NMR spectra of HFP/DMPC-d54 at 35°C at different dephasing times. The $\Delta\nu_Q$ for the methyl group is ~ 3.1 kHz. The splitting is consistent with the methyl group splitting of 3.5 kHz at 35°C obtained from the quecho experiment..... 223

Figure 5.52. Plots of best-fit T_2 values at different temperatures obtained from (a) quecho experiment and (b) cpquecho experiment..... 226

Figure C1. HPLC chromatogram of HA3fp20 (top row) and HA1fp23 (bottom row) purification. The peak at around ~ 15 mins in top was the diagnostic peak of HA3fp20 and the peak at around ~ 32 mins at the bottom was the diagnostic peak of HA3fp20 based on the MALDI-TOF mass spectrum.....245

Figure C2. MALDI mass spectrum of HA3fp20 after purification. The theoretical molecular weight of HA3fp20 is 2738 Da..... 246

Figure C3. MALDI mass spectrum of HA1fp23 after purification. The theoretical molecular weight of HA1fp23 is 3058 Da..... 247

Figure C4. MALDI mass spectrum of HFP after purification. The theoretical molecular weight of HFP is 3150 Da..... 248

Figure C5. MALDI mass spectrum of HA1fp23 – G1E mutant after purification. The theoretical molecular weight is 3132 Da..... . 249

Figure F1. ^{13}C detect ^{15}N dephased REDOR S_0 (black) and S_1 (colored) spectra of HA1fp23 G1E mutant at (a) pH 5 and (b) pH 7 at 40 ms dephasing time. Each spectrum is sum of ~ 60000 scans and processed with 100 Hz line broadening and polynomial baseline correction. The chemical shift of the higher ppm ^{13}CO Ala peak is 179.8 ppm and 175.4 ppm. 179.8 ppm corresponds to α-helical structure whereas the 175.4 ppm corresponds to a coil structure.....285

Figure F2. ^{13}CO – ^{15}N ($\Delta S/S_0$) REDOR experimental buildups at pH 5 and pH 7. The typical uncertainties are 0.04. Only the dephasing for the α-peak is plotted..... 286

KEY TO SYMBOLS AND ABBREVIATIONS

^{2}H NMR: Deuterium NMR

CSA: chemical shift anisotropy

CP: cross polarization

CD: Circular dichroism

DCM: dichloromethane

DEPBT: 3-(Diethoxyphosphoryloxy)-1,2,3-benzotriazin-4-(3H)-one

DIEA: N,N-diisopropylethylamine

DMF: N,N-dimethylformamide

DMPC: dimyristoylphosphatidylcholine

DPC: dodecylphosphocholine

DTPC: 1,2-di-O-tetradecyl-sn-glycero-3-phosphocholine

DTPG: 1,2-di-O-tetradecyl-sn-glycero-3-[phospho-(1'-rac-glycerol)]

ESR: Electron spin resonance

Fmoc: 9-fluorenylmethyloxycarbonyl

FID: free induction decay

FRET: fluorescence resonance energy transfer

FTIR: Fourier transform infrared spectroscopy

H_2SO_4: Sulfuric acid

HCl: Hydrochloric acid

HA: Hemagglutinin protein

HEPES: 4-(2- hydroxyethyl)-1-piperazeneethanesulfonic acid

HFP: HIV fusion peptide

HIV: Human immunodeficiency virus

HAfp: Influenza fusion peptide

HPLC: High pressure liquid chromatography

HSQC: Heteronuclear single quantum coherence

IR: Infrared spectroscopy

FWHM: Full width at half maximum

MALDI: Matrix assisted laser desorption ionization

MES: 2 – (N-morpholino) ethanesulfonic acid

n.a.: Natural abundance

NaOH: Sodium hydroxide

Na_2SO_4: Sodium sulfate

NMR: Nuclear magnetic resonance

NOE: Nuclear Overhauser effect

PAF: Principal axis frame

RDC: Residual dipolar coupling

REDOR: Rotational echo double resonance

rf: Radio frequency

SPPS: Solid phase peptide synthesis

SSNMR: Solid state NMR

t-Boc: tert-butyloxycarbonyl

TFA: Trifluroacetic acid

TPPM: Two pulse phase modulation

Chapter 1

Introduction

1.1 NMR Introduction

The net magnetization $\mathbf{M}$ arising from the nuclei in a sample is given by:[1]

$$\mathbf{M}=\sum_i \mu_i \qquad 1.1$$

Where $\vec{\mu}_i$ is the magnetic moment associated with the i-th nucleus. Each μ_i is related to nuclear spin $\mathbf{I_i}$ of the nucleus by;

$$\mu_i = \gamma \mathbf{I_i} \qquad 1.2$$

where γ is the gyromagnetic ratio. Therefore from equations 1.1 and 1.2 we can write:

$$\mathbf{M} = \gamma \mathbf{J} \qquad 1.3$$

where, $\mathbf{J}$ is the net nuclear spin angular momentum of the sample giving rise to the magnetization $\mathbf{M}$. When the nuclei are placed in a uniform magnetic field (**B**), the torque exerted $(\mathbf{T}=\frac{d\mathbf{J}}{dt})$ on $\mathbf{M}$ is given by; $\mathbf{T}=\mathbf{M}\times\mathbf{B}$ 1.4

Therefore, combining equations 1.3 and 1.4, we get:

$$\frac{d\mathbf{M}}{dt}=\gamma\mathbf{M}\times\mathbf{B} \qquad 1.5$$

Equation 1.5 describes the motion of **M** in the field **B**. Equation 1.5 predicts that **M** precess about **B** at a constant rate $\omega = \gamma B$.

In this dissertation the letters or symbols referring to a vector are displayed in bold letters, the quantum mechanical operators have hat on the letters and the vector-operators are displayed in bold and also have a hat on it.

1.1.1 Zeeman interaction

When a nucleus having a spin quantum number I is placed in an external static magnetic field ($\mathbf{B_0}$), the nuclear spin energy levels splits into (2I + 1) energy states. This interaction between the nuclear spin and $\mathbf{B_0}$ field is known as the Zeeman interaction and the energy states are often referred to as Zeeman States. The Zeeman Hamiltonian is given by:

$$\hat{H}_Z = -\hat{\boldsymbol{\mu}}.\mathbf{B_0} \qquad 1.6$$

where $\mathbf{B_0}$ represents the external static time independent magnetic field along the z- axis and is given by $\mathbf{B}_0 = B_o\vec{z}$. In turn, $\hat{\boldsymbol{\mu}}$ can be written as;

$$\hat{\mu} = \gamma\hbar\hat{\mathbf{I}} = \gamma\hbar(\mathbf{i}\hat{I}_x + \mathbf{j}\hat{I}_y + \mathbf{k}\hat{I}_z) \qquad 1.7$$

where, $\hbar$= reduced Planck's constant, 1.0546e-34 Js,

$\hat{\mathbf{I}}$ = nuclear spin operator. Here I am using the definition that the operators for the nuclear spin angular momentum as $\hbar\hat{\mathbf{I}}$.

$\hat{I}_x, \hat{I}_y, \hat{I}_z$ = nuclear spin operators for x, y and z components of nuclear spin respectively and are single spin operators. $\hat{I}_x, \hat{I}_y, \hat{I}_z$ are related to $\hat{\mathbf{I}}$ by $\hat{\mathbf{I}}^2 = \hat{I}_x^{\,2} + \hat{I}_y^{\,2} + \hat{I}_z^{\,2}$

$\mathbf{i, j, k}$ = unit vectors along the x, y and z-direction respectively.

Substituting equation 1.7 in equation 1.6, and using the dot product multiplication $(\vec{z}.\vec{z} = 1;\ \vec{x}.\vec{z} = 0)$ we get;

$$\hat{H}_Z = -\gamma\hbar\hat{I}_Z B_0 \qquad 1.8$$

Since $\hat{\mathrm{H}}_\mathrm{Z}$ is proportional to $\hat{\mathrm{I}}_\mathrm{Z}$, the eigenfunctions of $\hat{\mathrm{H}}_\mathrm{Z}$ are the eigenfunctions of $\hat{\mathrm{I}}_\mathrm{Z}$ and are written as $\left|\mathrm{I,m}\right\rangle$ or Ψ_{Im}. The eigenvalues are of $\hat{\mathrm{H}}_\mathrm{Z}$ obtained by:

$$\hat{H}_z|I,m\rangle = E_{I,m}|I,m\rangle = -\gamma\hbar B_0\hat{I}_z|I,m\rangle \quad 1.9$$

Where $E_{I,m}$ is the energy of the eigenstate $|I,m\rangle$

And m is the magnetic spin quantum number and can have (2I+1) values; I, I-1, I-2.....,-I.

Since $|I,m\rangle$ is an eigenfunction of $\hat{I}_z$ with eigenvalue m,

$$\hat{I}_z|I,m\rangle = m|I,m\rangle \quad 1.10$$

and $$\hat{I}^2|I,m\rangle = I(I+1)|I,m\rangle \quad 1.11$$

Using equation 1.9 in equation 1.10 we get:

$$\hat{H}_z|I,m\rangle = E_{I,m}|I,m\rangle = -\gamma\hbar B_0\hat{I}_z|I,m\rangle = -\gamma\hbar B_0 m|I,m\rangle \quad 1.12$$

Therefore the energies of the eigenstates are;

$$E_{I,m} = -\gamma\hbar B_0 m \quad 1.13$$

So for a spin ½ nucleus, I=1/2, m = ± ½ and there are two possible eigenstates with the energies

$$E_{\frac{1}{2},\pm\frac{1}{2}} = \mp\frac{1}{2}\gamma\hbar B_0 \quad 1.14$$

these states are referred to as Zeeman states. The m = +1/2 state is also known as α-state and m = -1/2 state is known as β-state. The transition energy, ΔE between the α and the β-state is given by; $\Delta E = E_\beta - E_\alpha = \gamma\hbar B_0$ 1.15

The nuclear magnetic moments associated with spin ± ½ states are shown in Figure 1.1.[2] The effect of the static field $\mathbf{B_0}$ is described in terms of classical mechanics. The $\mathbf{B_0}$ field imposes a torque on μ_α which therefore traces a circular path around the $\mathbf{B_0}$ with an angular frequency $\omega_0 = \gamma B_0$. This precession is known as Larmor precession and the corresponding frequency is called Larmor frequency. The direction of μ_α in Figure 1.1b is based on the projection of $\boldsymbol{\mu_\alpha}$

along x, y and z- axis as shown in Figure 1.1a. The projection of $\boldsymbol{\mu_\alpha}$ in z-direction μ_z is $m\hbar$ where m is the spin quantum number and is equal to $\frac{\hbar}{2}$. The magnitude of μ is given by $\hbar\sqrt{I(I+1)}$ where I = spin of nucleus.[2]

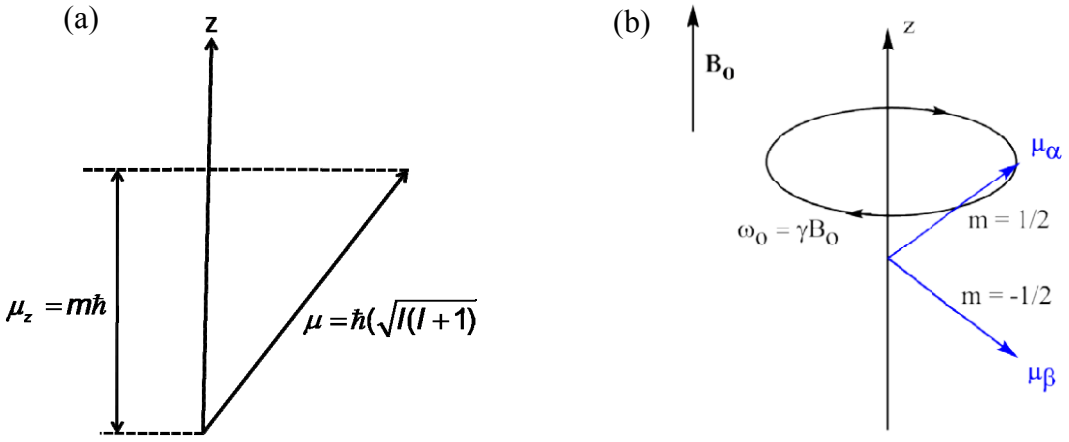

Figure 1.1. (a) The figure illustrates the magnitude of μ and the projection of μ on the z-axis. For spin ½ nuclei, μ_z = ½ and μ = (√3)/2 ($\hbar$is dropped in both the cases). (b) Precession of μ_α about the external magnetic field $\mathbf{B}_0$. The two Zeeman states of spin ½ nucleus in the presence of $\mathbf{B_0}$. The $\vec{B}_0$ field is in the z-direction. In this figure, μ_α and μ_β are precessing around the $\mathbf{B}_0$ field with an angular frequency $\omega_0 = \gamma B_0$. This precession is known as Larmor precession and the corresponding frequency is called Larmor frequency.

Therefore in a sample of non-interaction spin ½ nuclei each spin can exist in one of two possible eigenstates. At equilibrium, the population of each eigen state ψ is p_ψ is given by the Boltzmann distribution over these two states and is written as:[1]

$$p_\psi = \frac{\exp(-E_\psi / kT)}{\sum_{\psi'} \exp(-E_{\psi'} / kT)} \tag{1.16}$$

Where E_ψ is the energy of the ψ eigen state. The expectation value of the z-magnetization for the sample is given by a sum of contributions of the each possible eigen state scaled by the population of each eigen state. The ensemble average of the z-magnetization is given by;

$$\overline{\langle \hat{\mu}_z \rangle} = \gamma\hbar \overline{\langle \hat{I}_z \rangle} = \gamma\hbar \sum_\psi p_\psi \langle \psi | \hat{I}_z | \psi \rangle \tag{1.17}$$

Where $\gamma\hbar \langle \psi | \hat{I}_z | \psi \rangle$ denotes the expectation value of the z-magnetization for a spin in the eigenstate ψ. Expanding equation 1.12 for two level spin ½ system in the $\mathbf{B_0}$ field:

$$\begin{aligned} \overline{\langle \hat{\mu}_z \rangle} &= \gamma\hbar \left[p_{\frac{1}{2}} \left\langle \frac{1}{2}, \frac{1}{2} \middle| \hat{I}_z \middle| \frac{1}{2}, \frac{1}{2} \right\rangle + p_{-\frac{1}{2}} \left\langle \frac{1}{2}, -\frac{1}{2} \middle| \hat{I}_z \middle| \frac{1}{2}, -\frac{1}{2} \right\rangle \right] \\ &= \gamma\hbar \left(\frac{1}{2} p_{\frac{1}{2}} - \frac{1}{2} p_{-\frac{1}{2}} \right) \\ &= \frac{1}{2} \gamma\hbar \left(p_{\frac{1}{2}} - p_{-\frac{1}{2}} \right) \end{aligned} \tag{1.18}$$

Where the $p_{\pm 1/2}$ are the populations of the respective energy spin states. Therefore, the population difference between the two energy states corresponds to z-magnetization.

1.1.2 The effect of radiofrequency (rf) pulses

An rf pulse introduces an oscillating magnetic field, $\mathbf{B_1}(t)$, into the spin system. The time dependence of the $\mathbf{B_1}$ means that both the eigen states of the spin systems and their energies are time dependent. The $\mathbf{B_1}$ field for a 90_X pulse can be written as:

$$\mathbf{B_1}(t) = B_1 \cos(\omega t)\mathbf{x} \tag{1.19}$$

Where $\omega = 2\pi\nu$ and ν = frequency of the 90_x pulse,

x = unit vector along x-axis.

The $\mathbf{B_1}$ field is divided into two components, the resonant $\mathbf{B_1^{res}}$ and the non-resonant $\mathbf{B_1^{non\text{-}res}}$ part. The resonant component rotates clockwise in the xy-plane and the non-resonant part rotates counterclockwise. Since the magnetic moment precesses clockwise about $\mathbf{B_0}$ field, only the $\mathbf{B_1^{res}}$ affects the nuclear spin states.

$$\mathbf{B}_1^{\mathbf{res}} = \frac{1}{2}B_1[\cos(\omega t)\mathbf{x} - \sin(\omega t)\mathbf{y}] \qquad 1.20$$

$$\mathbf{B}_1^{non-\mathbf{res}} = \frac{1}{2}B_1[\cos(\omega t)\mathbf{x} + \sin(\omega t)\mathbf{y}] \qquad 1.21$$

In presence of the $\mathbf{B_1}$ field the magnetization **M** experiences a torque and precesses about the $\mathbf{B_1}$ with an angular frequency γB_1. This precession is known as Rabi precession and the frequency is called Rabi frequency. The direction of the torque **T** can be determined using the right hand rule or the cross product rule. For example, if **M** is along z-axis and $\mathbf{B_1}$ in along x-axis then the **T** is along y axis. (**T** = **M** x $\mathbf{B_1}$ = **z** x **x** = **y**). In NMR the nutation angle or the flip angle θ_{rf} is given by; $\theta = \omega_1\tau_p = \gamma B_1\tau_p$ where τ_p is the duration of the pulse. The Hamiltonian for an x-pulse is;

$$\hat{H}_{rf} = -\gamma B_1\hat{I}_x \qquad 1.22$$

The Hamiltonian for the above pulse is in the rotating frame (see rotating frame section) and the B_1 is static. In contrast, the $\mathbf{B_1}$ term in the equation 1.20 is in the laboratory frame and is oscillating as a function of time.

The Rabi oscillation between the two states α and β is given by:[3]

$$|\Psi(t)\rangle = \exp(\frac{i\phi}{2})\left[\cos\frac{\theta}{2}\exp\frac{-iE_\alpha t}{\hbar}|\Psi_\alpha\rangle - \sin\frac{\theta}{2}\exp\frac{-iE_\beta t}{\hbar}|\Psi_\beta\rangle\right] \qquad 1.23$$

Where, Ψ(t) represent a state vector of the system at time t, E_α and E_β correspond to the energies of α and β states and ϕ represent the phase factor. For a 90° pulse, equation 1.23 reduces to:

$$\begin{aligned}\left|\Psi(t)\right\rangle &= \exp(\frac{i\phi}{2})\left[\cos\frac{90}{2}\exp\frac{-iE_\alpha t}{\hbar}\left|\Psi_\alpha\right\rangle - \sin\frac{90}{2}\exp\frac{-iE_\beta t}{\hbar}\left|\Psi_\beta\right\rangle\right] \\ &= \frac{\sqrt{2}}{2}\exp(\frac{i\phi}{2})\left[\exp\frac{-iE_\alpha t}{\hbar}\left|\Psi_\alpha\right\rangle - \exp\frac{-iE_\beta t}{\hbar}\left|\Psi_\beta\right\rangle\right]\end{aligned} \qquad 1.24$$

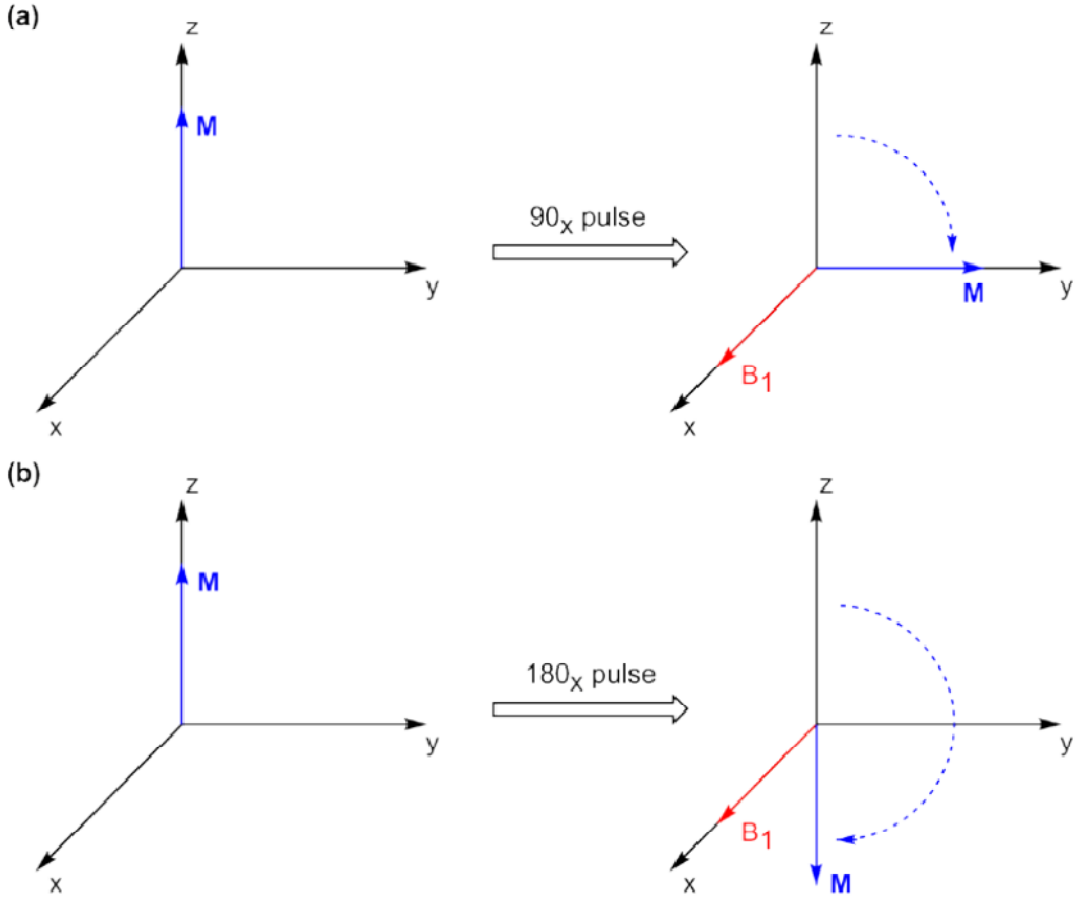

Figure 1.2. Rabi precession of **M** around the $\mathbf{B_1}$ field of (a) 90_x pulse and (b) 180_x pulse.

1.1.3 Zeeman truncation

The $\mathbf{B_0}$ field is in the orders of magnitude greater than the local fields like dipolar fields, chemical shift fields etc, the Zeeman interaction is stronger than these internal local fields. Truncation denotes the process that a weak interaction $\mathbf{B_1}$ in the presence of a stronger interaction $\mathbf{B_0}$ is effectively reduced to some components of $\mathbf{B_1}$ that commute with $\mathbf{B_0}$. The secular components of the Hamiltonian that commutes with the $\mathbf{B_0}$ affect the observable spectrum to the first order whereas the non-secular components do not and the non-secular components are truncated. Therefore, we only consider the secular components and this approximation is known as secular approximation. Truncation effect is provided in the following example. Consider a simultaneous action of a strong magnetic field $\mathbf{B_0}$, and a weak static field $\mathbf{B_1}$ with components B_{1a} along the $\mathbf{B_0}$ field and B_{1p} perpendicular to $\mathbf{B_0}$. The length of the resultant vector $\mathbf{B}_{tot} = \mathbf{B}_0 + \mathbf{B}_1$ is:[4]

$$\left|\mathbf{B}_{tot}\right| = \left(B_0 + B_{1a}\right)\sqrt{1+\left(\frac{B_{1p}}{B_0 + B_{1a}}\right)^2} \qquad 1.25$$

Since the projection of B_{1a} of $\mathbf{B_1}$ onto $\mathbf{B_0}$ is relevant to the first order and $B_{1p} / B_0 \ll 1$ equation 1.25 reduces to:

$$\left|\mathbf{B}_{tot}\right| \cong (B_0 + B_1) \qquad 1.26$$

This truncation is known as Zeeman truncation or secular approximation.

An alternative way of assessing the nuclear spin interactions is perturbation theory. The Zeeman interaction is the dominant interaction and is given by $\hat{H}_0$. The nuclear spin interactions are denoted by $\hat{H}_1$ and are considered as perturbation on the spin system. The total Hamiltonian is and the Schrodinger equation is:

$$\hat{H} = \hat{H}_0 + \hat{H}_1$$
$$\left(\hat{H} = \hat{H}_0 + \hat{H}_1\right)\Phi_n = E_n\Phi_n \qquad 1.27$$

The energy of the perturbed system to the first order is; $E_n^{\,1} = \langle \Psi_n | \hat{H}_1 | \Psi_n \rangle$ 1.28

The wavefunction $\phi_{n,}$ are the eigenfunctions of $\hat{H}_0$. These eigenfunctions are simply the Zeeman states for the spin system. The parts of $\hat{H}_1$ that affects the wavefunctions to zeroth order must have the same eigenfunctions as $\hat{H}_0$.The only parts of $\hat{H}_1$ that affects the spin system to zeroth order are the parts that commute with $\hat{H}_0$. Therefore, the Hamiltonians describing the nuclear spin interactions within the spin system are the ones that commute with the Zeeman interaction.

1.1.4 Density operator and magnetization

The density operator formalism permits the direct calculations of the time dependent and the time independent probability densities and observables without the intermediate step of calculating the probability amplitudes. For a spin system in a single well defined state, the state is represented by a state vector $|\Psi(t)\rangle$. The evolution of $|\Psi(t)\rangle$ is determined using Schrodinger equation:[4]

$$i\hbar \frac{d}{dt}|\Psi(t)\rangle = H(t)|\Psi(t)\rangle \qquad 1.29$$

Where the Hamiltonian operator H(t) represents the nuclear spin interactions. When H(t) is time independent, i.e. H(t) = H, then the solution of the equation is;

$$|\Psi(t)\rangle = \exp(-iHt)|\Psi(0)\rangle \qquad 1.30$$

When H(t) is time dependent, the solution of the equation is;

$$|\Psi(t)\rangle = U(t)|\Psi(0)\rangle \qquad 1.31$$

Where U(t) is the time evolution operator or the propagator and is given by:

$$U(t)=\hat{T}\exp[-i\int_0^t H(t')dt'] \qquad 1.32$$

Where $\hat{T}$ is the Dyson time ordering operator. This operator is necessary when the $\hat{H}(t)$ does not commute with itself at different t. If the time interval from 0 to t is divided into N intervals with lengths τ_j during which the Hamiltonian is H_j, equation 1.32 can be extended as:

$$U(t)=\exp(-iH_N\tau_N)\exp(-iH_{N-1}\tau_{N-1}).....\exp(-iH_2\tau_2)\exp(-iH_1\tau_1) \qquad 1.33$$

Equation 1.33 is just an extension of equation 1.32. In NMR samples we have an ensemble of spin states and therefore we use density operators instead of state vectors. The density operator is defined as; $\rho(t)=\overline{|\Psi(t)\rangle\langle\Psi(t)|}$ 1.34

where the bar represents the weighted average over the spin states in the NMR sample. The density operator can be represented in terms of the density matrix elements ρ_{ij} by:

$$\hat{\rho}(t)=\sum_{i,j}\hat{\rho}_{i,j}(t)|i\rangle\langle j| \qquad 1.35$$

The matrix elements of $\hat{\rho}(t)$ are:

$$\rho_{ij}(t)=\langle i|\hat{\rho}(t)|j\rangle \qquad 1.36$$

The diagonal elements of the density matrix ρ_{ii} or ρ_{jj} represents the populations and the off-diagonal elements ρ_{ij} or ρ_{ji} represents the states $|i\rangle$ or $\langle j|$. The $\hat{\rho}(t)$ and Hamiltonians are connected by von Neumann equation:

$$i\frac{d}{dt}\rho(t)=[H(t),\rho(t)] \qquad 1.37$$

The formal solution of the von Neumann equation is given by:

$$\hat{\rho}(t)=U(t)\hat{\rho}(0)U(t)^{-1} \qquad 1.38$$

Where $\hat{U}(t)=\exp(-i\hat{H}t)$

We assume that the initial condition is ρ(0) and is proportional to the sum of the z-components of the angular momentum at thermal equilibrium $\rho(0) \propto I_Z$. Signals in quantum mechanics are expectation values of the Hermitian operators and are evaluated as:

$$S_A(t)=\langle\Psi(t)|\hat{A}|\Psi(t)\rangle \quad 1.39$$

$$S_A=Tr\{A\rho(t)\} \quad 1.40$$

Where Tr{A} is the trace operator and is defined as; $Tr\{A\}=\sum_n\langle n|A|n\rangle$ if $\{|n\rangle\}$ is the basis set.

The NMR signals are the transverse components of the spin angular momentum. The NMR signal S(t) is written as:

$$\begin{aligned} S(t) &= S_{real}(t)+iS_{imag}(t) \\ &\propto Tr\{I_X\rho(t)\}+iTr\{I_y\rho(t)\} \\ &= Tr\{I_+\rho(t)\} \\ &= Tr\{I_+U(t)I_ZU(t)^{-1}\} \end{aligned} \quad 1.41$$

Where $I_\pm = I_x \pm iI_y$ and U(t) represents the evolution operator for a nuclear spin system.

1.1.5 Rotating frame of reference

It is convenient to define a frame of reference that is rotating in the xy-plane about the z-axis with an angular frequency of $\omega_{RotFram}$. In the laboratory frame, the $\mathbf{B_1}$ field rotates with an angular frequency of ω_{rf} in the xy-plane, where ω_{rf} is the transmitter frequency of the pulse. When we set the ω_{rf} same as the $\omega_{RotFrame}$, the $\mathbf{B_1}$ field of the pulse appears to be static and the time dependence of the $\mathbf{B_1}$ field is removed. In the rotating frame, the apparent precession will appear to be at $(\omega_0 - \omega_{RotFrame})$ where $\omega_0 = \gamma B_0$ is the Larmor frequency. Resonance offset or simply offset Ω, is given by:[5]

$$\Omega = \omega_0 - \omega_{RotFrame} \quad 1.42$$

The relation between the magnetic field and the precession frequency is $\omega = \gamma B$ and the resonance offset field is given by:

$$\mathbf{B_{r.o}} = (\Omega/\gamma)\mathbf{z} \quad 1.43$$

This apparent magnetic field is also known as reduced magnetic field and is along the z-axis. If we set the ω_{rf} close to the ω_0 and set $\omega_{RotFrame}$ the same as the ω_{rf}, the offset Ω will be closed to field is dominant and can cause nuclear spin transition. In the rotating frame, the reduced field (along z-axis) and the $\mathbf{B_1}$ field (along the x-axis) add vectorially to give an effective field, $\mathbf{B_{eff}}$.

For the Zeeman interaction, $\hat{H} = \omega_0 \hat{I}_z$, the time-evolution formula for $\hat{\rho}(0) = \hat{I}_\alpha$ is given by:

$$\hat{\rho}(t) = \exp(-i\omega_0 t \hat{I}_z)\, \hat{I}_\alpha \exp(i\omega_0 t \hat{I}_z) \quad 1.44$$

This represents the rotation of $\hat{I}_\alpha$ by an angle $\omega_0 t$ by z-axis. This precession is eliminated by considering a frame rotating at a frequency $\omega_{RotFrame} \cong \omega_0$. In rotating frame equation 1.40 is written as:

$$\hat{\rho}_R(t) = \exp[i(\omega_{RotFrame} - \omega_0) t \hat{I}_z]\, \hat{I}_\alpha \exp[-i(\omega_{RotFrame} - \omega_0) t \hat{I}_z] \quad 1.45$$

1.1.6 Important NMR interactions

The full NMR Hamiltonian is expressed as:

$$\begin{aligned} \hat{H}_t &= \hat{H}_{ext} + \hat{H}_{\text{int}} \\ &= (\hat{H}_Z + H_{RF}) + (\hat{H}_Q + \hat{H}_{DD} + \hat{H}_{CS} + \hat{H}_J) \end{aligned} \quad 1.46$$

Where, $\hat{H}_{ext}$ = Hamiltonian for the external interactions between the nuclear spin and the external fields like the static magnetic field ($\vec{B}_0$) and the radiofrequency field ($\vec{B}_1$).

$\hat{H}_{int}$ = Hamiltonian for the internal interactions between the nuclear spin and the intrinsic fields like J-coupling etc.

$\hat{H}_Z$ = Hamiltonian for the Zeeman interaction between the spin and $\vec{B}_0$ field. I carried out all of my experiments in 400 MHz spectrometer which corresponds to the external static $\vec{B}_0$.

$\hat{H}_{RF}$ = Hamiltonian for the spin interaction with the radiofrequency pulses, $\vec{B}_1$ field. In NMR experiments, I use ~ 62.5 kHz $\vec{B}_1$ field for ^{13}C - channel;

$\hat{H}_J$ = Hamiltonian for scalar or J-coupling, the relative order of magnitude is ~ 10 Hz;

$\hat{H}_{CS}$ = Hamiltonian for the chemical shift field. For 13- carbon the typical chemical shift range is ~ 20 kHz;

$\hat{H}_{DD}$ = Dipolar coupling Hamiltonian. In biopolymers, the heteronuclear dipolar coupling for the directly bonded (1.5 Å bond length) ^{13}C – ^{15}N is ~ 900 Hz whereas for the ^{13}C – ^{13}C (1.5 Å), the homonuclear dipolar coupling is ~ 2200 Hz.

$\hat{H}_Q$ = Quadrupolar coupling Hamiltonian and the typical value of quadrupolar interaction for aliphatic C – ^2H is ~ 170 kHz.

1.1.6.1 Dipolar coupling interaction

Nuclear spin possesses magnetic moment. When the magnetic moment of one spin interacts with the magnetic field generated by the other spin in space, the interaction is known as dipolar interaction. The interaction between the two spins in called dipolar coupling and the field is called dipolar field. The strength of the dipolar interaction depends on the internuclear distance as $1/r^3$ and orientation dependence of $(3\cos^2\theta - 1)$. The angle θ and r is defined in the Figure 1.3. There are two possible cases of dipolar coupling; Homonuclear and Heteronuclear dipolar coupling. The secular Hamiltonian for the homonuclear dipolar coupling between the two identical spins I and S is given by:[1]

$$\hat{H}_D^{II} = -\frac{\mu_0}{4\pi}\hbar\frac{\gamma_I\,\gamma_S}{r^3}\frac{1}{2}(3\cos^2\theta - 1)(3\hat{I}_z\hat{S}_z - \hat{\mathbf{I}}.\hat{\mathbf{S}}) \qquad 1.47$$

Where μ_0 = permeability of the free space,

$\hat{\mathbf{I}}$ and $\hat{\mathbf{S}}$ = vector operators for the spins I and S respectively and $\hat{\mathbf{I}}.\hat{\mathbf{S}} = \hat{I}_x\hat{S}_x + \hat{I}_y\hat{S}_y + \hat{I}_z\hat{S}_z$.

θ and r are defined in the figure 1.3, and γ = gyromagnetic ratio. The spin part $\left(3\hat{I}_z\hat{S}_z - \hat{\mathbf{I}}.\hat{\mathbf{S}}\right)$ can also be written as $\left\{\frac{1}{2}\left[\hat{I}_+\hat{S}_- + \hat{I}_-\hat{S}_+ - 2\hat{I}_z\hat{S}_z\right]\right\}$ in terms of raising and lowering operators.

The dipolar coupling constant is given by:

$$D = \frac{\mu_0}{4\pi}\hbar\frac{\gamma_1\gamma_2}{r^3}\ \text{(rad/s)} \qquad 1.48$$

The secular Hamiltonian for the heteronuclear dipolar coupling between the two identical spins I and S is given by:

$$\hat{H}_D^{IS} = -\frac{\mu_0}{4\pi}\hbar\frac{\gamma_1\gamma_2}{r^3}\frac{1}{2}(3\cos^2\theta - 1)2\hat{I}_z\hat{S}_z \qquad 1.49$$

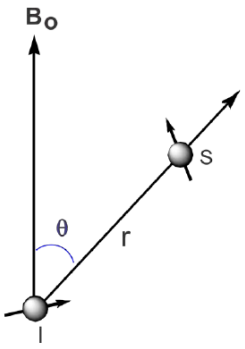

Figure 1.3. Definition of r and θ. 'r' is the distance between the nucleus I and S. θ is the angle between the internuclear vector and the external magnetic field $\mathbf{B_0}$ along z-axis.

The dipolar coupling, D, in units of Hz is given by:

$$D = (\frac{\mu_0}{4\pi}\hbar\frac{\gamma_1\gamma_2}{r^3})/2\pi = \frac{\mu_0 h\gamma_1\gamma_2}{16\pi^3 r^3} \qquad 1.50$$

From equation 1.50, the $^{13}C - ^{15}N$ dipolar coupling in Hz is given by; $D = 3066/r^3$.

From equations 1.47 and 1.49, we see that the spin part of the Hamiltonian of the heteronuclear dipolar coupling is even more truncated than the homonuclear dipolar coupling. This is because in case of homonuclear dipolar coupling, the term $\hat{\mathbf{I}}_1.\hat{\mathbf{I}}_2$ commutes with the Zeeman Hamiltonian, H_z whereas the term $\hat{\mathbf{I}}.\hat{\mathbf{S}}$ does not. The Zeeman Hamiltonian for homonuclear spins is; $\hat{H}_z = -\gamma\hbar B_0(\hat{I}_1 + \hat{I}_2)$ and $\left[\hat{H}_z, \hat{\mathbf{I}}_1.\hat{\mathbf{I}}_2\right] = 0$. In case of heteronuclear spins, the Zeeman Hamiltonian is $\hat{H}_z = -\hbar B_0(\gamma_I\hat{I}_z + \gamma_S\hat{S}_z)$ and $\left[\hat{H}_z, \hat{\mathbf{I}}.\hat{\mathbf{S}}\right] \neq 0$ because of the two different γ present in the H_Z. Therefore, the heteronuclear Hamiltonian is truncated even more.

1.1.6.2 Quadrupolar interaction

A nucleus with a spin greater than ½, is known as quadrupolar nucleus and posses an electric quadrupole moment. The electric quadrupole moment in the nucleus arises from the nuclear charge distribution. Figure 1.4 shows the charge distribution of a quadrupolar nucleus. Electric

quadrupoles interact with the electric field gradient at the nucleus. This interaction is known as quadrupolar coupling. The strength of the interaction depends on the magnitude of the nuclear quadrupole moment and the strength of the electric field gradient. The electric quadrupole moment of the nucleus is given as eQ, where e is the charge of a proton and Q is the quadrupole moment specific to a particular nucleus. A non-zero Q indicates that the charge distribution is not spherically symmetric. The quadrupolar interaction also affects the nuclear spin energy levels like the other magnetic interactions. The quadrupolar Hamiltonian is written as:[4]

$$\hat{H}_Q = \frac{eQeq}{2I(2I-1)\hbar}\frac{1}{2}\left[3\cos^2\theta - 1 - \eta_Q \sin^2\theta\cos(2\phi)\right]\frac{1}{2}\left[3\hat{I}_z^2 - I(I+1)\right] \quad 1.51$$

Where, e = charge of proton,

Q = magnitude of the quadrupole moment,

q = value associated with electric field gradient tensor,

θ, φ = polar angles of the $\mathbf{B_0}$ field in the PAF,

η_Q = asymmetry parameter,

I = nuclear spin quantum number, and

$\hat{I}_z$= z-component of the spin operator.

In equation 1.46, the constant $\frac{e^2Qq}{\hbar}$ is termed as quadrupolar coupling constant and is denoted by χ and is in the units of rad/s. In the units of Hz, χ is given by:

$$\chi = \frac{e^2Qq}{h} \quad 1.52$$

(a) (b)

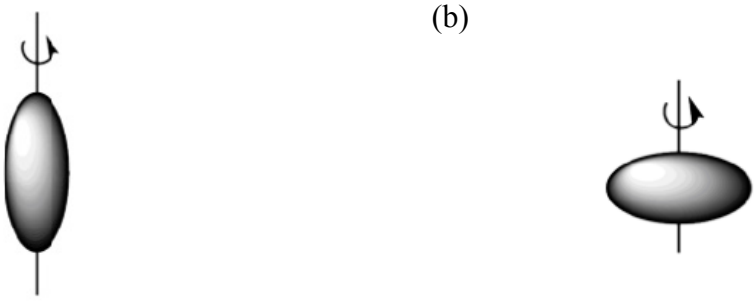

Figure 1.4. Charge distribution in a quadrupolar nucleus. (a) prolate and (b) oblate charge distribution. [6]

The quadrupolar interaction also has orientation dependence $\left[3\cos^2\theta - 1 - \eta_Q \sin^2\theta\cos(2\phi)\right]$. In this section we will discuss in details only about the ^{2}H nuclei because ^{2}H NMR was applied to study the T_2s of lipids and peptide bound lipids. ^{2}H is a spin 1 nucleus with relatively small Q values (Q = 2.8e-31 m^2) which gives rise to χs in the range 140 – 220 kHz in organic compounds. [1] The more relevant example of χ is for the aliphatic C – ^{2}H bond, ~ 170 kHz. [4] We will discuss the orientation dependence of the quadrupolar energy using the C – ^{2}H example. The quadrupolar energy E_Q is given by:

$$E_Q = \frac{eQeq}{2I(2I-1)\hbar}\frac{1}{2}\left[3\cos^2\theta - 1 - \eta_Q \sin^2\theta\cos(2\phi)\right]\frac{1}{2}\left[3m^2 - I(I+1)\right]$$

$$= \frac{\pi}{4}\chi\hbar\left[3\cos^2\theta - 1 - \eta_Q \sin^2\theta\cos(2\phi)\right]\left[3m^2 - 2\right] \qquad 1.53$$

Where, $\hat{I}_z^2|I,m\rangle = m^2|I,m\rangle$. In C – ^{2}H $\eta_Q \cong 0$, because of the approximate uniaxiality of the electron density in the σ bonds. For ^{2}H, I =1 m = -1, 0, +1.Using $\eta_Q \cong 0$, equation 1.51 reduces to:

$$E_Q = \frac{\pi}{4}\chi\hbar\left[3\cos^2\theta - 1\right]\left[3m^2 - 2\right] \qquad 1.54$$

Next we will discuss the θ-dependence on E_Q and its effect on ^2H resonance frequency and the origin of the powder pattern for ^2H.

Case-1: When θ = 0°; $E_Q = \frac{\pi}{2}\chi\hbar\left[3m^2 - 2\right]$. For m = -1, $E_{-1} = \frac{\pi}{2}\chi\hbar$; m = 0, $E_0 = -\pi\chi\hbar$;and m = 1, $E_1 = \frac{\pi}{2}\chi\hbar$. Since in NMR spectroscopy, the allowed transitions are Δm = ±1, there are two allowed transitions in ^2H. The transition energies for m = 1 to m = 0 is $E_{1\to 0} = E_z - \frac{3\pi}{2}\chi\hbar$ and from m = 0 to m = -1 is $E_{0\to -1} = E_z + \frac{3\pi}{2}\chi\hbar$. Here $-E_Z$, 0, $+E_Z$ represents the Zeeman energies for the states m = 1, 0, -1 respectively. Therefore, the transition frequencies for m = 1 → 0 transition is $\nu_{1\to 0} = \nu_z - \frac{3}{4}\chi$ and for m = 0 → -1 is $\nu_{0\to -1} = \nu_z + \frac{3}{4}\chi$ where ν = E_Z / h. ν is the Larmor frequency of ^2H in absence of quadrupolar interaction. When the transmitter frequency is set at ν, two signals will be observed in the ^2H spectrum, one at (+3/4)χ (in Hz) and the other at (-3/4)χ (in Hz) (Figure 1.5a).

Case - 2: When θ = 54.7°; $E_Q = 0$ for all values of m. In this case the transitions from m = 1 → 0 and from m = 0 → -1 yields a single signal at the same frequency in ^2H spectrum (Figure 1.5b).

Case – 3: When θ = 90°; $E_Q = -\frac{\pi}{4}\chi\hbar\left[3m^2 - 2\right]$. For m = -1, $E_{-1} = -\frac{\pi}{4}\chi\hbar$; m = 0, $E_0 = \frac{\pi}{2}\chi\hbar$ and m = 1, $E_1 = -\frac{\pi}{4}\chi\hbar$. Doing the similar calculations as in case-1, the transition frequencies for m = 1 → 0 transition is $\nu_{1\to 0} = \nu_z + \frac{3}{8}\chi$ and for m = 0 → -1 is $\nu_{0\to -1} = \nu_z - \frac{3}{8}\chi$ where ν = E_Z/h. In this case, two signals will be observed in the ^2H spectrum, one at (+3/8)χ and the other at (-3/8)χ (Figure 1.5c).

For the all possible values of θ, a ^{2}H quadrupolar powder pattern will be observed. Powder NMR spectra of static samples consist of doublet patterns (Figure 1.5d), the doublet arising from the two possible spin transitions; +1 → 0 and 0 → -1. The ^{2}H powder spectra are often called Pake doublets; their horns are split by (3/4)χ.

1.1.6.3 Isotropic and anisotropic chemical shift interactions

The motion of the electrons surrounding the nucleus in presence of $\mathbf{B_0}$ creates a secondary magnetic field. This secondary field contributes to the total field felt by the nucleus and can affect the resonance frequency of the nucleus. The interaction of the secondary field produced by the electrons with the nucleus is known as shielding interaction and the field is termed as shielding field. The shielding field varies with the orientations of the molecule relative to $\mathbf{B_0}$. The chemical shielding Hamiltonian operating on spin **I** is: [1]

$$\hat{H}_{cs} = \gamma \hat{\mathbf{I}}.\boldsymbol{\sigma}.\mathbf{B_0} \qquad 1.55$$

When $\mathbf{B_0}$ is in z-direction equation 1.55 reduces to:

$$\hat{H}_{cs} = \gamma \hbar B_0 \sigma^{lab}{}_{zz} \hat{I}_z \qquad 1.56$$

Where $\hat{\mathbf{I}}$ is the nuclear spin operator and $\boldsymbol{\sigma}$ is the second rank Cartesian tensor called shielding tensor. The shielding tensor is associated with the principal axis frame (PAF). The three principal values associated with the PAF of σ are σ_{xx}, σ_{yy} and σ_{zz}. The elements of σ depends on the molecular orientation of the molecule relative to the $\mathbf{B_0}$ field. Chemical shift anisotropy (CSA) means the orientation dependence of the chemical shift which arises due to the fact that in nuclei the charge distribution is rarely symmetrical. The degree to which the electron density affects the resonance frequency of the nucleus depends on the orientation of electron cloud.

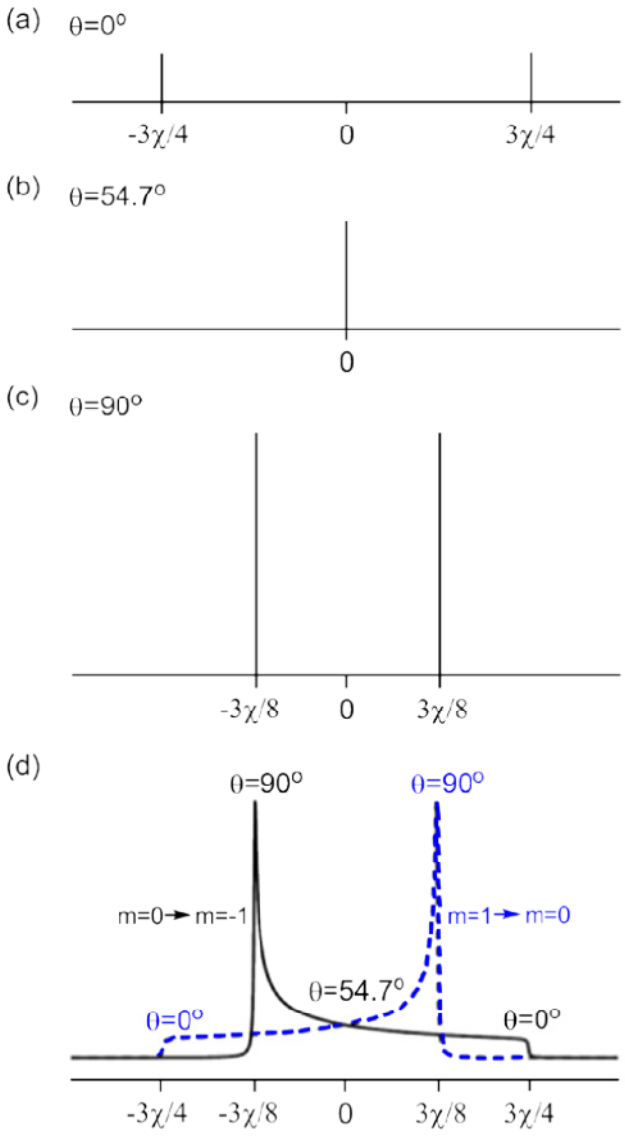

Figure 1.5. Stick diagram showing the orientation dependence of the ^2H spectra for C – ^2H bond. θ is the angle between the C – ^2H bond and $\mathbf{B_0}$ field. (a) θ = 0°, (b) θ = 54.7°, (c) θ = 90°. (d) The form of a quadrupolar powder pattern. The doublet nature of the pattern is due to there being two allowed spin transitions (m = +1 → m = 0, and m = 0 → m = -1). [6]

The ^{13}CO chemical shifts in terms of Euler angles α, β, and γ is given by:

$$\sigma=\sigma_{xx}\cos^2\alpha+\sigma_{yy}\cos^2\beta+\sigma_{zz}\cos^2\gamma \qquad 1.57$$

Where α,β, and γ are the angles between B_0 and the three PAF axes (Figure 1.6c). σxx, σ_{yy} and σ_{zz} are the three principal values associated with the PAF.

In solutions or in solids under MAS (refer to MAS section), the isotropic chemical shift as is given by:

$$\sigma_{iso}=\frac{1}{3}\left(\sigma_{xx}+\sigma_{yy}+\sigma_{zz}\right) \qquad 1.58$$

The total Hamiltonian for chemical shift is given by:

$$\hat{H}_{cs}=\left\{\sigma_{iso}\gamma\hbar B_0+\frac{1}{2}\delta_{cs}\hbar\left[3\cos^2\theta-1-\eta_{cs}\sin^2\theta\cos(2\phi)\right]\right\} \qquad 1.59$$

Where σ_{iso} is the isotropic chemical shift, $\delta_{cs}=-\gamma B_0(\sigma_{zz}^{PAF}-\sigma_{iso})$, and the asymmetry parameter η is given by; $\eta_{cs}=\frac{(\sigma_{yy}-\sigma_{xx})}{(\sigma_{zz}-\sigma_{iso})}$, θ and ϕ are the polar angles of $\mathbf{B_0}$ in PAF. The first term in equation 1.59 corresponds to isotropic chemical shift and the second term corresponds to anisotropic chemical shift. In powder sample all molecular orientations are present. Each different molecular orientation corresponds to different PAF relative to $\mathbf{B_0}$ and therefore has a different chemical shift associated with it. The spectrum will therefore appear as a powder pattern [4] (Figure 1.6b) with the lines from different molecular orientations. The lines of different orientations overlap and form a continuous shape. In a powder pattern, the relative intensity at a given frequency is proportional to the number of the molecules present at that particular orientation which have that particular frequency. Figure 1.7 shows the structure of n-th peptide plane in a protein backbone. [7] The ^{13}CO chemical shift of a protein backbone depends

on the orientation of σ relative to B_0 field. The most shielded principal component σ_{zz} is perpendicular to the peptide plane, whereas the least shielded component σ_{xx} makes an angle β ith respect to CN bond andσ_{yy} lies parallel to C=O bond.

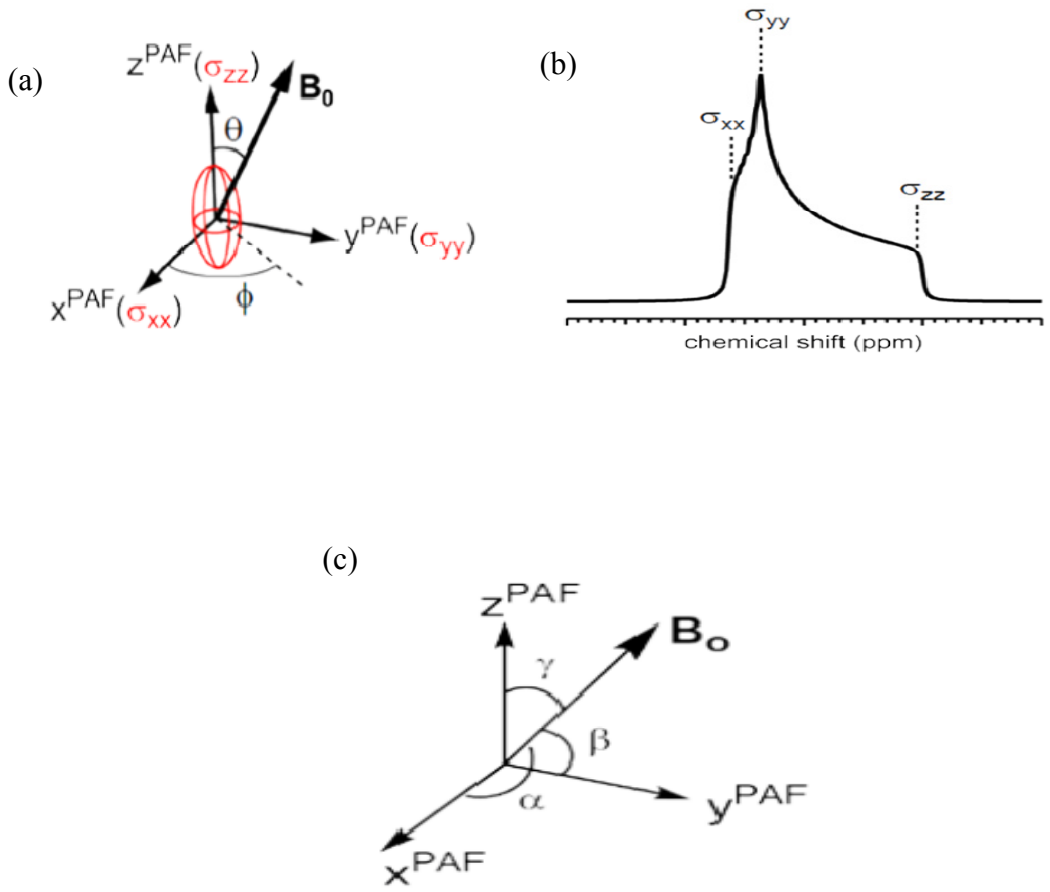

Figure 1.6. (a) PAF and shielding tensor (red). θ is the angle between $\mathbf{B_0}$ and the z-axis of PAF. ϕ is the angle between the x-axis of PAF and the projection of $\mathbf{B_0}$ in the xy-plane of PAF. (b) The principal values associated with PAF are σ_{xx}, σ_{yy} and σ_{zz} which also correspond to three principal values of chemical shifts in the powder pattern. (c) Definition of Euler angles, α, β, and γ with respect to $\mathbf{B_0}$ field. [6]

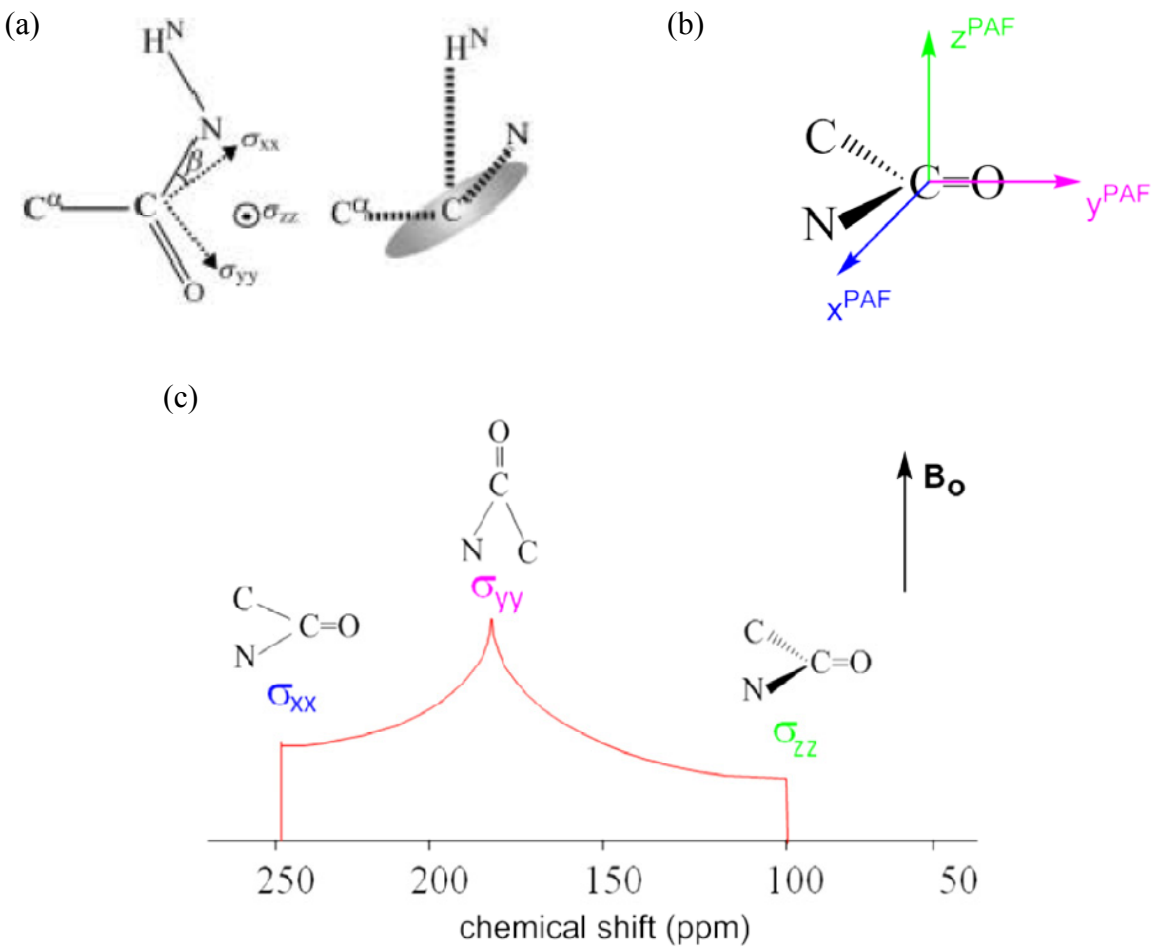

Figure 1.7. (a) Structure of peptide plane in a protein. The grey ellipsoid shows the CSA tensor of ^{13}CO. (b) The PAF of ^{13}CO in protein backbone. The x^{PAF} and y^{PAF} are in the C -CO- N plane whereas the z^{PAF} is perpendicular to the C-CO-N plane. (c) CSA powder pattern of ^{13}CO. σ_{xx} = 247 ppm, σ_{yy} = 176 ppm and σ_{zz} = 99 ppm corresponds to three chemical shifts. Note that the most shielded component σ_{zz} appears at lower chemical shift (upfield) and the least shielded component σ_{xx} is at higher chemical shift (downfield).

1.2 NMR Methods

1.2.1 Magic Angle Spinning (MAS)

In solution NMR spectra, effects of CSA, dipolar coupling etc are rarely observed. This is because of the rapid molecular tumbling of the molecules in a solution averages the molecular orientation dependence and as a result sharp narrow peaks are observed. Whereas in solid state NMR there is no such molecular tumbling and as a result the anisotropic interactions are not averaged out giving broad NMR peaks. To get high resolution solid state NMR spectra, MAS was developed.[8] MAS spinning achieve the same result for the solids because under MAS all the anisotropic interactions are averaged out. As a result only the isotropic chemical shift is observed. However, in order for MAS to reduce the powder pattern to a single isotropic shift the rate of MAS should be greater than the anisotropy of the interaction that is being averaged out. Slower spinning produces a set of spinning sidebands in addition to the isotropic line. The spinning sidebands are sharp lines set at a spinning rate apart that radiate out from the isotropic line (see figure 1.9). Figure 1.8 displays the geometry of the MAS; the angle between the rotor axis or the spinning axis and the external magnetic field $\mathbf{B_0}$, α, is the magic angle and is equal to 54.7°. In Figure 1.8, θ is the angle between the ^{13}C- ^{15}N internuclear vector and $\mathbf{B_0}$, α is the angle between the rotor axis and $\mathbf{B_0}$ and β is the angle between the rotor axis and the ^{13}C – ^{15}N internuclear vector. When the sample is spin at MAS (α = 54.7°), then the angle θ varies with time as the molecule rotates with the sample. Then the average of $3\cos^2\theta(t)$ -1 over each rotor period becomes:

$$\left\langle 3\cos^2\theta(t)-1\right\rangle=\frac{1}{2}(3\cos^2\alpha-1)\left(3\cos^2\beta-1\right)=0 \qquad 1.60$$

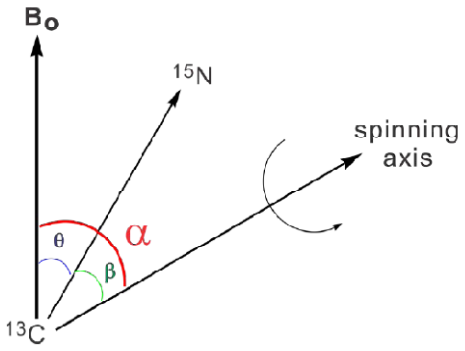

Figure 1.8. Schematic representation of the geometry of the ^{13}C – ^{15}N vector in solid state NMR sample under MAS. The sample is spun rapidly in a cylindrical rotor about a spinning axis oriented at the magic angle ($\alpha = 54.7°$) with respect to $\mathbf{B_0}$.

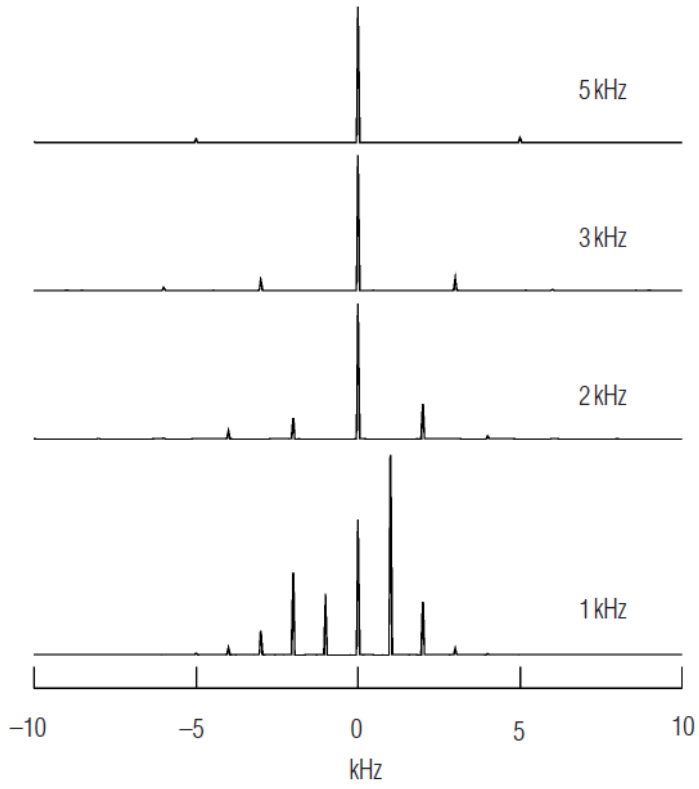

Figure 1.9. The effect of slow rate of MAS. A set of spinning sidebands appears with the isotropic shift. The spinning sidebands are spaced at the spinning frequency. [1]

Where the angles θ, α, and, β are described in Figure 1.8. This technique averages the anisotropy associated with the interactions that causes a shift in the Zeeman energies (eg CSA, heteronuclear dipolar coupling, etc) but no mixing of the Zeeman states. However, it has an effect on secular interactions which mixes the Zeeman functions i.e. homonuclear dipolar coupling.

1.2.2 Cross Polarization (CP)

Cross polarization is usually used to assist in observing dilute spins like ^{13}C. The two major disadvantages in observing dilute or rare spins are;

1. Low sensitivity - low sensitivity is a result from the low natural abundance of rare nuclei.
2. Long relaxation times or T_1 - the relaxation times of the rare nuclei tend to be very long.

For the spin ½ nuclei, the nuclear spin energy is coupled to the surrounding environment or the lattice by the fluctuating magnetic fields. The strength of the coupling and therefore the rate at which the spins will return to the equilibrium is governed by the gyromagnetic ratios (γ). All of the spin ½ NMR nuclei of rare isotropic abundance have relatively low γ, and therefore have long T_1 values. The long T_1 values means that long gaps must be left in between the scans. In solid state NMR experiments several thousand scans are required to lower the noise to a suitable level, the spectra can tale a very long time to collect.

The most commonly used method to increase the sensitivity and decrease the experiment time is by transferring the polarization from the abundant nuclei (usually ^{1}H) to the rare nuclei (eg ^{13}C). The transfer is known as cross polarization (CP) and the pulse sequence is shown in Figure 1.10.

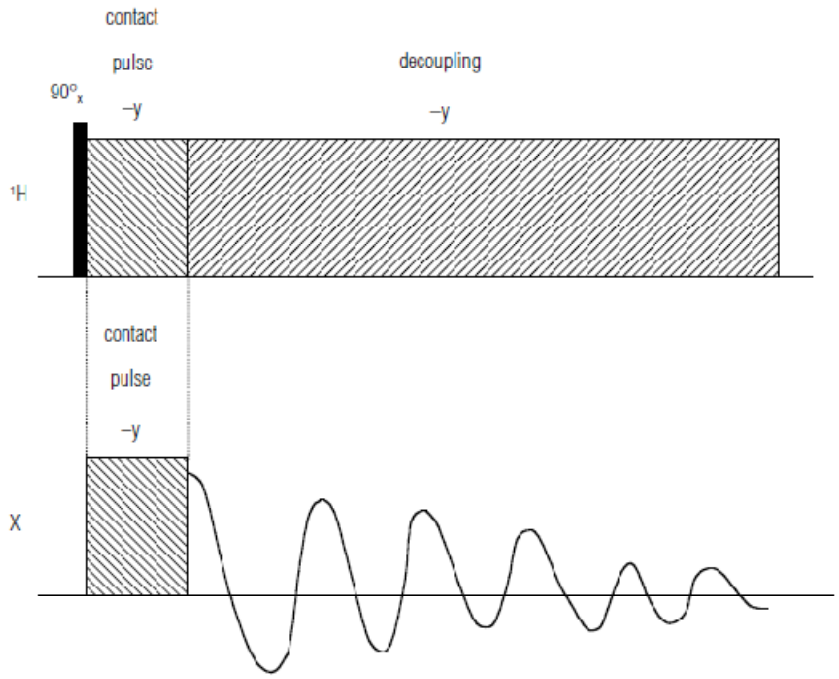

Figure 1.10. The CP pulse sequence. The effect of the CP pulse sequence is to transfer magnetization from the abundant spins (^{1}H) to the rare spins, X (eg. ^{13}C) via the heteronuclear dipolar coupling between the ^{1}H and X spins.

The CP transfer occurs in the doubly rotating frame, the one in which the ^{1}H B_1 field is static and the other in which the X spin B_1(X) field is static. The first step of CP is to apply a ^{1}H 90° pulse to rotate the ^{1}H magnetization along -y axis. Next the ^{1}H contact pulse is then applied along -y-direction to spinlock the ^{1}H magnetization along –y axis. The spinlock field for ^{1}H is represented by $\mathbf{B_1}(^1\mathrm{H})$. At this point the rf in the X channel is switched on and the amplitude of the magnetic field B_1(X). Now the amplitudes of the two contact pulses in the CP experiment are set so as to achieve the Hartmann-Hahn matching condition: [9, 10]

$$\gamma_H B_1(^1H) = \gamma_X B_1(X) \qquad 1.61$$

In practical terms, it means that the length of the $\pi/2$ pulse is same for the ^{1}H and X spins. During the few milliseconds of the simultaneous irradiation, a substantial magnetization

develops in the irradiation axis of X-spin due to the heteronuclear dipolar coupling between ^{1}H and X. At equilibrium the degree of ^{1}H and X magnetization is given by; $M_0(H) \propto \frac{\gamma_H \mathbf{B_0}}{T_L}$ and $M_0(C) \propto \frac{\gamma_C \mathbf{B_0}}{T_L}$ respectively, where T_L = lattice temperature. Therefore the magnetization for different nucleus is proportional to their respective γ's and is given by:

$$\frac{M_0(H)}{M_0(X)} = \frac{\gamma_H}{\gamma_X} \qquad 1.62$$

In case of ^{1}H → ^{13}C CP, a gain in $\frac{\gamma_H}{\gamma_C} = \frac{26.75}{6.73} \approx 4$ is apparent. Following a ^{13}C FID, the ^{13}C magnetization is nearly zero but the ^{1}H magnetization is not zero as it is spinlocked. Eventually, the ^{1}H magnetization will be attenuated because; (i) transfer of M_0 (H) → M(X) and, (ii) the decay of ^{1}H magnetization due to $T_1\rho$. $T_1\rho$ is the relaxation in the rotating frame of magnetization along the B_1 field of the spinlock pulse. $T_1\rho$ is essentially a decay of transverse magnetization in the rotating frame under spinlock field.

The Hartman-Hahn conditions can be explained as follows;

In the doubly rotating reference frame of Zeeman interactions, the Hamiltonian can be written as:

$$\hat{H}_R = \omega_{1H}\hat{I}_y + \omega_{1X}\hat{S}_y + \omega_{HX}\hat{I}_z\hat{S}_z \qquad 1.63$$

Where, ω_{1H} and ω_{1X} is the rf frequency, ω_{HX} is a constant and all other Hamiltonian terms have been omitted. When Hartmann-Hahn condition is matched $\omega_{1H} = \omega_{1C} = \omega_{1,}$ equation 1.63 reduces to:

$$\hat{H}_R = \omega_1(\hat{I}_y + \hat{S}_y) + \omega_{HX}\hat{I}_z\hat{S}_z \qquad 1.64$$

The two terms in the equation 1.64 does not commute. When $\omega_1 >> \omega_{HX}$, transforming equation 1.63 to the interaction frame $\omega_1(\hat{I}_y + \hat{S}_y)$, equation 1.64 can be written as:

$$\omega_{HX}\hat{I}_z\hat{S}_z \xrightarrow{\omega_1(\hat{I}_y+\hat{S}_y)} \omega_{HX}\left[\hat{I}_z\cos(\omega_1 t)+\hat{I}_x\sin(\omega_1 t)\right]\left[\hat{S}_z\cos(\omega_1 t)+\hat{S}_x\sin(\omega_1 t)\right]=\hat{H}^{\text{int}} \qquad 1.65$$

where $\hat{H}^{\text{int}}$ represents Hamiltonian in the interaction frame. Keeping only the secular terms:

$$\hat{H}^{\text{int}} = \omega_{HX}\left[\hat{I}_z\hat{S}_z + \hat{I}_x\hat{S}_x\right] \qquad 1.66$$

which is the first order average Hamiltonian and commutes with $\omega_1(\hat{I}_y + \hat{S}_y)$. The equation 1.66 represents a form of heteronuclear dipolar coupling that causes the magnetization transfer from I spins to S spins due to the components $\hat{I}_z\hat{S}_z$ and $\hat{I}_x\hat{S}_x$. This is explained below for a pair of spin ½ nuclei. Initially after the $90°_x$ pulse on the I channel, only y magnetization of the I nucleus exists: therefore,

$$\rho(0)=\hat{I}_y \qquad 1.67$$

and $\hat{H}^{\text{int}} = \omega_{HX}\left[\hat{I}_z\hat{S}_z + \hat{I}_x\hat{S}_x\right]$

For the time evolution, we have to evaluate the expression:

$$\hat{\rho}(t) = \hat{\rho}(0)\cos(\omega t) - i\frac{\hat{r}_1}{\omega}\sin(\omega t) \qquad 1.68$$

Now ,

$$\hat{r}_1 = \left[\hat{H},\hat{\rho}(0)\right] = \omega_{HX}\left[\hat{I}_z\hat{S}_z + \hat{I}_x\hat{S}_x, \hat{I}_y\right] = i\omega_{HX}(\hat{S}_z\hat{I}_x - \hat{S}_x\hat{I}_z) \qquad 1.69$$

Now using equation 1.69 into the time evolution expression 1.68, we get:[4]

$$\mathbf{I}_y \xrightarrow{(\hat{S}_z\hat{I}_z+\hat{S}_x\hat{I}_x)} \mathbf{I}_y\frac{1}{2}(1+\cos\omega_{HX}t)+\mathbf{S}_y\frac{1}{2}(1-\cos\omega_{HX}t)+(\mathbf{S}_z\mathbf{I}_x-\mathbf{S}_x\mathbf{I}_z)\sin\omega_{HX}t \qquad 1.70$$

In the equation 1.70, a term proportional to $\mathbf{S_y}$ appears and represents the magnetization transfer from $\mathbf{I_y} \rightarrow \mathbf{S_y}$. If the Hartmann-Hahn condition is not met there is no secular part in equation 1.66.

1.2.3 Rotational Echo Double Resonance (REDOR)

REDOR has been extensively used in solid state NMR to recouple the heteronuclear dipolar couplings under MAS with the subsequent determination of the internuclear distances in the spin system. This technique was developed by Gullion and Schafer. [11] In REDOR a series of rotor synchronized π-pulses are applied to S-channel to recouple the heteronuclear dipolar coupling under MAS. Since the heteronuclear dipolar coupling strength is inversely proportional to r^3, REDOR method is very sensitive to the separation between the coupled spins. Figure 1.11 represents the ^{13}C – ^{15}N REDOR pulse sequence.

At the beginning of the REDOR pulse sequence there is a cross polarization pulse sequence to transfer the ^{1}H magnetization to ^{13}C nucleus. As discussed in the previous section, to get an efficient cp Hartmann-Hahn condition should be fulfilled and is given by equation 1.61.

The above condition holds good if there is no resonance offset. However, in real experiments there is a resonance offset field, $\mathbf{B_{r.o.}}$. In presence of $\mathbf{B_{r.o}}$, the effective magnetic field $\mathbf{B_{eff}}$ the Hartmann-Hahn condition is reduces to:

$$\gamma_H B_{eff}(^1H) = \gamma_C B_{eff}(^{13}C) \qquad 1.71$$

Where, $\mathbf{B_{eff}} = \sqrt{(\mathbf{B_1} + \mathbf{B_{r.o.}})^2}$. The equations describe the Hartmann- Hahn matching conditions for static sample. However under MAS, the above equation is modified because the MAS affect the $^{1}H \rightarrow {}^{13}C$ dipolar coupling. For example, the closest distance between the ^{13}CO backbone label and ^{1}H is ~ 2 Å in a peptide. So the largest dipolar coupling present in the peptide sample is ~ 4 kHz. In REDOR experiments, the MAS speed is 9 kHz and so the ~ 4kHz ^{13}C – ^{1}H dipolar

coupling is supposed to average out. Although the ^{13}C - ^{1}H dipolar coupling is supposed to average out, the ^{1}H -^{1}H dipolar coupling is not averaged out under 9 kHz MAS. This is because in peptides the ^{1}Hs are dipolar-coupled as a network and as a result there is a rapid flip-flop ($\alpha \leftrightarrow \beta$ transition) between the ^{1}Hs via ^{1}H - ^{1}H homonuclear dipolar coupling. The rate of $\alpha \leftrightarrow \beta$ transition on the ^{1}H spin is fast relative to the strength of the ^{1}H - ^{1}H dipolar coupling (typically in the range of 10 – 50 kHz). [12] Therefore under 9 kHz MAS, the ^{1}H flip-flop disrupts the averaging of the ^{1}H – ^{13}C dipolar coupling over each rotor period and results in efficient polarization transfer. Therefore, the match condition under MAS is given by:[13]

$$\gamma_H B_{eff}(^1H) = \gamma_C B_{eff}(^{13}C) + n\omega_R \qquad 1.72$$

where, ω_R = MAS frequency and n = 0, ±1, ±2 and represents the nth spinning sideband. MAS introduce time dependence into the dipolar coupling. Therefore under MAS the $\hat{H}_{HC}$ terms is no longer constant and oscillates between $\pm\omega_R$, $\pm 2\omega_R$ because $\hat{H}_{HC} \propto \left[3\cos^2\theta(t) - 1\right]$ and θ becomes time-dependent.

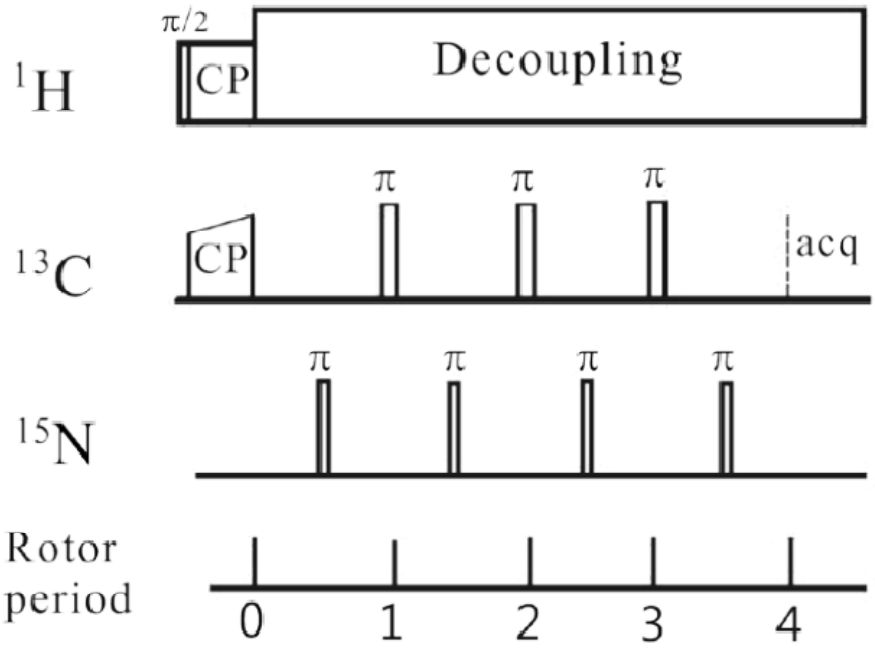

Figure 1.11. A typical REDOR NMR pulse sequence. In this case, the observed spin is ^{13}C and the dephased spin is ^{15}N.

In REDOR experiment, a ramp is applied to the ^{13}C spinlock field. This is because there is a distribution of Larmor frequencies and the resonance offset field, $\mathbf{B_{r.o.}}$ As a result, in a powder sample, molecules with different orientations are associated with different cross-polarization efficiencies. Therefore, a ramped CP is used to increase the efficiency of the magnetization transfer from ^{1}H → ^{13}C under MAS.

After ^{1}H → ^{13}C CP, REDOR is performed in two parts; one with rotor synchronized dephasing pulses (S_1) and one without dephasing pulses (S_0). As discussed earlier the heteronuclear dipolar coupling Hamiltonian is given by:

$$\hat{H}_D^{CN} = -\frac{\mu_0}{4\pi}\hbar\frac{\gamma_C\gamma_N}{r^3}\frac{1}{2}(3\cos^2\theta - 1)2\hat{C}_z\hat{N}_z \qquad 1.73$$

where, C and N represent the ^{13}C and ^{15}N respectively. This interaction can be split into three key contributions; space part, C spin and N spin part. The space part is affected by MAS whereas

the application of the π-pulses modulate the spin part. The function of π-pulse is to flip the spins by 180° (for example, x → -x). This changes the sign of the dipolar coupling for the observed spins coupled to the dephasing spins which leads to the reversal of the sense of the rotation of the observed spins. In S_0 experiment, the $^{13}C - ^{15}N$ dipolar coupling is averaged out over each rotor period. Additionally, ^{13}C CSA is also averaged out by MAS. Rotor synchronized π-pulses on ^{13}C channel refocus the ^{13}C isotropic chemical shift. Acquisition coincides with the completion of the rotor cycle. Figure 1.12 illustrates how the dipolar interactions are averaged out by MAS. In the S_1 experiment, π-pulses are applied at the middle of each rotor period of ^{15}N-channel. Figure 1.13 illustrates how the ^{15}N π-pulses recouples the $^{13}C - ^{15}N$ dipolar coupling under MAS. The sign change of the Hamiltonian in the later half of each rotor period as an oscillating space component is cancelled by the ^{15}N π-pulses at the middle of each rotor period. The π-pulses are positioned in the middle of each rotor period to ensure that the dipolar coupling is accumulated from one cycle to the next. The impact of the accumulated dipolar coupling results in the reduction of the observed echo intensity.

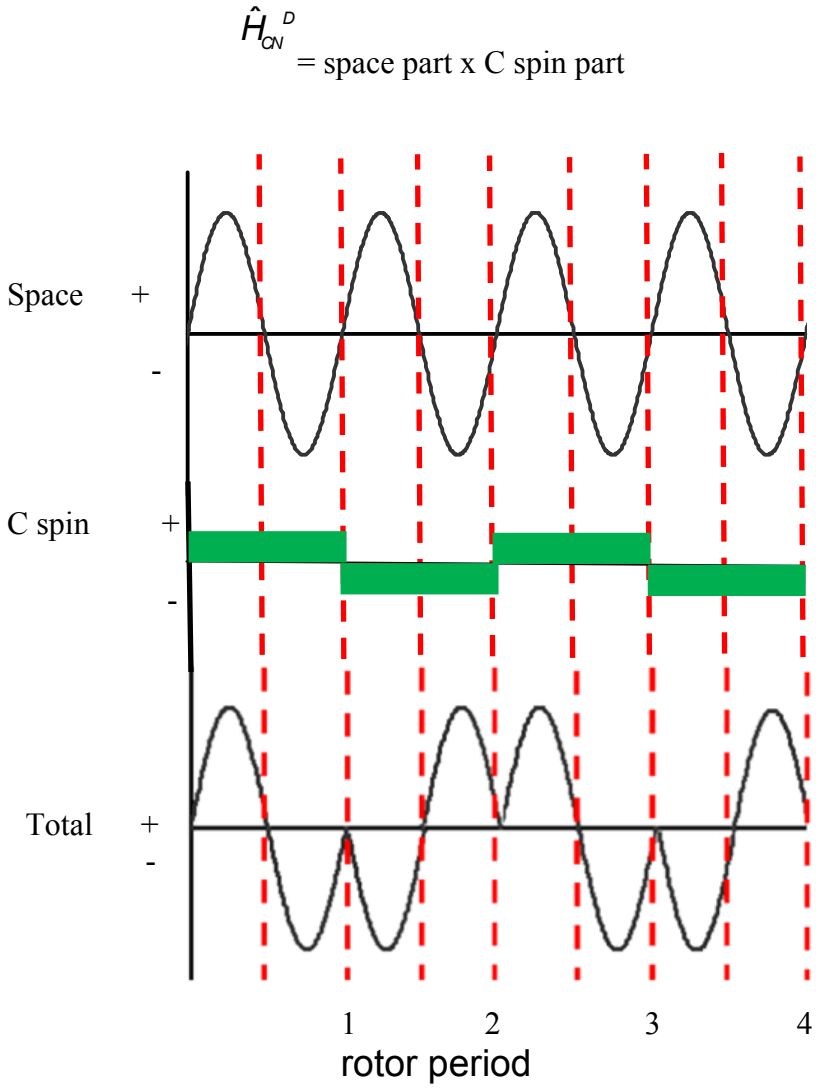

Figure 1.12. Evolution of dipolar coupling as a function of rotor period in S_0 experiment. Rotor synchronized ^{13}C π-pulses does not interfere with the MAS averaging of the heteronuclear dipolar interaction.

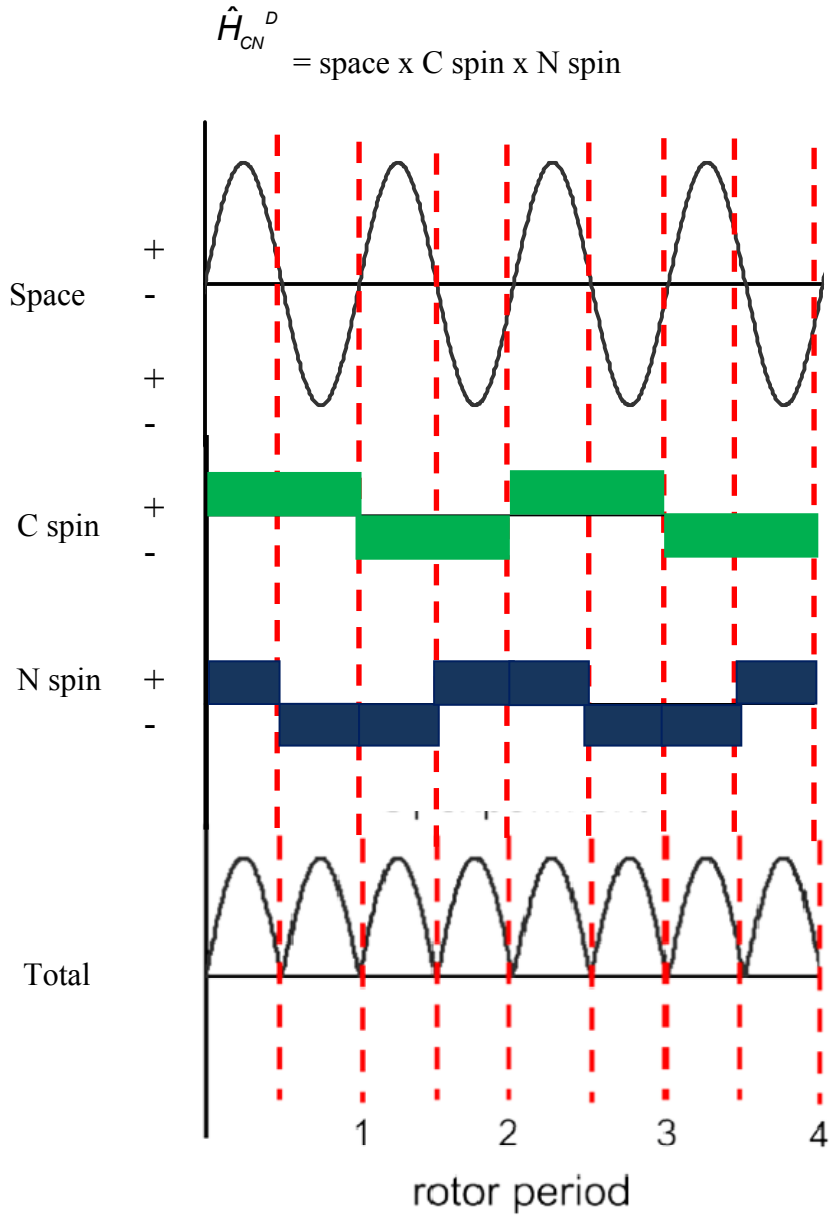

Figure 1.13. Evolution of dipolar coupling as a function of rotor period in S_1 experiment. Rotor-synchronized ^{15}N π-pulses prevent MAS averaging of the heteronuclear dipolar coupling.

The density operator for the S_1 experiment is given by:

$$\hat{\rho}(t) = \exp\{-i\tilde{\omega}_{CN} 2C_z N_z t\} C_x \exp\{i\tilde{\omega}_{CN} 2C_z N_z t\}$$
$$= C_x \cos(\tilde{\omega}_{CN} t) + 2C_y \mathbf{N}_z \sin(\tilde{\omega}_{CN} t) \quad 1.74$$

Where, $\tilde{\omega}_{CN}(t) \propto \frac{3\cos^2\theta(t) - 1}{r^3}$ and is the average dipolar coupling frequency over each rotor period. $C_y^2 = 1$ and tr($\mathbf{N_z}$) =0 and $C_y$tr ($\mathbf{N_z}$) = 0, therefore only the S_x component represents the observable magnetization 0). Due to the distribution of the θ in powder sample, there is also a distribution of $\tilde{\omega}_{CN}$ in the powder sample and as a result there is a decay in the ^{13}C transverse magnetization as a function of dephasing time, τ. Therefore, the integrated ^{13}C signal intensity of S_1 spectrum is smaller than S_0 spectrum. In REDOR the difference in the signal intensity for the ^{13}C spin for S_0 and S_1 experiment is given by:

$$\frac{\Delta S}{S_0} = \frac{(S_0 - S_1)}{S_0} \quad 1.75$$

The ($\Delta S/S_0$) buildup at different τ can be fitted using SIMPSON program [14] or the analytic solution of the dipolar dephasing to obtain the dipolar coupling. [15] Once the ^{13}C – ^{15}N dipolar coupling is known, the internuclear distance can be calculated using the equation:

d_{CN} (Hz) = 3066 / r^3 (Å). 1.76

1.2.4 Quadrupolar Echo (QUECHO)

A solid or quadrupolar echo refocuses the time evolution of spins such as homonuclear spin ½ or quadrupolar coupling. [4] It is generated by a 90° pulse applied at a time τ_1 after the application of a 90° excitation pulse. The two 90° pulses must be out of phase. The echo maximum is observed at a time τ_1 after the second pulse. Figure 1.14 shows the pulse sequence of the solid echo or quecho experiment. The solid echo can be generated for quadrupolar interaction by the application of 90° pulse. If the pulse is applied at a time τ_1 after the start of the precession in the xy-plane, the echo occurs with its maximum at a time τ_1 after the pulse. The echo can be derived quantum mechanically by using density operator formalism:

$$\hat{\rho}(t)=\hat{U}(t)\hat{\rho}(0)\hat{U}^{-1}(t)$$

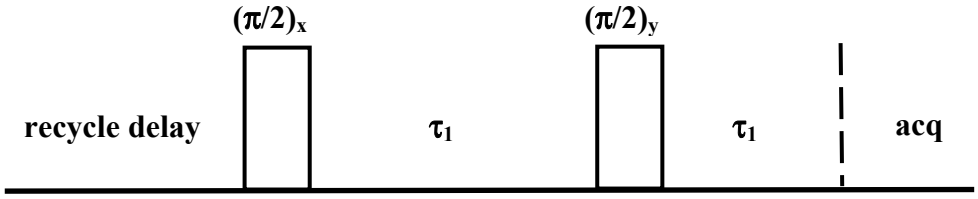

Figure 1.14. Solid echo pulse sequence. The quecho pulse sequence is used for ^{2}H T_2 measurements. Theoretically $\tau_1 = \tau_1$ and the total time is $2\tau_1$.

For the quadrupolar coupling $\hat{H}_Q = \omega_Q(\hat{I}_z^2 - \frac{1}{3}I^2)$ the evolution operator is:

$$\begin{aligned}\hat{U}(2\tau_1) &= \exp(-i\hat{H}_Q\tau)\exp(-i\frac{\pi}{2}\hat{I}_y)\exp(-i\hat{H}_Q\tau)\exp(-i\frac{\pi}{2}\hat{I}_x)\\ &= \exp(-i\hat{H}_Q\tau)\exp(-i\bar{\hat{H}}_Q\tau)\exp(-i\frac{\pi}{2}\hat{I}_y)\exp(-i\frac{\pi}{2}\hat{I}_x)\\ &= \exp\{-i(\hat{H}_Q+\bar{\hat{H}}_Q)\tau\}\exp(-i\frac{\pi}{2}\hat{I}_y)\exp(-i\frac{\pi}{2}\hat{I}_x)\\ &\approx \exp(i\bar{\bar{\hat{H}}}_Q\tau)\exp(-i\frac{\pi}{2}\hat{I}_y)\exp(-i\frac{\pi}{2}\hat{I}_x)\end{aligned} \quad 1.77$$

Where,

$$\begin{aligned}\bar{\hat{H}}_Q &= \omega_Q(\hat{I}_x^2-\frac{1}{3}I^2)\\ \bar{\bar{\hat{H}}}_Q &= \omega_Q(\hat{I}_y^2-\frac{1}{3}I^2)\end{aligned} \quad 1.78$$

Equation 1.77 depends on the relation

$$\begin{aligned}&\hat{H}_Q+\bar{\hat{H}}_Q+\bar{\bar{\hat{H}}}_Q=0\\ &\therefore \hat{H}_Q+\bar{\hat{H}}_Q=-\bar{\bar{\hat{H}}}_Q\end{aligned} \quad 1.79$$

$$[\hat{H}_Q,\bar{\hat{H}}_Q]=0$$

For spin-1 nuclei .When quadrupolar sequence is applied to initial stage $\rho(0) \propto I_z$,

$$\begin{aligned}\hat{U}(2\tau_1) &\approx \exp(i\bar{\bar{\hat{H}}}_Q\tau)\exp(-i\frac{\pi}{2}\hat{I}_y)\exp(-i\frac{\pi}{2}\hat{I}_x)\ \hat{I}_z\ \exp(i\frac{\pi}{2}\hat{I}_x)\exp(i\frac{\pi}{2}\hat{I}_y)\exp(-i\bar{\bar{\hat{H}}}_Q\tau)\\ &= \exp(i\bar{\bar{\hat{H}}}_Q\tau)\ (-\hat{I}_y)\exp(-i\bar{\bar{\hat{H}}}_Q\tau)\\ &= -I_y\end{aligned} \quad 1.78$$

For $\hat{\rho}(0)=\hat{I}_y$ created by the 90° x-pulse from z-magnetization, we see that the echo condition $\hat{\rho}(2\tau_1)=\hat{U}(2\tau_1)\hat{I}_y\hat{U}^{-1}(2\tau_1)=-\hat{I}_y$ based on the relation $[\hat{I}_y,\bar{\bar{\hat{H}}}_Q]=0$. Thus the state of the spin system and the signal at time $2\tau_1$ are the same as at time 0. Moreover, the solid echo is independent of the sign of the second 90° refocusing pulse.

1.3 Introduction to the Influenza

Influenza commonly known as the flu is a contagious respiratory tract illness caused by the influenza virus. Influenza viruses cause infections of variable severity in humans, other mammals and birds. According to WHO, influenza infects ~ 3-5 million people each year causing ~ 250,000 – 500,000 deaths annually across the world. In the US alone, there are ~ 200,000 hospitalizations and ~ 36,000 deaths reported each year. [16] In the last ~100 years there were four major influenza outbreaks- 1918, 1957, 1968 and 2009. Influenza pandemics are associated with large number of deaths. For example, the Spanish flu claimed ~ 50 million deaths in 1918 – 1919. Flu viruses are constantly changing and mutating and these changes can occur slowly (antigenic drift) or suddenly (antigenic shift). As a result, each year people get infected with a new strain of virus. Despite having an influenza vaccine, flu virus poses a significant threat to human health.

Influenza virus is an enveloped virus which means that the viruses are encapsulated with a membrane acquired during the budding process from an infected cell. Enveloped viruses enter the host cells by fusing their lipid membrane with a cellular membrane. After the fusion of the viral and the host cell membranes, a fusion pore is formed which allows the transfer of the viral genome into the host cell. [17-19] The free energies of the membranes before and after fusion are approximately the same; the rates of membrane fusion are negligible in absence of catalyst. For this reason the fusion proteins present in the enveloped viruses catalyze the fusion process. Typically for the class-1 viral fusion proteins (eg hemagglutinin, the fusion protein of influenza virus) the ~ 25 residue N-terminal region is relatively hydrophobic and plays an important role in the process of membrane fusion. [20] The N-terminal region is termed fusion peptide (fp). The synthetic analogs of fp in absence of the rest of the fusion protein induce vesicle fusion. In

addition, the site directed mutational studies in the fp region showed similar mutation-fusion activity relationship with the viral/cell fusion.[21, 22] Therefore, it is important to understand the structure of fp to understand the mechanism of fusion which will eventually aids in vaccine development.

The overall goal of the research presented in this dissertation is to understand the fp-induced membrane fusion. Influenza viral fusion is induced by the pH (fusion pH of influenza ≈ 5) change and is one of the most studied systems for fusion research. However, the exact mechanism of flu infection is still under debate. For this research my approach has been to study the structure of influenza fusion peptide (HAfp) in membranes and then the structure was correlated with the function by performing vesicle fusion assays. My second project is to develop a new solid state NMR method which probes the local motion of the lipids adjacent to the peptide.

1.3.1 Influenza virus

Influenza is an Orthomyxovirus and is pleomorphic i.e. they differ greatly in shape and size. [23] Flu viruses can be filamentous or spherical. However, the pathogenic flu viruses are mainly filamenteous (100 nm by 20 μm). Spherical flu viruses have diameter of ~ 80 – 120 nm. The viral envelope contains three proteins: hemagglutinin (HA), which is present ~ 500 copies per virion; neuraminidase (NA), which is present ~ 100 copies per virion; and M2 channel, with ~ 14 – 68 copies per virion. HA and NA protrude as spikes from the viral envelope. [24]

The fusion protein HA is a homotrimer in viral membrane and consists of two subunits: HA1 and HA2 subunit. [25] The HA1 subunit is responsible for attachment of the virus with the host cell by binding with the sialic acids present on the cell surface glycoproteins. The HA2 plays an important role in membrane fusion. An important function of NA is to cleave the terminal

neuraminic acids (sialic acids) from glycoproteins. Newly released viruses can potentially aggregate by binding of HA to the sialic acids present on the cell surface. NA cleaves the sialic acids and thereby releases the viruses allowing them to spread. [26] The different subtypes of the influenza virus are based on the surface proteins HA and NA. For example, H1N1, H3N1 etc, where H1 refers to the H1 subtype of HA protein and N1 refers to the N1 subtype of NA protein. There are 18 different HA subtypes (H1 to H18) and 11 different NA (N1 to N11) subtypes, and many combinations of HA and NA are possible.[27] M2 is an integral proton channel and helps in the release of nuclear-proteins (NP) from endosomes. [24, 28] The matrix protein or M1 protein is associated with the interior side of the viral envelope and is active during viral morphogenesis. The NP is the main component of viral nucleocapsid. The basic arginine rich NP is associated with each single stranded RNA. The RNA genome is associated throughout its entire length with the NP polypeptide which mediates its transport to the nucleus. The P protein complexes PB1, PB2 and PA are attached at the end of the genomic segments. PB1, PB2 and PA have RNA-dependent RNA polymerase activity. The nuclear export protein (NEP) is present in small amount and is responsible for export of viral RNPs from the nucleus into the cytoplasm. [28, 29] Figure 1.15 displays a schematic representation of a influenza virus. [30]

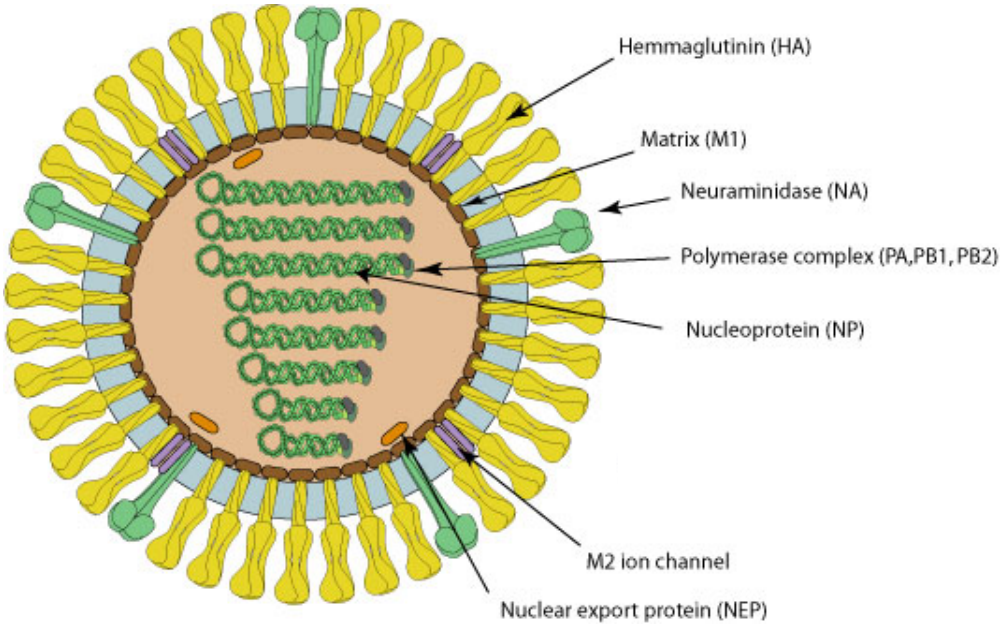

Figure 1.15. Schematic represention of the structure of influenza virus. [30] The single stranded genome is constituted of eight segments which are complexed with nucleoprotein. The nucleocapsid segments are surrounded by the envelope containing three membrane proteins.

1.3.2 Cell biology of influenza virus

Influenza virus uses endocytic pathway to enter the host cell. Influenza infection starts when the HA1 subunit of the virus binds to the sialic acid containing glycoproteins present on the surface of the host cell. [31] After the binding, the virus is internalized inside the host cell by the process of endocytosis. During the endocytic pathway, the pH of the endosomes drops to ~ 5. The low pH triggers some conformational change in the HA protein. [32, 33] As a result of the conformational changes, the N-terminus of the HA2 subunit (~ 23 residues) is exposed which plays an important part in fusion process. These conformational changes initiate fusion between the viral membrane and the endosomal membrane. After the fusion, the M1 protein and viral RNPs separate from each other and are released from the endosomes. Next the viral RNPs are transported to the nucleus where transcription and viral RNA synthesis occur. The newly assembled RNPs together with the M1 protein proceed toward the plasma membrane and they bud into mature virions. The viral membrane proteins are synthesized into endoplasmic reticulum and are separately transported to the plasma membrane where they combine with the budding viruses.

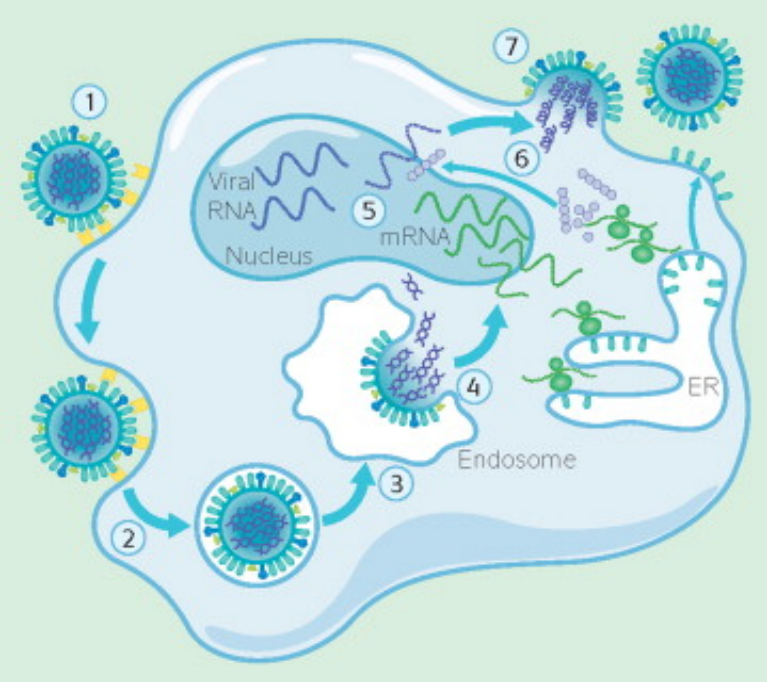

Figure 1.16. Life cycle of influenza virus. [34] (1) Binding of the virus to the sialic acid containing glycolipids; (2) - (3) Entry of the virus inside the cell by the process of endocytosis; (4) Fusion of the viral membrane and the endosomal membrane in acidic pH of the endosomes. (5) Transport of the viral RNAs to the nucleus. Influenza contains negative stranded RNA. First a positive stranded RNA or mRNA is transcribed from the negative sense RNA and the process is aided by the RNA polymerase initially present in the virus. (6) Next the mRNAs exit the nucleus. Synthesis of the viral protein components in the cytosol and endoplasmic reticulum. (7) The newly synthesized viral RNAs and the viral proteins proceed towards the host cell plasma membrane. Finally assembly and the budding of the progeny virus occur.

1.3.3 Proposed mechanism of membrane fusion

Membrane fusion is a process where two separate bilayers merge into a single bilayer. Figure 1.17 shows the different stages of the membrane fusion process. [35] For the influenza virus, the fusion protein is HA and is composed of HA1 and HA2 subunit. In Figure 1.17A, HA1 is represented by the blue cylinders and HA2 by red cylinders. Before influenza infection, the exterior of the virus is at pH ~ 7.4 (Figure 1.16). The crystal structure of HA protein at pH 7.5 showed that HA is a trimer formed by the association of three HA2 subunits and the three HA1 subunits, HA1 was situated outside the HA2 core (Figure 1.18a). [25] However, the crystal structure does not contain the transmembrane and the endodomain. After endocytosis, the pH of the endosomes drops to ~ 5 which causes a conformational change in the HA2 subunit. [32] The pH 7.5 structure undergoes drastic change during the process of fusion and is shown in figure 1.18b. Due to the conformational change, the N-terminal region of HA2 subunit gets exposed. The N-terminus of the HA2 domain interacts with target cell membrane and forms an extended intermediate also known as prehairpin intermediate. Several trimers are thought to be involved in the whole process. [35, 36] Next the protein refolding begins, and the energy released during the refolding process causes the membranes to bend towards each other. However, there is no experimental evidence for this energy released due to the protein refolding process. Then the formation of the hemifusion stalk happens which allows the mixing of the lipids present in the outer leaflets of the membranes. Finally the protein refolding completes, forming the stable form of the fusion protein. Only A and F structures have been observed by crystallography, but biochemical studies support many of the proposed steps. [25, 32, 37]

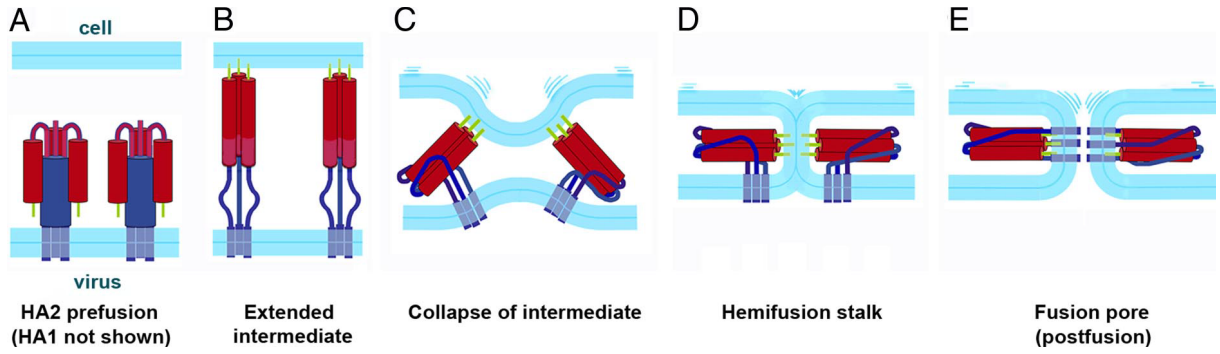

Figure 1.17. Proposed mechanism of membrane fusion. (A) In the prefusion state, the protein is attached to the viral membrane by a C-terminal transmembrane domain. (*B*) Low pH (pH ~ 5) triggers a conformational change in which the fusion peptide projects toward the target membrane, forming an extended intermediate that bridges the two membranes. (*C*) The intermediate collapses. (*D*) The collapse pulls the two membranes together, leading to formation of a hemifusion stalk. (*E*) A fusion pore opens up, and snapping into place of the membrane-proximal and transmembrane segments of the protein completes the conformational transition and stabilizes the fusion pore.

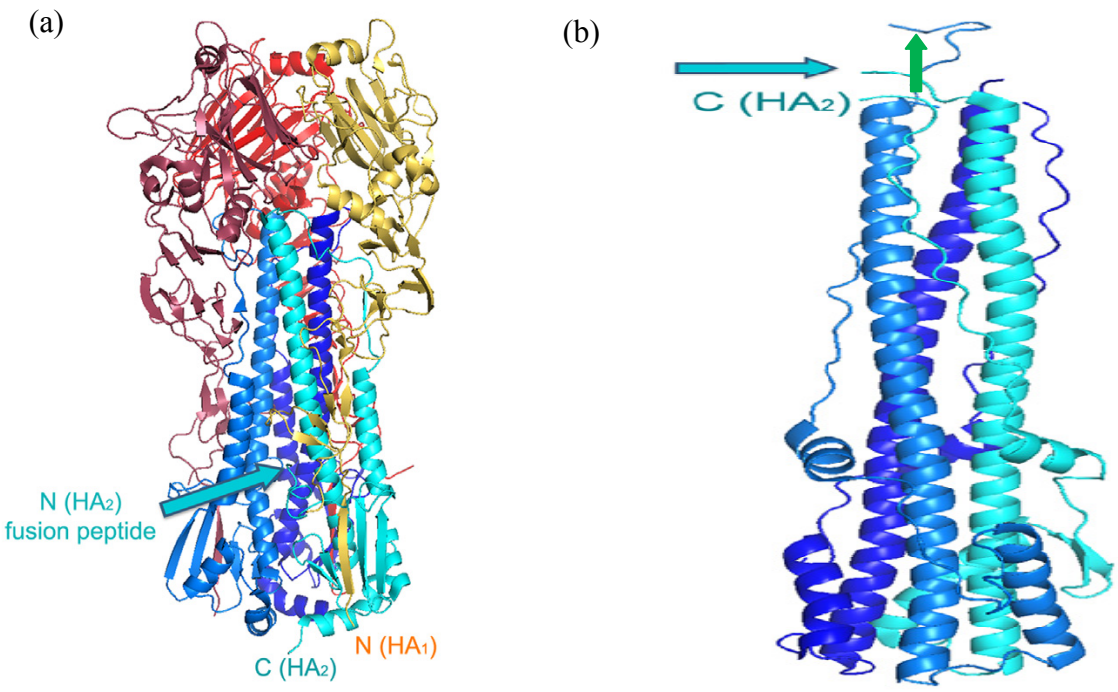

Figure 1.18. Pre- and post-fusion structures of HA. (a) HA ectodomain (Protein Data bank entries 1RD8 [25] and 1QU1 [32] for pre- and post fusion forms of the ectodomain, respectively).HA1 chains in shades of red/gold and HA2 chains in shades of blue (paired as red-blue, gold-cyan, and dark red-marine blue). The N-terminus of HA1 and the C-terminus of the HA2 ectodomain are labeled. Blue arrow: position of fusion peptides inserted near three fold axis in pre-fusion form. (b) Crystal structure of HA2 at pH 5. Only HA2 is shown. The N-terminus (green arrow; Note: the fusion peptide is not part of the structure shown) and C-terminus of the cyan-colored subunit is indicated.

1.3.4 Structural studies of hemagglutinin protein

Hemagglutinin is the fusion protein present in influenza virus and is required for the fusion process. HA is synthesized as a single ~85 kDa precursor polypeptide chain HA0. HA consists of two polypeptide chain; HA1 and HA2 and they are linked by a single disulphide bond. HA1 subunit contains 328 residues and HA2 subunit contains 185 residues. The HA1 subunit contains the sialic acid binding sites whereas the HA2 subunit contains the transmembrane domain near the C-terminus. Figure 1.18a shows the crystal structure of HA1 at pH 7.5. In the structure, the globular containing the sialic acid binding sites of HA1 subunit is present at the top of the structure. The long coiled- coil stem region consists of three alpha helices from HA2 subunit. In this pre-fusion state at pH 7.5, the fusion peptide is buried at the interface between monomers, ~ 35 Å from the virus bilayer and ~ 100 Å from the tip of the trimer. [25]

The crystal structure of the HA2 subunit at pH 5 is shown in Figure 1.18b. In this hairpin structure, the residues from 35 – 105 forms a long helix and short 180° turn followed by a short helix from the residues 113 – 129. [32] One problem of the pH 5 structure is that the crystal structure does not contain HA1 subunit. So it is not definitive that the structural changes at pH 5 are solely due to the effect of low pH or due the lack of HA1 subunit. A more difficult problem is that the conformational changes that are important for fusion are those that occur when HA is facing its target membrane, which might not be adequately modeled when HA is facing bulk water. Besides, the pH 5 structure lacking the transmembrane (TM) domain and also the first ~35 N-terminal residues that contains HAfp. The function of the TM domain is the anchoring of the HA2 to the viral envelope. In the crystal structure of HA2 at pH 5, both the TM domain and the N-terminus are at the same side, which is difficult to visualize/understand how the structural changes in the HA2 domain will cause destabilization of the host cell membrane and induce

fusion. However, there is a broad agreement that exposure of N-terminus of HA2 subunit is crucial for fusion activity of HA. The ~ 25 N-terminal residues of HA2 domain are known as influenza fusion peptide (*HAfp*). The HAfp region is relatively hydrophobic and is highly conserved. Out of 23 residues 18 residues are strictly conserved across 16 HA subtypes. [38] HAfp plays an important role in fusion activity; (1) the uncleaved HA0 is not fusion active; [39] (2) site specific mutations within the N-terminus of HA2 severely affect the fusion activity of HA. [40, 41] For example, there are eight Gly in the HAfp sequence and all of them are highly conserved. Mutation Gly-1 to Val or Glu will completely abolish the fusion activity of HA.

Peptides having similar sequence as the ~23 N- terminal residues of the HA2 subunit have been studied as models to understand the role of HAfp in the viral fusion process. There is evidence that supports the utility of studying the peptide model systems in the influenza fusion process: (1) HAfp promotes lipid mixing between the vesicles and destabilize the lipid bilayer. Lipid mixing is one characteristic of vesicle fusion. [42] (2) There is a correlation between the mutation – activity relation of HA- catalyzed fusion of cell membranes and HAfp induced vesicle fusion. [41] There are studies of HAfp with the same site specific mutations as were studied in the HAfp region of the full HA protein. Another interesting feature is that HAfp induces greater vesicle fusion at pH 5, the fusion pH of influenza, than at pH 7. Therefore the isolated HAfp can be used as a model system to study the interaction between the HAfp domain of HA protein and lipid membranes.

The main advantage of using isolated HAfp is that the structure of HAfp can be studied in detail in lipidic environment. Therefore, there have been several NMR studies on HAfp in detergents at both the low pH and pH 7. One NMR study concluded that in detergents, HAfp has an N-helix/ turn/ C-helix structure at pH 5 with an open interhelical geometry (interhelical angle ~

100°) and an N- helix/ turn/C-coil structure at pH 7. [43] Another NMR study showed that in detergents, HAfp adopts an N-helix/turn/C-helix structure at both pHs with a closed interhelical geometry with a ~ 158° interhelical angle. [44] A solid state NMR study of HAfp reported an N-helix/turn /C-helix structure in membranes lacking cholesterol. [45] A further detailed background on the NMR structures of HAfp is given the introduction of chapter 3.

REFERENCES

REFERENCES

1. Duer, M.J., *Introduction to Solid State NMR*. 2008: Blackwell.

2. Harris, R.K., *Nuclear Magnetic Resonance Spectroscopy*. 1986.

3. Tannoudji, C.C., *Quantum Mechanics*. Vol. 1. 1978: John Wiley & Sons Inc.

4. Schmidt-Rohr, K.a.S., H.W. , *Multidimensional Solid State NMR And Polymers*. 2005.

5. Keeler, J., *Understanding NMR Spectroscopy*. 2002.

6. Xie, L., *Solid State Nuclear Magnetic Resonance Studies Of Structures And Membrane Locations Of Peptides*, in *Chemistry*. 2014, Michigan State University.

7. Cisnetti, F., et al., *Determination Of Chemical Shift Anisotropy Tensors Of Carbonyl Nuclei In Proteins Through Cross-Correlated Relaxation In NMR.* Chemphyschem, 2004. **5**(6): p. 807-814.

8. Andrew, E.R., A. Bradbury, and R.G. Eades, *Nuclear Magnetic Resonance Spectra From A Crystal Rotated At High Speed.* Nature, 1958. **182**(4650): p. 1659-1659.

9. Hartmann, S.R. and E.L. Hahn, *Nuclear Double Resonance In Rotating Frame.* Physical Review, 1962. **128**(5): p. 2042-&.

10. Pines, A., M.G. Gibby, and J.S. Waugh, *Proton-Enhanced Nmr Of Dilute Spins In Solids.* Journal of Chemical Physics, 1973. **59**(2): p. 569-590.

11. Gullion, T. and J. Schaefer, *Rotational-Echo Double-Resonance NMR.* Journal of Magnetic Resonance, 1989. **81**(1): p. 196-200.

12. Yannoni, C.S., *High-Resolution NMR In Solids - The CPMAS Experiment.* Accounts of Chemical Research, 1982. **15**(7): p. 201-208.

13. Meier, B.H., *Cross Polarization Under Fast Magic Angle Spinning - Thermodynamical Considerations.* Chemical Physics Letters, 1992. **188**(3-4): p. 201-207.

14. Bak, M., J.T. Rasmussen, and N.C. Nielsen, *SIMPSON: A General Simulation Program For Solid-State NMR Spectroscopy.* Journal of Magnetic Resonance, 2000. **147**(2): p. 296-330.

15. Mueller, K.T., *Analytic Solutions For The Time Evolution Of Dipolar-Dephasing NMR Signals.* Journal of Magnetic Resonance Series A, 1995. **113**(1): p. 81-93.

16. WHO, W., *Influenza (Seasonal)* 2015.

17. Eckert, D.M. and P.S. Kim, *Mechanisms of viral membrane fusion and its inhibition.* Annual Review of Biochemistry, 2001. **70**: p. 777-810.

18. Dimitrov, D.S., *Cell biology of virus entry.* Cell, 2000. **101**(7): p. 697-702.

19. Hernandez, L.D., et al., *Virus-cell and cell-cell fusion.* Annual Review of Cell and Developmental Biology, 1996. **12**: p. 627-661.

20. Kielian, M. and F.A. Rey, *Virus membrane-fusion proteins: more than one way to make a hairpin.* Nature Reviews Microbiology, 2006. **4**(1): p. 67-76.

21. Durell, S.R., et al., *What Studies Of Fusion Peptides Tell Us About Viral Envelope Glycoprotein-Mediated Membrane Fusion.* Molecular Membrane Biology, 1997. **14**(3): p. 97-112.

22. Rafalski, M., J.D. Lear, and W.F. Degrado, *Phospholipid Interactions Of Synthetic Peptides Representing The N-Terminus Of HIV GP41.* Biochemistry, 1990. **29**(34): p. 7917-7922.

23. Harris, A., et al., *Influenza Virus Pleiomorphy Characterized By Cryoelectron Tomography.* Proceedings of the National Academy of Sciences of the United States of America, 2006. **103**(50): p. 19123-19127.

24. Bentz, J., *Viral Fusion Mechanisms*. 1993: CRC Press Inc.

25. Wilson, I.A., J.J. Skehel, and D.C. Wiley, *Structure Of The Hemagglutinin Membrane Glycoprotein Of Influenza-Virus At 3-A Resolution.* Nature, 1981. **289**(5796): p. 366-373.

26. Gubareva, L.V., L. Kaiser, and F.G. Hayden, *Influenza Virus Neuraminidase Inhibitors.* Lancet, 2000. **355**(9206): p. 827-835.

27. CDC, *Types of Influenza Viruses*. 2014.

28. Modrow, S., *Molecular Virology*. 2013: Springer.

29. O'Neill, R.E., J. Talon, and P. Palese, *The Influenza Virus NEP (NS2 Protein) Mediates The Nuclear Export Of Viral Ribonucleoproteins.* Embo Journal, 1998. **17**(1): p. 288-296.

30. www.http://viralzone.expasy.org.

31. Gamblin, S.J., et al., *The Structure And Receptor Binding Properties Of The 1918 Influenza Hemagglutinin.* Science, 2004. **303**(5665): p. 1838-1842.

32. Bullough, P.A., et al., *Structure Of Influenza Hemagglutinin At The PH Of Membrane-Fusion.* Nature, 1994. **371**(6492): p. 37-43.

33. Wiley, D.C. and J.J. Skehel, *The Structure And Function Of The Hemagglutinin Membrane Glycoprotein Of Influenza-Virus.* Annual Review of Biochemistry, 1987. **56**: p. 365-394.

34. http://www.rapidreferenceinfluenza.com/.

35. Floyd, D.L., et al., *Single-Particle Kinetics Of Influenza Virus Membrane Fusion.* Proceedings of the National Academy of Sciences of the United States of America, 2008. **105**(40): p. 15382-15387.

36. White, J.M., et al., *Structures And Mechanisms Of Viral Membrane Fusion Proteins: Multiple Variations On A Common Theme.* Critical Reviews in Biochemistry and Molecular Biology, 2008. **43**(3): p. 189-219.

37. Kemble, G.W., T. Danieli, and J.M. White, *Lipid-Anchored Influenza Hemagglutinin Promotes Hemifusion, Not Complete Fusion.* Cell. **76**(2): p. 383-391.

38. Nobusawa, E., et al., *Comparison Of Complete Amino-Acid-Sequences And Receptor-Binding Properties Among 13 Serotypes Of Hemagglutinins Of Influenza A-Viruses.* Virology, 1991. **182**(2): p. 475-485.

39. Klenk, H.D., et al., *Activation Of Influenza-A Viruses By Trypsin Treatment.* Virology, 1975. **68**(2): p. 426-439.

40. Gething, M.J., K. McCammon, and J. Sambrook, *Expression Of Wild-Type And Mutant Forms Of Influenza Hemagglutinin - The Role Of Folding In Intracellular-Transport.* Cell, 1986. **46**(6): p. 939-950.

41. Steinhauer, D.A., et al., *Studies Of The Membrane-Fusion Activities Of Fusion Peptide Mutants Of Influenza-Virus Hemagglutinin.* Journal of Virology, 1995. **69**(11): p. 6643-6651.

42. Lear, J.D. and W.F. Degrado, *Membrane-Binding And Conformational Properties Of Peptides Representing The Nh2 Terminus Of Influenza HA-2.* Journal of Biological Chemistry, 1987. **262**(14): p. 6500-6505.

43. Han, X., et al., *Membrane Structure And Fusion-Triggering Conformational Change Of The Fusion Domain From Influenza Hemagglutinin.* Nature Structural Biology, 2001. **8**(8): p. 715-720.

44. Lorieau, J.L., J.M. Louis, and A. Bax, *The Complete Influenza Hemagglutinin Fusion Domain Adopts A Tight Helical Hairpin Arrangement At The Lipid:Water Interface.* Proceedings of the National Academy of Sciences of the United States of America, 2010. **107**(25): p. 11341-11346.

45. Sun, Y. and D.P. Weliky, *C-13-C-13 Correlation Spectroscopy Of Membrane-Associated Influenza Virus Fusion Peptide Strongly Supports A Helix-Turn-Helix Motif And Two Turn Conformations.* Journal of the American Chemical Society, 2009. **131**(37): p. 13228-13229.

Chapter 2

Materials and Method

2.1 Materials

Wang resins and FMOC protected amino acids were obtained from Peptides International (Louisville, KY), Calbiochem - Novabiochem (La Jolla, CA) and Sigma Aldrich (St. Louis, MO). BOC-Gly-PAM-resin and TBOC protected amino acids were obtained from Dupont (Wilmington, Delaware). 1-^{13}C Gly, ^{15}N Phe and Phe-^{2}H ring were obtained from Cambridge Isotope Laboratories (Andover, MA) and were N-FMOC or N-t-BOC protected in our laboratory using literature procedures.[1, 2] Other reagents are typically obtained from Sigma - Aldrich (St. Louis, MO). The lipids DTPC, DTPC, and DMPC were obtained from Avanti Lipids (Alabaster, Al). HEPES and MES were purchased from Sigma –Aldrich. The buffer solutions used in the experiments contained 10 mM HEPES, 5 mM MES at pH 5.0 or 7.0 with 0.01% sodium azide as preservatives.

2.2 Peptide sequences, preparation and purification

All HAfp contained either one of the sequences

HA3fp20: GLFGAIAGFIENGWEGMIDGGGKKKKG-NH_2

HA1fp23: GLFGAIAGFIEGGWEGMIDGWYGGGKKKKG-NH_2

Where the underlined residues are N-terminal residues of HA2 subunit of the hemagglutinin protein of the influenza A virus. HA3fp20 and HA1fp23 were used because their structures were widely studied in detergents and in detergent - rich bicelles. HA1 and HA3 refer to the H1 and H3 subtype of hemagglutinin protein respectively with sequence variations Asn-12/Gly-12 and Glu-15/Thr-15. The highlighted region in HA1fp23 is conserved in both the subtypes. In detergent micelles, the structure of HA3fp20 is predominantly open with an interhelical angle of

~ 100° formed by the N- and C-terminal helices.[3] In contrast, HA1fp23 adopts a tightly packed closed structure in micelles with an interhelical angle of ~ 160°. [4] Both the peptides have a non-native C-terminal tag to increase the aqueous solubility of the peptides which aids in purification and NMR sample preparation. A set of peptides with a three different labeling schemes were synthesized to probe the interhelical geometry of HAfp. The labeling schemes of the synthesized HAfp are listed in Table 2.1.

HA3fp20 was manually synthesized by FMOC solid phase peptide synthesis. HA1fp23 was made with manual TBOC synthesis and HF cleavage after the TBOC synthesis was performed by Midwest Biotech. The mutant, HA1fp23 Gly1Glu mutants were synthesized manually using TBOC synthesis. The synthesized peptides were purified using reversed phase HPLC with a semi-preparative C18 column using water - acetonitrile gradient containing 0.1% TFA. TFA helps to maintain the acidic pH (~ 4) and also neutralizes the carboxylate group present in the peptide. The purity of the peptides were checked by MALDI and ESI and resulted in > 95% peptide purity.

Table 2.1. Labeling scheme of HAfps

Peptide	Labeled residues
HAfp- $A5_C$ - $M17_N$	Ala- 5 ^{13}CO and Met- 17 ^{15}N
HAfp - $G16_C$ – $F9_N$	Gly- 16 ^{13}CO and Phe- 9 ^{15}N
HAfp – $G16_C$ – $F9_{D5}$(ring)	Gly- 16 ^{13}CO and Phe- 9 ^{2}H (ring)
HAfp – G1E - $A5_C$ - $M17_N$	Ala- 5 ^{13}CO and Met- 17 ^{15}N
HAfp – G1E – $A5_C$ – $G20_N$	Ala- 5 ^{13}CO and Gly- 9 ^{15}N

2.3 Vesicle preparation

Lipids were dissolved in 9:1 solution of chloroform and methanol and the solvent was evaporated by nitrogen gas followed by vacuum pumping overnight. The lipid film was suspended in aqueous buffer either at pH 5 or at pH 7 followed by 10 freeze/thaw cycles. Large unilamellar vesicles were prepared by repeated extrusion through a 100 nm diameter polycarbonate filter.

2.4 Membrane sample preparation for MAS and static solid state NMR

The vesicle samples were predominantly prepared with DTPC and DTPG in the ratio 4:1. This lipid composition of the PC lipids reflects the large fraction of PC in the membranes of the respiratory epithelial cells infected by influenza virus and the negative charge of these membranes.[5] Ether rather than ester-linked lipids were used because of the lack of carbonyl (C=O) carbons and therefore do not contribute natural abundance (na) ^{13}CO signal to the solid state NMR spectrum. Static samples for ^{2}H – ^{1}H experiments were made with DMPC-d54. Stock peptide solution in water (typically 0.1 mM or 0.2 mM) was added dropwise to the extruded vesicles while maintaining the pH either at 5 or 7. The final peptide: lipid mole ratio is either

1:25 and or 1:50. The lipid and peptide solution was vortexed overnight and ultracentrifuged at 100000 g for four hours. The quantitative binding of the peptide to the membrane was confirmed by measuring A_{280} and ε_{280} = 5700 cm^{-1} M^{-1} and was evidenced by $A_{280} < 0.01$ in the supernatant solution. The proteo-liposome complex was lyophilized overnight and packed in 4 mm MAS rotor. Typically ~ 10 μL of buffer (either pH 5 or pH 7) was added to the rotor to rehydrate the proteo-liposome complex.

2.5 Vesicle fusion assay

Vesicle fusion assays or FRET assays are used to compare the extent of vesicle fusion among different protein / peptide sequences.[6] The assay depends on the resonance energy transfer between the fluorophores N-NBB-DPPE (donor) and N-Rh-PE (acceptor) which were covalently coupled to the lipids. The assay also relies on the emission band of the donor, N-NBD-PE, at ~ 470 nm overlaping with the excitation band of the acceptor, N-Rh-DPPE, at ~ 537 nm. The efficiency of the FRET depends on the distance and is inversely proportional to the sixth power of the distance between the donor and the acceptor.

Unlabeled vesicles were prepared as above. “Labeled” vesicles were similarly prepared and contained an additional 2 mole % donor lipid and 2 mole % acceptor lipid. Labeled and unlabeled vesicles were mixed in 1:9 ratio and the temperature was maintained at 37 ^{o}C. The initial vesicle fluorescence (F_0) was measured, an aliquot of peptide stock was then added, and the time-dependent fluorescence $F(t)$ was subsequently measured in 1 s increments for a total time of 10 min. Peptide-induced fusion between labeled and unlabeled vesicles increased the average donor-accepter distance and resulted in higher fluorescence. An aliquot of Triton X-100 detergent stock was then added to solubilize the vesicles with resultant further increase in the fluorophore - quencher distance and maximal fluorescence, F_{max}. The percent vesicle fusion was

calculated as $M(t) = [(F(t) - F_0) \times 100]/\{[F_{max} - F_0]\}$. Experimental conditions typically included: (1) initial 1500 µL vesicle suspension with [total lipid] = 150 µM; (2) 467nm excitation and 530 nm detection wavelengths; (3) 90 µL aliquot of 50 µM peptide stock in water with final [peptide] = 3 µM and peptide : lipid mole ratio = 1:50; (4) 4 s assay dead-time after peptide addition; and (5) 12 µL aliquot of 20% v/v Triton X-100 with final 0.19% v/v Triton X-100.

2.6 Solid state NMR

2.6.1 MAS solid state NMR spectroscopy

To investigate the structure of HAfp in membranes, Rotational Echo Double Resonance (REDOR) solid state NMR was used to measure the heteronuclear dipolar coupling.[7, 8] Spectra were acquired with a 9.4T Agilent Infinity Plus spectrometer and triple - resonance MAS probe tuned to ^{1}H, ^{13}C, and ^{15}N frequencies, or ^{1}H, ^{13}C, and ^{2}H frequencies. The sample rotor was cooled with nitrogen gas at – 50 °C and the expected sample temperature is ~ – 30 °C. The REDOR pulse sequence is shown in figure 2.1which includes: (1) a ^{1}H $\pi/2$ pulse; (2) ^{1}H to ^{13}C cross-polarization (CP); (3) dephasing period of variable duration τ; and (4) ^{13}C detection. ^{1}H decoupling was applied during the dephasing and detection periods. There was alternate acquisition of the S_0 and S_1 data. The dephasing periods of both acquisitions included a ^{13}C π - pulse at the end of each rotor cycle except the last cycle and the dephasing period of the S_1 acquisition included an additional ^{15}N π - pulse or ^{2}H π - pulse at the midpoint of each cycle. For the S_0 acquisition, there was no net ^{13}C evolution due to ^{13}C - ^{15}N or ^{13}C - ^{2}H dipolar coupling over a full rotor cycle. For the S_1 acquisition, there was net evolution with consequent reduction in the ^{13}C signal. Spectra were acquired for different dephasing time (τ) with XY-8 phase cycling for (x, y, x, y, y, x, y, x) applied to all the ^{15}N or ^{2}H and ^{13}C π- pulses.[9] The difference in the

S_0 and S_1 signal intensity as a function of τ was used to measure the dipolar coupling (d) and calculate the internuclear distance (r) between the ^{13}C-^{15}N/^{2}H nuclei.

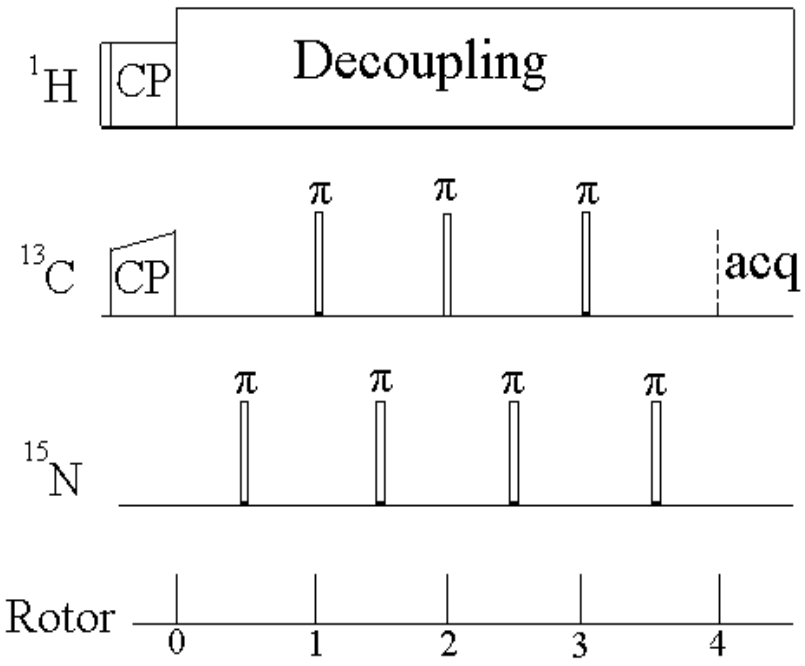

Figure 2.1. ^{13}C – ^{15}N REDOR pulse sequence. Each sequence starts with a CP from ^{1}H to the observed ^{13}C nucleus to enhance the intensity of ^{13}C signal followed by a dephasing and acquisition period. TPPM ^{1}H decoupling was applied during the dephasing and the acquisition time.

Both the ^{1}H - ^{13}C cross polarization matching conditions and the ^{13}C - ^{15}N REDOR π - pulses were calibrated using I4 peptide. [10] The sequence of the I4 peptide is: Ac-AEAAAKEAAAKEAAAKA-NH_2 with N-terminal acetylation and C-terminal amidation. The I4 peptide was synthesized chemically with a ^{13}CO label at residue Ala-9 and ^{15}N label at residue Ala-13. Earlier solid state NMR studies have shown that I4 peptide is majorly helical (83 ±6) % at the residue Ala-9 and the internuclear distance between Ala-9^{13}CO and Ala-13^{15}N is ~ 4.1 Å. The ~ 4.1 Å internuclear distance corresponds to ~ 44 Hz ^{13}CO – ^{15}N heteronuclear dipolar coupling. The solid state NMR spectra were externally referenced to adamantane. The assignment of the methylene peak to 40.5 ppm allowed us to make a direct comparison with the solution state ^{13}C chemical shift. Typical NMR parameters included 10 kHz MAS frequency, 5.0 μs ^{1}H $\pi/2$-pulse, 50 kHz ^{1}H CP, 60 – 65 kHz ramped ^{13}C CP, 80 kHz ^{1}H decoupling, and 8.1 μs ^{13}C, 10.0 μs ^{15}N, and 5.0 μs ^{2}H π-pulses with XY - 8 phase cycling applied to both pulse trains. The typical durations of the cross polarization contact time was 2 ms. The pulse delay for τ = 2 ms, 8 ms and 16 ms was 1s, for τ = 24 ms and 32 ms was 1.5 s, and for τ = 40 ms, 48 ms was 2 s. The data collection time was ~ 3-5 hours for τ = 2 ms and 8 ms, ~ 6-12 hours for τ = 16 ms, ~ 1 day for τ = 24 ms, ~ 1.5 days for τ = 32 ms, ~ 2 days for τ = 40 ms and ~3-4 days for τ = 48 ms. Spectra were typically processed using 100 Hz Gaussian line broadening and baseline correction. The S_0^{exp} and S_1^{exp} intensities were determined from integration of 3 ppm windows centered at the peak ^{13}CO shift. The uncertainties were the RMSD's of spectral noise regions with 3-ppm widths.

2.6.2 Static solid state NMR spectroscopy

The overall lipid motions with or without the peptide were measured using quadrupolar (quecho) pulse sequence under static conditions.[11] The experiments were done on a 9.4 T solid state NMR spectrometer using a triple resonance MAS probe converted to a double resonance probe tuned to ^{1}H and ^{2}H frequencies. The ^{2}H 90° pulse was calibrated using D_2O. The ^{2}H frequency was 61. 520724 MHz. The quecho pulse sequence is, $(\pi/2)_x$ - τ - $(\pi/2)_y$ - τ_1 - detect as shown in the Figure 2.2. The first 90° pulse is the excitation pulse while the second 90° pulse is the refocusing pulse. ^{2}H spectra were acquired for a fixed τ and τ_1 value at different temperatures. for T_2 measurements, ^{2}H spectra were acquired for different τ and τ_1 with fixed (τ - τ_1) value. Typical solid state NMR parameters include 1.62 μs ^{2}H 90° pulse, dwell time = 2 μs, τ = 30 μs and τ_1 = 11 μs. As we process the quecho ^{2}H FID data, we need to do data shift before Fourier Transform (FT) to move the maximum echo signal at t = 0. All the HAfp and HFP samples were processed with -11 and -10 data shifts respectively with 500 Hz Gaussian line broadening.

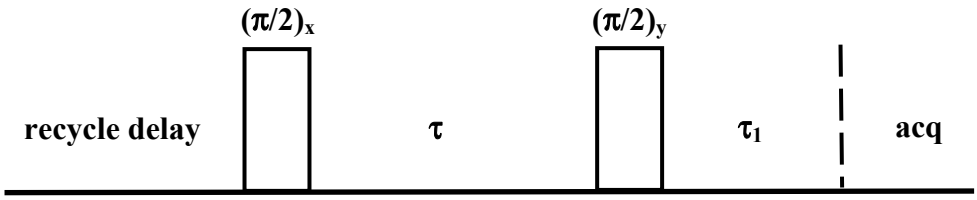

Figure 2.2. "Quecho" pulse sequence used to measure ^{2}H T_2. The phase of the second 90° pulse is always 90° out of phase with respect to the first 90° pulse. Theoretically $\tau = \tau_1$. However, experimentally $\tau_1 < \tau$.

REFERENCES

REFERENCES

1. Chang, C.D., et al., *Preparation And Properties Of N-Alpha-9-Fluorenylmethyloxycarbonylamino Acids Bearing Tert-Butyl Side-Chain Protection.* International Journal of Peptide and Protein Research, 1980. **15**(1): p. 59-66.

2. Lapatsanis, L., et al., *Synthesis Of N-2,2,2-(Trichloroethoxycarbonyl)-L-Amino Acids And N-(9-Fluorenylmethoxycarbonyl)-L-Amino Acids Involving Succinimidoxy Anion As A Leaving Group In Amino-Acid Protection.* Synthesis-Stuttgart, 1983(8): p. 671-673.

3. Han, X., et al., *Membrane Structure And Fusion-Triggering Conformational Change Of The Fusion Domain From Influenza Hemagglutinin.* Nature Structural Biology, 2001. **8**(8): p. 715-720.

4. Lorieau, J.L., J.M. Louis, and A. Bax, *The Complete Influenza Hemagglutinin Fusion Domain Adopts A Tight Helical Hairpin Arrangement At The Lipid:Water Interface.* Proceedings of the National Academy of Sciences of the United States of America, 2010. **107**(25): p. 11341-11346.

5. Worman, H.J., et al., *Relationship Between Lipid Fluidity And Water Permeability Of Bovine Tracheal Epithelial-Cell Apical Membranes.* Biochemistry, 1986. **25**(7): p. 1549-1555.

6. Struck, D.K., D. Hoekstra, and R.E. Pagano, *Use Of Resonance Energy-Transfer To Monitor Membrane-Fusion.* Biochemistry, 1981. **20**(14): p. 4093-4099.

7. Gullion, T. and J. Schaefer, *Rotational-Echo Double-Resonance NMR.* Journal of Magnetic Resonance, 1989. **81**(1): p. 196-200.

8. Zheng, Z., et al., *Conformational Flexibility And Strand Arrangements Of The Membrane-Associated HIV Fusion Peptide Trimer Probed By Solid-State NMR spectroscopy.* Biochemistry, 2006. **45**(43): p. 12960-12975.

9. Gullion, T., D.B. Baker, and M.S. Conradi, *New, Compensated Carr-Purcell Sequences.* Journal of Magnetic Resonance, 1990. **89**(3): p. 479-484.

10. Long, H.W. and R. Tycko, *Biopolymer Conformational Distributions From Solid-State NMR: Alpha-Helix And 3(10)-Helix Contents Of A Helical Peptide.* Journal of the American Chemical Society, 1998. **120**(28): p. 7039-7048.

11. Davis, J.H., *The Description Of Membrane Lipid Conformation, Order And Dynamics By ^{2}H- NMR*. Biochimica Et Biophysica Acta, 1983. **737**(1): p. 117-171.

Chapter 3

Structural Studies of Membrane Associated Influenza Fusion Peptide

3.1 Introduction

Enveloped viruses, like influenza virus are coated with a lipid membrane, and fusion peptides present in the lipid envelope contribute to the fusion between the viral and the host cell membranes upon infection.[1, 2] The influenza fusion peptide is highly conserved such that a single point mutation can arrest membrane fusion. [3-7] Despite the fusion peptide's critical role in fusion, there is no clear consensus in the literature of the structure and mode of function of the influenza fusion peptide. Research over the last 25 years on the influenza fusion peptide proposed very different structures. FTIR,[8] CD [9] and ESR [10] showed that HAfp adopts majorly helical conformation in membranes. However, in presence of 33 mol % of cholesterol, [11] or when the HAfp: lipid > 0.1 at pH 7.4, [12] HAfp adopts beta-sheet structure.

The structure of HAfp depends on the sequence and also on the medium content of detergents or membranes. In 2001, there was a solution NMR (^{1}H chemical shifts and NOEs) study led by Tamm group of the HA3fp20 in detergent micelles. [13] In HA3fp20, HA3 and fp20 refers to the subtype of hemaglutinin protein and the number of the residues in the fusion peptide sequence respectively. The sequence used for the study was GLFGAIAGFIENGWEGMIDGGCGKKKK. The underlined part represents the native HAfp sequence and the seven residues were added at the end of the sequence to increase the aqueous solubility of the peptide. In detergent micelles, HA3fp20 displays N-terminal helical structure from the residues Leu-2 to Ile-10 and C-terminal helical structure from Trp-14 to Ile-18 at pH 5 (Figure 3.1a). At pH 7.4, HA3fp20 is helical from Leu-2 to Ile-10 at N-terminus and an extended structure at C-terminus (Figure 3.1b). At both the pHs, there is a kink/turn at the residues Glu-11, Asn-12 and Gly-13. The turn is stabilized by H-

bonds from NHs of Glu-11, and Asn-12 to the carbonyls (C=O) of Gly-8 and Phe-9 respectively. The pH 5 helix/turn/helix structure is referred to as "open boomerang' structure and the interhelical angle of the open structure is ~ 100°. Due to the formation of the C-terminal 3_{10} helix, Glu-15 and Asp-19 are repositioned relative to their positions at pH 7.4 as shown in Figure 3.1. Due to the rotation of these two charged residues at pH 5, a hydrophobic pocket is created which might favor the deeper insertion of the peptide inside the membrane at fusogenic pH relative to at neutral pH. Additionally, EPR experiments were also performed with spin-labels to determine the insertion depth of the HA3fp20 in membranes. HA3fp20 is inserted in the membrane in an inverted V-shaped manner where the turn / tip of the boomerang structure exposed to the solvent. For the EPR studies 20 single site mutants of HA3fp20 were synthesized with each residue separately mutated to Cys from Gly-1 to Gly-20. However, spin-labeling of Gly-4-Cys and Gly-8-Cys caused aggregation of the peptides at the membrane interface and were not included in the above mentioned study. These mutated positions were labeled with the nitroxide spin labels and the depths of immersion of the spin labels were measured using EPR spectra of the labeled peptides. EPR studies showed that the N-and C-terminal domain penetrate ~ 3 – 6 Å more deeply at pH 5.0 than at pH 7.4. For example, the distance of the Phe-3 Cys mutant from the phosphate headgroup of the membrane was ~ 14 Å and ~ 8 Å at pH 5.0 and 7.4 respectively. In the above-mentioned EPR study, the distances that were measured referred to the distances to the EPR spin labels and not the backbone of the peptide. The inverted V-shaped insertion was not supported by solid state NMR studies of membrane-associated HA3fp20 because: (1) In HA3fp20, Gly-1 and Gly-20 are ~ 4.5 Å and ~6 Å away from the phosphorous head groups respectively, and Leu-2 and Phe-3 ^{13}COs are ~ 7 Å away. Therefore these four residues are in contact with the phosphorous head groups. (2) Ala-7 shows substantial ^{13}CO – ^{2}H

REDOR dephasing in ^{2}H labeled (10 position) PC lipids, which is in contrast with the EPR results (Ala-7 is ~ 3.5 Å from the phosphate head groups according to the EPR studies). In 2010 another solution NMR study of HA1fp23 in detergent by the Bax group showed a very different result. [14] The sequence used for the study was GLFGAIAGFIEGGWTGMID GWYGSGKKKKD, where the underlined part represents the native HA1fp23 sequence. The difference between the two HAfp sequences is the presence of Asn-12 and Glu-15 in the HA3fp20 in place of Gly-12 and Thr-15 respectively and also the presence of Trp-21, Tyr-22, and Gly-23 at the C-terminus of the HA1fp23. In detergents, HA1fp23 adopts a tightly packed helix/turn/helix structure at both pH 4.0 and pH 7.4 (Figure 3.1c). The tightly packed closed hairpin structure was determined using solution state NMR measurements (HSQC, RDC, NOE, and 3 bonds J-coupling). The formation of very different structure in detergents was attributed to the presence of three additional C-terminal residues, Trp, Tyr, Gly. These three terminal residues are highly conserved across all the subtypes of influenza virus. [15] The helical hairpin structure was stabilized by the interhelical H-bonds from the $C^{\alpha}Hs$ of Ala-5, Phe-9, Met-17 and Trp-21 to the C=O of Gly-1, Ala-5, Gly-13, and Met-17 respectively. The closed structure was amphipathic and has a distinct hydrophobic and hydrophilic face. The interfacial location of the HAfp in DPC micelles was probed by the NOE contacts between the micelle Hs and NHs of the HA1fp23 backbone. The NOE intensities between the methylene Hs of the DPC micelle and the backbone NHs for the hydrophobic residues present at the bottom were the strongest relative to the residues present on the hydrophilic side of the closed structure. The NOEs to the alkyl chains for the Gly-4, Gly-8, Gly-16 and Gly-20 were weaker. These observed NOE intensity pattern was interpreted to support an interfacial micelle location for HA1fp23; where the hydrophobic side chains were pointing downwards towards the hydrophobic core and the hydrophilic side was

exposed to the solvent. However, the above mentioned NOE data also supports a trans-micellar HA1fp23 location because: (1) Almost all the residues showed NOE contacts between the DPC H3-H11 methylene protons and the backbone NH protons of the HA1fp23, (2) Ala-7 is present on the hydrophilic face of the closed structure and yet showing a significant contact with the methylene Hs of the DPC micelles (Figure 3.1d), (3) Ala-5, Ile-6 and Ile-18 showing NOE contacts with the terminal methyl group of DPC. Ala-5 is present on the hydrophilic face whereas Ile-6 and Ile-18 are present on the hydrophobic face. (4) The four Gly residues at position 4, 8, 16 and 20 are present at the inner faces of the two helices and are showing contacts with the methylene Hs of the DPC micelle. The reduced NOE intensities for the Gly- residues could be due to the fact that the Gly –residues are engaged in interhelical interactions. (5) For a trans-micellar orientation one would expect higher backbone NHs exchange rates with solvent for the C- and N- terminal residues and the residues present at the turn region. Similar pattern for the solvent H exchange rate with the backbone NHs was observed for HA1fp23. Besides, the residues present at the C-terminus (Trp-21, Tyr-21 and Gly-23) and the residues present at the turn region (Gly-12 and Gly-13) showed significant NOE contacts with the choline methyl Hs of the DPC micelles.

Additional solution state NMR studies of the wt HA1fp23 and HA1fp23 – Gly8Ala were done, where the residue Gly-8 was mutated to Ala. [16] Relaxation studies of HA1fp23 supported the presence of fully closed hairpin structure at pH 7.4 in DPC micelles. However, at pH 4.0, wt HA1fp23 have ~ 80 % closed and ~ 20 % open structure. The exchange rate between the open and the closed structures was ~ 40 kHz. The open structures were very similar to the open structures of HA1fp23-Gly8Ala mutant at pH 7. In detergents at pH 7, Gly8Ala mutant had ~ 15 % closed and ~ 85 % open structure. A minimum of two different open conformations were

present and are classified as L - shaped and extended structures respectively (Figure 3.1g). The interhelical angles between the closed, L - shaped, and extended structures were 159 ° ± 1 °, 110 ° ± 6 °, and 73 ° ± 11 ° respectively. It was hypothesized that the opening of the closed structure of HAfp was a critical step for adopting a transmembrane helical structure that allows pore formation. The HA1fp23 Gly8Ala is less fusion active as compared to wt HA1fp23. [6] One possible reason for the reduced fusion activity could be due to the opening of the closed structure. Since, Gly-8 is present at the inner face of the closed structure and hence mutating the Glys to any other residue (even the smallest one, Ala) could potentially opens the closed structure. Therefore, it is less intuitive how the open structures of a less fusion active construct are compared to the fusion active wt HA1fp23. Additional solution NMR studies of the 20 residue HA1fp20 showed the presence of ~ 90 % open structure at pH 7 in detergent micelles. [17] More recently, another solution NMR study showed that HA3fp23 also adopts a tight helical hairpin structure in DPC micelle. [18] The above result rules out any subtype dependence on the structure of HAfp. Additional ^{1}H – ^{15}N HSQC NMR data suggests that the although the HA3fp23 mutants Gly1Ser and Gly1Val retained the N-helix/turn/C-helix structure, the distance between the C- and N-helix increased i.e. the hairpin structure opened up.

Solid state NMR studies have shown that the secondary structure of HA3fp20 was majorly beta sheet in the membranes containing ~33 mole % cholesterol. [11] In membranes without cholesterol, HA3fp20 adopts a helix / turn / helix structure at both pH 5.0 and 7.4 (Figure 3.1e and 3.1f). [19] However, at pH 5.0 two different sets of ^{13}C – chemical shifts of Glu-11 were observed suggesting the presence of two different turn conformations at low pH. The gross secondary structure of HA3fp20 in membranes was very similar to the structure of HA3fp20 at

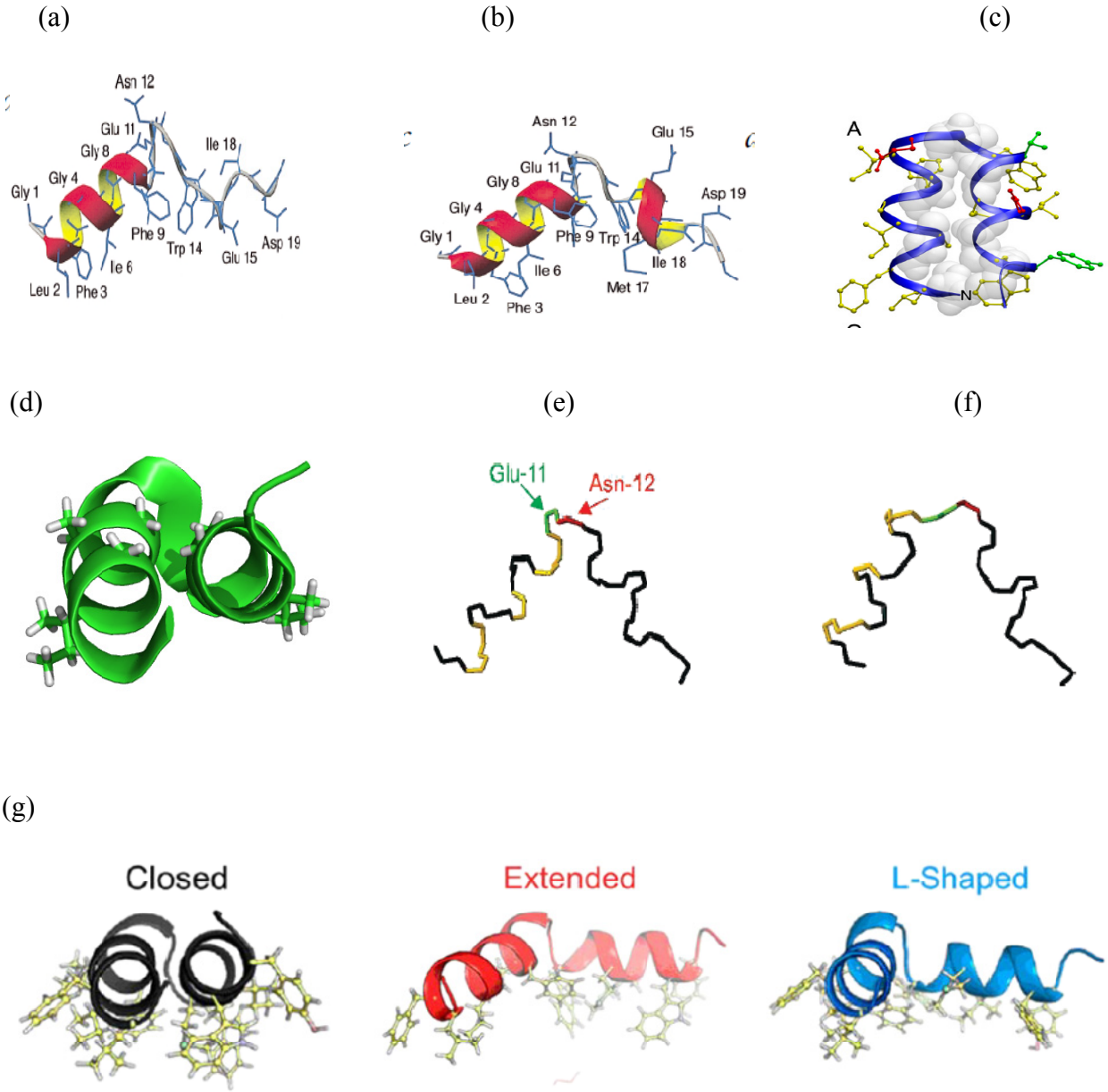

Figure 3.1. Structures of HAfp in DPC micelles; (a) HA3fp20 at pH 5, (b) HA3fp20 at pH 7.4, and [13] (c) HA1fp23 at both pH 4 and pH 7.4. [14] The structure (a) and (c) are refered to as open boomerang and closed structure respectively. (d) Ribbon diagram of the closed structure of HA1fp23 showing the orientation of Gly residues and side chains of Ala-5, Ile-6 and Ile-18. Helix/turn/helix structure of HA3fp20 in PC/PG membranes at (e) pH 5, and (f) pH 7.4. [19] (g) Closed, extended and L-shaped N-helix/turn/C-helix structure of HA1fp23-G8A mutant at pH 7. [16]

pH 5 and HA1fp23 in detergent, but there was no information about the interhelical geometry of the HA3fp20 in membranes.

This chapter presents a detailed investigation of the detailed interhelical geometry and the structure of the HAfp in membranes using REDOR solid state NMR method. It is important to know the interhelical geometry of HAfp in membranes because based on the different interhelical geometry different modes of membrane / micelle location were proposed which eventually leads to different mechanisms for fusion catalysis. The present study focuses on HAfp in membranes without cholesterol to understand the structural dependence on:

(1) sequence length of HAfp, and

(2) effect of pH.

To measure the interhelical geometry, two different interhelical distances were measured using ^{13}C – ^{15}N REDOR. The two different labeling schemes that were used for solid state NMR experiments: G16^{13}CO – F9^{15}N and A5^{13}C – M17^{15}N. Here the C=O of Gly-16 was ^{13}C labeled and the Phe-9 was ^{15}N labeled at the backbone. These labeling schemes were based on earlier solution NMR closed and open structures of HAfp in detergents. These distances were chosen because they differed greatly in the previously observed NMR structures and are shown below:

Table 3.1. Interhelical distances of HA3fp20 at pH 5 in the open structure and HA1fp23 in the closed structure based on the previously observed solution NMR data. The distances were measured in PYMOL.

Labeling Scheme	Distance (Å)	
	Open (r_o)	Closed (r_c)
G16^{13}CO – F9^{15}N	11.5	3.9
A5^{13}CO – M17^{15}N	13.8	5.5

To study the effect of the sequence length on the structure of membrane associated HAfp, both the HA3fp20 and HA1fp23 peptide were used. The peptides were chemically synthesized with ^{13}C and ^{15}N label as mentioned in chapter 2. The NMR samples were prepared using the procedure given in the previous chapter. For pH dependence, NMR samples were prepared either at pH 5.0 or at pH 7.0 using HEPES / MES buffer.

The ^{13}CO chemical shifts are correlated to the local secondary structures of protein backbone. The empirical databases have been created by solution NMR ^{13}CO chemical shift assignments of the proteins. [20, 21] These databases are also relevant for the ^{13}CO chemical shifts measured by solid state NMR as because similar ^{13}CO chemical shifts were observed for the same protein in aqueous solution state or the microcrystalline state. [22]

The ^{13}C – ^{15}N distances were measured using REDOR solid state NMR technique. [23] In REDOR there are two sets of experiment: S_0 and S_1. S_0 spectrum represents the full ^{13}C spectrum where all the ^{13}C nuclei in the sample contributes to the signal, and in the S_1 spectrum we obtain the signal from all the ^{13}C nuclei that are not directly coupled to the ^{15}N nuclei. The difference in

the ^{13}CO integrated signal intensities of the S_0 and S_1 spectra as a function of dephasing time (τ) was used to calculate the dipolar coupling (d). The dipolar dephasing ($\Delta S / S_0$) is calculated by:

$$\frac{\Delta S}{S_0} = \frac{(S_0 - S_1)}{S_0} \qquad 3.1$$

S_0 and S_1 represent the signal intensity of S_0 and S_1 spectrum integrated over 3 ppm range respectively as a function of τ. The ($\Delta S / S_0$) for the observed spin is directly related to the directly related to the dipolar coupling (d) between detected (^{13}C nucleus) and the dephased (^{15}N nucleus) spins. The d depends on ^{13}CO-^{15}N internuclear distance (r) as:

$$d(Hz) = \frac{3066}{r^3(\text{Å})} \qquad 3.2$$

There the ($\Delta S / S_0$) buildup in inversely related to the third power of r between the ^{13}C and ^{15}N nuclei and thus is extremely sensitive to the separation of the coupled spins. When the distance between the ^{13}C and the ^{15}N spin decreases, a significant REDOR ($\Delta S / S_0$) dephasing buildup is observed and vice versa (see Figure 3.6a and 3.6b). Figures 3.6a and 3.6b displays the simulated REDOR ($\Delta S / S_0$) buildups for the closed and the open structure. In figure 3.6a, the closed and the open G16^{13}CO-F9^{15}N distances are 3.9 Å and 11.5 Å respectively. When r = 3.9 Å, a significant REDOR ($\Delta S / S_0$) dephasing buildup was observed and when r = 11.5 Å, no ($\Delta S / S_0$) buildup was observed. Therefore, the experimental REDOR buildup curve will allow us to identify the correct interhelical geometry of the membrane-associated HAfp.

3.2 Results

3.2.1 ^{13}C Chemical shifts

The ^{13}C labeled REDOR solid state NMR spectra of the membrane associated HAfp provides information about the secondary structure at the labeled sites. [21] For REDOR experiments, the samples were made using ether-linked lipids as they lack C=O group and do not contribute to the natural abundance (na) ^{13}CO signal. The unfiltered ^{13}CO intensities include dominant labeled (lab) and minor na signals containing ~ 75 % and ~ 25 % respectively of the S_0 signal intensity integrated over ~ 3 ppm range. For example, in case of HA1fp23 there are 29 ^{13}CO na sites including the seven residue tag; 29 from the amide (CONH) bond and 1 from the Glu-11 C=O bond of the carboxylic acid side chain. Therefore the total ^{13}CO na contribution is; 30 × 0.011 = 0.33. The fractional contribution of na ^{13}CO to S_0 signal is: $\frac{0.33}{0.99(\text{from lab } ^{13}\text{CO})+0.33}=\frac{0.33}{1.32}=0.25$. Therefore the lab signals to ^{13}CO Gly-16 is (1-0.25) = 0.75. Similarly for HA3fp20, spin counting supports the ^{13}CO intensities have ~ 0.77 fractional contributions from the lab nuclei. The lineshape of single ^{13}CO nucleus provides a means of assessing the local conformational distribution around the ^{13}CO nucleus. For example, if more than one conformation is present, one would expect two separate peaks or asymmetric lineshape. In Figure 3.2, the typical half maximum linewidth for Gly was ~ 3 ppm and for Ala was ~ 1.5 ppm, which reflected a narrow conformational distribution of HAfp. [24] In Figures 3.2b, 3.2c and 3.2d there is a small shoulder in each spectrum at lower ppm. The higher ppm (~ 179 ppm in Figures c and d) distribution represents the major fraction and most likely resembles the actual structure of PC: PG bound HAfp. In contrast, the lower ppm distribution (~ 174 ppm) represents a minor population and corresponds to some other conformation. For our data analysis we only considered the major α-helical population. The sample temperature was – 30 °C to minimize the

motion of the lipids and the peptides resulting in higher S/N. The motion of the lipids can yield higher S/N because the heteronuclear dipolar coupling has orientation dependence and is given by:

$$\hat{H} \propto (3\cos^2\theta - 1) \qquad 3.3$$

Where, θ = angle between the external magnetic field and the internuclear vector. The angle θ is affected by the molecular motions. In S_0 experiment, MAS averages the dipolar interaction. In S_1 experiment, rotor syncronized π-pulses are applied to the dephasing spin at the center of the rotor period which reintroduces the heteronuclear dipolar coupling. However, any type of molecular motion present in the sample will partially average out the reintroduced dipolar coupling because of the averaging of the ($3\cos^2\theta$ -1) term. Due to the partial averaging of dipolar coupling, the measured ($\Delta S/S_0$) will not reflect the actual dipolar coupling strength. Additionally, the S/N will also decrease. The reduction in S/N is because at higher temperature the efficiency of cross-polarization decreases because of the averaging of the heteronuclear dipolar coupling due to motion. Figure 3.3 displays $(\Delta S/S_0)^{exp}$ buildups with sample temperatures of ~ -30 and ~ 0°C (cooling gas temperatures of -50 and -20 °C, respectively). The signal-per scan at 0 °C is about half that at -30 °C. At 0 °C there is still considerable motion left in the sample which partially averages the dipolar coupling and hence the observed ($\Delta S/S_0$) buildup is less than at ~ 30 °C.

The interpretation of the ^{13}CO chemical shifts was based on the correlation between the ^{13}CO chemical shift and the local secondary structure of the peptide/protein at the particular residue. The Gly-16 and Ala-5 ^{13}CO chemical shifts were 177.0 ± 0.3 ppm and 179.4 ± 0.4 ppm respectively. These peak shifts correlate with the helical conformation at Gly-16 and Ala-5 which suggests that both the N- and C- terminals are helical at both the pHs for both the HA1fp23 and HA3fp20. This result is consistent with the earlier work of HA3fp20 in

membranes. In membranes containing PC and PG in 4:1 mole ratio, HA3fp20 adopts helical structure at both the N- and C-terminus at both pHs. Figure 3.2 displays representative REDOR spectra of the membrane associated HAfp at either at pH 5 or pH 7. Figure 3.4 shows experimental plots of $(\Delta S/S_0)^{exp}$ vs τ. The similar REDOR dephasing for all the samples suggests that both HA1fp23 and HA3fp20 have very similar structures at both pH 5.0 and 7.0. Figures 3.3 – 3.6 shows the representative experimental REDOR S_0 spectra for both the 20- and the 23-residue HAfp at two pHs and two dephasing times. Table 3.2 displays the line-widths of the spectra displayed in the Figures 3.3 – 3.6. The results in the Table 3.2 show that the linewidths for the HAfp sample labeled with the Gly ^{13}CO are greater than for the samples labeled at the Ala-5 position.

To obtain quantitative structural information, the na contributions to $(\Delta S/S_0)^{exp}$ were removed to give $(\Delta S/S_0)^{lab}$ which represents the $(\Delta S/S_0)$ only from the labeled residues, either Gly-16 or Ala-5 ^{13}CO carbons.

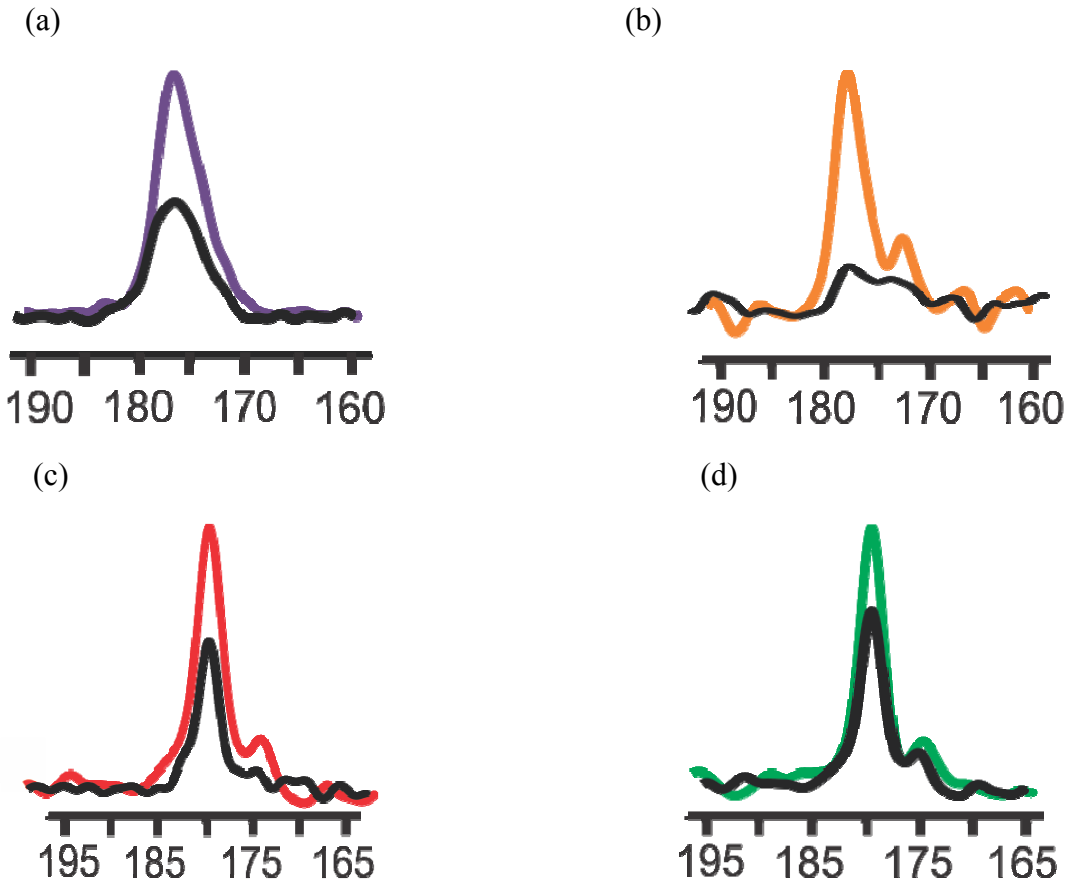

^{13}CO Chemical Shifts

Figure 3.2. ^{13}C detect / ^{15}N - dephase REDOR S_0 (colored) and S_1 (black) experimental spectra of membrane - associated HAfp at τ = 40 ms. Each spectrum is the sum of ~ 50000 scans and processed with 100 Hz Gaussian line broadening and polynomial baseline correction. (a) HA3fp20, pH 5 G16c-F9n, (b) HA1fp23, pH7 G16c –F9n, (c) HA3fp20, pH 7 A5c-M17n, and (d) HA1fp23, pH 5 A5c-M17n. The observed chemical shifts for Gly-16 and Ala-5 are consistent with α - helical conformation of HAfp in membranes. The spectra were taken with samples containing 1 µmole of either HA1fp23 or HA3fp20 and membranes composed of 20 µmole of DTPC and 5 µmole of DTPG. The cooling gas temperature was ~ -50 °C and the sample temperature was ~ -30 °C.

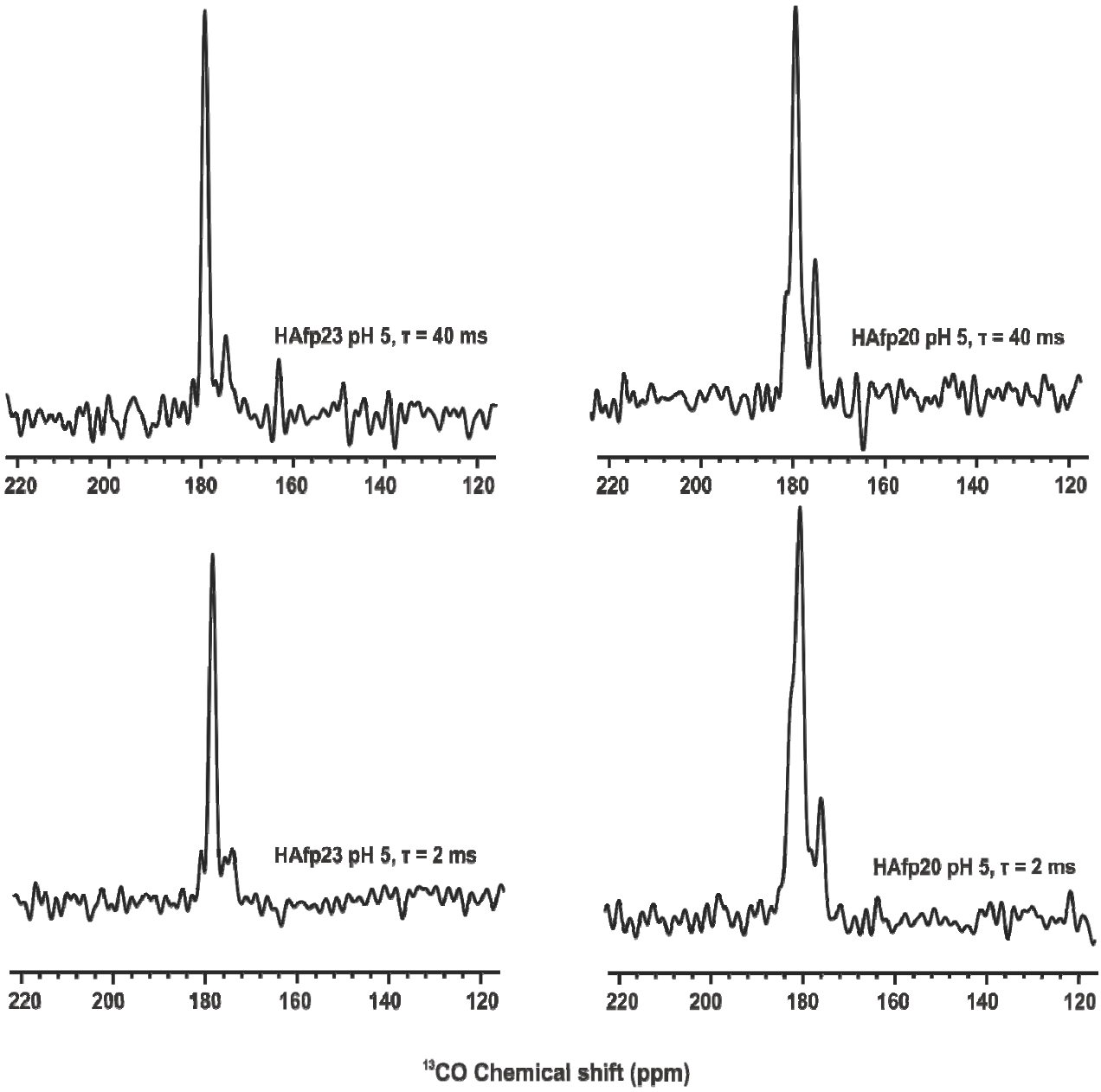

Figure 3.3. Experimental ^{13}CO Ala-5 REDOR S_0 spectra of both the HAfp constructs at pH 5 for A5c-M17n labeling scheme at 2 ms and 40 ms dephasing times. Each spectrum was processed with 20 Hz Gaussian line broadening and baseline polynomial correction of the order 5. The typical ^{13}CO chemical shift was 179.6 ppm which correlates with the alpha helical secondary structure.

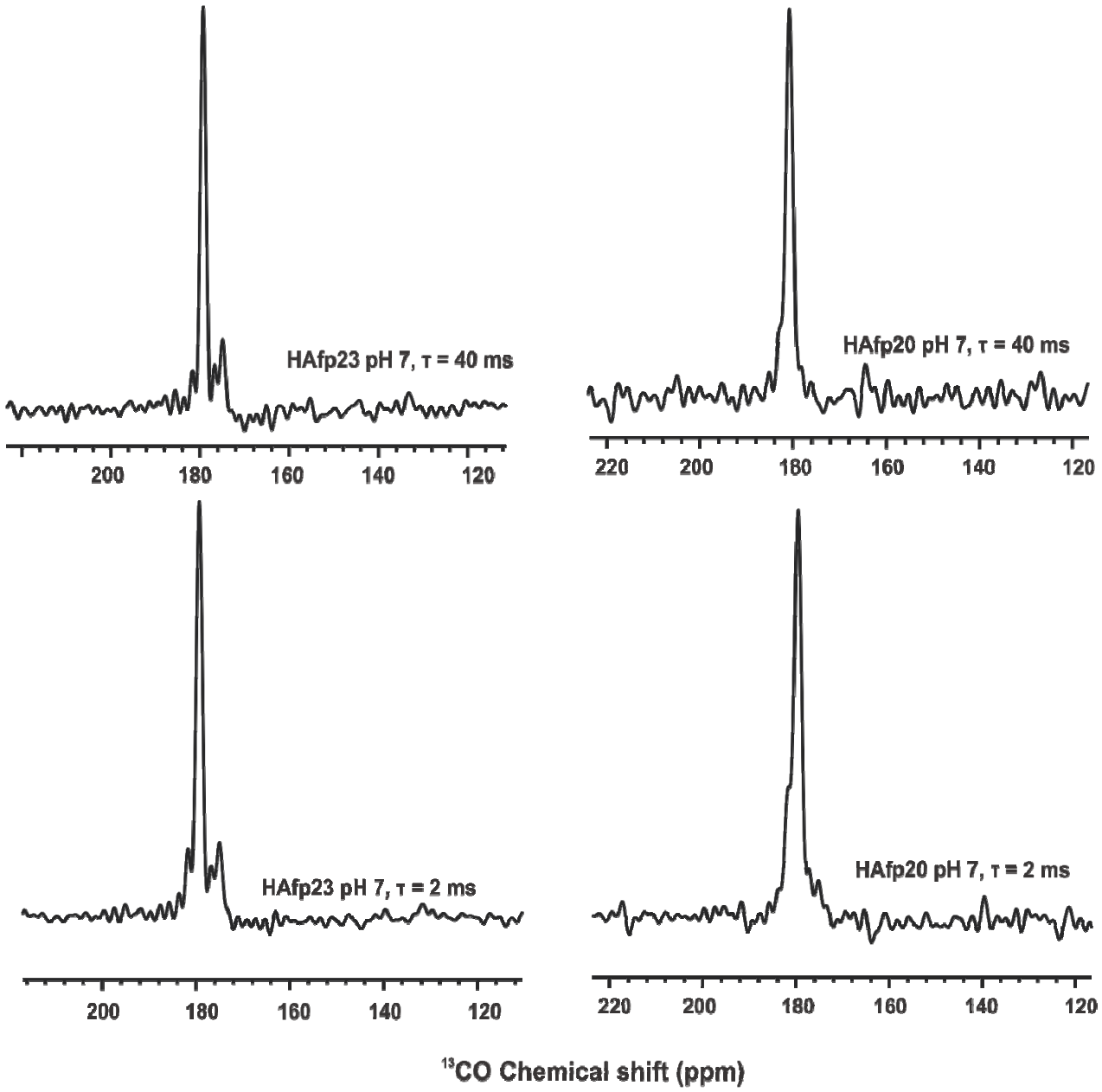

Figure 3.4. Experimental ^{13}CO Ala-5 REDOR S_0 spectra of both the HAfp constructs at pH 7 for A5c-M17n labeling scheme at two different dephasing times. Each spectrum was processed with 20 Hz Gaussian line broadening and baseline polynomial correction of the order 5. The typical ^{13}CO chemical shift was 179.6 ppm which correlates with the alpha helical structure.

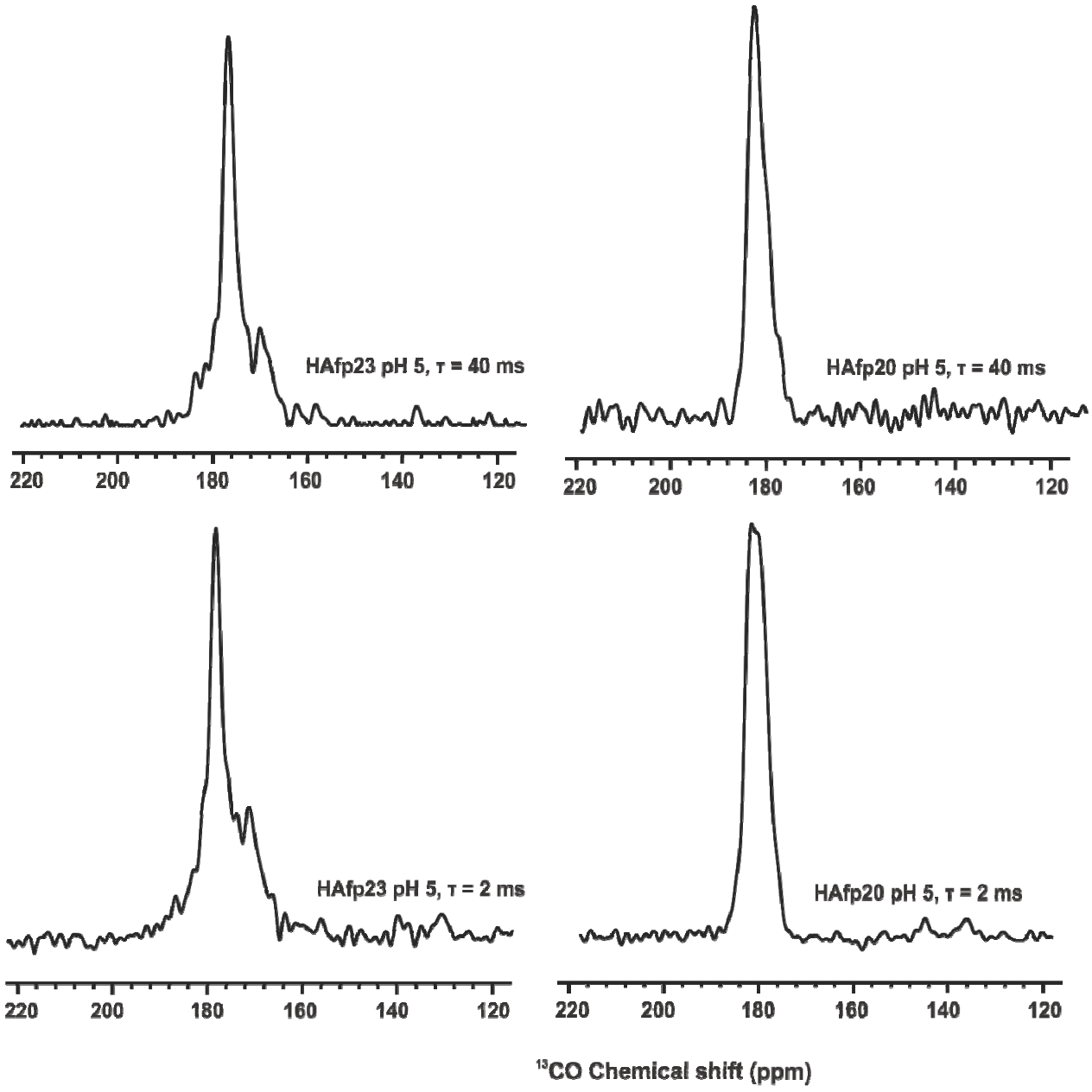

Figure 3.5. Experimental ^{13}CO Gly-16 REDOR S_0 spectra of both the HAfp constructs at pH 5 for G16c-F9n labeling scheme. Each spectrum was processed with 20 Hz Gaussian line broadening and baseline polynomial correction of the order 5. The typical ^{13}CO chemical shift for each spectrum was 177 ppm which correlates with the alpha helical structure.

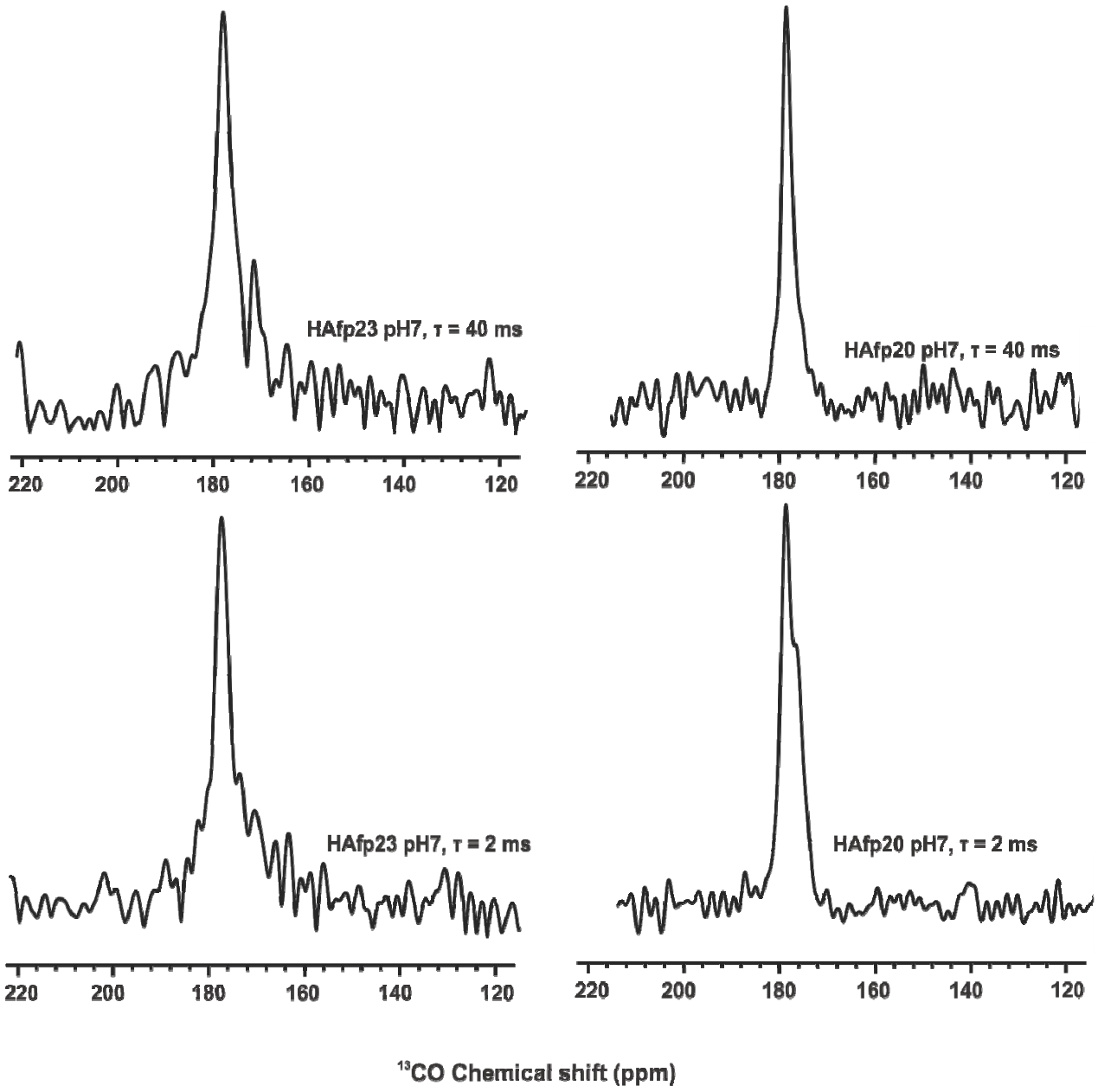

Figure 3.6. Experimental ^{13}CO Gly- 16 REDOR S_0 spectra of both the HAfp constructs at pH 7 for G16c-F9n labeling scheme. Each spectrum was processed with 20 Hz Gaussian line broadening and baseline polynomial correction of the order 5. The typical ^{13}CO chemical shift was ~ 177.1 ppm which correlates with the alpha helical structure.

Table 3.2. Linewidths of membrane associated HAfp at τ = 2 ms and τ = 40 ms. The line broadening used for the each spectrum during processing was 20 Hz.

Labeling	HA1fp23 pH 5 FWHM (ppm)	HA1fp23 pH 7 FWHM (ppm)	HA3fp20 pH 5 FWHM (ppm)	HA3fp20 pH 7 FWHM (ppm)	Dephasing time (ms)
G16c-F9n	2.3	2.6	4.6	3.8	2
	2.7	2.8	4.3	2.7	40
A5c-M17n	1.3	1.0	2.0	1.6	2
	1.3	1.1	1.7	1.5	40

All the spectra were first de-convoluted and the linewidths were measured at FWHM except for HA3fp20 at pH 5 for τ = 2 ms and τ = 40 ms, Ha3fp20 pH 7 at τ = 2 ms.

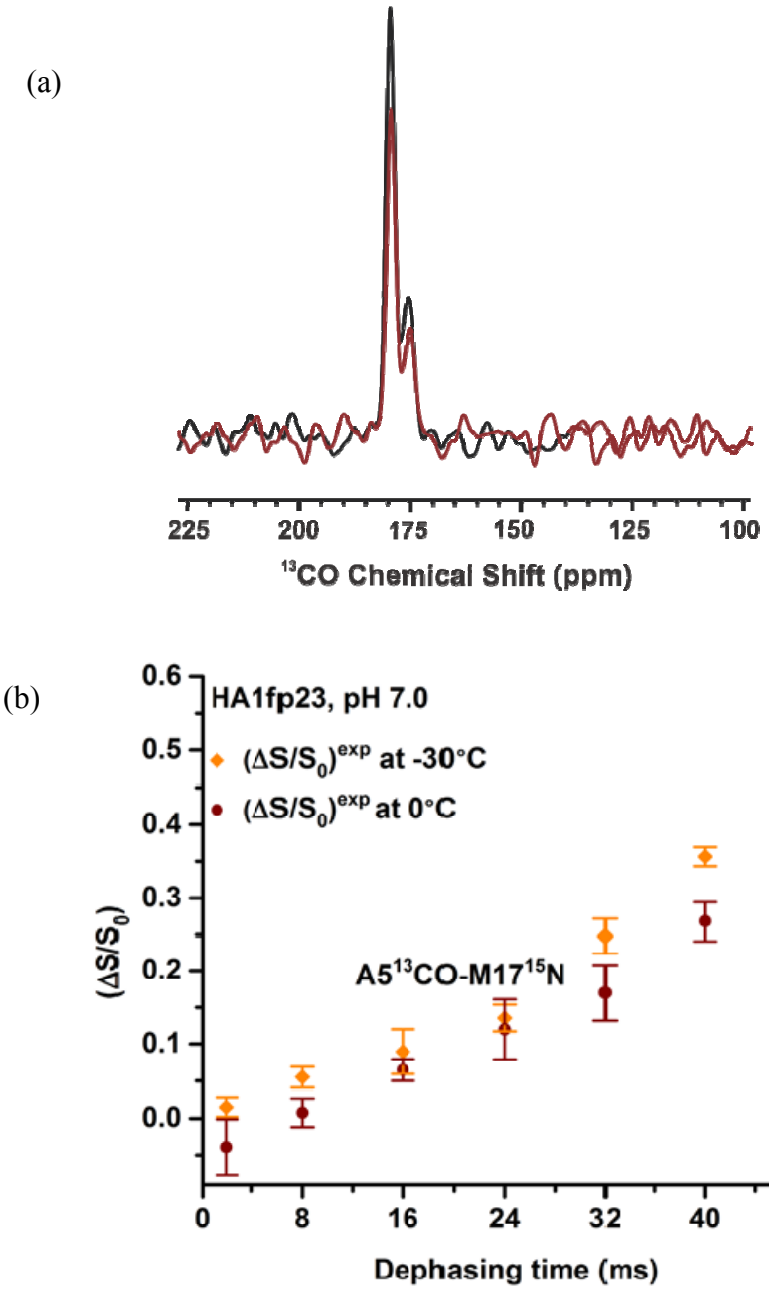

Figure 3.7. (a) ^{13}C detect / ^{15}N - dephase REDOR S_0 (colored) and S_1 (black) experimental spectra of membrane - associated HA1fp23 at τ = 40 ms at 0°C. the pH of the sample was 7. (b) ^{13}CO - ^{15}N $(\Delta S/S_0)^{exp}$ buildups with sample temperatures of ~ -30 and ~ 0°C (cooling gas temperatures of -50 and -20 °C, respectively). The signal-per scan at 0 °C is about half that at -30 °C.

(a)

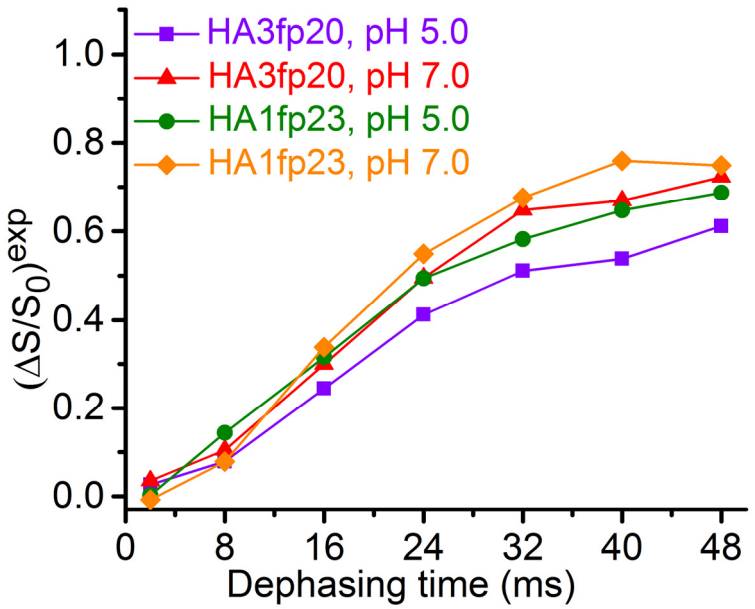

(b)

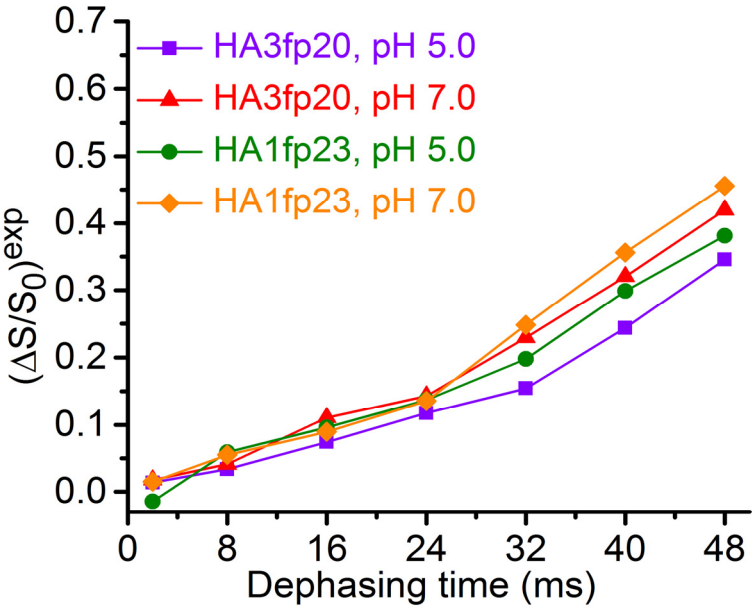

Figure 3.8. Experimental REDOR dephasing buildup of ($\Delta S/S_0$) vs τ. (a) G16 ^{13}CO – F9 ^{15}N, and (b) A5 ^{13}CO – M17 ^{15}N. The typical uncertainty in ($\Delta S/S_0$) is 0.03 based on the standard deviation of the integrals of 12 different spectral regions of the noise.

3.2.2 Calculation of $(\Delta S/S_0)^{lab}$

Quantitative analysis of ^{13}CO-^{15}N REDOR includes determination of the $(\Delta S/S_0)^{lab}$ and $(\Delta S/S_0)^{na}$ contributions to $(\Delta S/S_0)^{exp}$ from the lab and na ^{13}CO nuclei. A $S_0^{lab} = 0.99$ contribution was estimated from the fractional labeling and $S_0^{na} = N \times 0.011$ was estimated for N unlabeled (unlab) ^{13}CO sites which contribute to the S_0^{exp} signal. The value of N is not precisely known because the individual spectra of some of the unlab sites will not completely overlap with the dominant lab spectrum used to set the 3 ppm integration window for S_0^{lab}. We approximate that all the backbone and none of the sidechain ^{13}CO sites contribute to S_0^{exp} so that $N = 26$ for HA3fp20 and N = 29 for HA1fp23. The calculated $(\Delta S/S_0)^{lab}$ was typically < 10 % different than the corresponding $(\Delta S/S_0)^{exp}$ and was not strongly dependent on the precise value of N (Table 3.2).

The derivation of $(\Delta S/S_0)^{lab}$ was done as follows:

$$S_0^{exp} = S^{lab}_0 + S_0^{na} = 0.99 + 0.011 \times N \qquad 3.4$$

$$S_1^{exp} = S^{lab}_1 + S_1^{na} = S_1^{lab} + \sum_{k=1}^{N} S_{1k} \qquad 3.5$$

For each unlabeled backbone site, $S_0^{na} = 0.011$:

$$\left(\frac{\Delta S}{S_0}\right)^{na} = \left(\frac{S_0^{na} - S_1^{na}}{S_0^{na}}\right) = \frac{0.011 - S_1^{na}}{0.011} \qquad 3.6$$

$$S_1^{na} = 0.011 - 0.011 \times \left(\frac{\Delta S}{S_0}\right)^{na} \qquad 3.7$$

Summing over all unlab sites:

$$\sum_{k=1}^{N} S_{1k}^{na} = \sum_{k=1}^{N} \left\{0.011 - 0.011 \times \left(\frac{\Delta S}{S_0}\right)_k^{unlab}\right\} = 0.011 \times N - 0.011 \times \sum_{k=1}^{N} \left(\frac{\Delta S}{S_0}\right)_k^{unlab} \qquad 3.8$$

Substituting Equation 3.7 into Equation 3.4:

$$S_1^{exp} = S_1^{lab} + 0.011 \times N - 0.011 \times \sum_{k=1}^{N} \left(\frac{\Delta S}{S_0}\right)_k^{unlab} \qquad 3.9$$

Combining Equations 3.3, 3.4, and 3.7 followed by algebra:

$$(\frac{\Delta S}{S_0})^{exp} = \frac{S_0^{exp} - S_1^{exp}}{S_0^{exp}} = \frac{0.99 - S_1^{lab} + 0.011 \times \sum_{k=1}^{26} (\frac{\Delta S}{S_0})_k^{unlab}}{1.276} \quad 3.10$$

Rearranging Equation 3.9:

$$(\frac{\Delta S}{S_0})^{lab} = \frac{0.99 + 0.011 \times N}{0.99} \times (\frac{\Delta S}{S_0})^{exp} - 0.011 \times \sum_{k=1}^{N} (\frac{\Delta S}{S_0})_k^{unlab} \quad 3.11$$

$$\text{with } (\frac{\Delta S}{S_0})^{na} = 0.011 \times \sum_{k=1}^{N} (\frac{\Delta S}{S_0})_k^{unlab} \quad 3.12$$

For HA3fp20:

$$(\frac{\Delta S}{S_0})^{lab} = 1.2889 \times (\frac{\Delta S}{S_0})^{exp} - 0.011 \times \sum_{k=1}^{26} (\frac{\Delta S}{S_0})_k^{na} \quad 3.13$$

For HA1fp23:

$$(\frac{\Delta S}{S_0})^{lab} = 1.3222 \times (\frac{\Delta S}{S_0})^{exp} - 0.011 \times \sum_{k=1}^{29} (\frac{\Delta S}{S_0})_k^{na} \quad 3.14$$

Each of the $(\Delta S/S_0)_k^{unlab}$ was calculated using the $^{13}CO_k$ – F9 ^{15}N or the $^{13}CO_k$ – M17^{15}N separation ≡ r_k, the corresponding dipolar coupling d_k (Hz) = 3066/ $[r_k$ (Å)$]^3$, and the quantum-mechanically-derived expression for a pair of coupled spin ½ heteronuclei: [25]

$$(\frac{\Delta S}{S_0})^{sim}\{d,\tau\} = 1 - [J_0(\sqrt{2}\lambda)]^2 + \{2 \times \sum_{k=1}^{5} \frac{[J_k(\sqrt{2}\lambda)]^2}{16k^2 - 1}\} \quad 3.15$$

with $\lambda = d \times \tau$, τ ≡ duration of the dephasing period, and $J_k \equiv k^{th}$ - order Bessel function of the first kind. Table 3.2 lists the r_k's calculated using the closed structure of HA1fp23. The ^{13}CO – ^{15}N distances greater than 8 Å are not listed in the Table 3.2 because the corresponding $(\Delta S/S)_0^{na} \approx 0$.

Table 3.3. CO_k– F9 N distances.[a]

Residue	r_k (Å)	d_k (Hz)
F3	7.38	7.63
G4	5.40	19.47
A5	3.81	55.44
I6	3.74	58.61
A7	3.14	99.03
G8	1.33	1303.22
F9	2.45	208.48
I10	4.69	29.72
E11	5.64	17.09
G12	5.27	20.95
G13	5.23	21.43
W14	6.58	10.76
T15	6.52	11.06
M17	5.36	19.91
I18	7.73	6.64
D19	7.47	7.36
G20	7.28	7.95

[a] The r_k were calculated from the HA1fp23 closed structure. Residues that are not listed have $r_k > 8$ Å and $(\Delta S/S_0)^{na} < 0.01$ for all τ values.

Table 3.4. ($\Delta S/S_0$) values for the G16 ^{13}CO / F9 ^{15}N samples.[a] The uncertainties are in parenthesis.

τ (ms)	HA3fp20					HA1fp23			
	pH 5.0		pH 7.0			pH 5.0		pH 7	
	$(\Delta S/S_0)^{exp}$	$(\Delta S/S_0)^{lab}$	$(\Delta S/S_0)^{exp}$	$(\Delta S/S_0)^{exp}$	$(\Delta S/S_0)^{na}$	$(\Delta S/S_0)^{exp}$	$(\Delta S/S_0)^{lab}$	$(\Delta S/S_0)^{exp}$	$(\Delta S/S_0)^{lab}$
2	0.026 (15)	0.032 (19)	0.036 (23)	0.003 (29)	0.002	0.003 (29)	0.001 (38)	-0.008 (28)	-0.012 (36)
8	0.079 (11)	0.082 (15)	0.105 (19)	0.144 (23)	0.019	0.144 (23)	0.167 (30)	0.078 (33)	0.082 (43)
16	0.244 (11)	0.278 (15)	0.299 (21)	0.316 (17)	0.037	0.316 (17)	0.374 (22)	0.338 (25)	0.403 (32)
24	0.412 (8)	0.476 (11)	0.495 (19)	0.494 (16)	0.055	0.494 (16)	0.588 (21)	0.549 (23)	0.659 (29)
32	0.511 (8)	0.593 (11)	0.648 (31)	0.582 (22)	0.066	0.582 (22)	0.691 (28)	0.676 (23)	0.812 (30)
40	0.538 (12)	0.616 (16)	0.669 (30)	0.647 (15)	0.078	0.647 (15)	0.763 (19)	0.759 (21)	0.909 (28)
48	0.612 (13)	0.699 (17)	0.723 (40)	0.687 (16)	0.089	0.687 (16)	0.805 (21)	0.749 (42)	0.884 (55)

[a]The calculated $(\Delta S/S_0)^{na}$ are the same for all samples.

Table 3.5. ($\Delta S/S_0$) values for the A5 ^{13}CO / M17 ^{15}N samples.[a] The uncertainties are in parenthesis.

τ (ms)	HA3fp20					HA1fp23			
	pH 5.0		pH 7.0			pH 5.0		pH 7.0	
	$(\Delta S/S_0)^{exp}$	$(\Delta S/S_0)^{lab}$	$(\Delta S/S_0)^{exp}$	$(\Delta S/S_0)^{lab}$	$(\Delta S/S_0)^{na}$	$(\Delta S/S_0)^{exp}$	$(\Delta S/S_0)^{lab}$	$(\Delta S/S_0)^{exp}$	$(\Delta S/S_0)^{lab}$
2	0.014 (33)	0.012 (43)	0.017 (17)	0.016 (22)	0.006	0.014 (24)	0.013 (32)	0.015 (13)	0.014 (17)
8	0.034 (26)	0.023 (34)	0.041 (21)	0.033 (27)	0.021	0.059 (41)	0.057 (55)	0.055 (14)	0.052 (18)
16	0.074 (25)	0.054 (32)	0.111 (30)	0.102 (39)	0.042	0.096 (42)	0.085 (56)	0.089 (30)	0.076 (40)
24	0.117 (31)	0.084 (40)	0.143 (22)	0.117 (29)	0.068	0.137 (36)	0.113 (47)	0.136 (18)	0.111 (24)
32	0.154 (27)	0.121 (35)	0.229 (23)	0.219 (29)	0.079	0.198 (42)	0.183 (56)	0.248 (23)	0.249 (31)
40	0.244 (30)	0.227 (39)	0.320 (31)	0.327 (40)	0.090	0.299 (35)	0.305 (46)	0.356 (12)	0.381 (17)
48	0.346 (23)	0.351 (29)	0.419 (20)	0.448 (26)	0.098	0.381 (30)	0.406 (40)	0.456 (14)	0.504 (18)

[a]The calculated $(\Delta S/S_0)^{na}$ are the same for all samples.

Tables 3.3 and 3.4 list the $(\Delta S/S_0)^{exp}$, $(\Delta S/S_0)^{lab}$, and $(\Delta S/S_0)^{na}$ for the eight data sets. The error bars in Figures 3.6c and 3.6d were corrected for natural abundance and were derived from $(\Delta S/S_0)^{exp.}$

3.2.3 Intermolecular vs intramolecular G16^{13}CO – F9^{15}N proximity

For all the REDOR buildups significant dephasing was observed and reflects intra- rather than inter-molecular interaction. Close intermolecular proximity [G16 ^{13}CO (molecule 1) to F9 ^{15}N (molecule 2)] is possible if there are large populations of dimers or higher-order oligomers. This proximity was probed by comparison of the $\Delta S/S_0$ buildups between HA3fp20 samples prepared with either 2 μmole labeled HA3fp20 or 1 μmole labeled and 1 μmole unlabeled HA3fp20 (Figure 3.5). Dominant intermolecular proximity would result in $(\Delta S/S_0)^{mixed} / (\Delta S/S_0)^{fully\ lab} < 1$ and dominant intramolecular proximity would result in$(\Delta S/S_0)^{mixed} / (\Delta S/S_0)^{fully\ lab} \approx 1$. The latter result is observed with much better agreement of $(\Delta S/S_0)^{mixed}$ with calculated $(\Delta S/S_0)^{intra}$ than with calculated $(\Delta S/S_0)^{inter}$.

3.2.3.1 Derivation of $(\Delta S/S_0)^{inter}$

Figure 3.3 displays an antisymmetric dimer model with the three possible configurations for a mixture containing p_L fraction labeled peptide and $(1-p_L)$ fraction unlabeled peptide: (i) both labeled with fractional population p_L^2; (ii) one labeled and one unlabeled with population $[2 \times p_L \times (1-p_L)]$; and (iii) both unlabeled with population $(1 - p_L)^2$.

The model includes:

1. All labeled molecules contain G16 ^{13}CO and F9 ^{15}N *lab* nuclei. The experimental fractional labeling is 0.99 and the approximation of 1.0 simplifies the calculations.

2. There is G16 ^{13}CO-F9 ^{15}N proximity for both *lab* spin pairs molecules in configuration **i**. Similar results are also obtained for one proximal and one distant *lab* spin pair.

3. There isn't ^{13}CO-^{15}N proximity for *lab* ^{13}CO nuclei in configuration **ii** or *na* ^{13}CO nuclei in all configurations. The consequent approximation $S_1 = S_0$ simplifies the calculations.

Table 3.5 summarizes the calculated S_0^{lab} and S_0^{na} contributions.

$$S_0^{inter} = S_0^{lab} + S_0^{na} \quad 3.15$$

$$S_1^{inter} = S_1^{lab} + S_1^{na} \quad 3.16$$

The only significant contribution to $(\Delta S/S_0)^{inter}$ are from *lab* spin pairs of configuration **i** and are denoted $(\Delta S/S_0)^{lab,i}$. For HA3fp20 with N+1=27, algebraic manipulation results in:

$$\left(\frac{\Delta S}{S_0}\right)^{inter} = \frac{2.00\left(\frac{\Delta S}{S_0}\right)^{lab,i}}{2.57\, p_L^2 + 3.17\, p_L(1-p_L) + 0.59\,(1-p_L)^2} \quad 3.17$$

When p_L = 1.0:

$$\left(\frac{\Delta S}{S_0}\right)^{inter}_{p_L=1.0} = 0.778 \times \left(\frac{\Delta S}{S_0}\right)^{lab,i} \quad 3.18$$

When p_L= 0.5:

$$\left(\frac{\Delta S}{S_0}\right)^{inter}_{p_L=0.5} = 0.316 \times \left(\frac{\Delta S}{S_0}\right)^{lab,i} \quad 3.19$$

The blue up triangles in Figure 3.4 are calculated:

$$\left(\frac{\Delta S}{S_0}\right)^{inter}_{p_L=0.5} = 0.316 \times \left(\frac{\Delta S}{S_0}\right)^{lab,i} = \frac{0.316}{0.778} \times \left(\frac{\Delta S}{S_0}\right)^{lab,i}_{p_L=1.0} = 0.406 \times \left(\frac{\Delta S}{S_0}\right)^{exp}_{p_L=1.0} \quad 3.20$$

An alternate dimer structure was also considered in which configuration **i** contains one *lab* pair with close proximity as well as one *lab* pair with distant proximity and S_1=S_0:

$$\left(\frac{\Delta S}{S_0}\right)^{inter}_{p_L=0.5} = 0.158 \times \left(\frac{\Delta S}{S_0}\right)^{lab,i} = \frac{0.158}{0.389} \times \left(\frac{\Delta S}{S_0}\right)^{lab,i}_{p_L=1.0} = 0.406 \times \left(\frac{\Delta S}{S_0}\right)^{exp}_{p_L=1.0} \quad 3.21$$

Relative to a dimer structure with both *lab* pairs in close proximity, the ($\Delta S/S_0$) values are smaller for a structure with one *lab* pair in close proximity. However, the (p_L=0.5)/(p_L=1.0) ratio = 0.41 remains the same for either dimer structure.

3.2.3.2 Derivation of $(\Delta S/S_0)^{intra}$

The model includes: (1) every labeled peptide contains a *lab*^{13}CO-^{15}N pair in close intramolecular but not intermolecular proximity; and (2) $S_1^{na}=S_0^{na}$.

$$S_0^{intra} = S_0^{lab} + S_0^{na} \quad 3.22$$

$$S_1^{intra} = S_1^{lab} + S_1^{na} \quad 3.23$$

The expressions from Table 3.5 and algebraic manipulation with N+1=27 result in:

$$\left(\frac{\Delta S}{S_0}\right)^{intra} = \frac{p_L \times \left(\frac{\Delta S}{S_0}\right)^{lab}}{p_L + 0.286} \quad 3.24$$

For p_L = 1.0, the result is the same as the intermolecular model:

$$\left(\frac{\Delta S}{S_0}\right)^{intra}_{p_L=1.0} = 0.778 \times \left(\frac{\Delta S}{S_0}\right)^{lab} \quad 3.25$$

For p_L = 0.5:

$$\left(\frac{\Delta S}{S_0}\right)^{intra}_{p_L=0.5} = 0.636 \times \left(\frac{\Delta S}{S_0}\right)^{lab} \quad 3.26$$

The red down triangles in Figure 3.4 are calculated:

$$\left(\frac{\Delta S}{S_0}\right)^{intra}_{p_L=0.5} = 0.636 \times \left(\frac{\Delta S}{S_0}\right)^{lab} = \frac{0.636}{0.778} \times \left(\frac{\Delta S}{S_0}\right)^{lab}_{p_L=1.0} = 0.818 \times \left(\frac{\Delta S}{S_0}\right)^{exp}_{p_L=1.0} \quad 3.27$$

Equations 3.20 and 3.27 show that decreasing p_L results in much greater reduction of $(\Delta S/S_0)^{inter}$ than $(\Delta S/S_0)^{intra}$. There is much better agreement of $(\Delta S/S_0)^{exp}_{pL=0.5}$ with $(\Delta S/S_0)^{intra}_{pL=0.5}$ than with $(\Delta S/S_0)^{inter}_{pL=0.5}$ as shown in Figure 3.4.

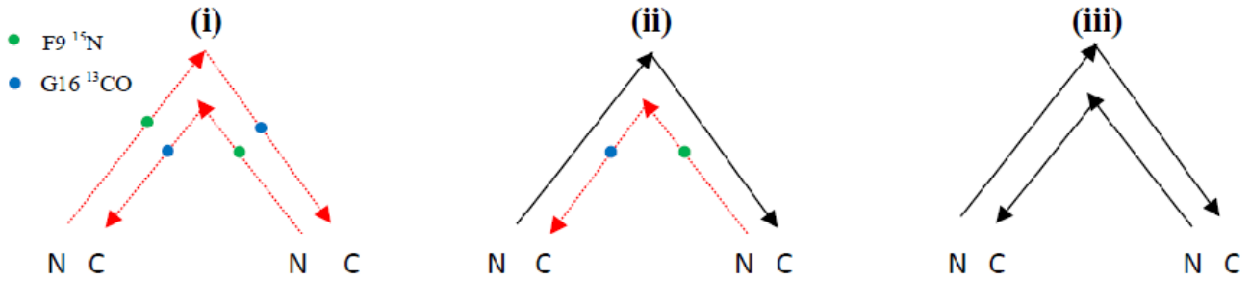

Figure 3.9. Antisymmetric dimer configurations of the HAfp. Each arrow represents either N- or C- terminal helices. Labeled HAfp is a red dashed line and unlabeled HAfp is a black line.

Table 3.6. S_0 expressions for intermolecular and intramolecular models[a]

	Intermolecular Model			Intramolecular Model
	Configuration i	Configuration ii	Configuration iii	
S_0^{lab}	$2p_L^2$	$2p_L^2 \times (1 - p_L)$	0	p_L
S_0^{na}	$p_L^2 \times 2N \times 0.011$	$2p_L \times (1 - p_L) \times (2N + 1) \times 0.011$	$(1 - p_L^2) \times 2(N + 1) \times 0.011$	$(N + 1 - p_L) \times 0.011$

[a]$N + 1 \equiv$ number of residues in peptide

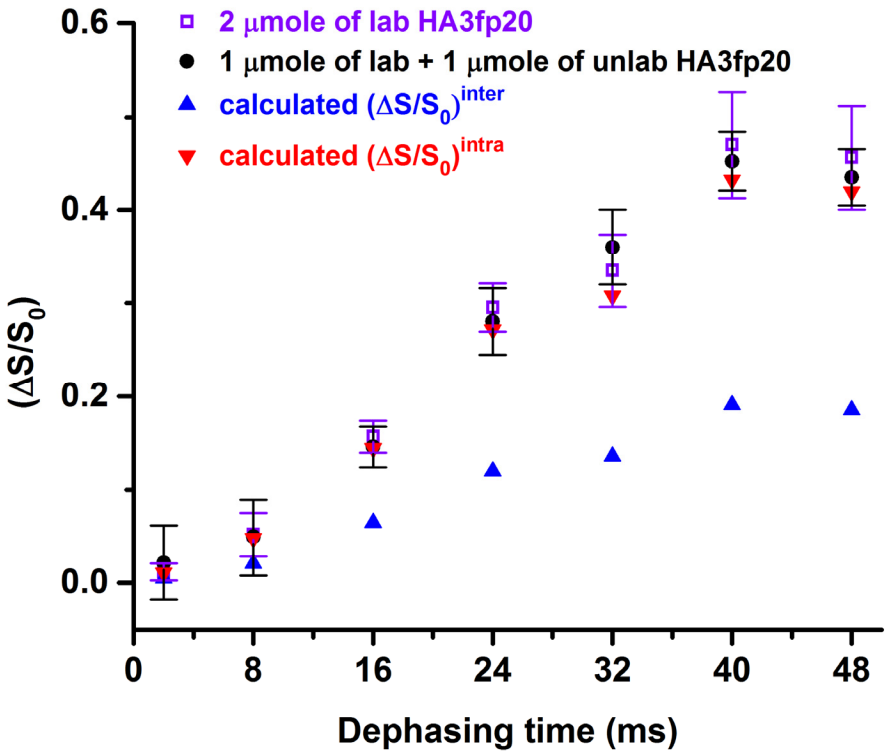

Figure 3.10. $(\Delta S/S_0)^{exp}$ buildups for pH 5 samples with either 2 μmole G16 ^{13}CO/F9 ^{15}N labeled HA3fp20 or 1 μmole labeled and 1 μmole unlabeled HA3fp20. The calculated $(\Delta S/S_0)^{intra}$ and $(\Delta S/S_0)^{inter}$ for the mixed sample are also displayed. The blue up triangles (▲) and red down triangles (▼) were calculated according to the equations 3.20 and 3.27 respectively. The HAfp: lipid ratio was 1:25 in all the NMR samples. The lipids were composed of DTPC/DTPG in 4:1 ratio.

3.2.4 Fitting of the ^{13}CO – ^{15}N REDOR data

Figure 3.11 shows that the $(\Delta S/S_0)^{lab}$ buildups do not quantitatively match with the $(\Delta S/S_0)^{sim}$ closed or open structures.

Quantitative analysis of $(\Delta S/S_0)^{lab}$ vs τ was done using three structural models:

1. Single structure model,
2. Two structure model, and
3. Three structure model.

Global fitting was performed because dephasing buildups for all the samples were very similar. The experimentally-derived $(\Delta S/S_0)^{lab}$ buildups fit poorly to a single structure with one dipolar coupling or with three structural model. Fitting was therefore done using models with two or more populations each with different couplings. The **closed/semi-closed model** was based on: (1) a single closed structure with associated distances $r_{cG} \equiv$ G16 ^{13}CO-F9 ^{15}N and $r_{cA} \equiv$ A5^{13}CO-M17^{15}N and corresponding dipolar couplings d_{cG} and d_{cA}; and (2) a single semi-closed structure with distances r_{sG} and r_{sA} and couplings d_{sG} and d_{sA}. Each sample type (HA3fp20 vs HA1fp23 and pH 5 vs pH 7) was a mixture of a closed and semi-closed peptides with respective fractions f_c and $f_s = 1 - f_c$. The f_{c1}, f_{c2}, f_{c3}, and f_{c4}respectively correspond to the HA3fp20/pH 5, HA3fp20/pH 7, HA1fp23/pH 5, and HA1fp23/pH 7 samples. The χ^2 are calculated for an array of d_{cG}, d_{cA}, d_{sG}, d_{sA}, f_{c1}, f_{c2}, f_{c3}, and f_{c4} values with the $(\Delta S/S_0)^{sim}$ for each d calculated by:

$$\chi^2(f_{c1},f_{c2},f_{c3},f_{c4},d_s,d_c) = \sum_{i=1}^{7} \frac{[(\frac{\Delta S}{S_0})_i^{lab} - \{f_{c1} \times (\frac{\Delta S}{S_0})_i^{sim}(d_c)\} - (1-f_{c1}) \times (\frac{\Delta S}{S_0})_i^{sim}(d_s)]^2}{(\sigma_i^{lab})^2} + \sum_{j=1}^{7} \frac{[(\frac{\Delta S}{S_0})_j^{lab} - \{f_{c2} \times (\frac{\Delta S}{S_0})_j^{sim}(d_c)\} - (1-f_{c2}) \times (\frac{\Delta S}{S_0})_j^{sim}(d_s)]^2}{(\sigma_j^{lab})^2}$$
$$+ \sum_{k=1}^{7} \frac{[(\frac{\Delta S}{S_0})_k^{lab} - \{f_{c3} \times (\frac{\Delta S}{S_0})_k^{sim}(d_c)\} - (1-f_{c3}) \times (\frac{\Delta S}{S_0})_k^{sim}(d_s)]^2}{(\sigma_k^{lab})^2} + \sum_{l=1}^{7} \frac{[(\frac{\Delta S}{S_0})_l^{lab} - \{f_{c4} \times (\frac{\Delta S}{S_0})_l^{sim}(d_c)\} - (1-f_{c4}) \times (\frac{\Delta S}{S_0})_l^{sim}(d_s)]^2}{(\sigma_l^{lab})^2}$$

3.28

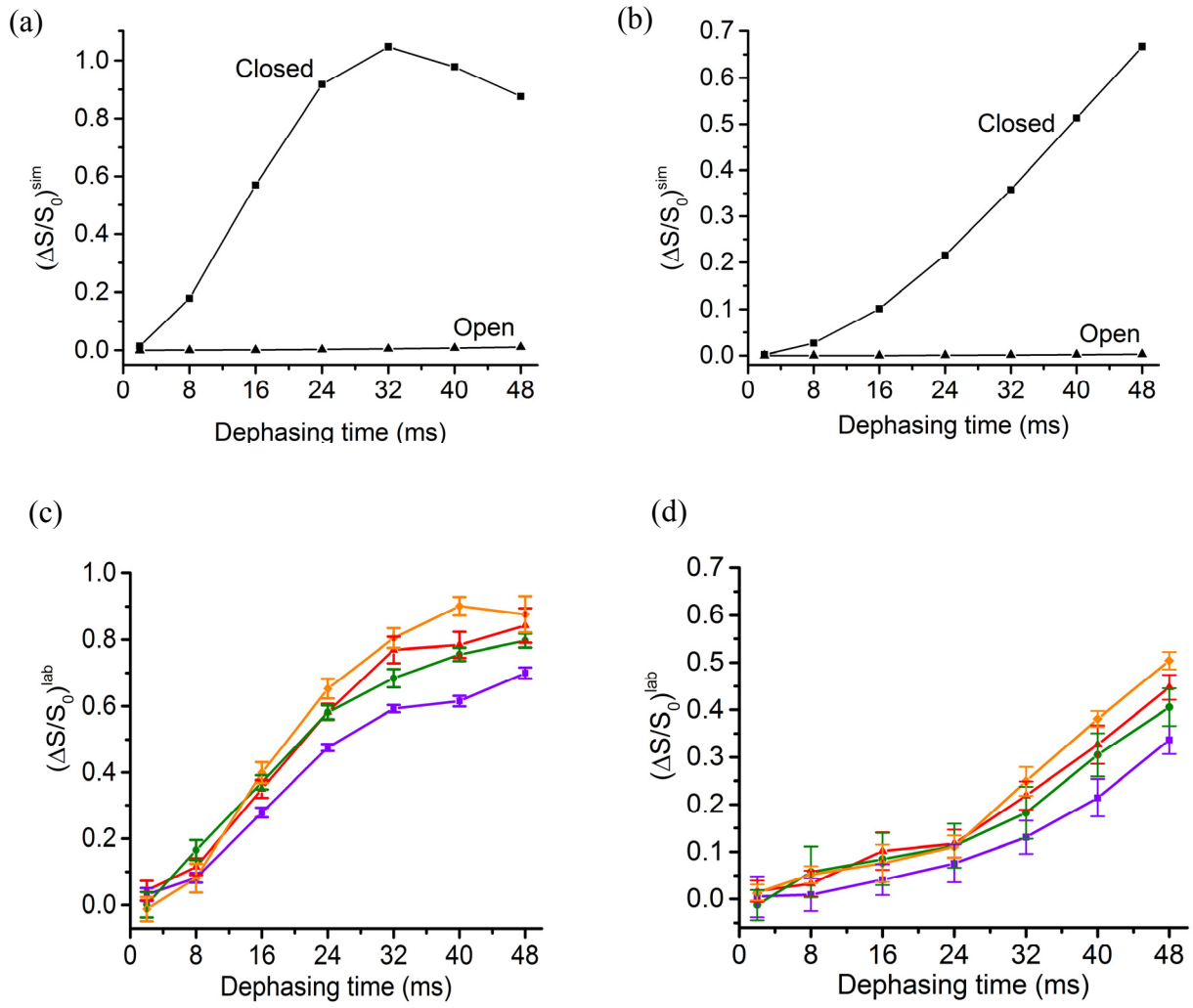

Figure 3.11. Simulated ^{13}C-^{15}N REDOR dephasing curves of $(\Delta S/S_0)$ vs τ for (a) G16^{13}CO-F9^{15}N and (b) A5^{13}CO-M17^{15}N. (a) The F9n-G16c distance in the closed structure of HA1fp23 and the open structure of HA3fp20 are 3.9 and 11.5 Å respectively. (b) The A5c-M17n distance in the closed and the open structures are 5.5 and 11.9 Å respectively. Natural abundance corrected $(\Delta S/S_0)^{lab}$ vs τ for (c) G16^{13}CO-F9^{15}N and (d) A5^{13}CO-M17^{15}N. The uncertainties are represented by the error bars and are typically ± 0.03 – 0.04. Color coding: HA3fp20 at pH 5, HA3fp20 at pH 7, HA1fp23 at pH 5, and HA1fp23 at pH 7.

Each summation was for one buildup with seven dephasing times. The σ^{lab} is the $(\Delta S/S_0)^{lab}$ uncertainty and is calculated using the RMSD spectral noise. The best-fit corresponds to minimum $\chi^2 \equiv \chi^2_{min}$.

Table 3.7 lists the best-fit parameters including uncertainties and χ^2_{min} using closed / semi-closed model.

Table 3.7. Best-fit parameters of the closed/semi-closed model[a,b]

HA3fp20 pH 5.0 f_{c1}	HA3fp20 pH 7.0 f_{c2}	HA1fp23 pH 5.0 f_{c3}	HA1fp23 pH 7.0 f_{c4}	d_{cG} Hz	d_{cA} Hz	d_{sG} Hz	d_{sA} Hz	r_{cG} Å	r_{cA} Å	r_{sG} Å	r_{sA} Å
0.35 (2)	0.55 (4)	0.51 (3)	0.71 (3)	52.1 (1.2)	19.5 (5)	19.7 (6)	5.5 (8)	3.89 (3)	5.40 (5)	5.38 (5)	8.25 (40)

[a] Fitting was done with the f_c's ≡ fractional populations of closed structure and d 's ≡ dipolar couplings. The corresponding best-fit r's were calculated from the best-fit d's using r(Å) = $[3066/d(\text{Hz})]^{1/3}$ which reflects a coupling that isn't motionally-averaged.

[b] The fitting is statistically reasonable because χ^2_{min} = 52 was comparable to the number of degrees of fitting = 48. The uncertainty of a best-fit parameter value in parentheses is based on the difference between parameter values for χ^2_{min}+ 2 vs χ^2_{min}.

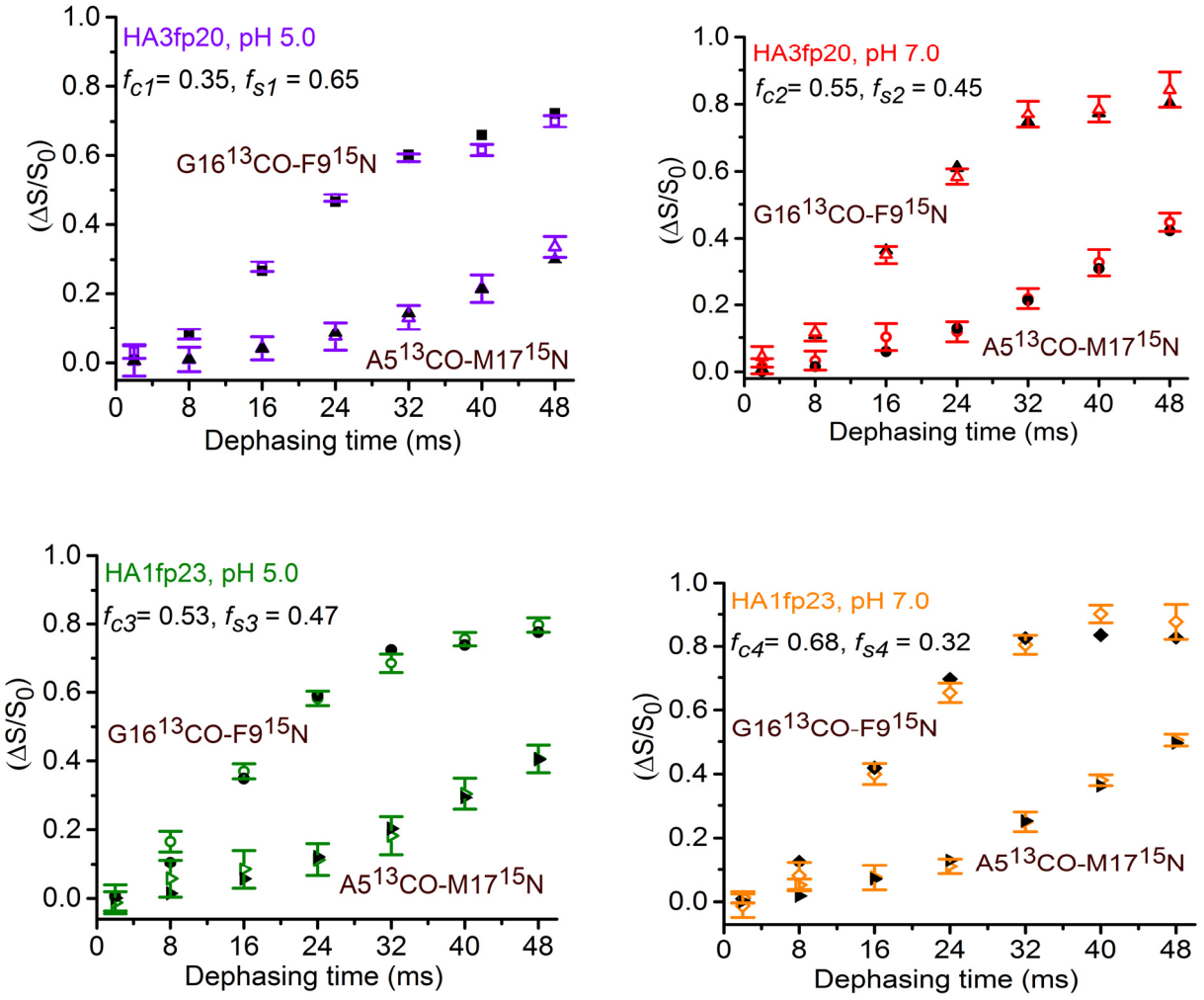

Figure 3.12. Plots of the experimental $(\Delta S/S_0)^{lab}$ and the best-fit $(\Delta S/S_0)^{sim}$ for the closed/semiclosed model. The colored and the black points represent the experimental $(\Delta S/S_0)^{lab}$ and the $(\Delta S/S_0)^{sim}$ from the closed/semiclosed model. The f_c and f_s represent the fraction of the closed and the semiclosed population. The best-fit closed distance for the G16c-F9n (r_{cG}) = 3.9 Å and A5c-M17n (r_{cA}) = 5.4 Å common to all four samples. The best-fit semiclosed distance for r_{sG} = 5.4 Å and r_{sA} = 8.2 Å common to all four samples. The χ^2_{min} = 52 and is close to the degrees of freedom = 48. Table 3.6 lists all the best-fit parameters for the closed/semiclosed model used for the global fitting for all four samples.

3.2.5 Alternate fitting models

Fitting was done using alternative models but none of these fittings resulted in χ^2 values as statistically reasonable as the closed/semi-closed model. These fittings are done with the G16/F9 ($\Delta S/S_0$) buildups because they are significantly larger than the A5/M17 buildups. Fitting was first done with the closed/semi-closed model for the twoHA3fp20 buildups and separately for the twoHA1fp23 buildups.

The single structural model or **closed/open model** was based on a single closed structure with r_c and d_c and an open structure which does not contribute to ($\Delta S/S_0$) because r_o was large and $d_o \approx$ 0.The four buildups are fitted simultaneously to the f_c and d_c parameters:

$$\chi^2(f_{c1},f_{c2},f_{c3},f_{c4},d_c) = \sum_{i=1}^{7} \frac{[(\frac{\Delta S}{S_0})_i^{lab} - \{f_{c1} \times (\frac{\Delta S}{S_0})_i^{sim}(d_c)\}]^2}{(\sigma_i^{lab})^2} + \sum_{j=1}^{7} \frac{[(\frac{\Delta S}{S_0})_j^{lab} - \{f_{c2} \times (\frac{\Delta S}{S_0})_j^{sim}(d_c)\}]^2}{(\sigma_j^{lab})^2}$$
$$+ \sum_{k=1}^{7} \frac{[(\frac{\Delta S}{S_0})_k^{lab} - \{f_{c3} \times (\frac{\Delta S}{S_0})_k^{sim}(d_c)\}]^2}{(\sigma_k^{lab})^2} + \sum_{l=1}^{7} \frac{[(\frac{\Delta S}{S_0})_l^{lab} - \{f_{c4} \times (\frac{\Delta S}{S_0})_l^{sim}(d_c)\}]^2}{(\sigma_l^{lab})^2} \quad 3.29$$

The three structural models or the **closed/semi-closed/open model** was based on earlier studies interpreted to support ~ 0.2 fraction of open structure at low pH. The two pH 5 buildups are fitted with a 0.2 fraction open structure:

$$\chi^2\{f_{c1},f_{c3},d_c\} = \sum_{i=1}^{7} \frac{[(\frac{\Delta S}{S_0})_i^{lab} - f_{c1} \times (\frac{\Delta S}{S_0})_i^{sim}\{d_c\} - (0.8-f_{c1}) \times (\frac{\Delta S}{S_0})_i^{sim}\{d_s\} - 0.2 \times (\frac{\Delta S}{S_0})_i^{sim}\{d_o\}]}{(\sigma_i^{lab})^2}$$
$$+ \sum_{k=1}^{7} \frac{[(\frac{\Delta S}{S_0})_k^{lab} - f_{c3} \times (\frac{\Delta S}{S_0})_k^{sim}\{d_c\} - (0.8-f_{c3}) \times (\frac{\Delta S}{S_0})_k^{sim}\{d_s\} - 0.2 \times (\frac{\Delta S}{S_0})_k^{sim}\{d_o\}]}{(\sigma_k^{lab})^2} \quad 3.30$$

Fitting was done with r_o = 11.5 Å and with r_o = 7.2 Å which were respectively for the open structure of HA3fp20 in detergent and membranes. The membrane structure was the *N*-helix

from residues 1-10, *C*-helix from residues 13-20, and turn determined using the ^{13}C shifts of a minor set of E11 inter-residue crosspeaks. Fitting was done for an array of either d_c, d_s, and f_c values or only f_c values with fixed d_c, d_s, and d_o derived from structures of HAfp in detergent and membranes. Table 3.8 lists the best-fit parameters for the different models and Figures 3.13 – 3.15 display plots of experimental and best-fit ($\Delta S/S_0$).

In Table 3.8, fitting parameters include d (r) ≡ dipolar coupling (G16^{13}CO – F9^{15}N distance) and f ≡ mole fraction.

The typical χ^2_{min} + 2 based parameter uncertainties for the closed/semi-closed model are: *f*, 0.03; and *d (r)*, 1 Hz (0.02 Å).

Table 3.8. Best-fit parameters of the models used to fit the G16/F9 SSNMR REDOR data

Model	HA3fp20 pH 5.0 f_{c1}	HA3fp20 pH 7.0 f_{c2}	HA1fp23 pH 5.0 f_{c3}	HA1fp23 pH 7.0 f_{c4}	d_c (Hz) r_c (Å)	d_s (Hz) r_s (Å)	χ^2_{min}	Deg. of freedom
Closed/semi-closed								
Simultaneous fit	0.36	0.55	0.53	0.68	52.1 (3.89)	19.2 (5.42)	34	22
HA3fp20 fit	0.33	0.53			56.8 (3.78)	20.2 (5.33)	15	10
HA1fp23 fit			0.51	0.66	55.0 (3.82)	20.7 (5.29)	19	10
Closed/open	0.60	0.78	0.71	0.90	47.9 (4.00)		142	23
Closed/semi-closed/open								
d_o (r_o) = 2.0 Hz (11.5 Å)	0.58		0.68		43.2 (4.14)	18.1 (5.14)	92	10
d_o (r_o) = 8.2 Hz (7.2 Å)	0.51		0.61		41.4 (4.20)	21.8 (5.20)	77	10
d_c (r_c) = 51.7 Hz (3.9 Å) d_s (r_s) = 18.4 Hz (5.5 Å) d_o (r_o) = 2.0 Hz (11.5 Å)	0.47		0.67				137	12
d_c (r_c) = 51.7 Hz (3.9 Å) d_s (r_s) = 18.4 Hz (5.5 Å) d_o (r_o) = 2.0 Hz (11.5 Å)	0.44		0.60				83	12

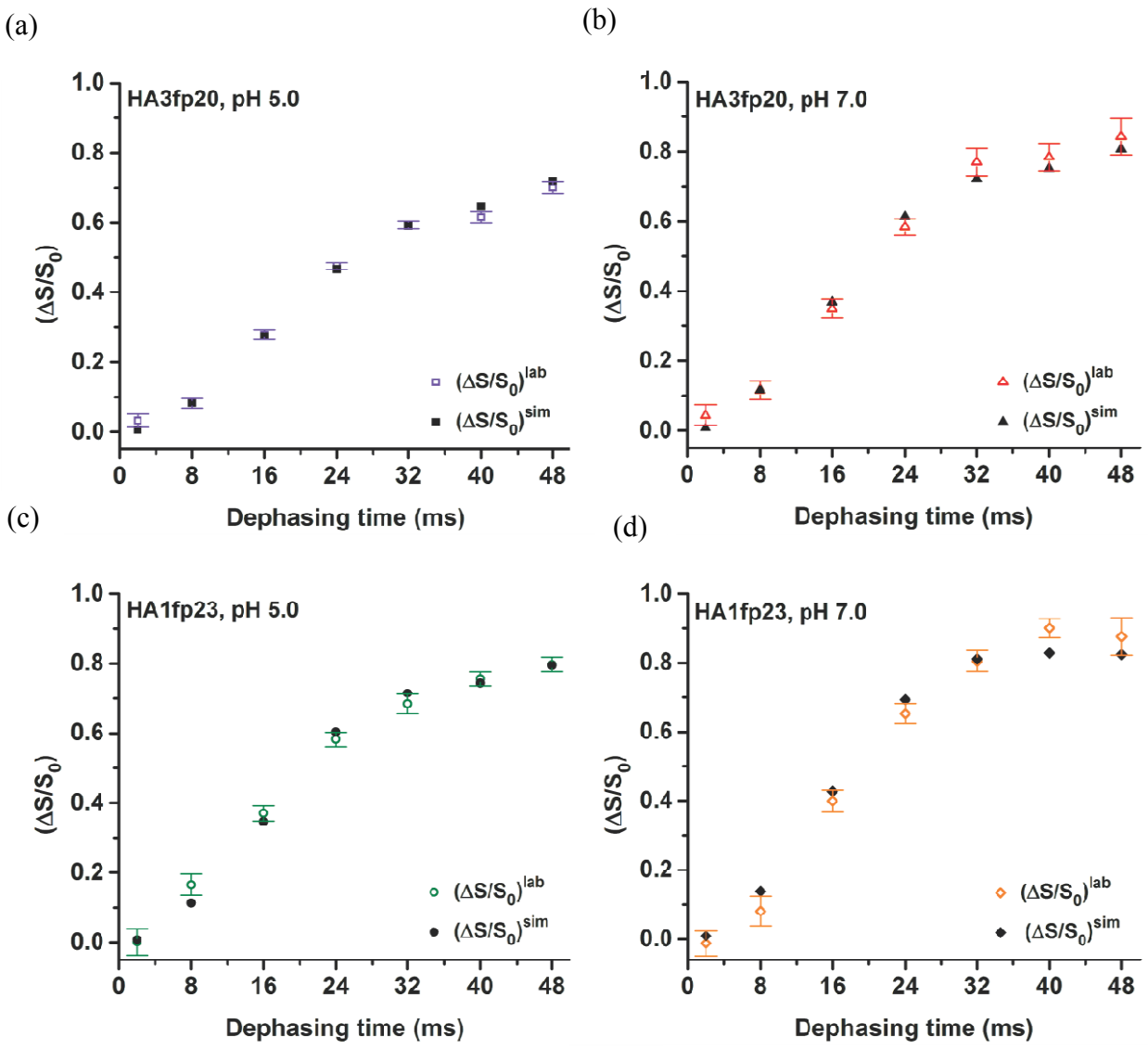

Figure 3.13. Plots of experimental G16c-F9n and best-fit ($\Delta S/S_0$) from the closed/semiclosed model. The top, HA3fp20 and the bottom, HA1fp23 data are fitted separately. The best-fit closed and the semiclosed fractions for (a) $f_{c1} = 0.33$, $f_{s1} = 0.67$; (b) $f_{c2} = 0.53$, $f_{s2} = 0.47$; (c) $f_{c3} = 0.51$, $f_{s3} =$ and (d) $f_{c4} = 0.66$, $f_{s4} = 0.34$. The best-fit closed and semiclosed distances for a/b are 3.78 Å and 5.33 Å and for c/d are 3.82 Å and 5.29 Å respectively.

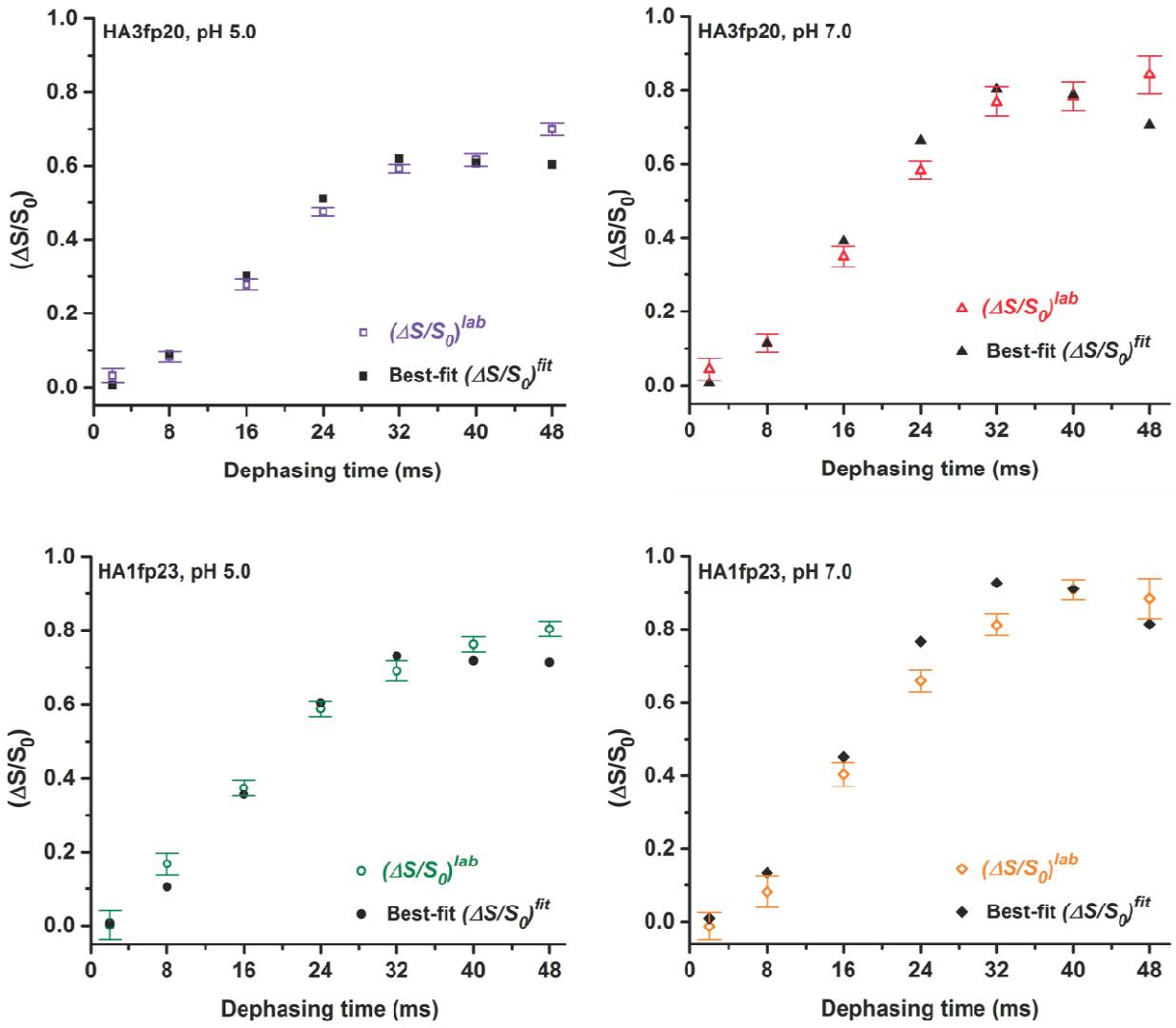

Figure 3.14. Plots of the experimental G16c-F9n and the best-fit ($\Delta S/S_0$) from the closed/open model using $r_c = 4$ Å.

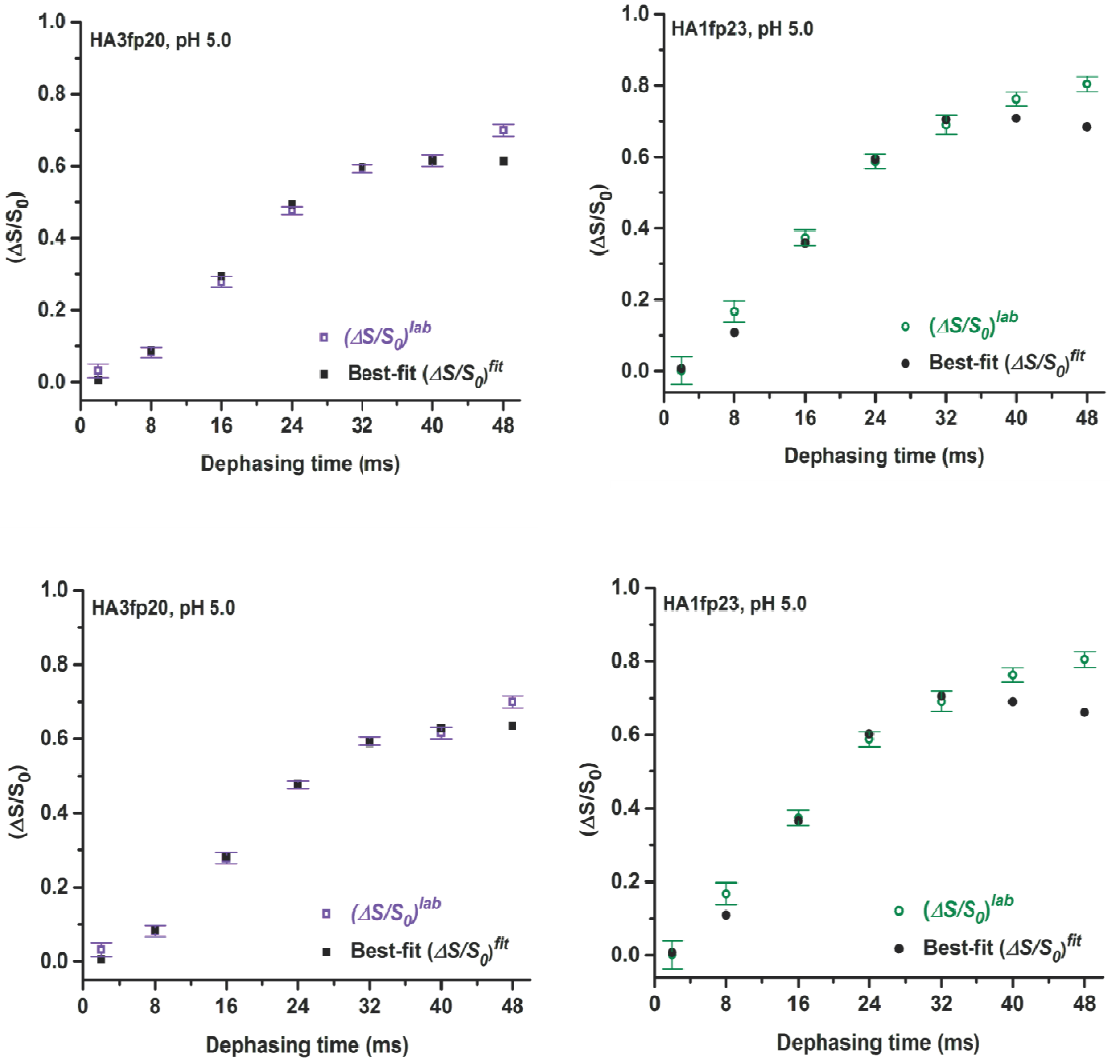

Figure 3.15. Plots of experimentally-derived $(\Delta S/S_0)^{lab}$ and best-fit $(\Delta S/S_0)$ from the closed/semi-closed/open model using (top) $d_o(r_o)$ = 2.0 Hz (11.5 Å) and (bottom) $d_o(r_o)$ = 8.2 Hz (7.2 Å). The d_c and d_s are fixed.

The calculated ($\Delta S/S_0$) values using the analytical expression of equation 3.14 are typically within 0.01 of the values calculated using the SIMPSON program [26] which incorporates the experimental MAS frequency, pulse fields and durations, and chemical shift offsets and anisotropies. Table 3.9 displays calculated ($\Delta S/S_0$) from both approaches for d = 51.7 Hz which corresponds to r = 3.90 Å.

Table 3.9. ($\Delta S/S_0$) values for d = 51.7 Hz [a]

τ (ms)	($\Delta S/S_0$) Eq. 3.15	($\Delta S/S_0$) SIMPSON
2	0.011	0.014
8	0.171	0.179
16	0.562	0.570
24	0.913	0.918
32	1.043	1.046
40	0.972	0.978
48	0.866	0.876

[a] This d corresponds to r = 3.90 Å.

[b] The SIMPSON calculation is based on the experimental pulse sequence with input parameters that include the MAS frequency, ^{13}C and ^{15}N pulse fields and durations, and ^{13}CO chemical shift offset and anisotropy.

3.3 Discussion

The fusion of the influenza viral membrane to the target membranes is one of the most widely studied fusion process. The ~23 residue fusion domain of the HA2 subunit is highly conserved and plays a key factor in the fusion process. [15] The importance of the fusion domain has been demonstrated by several mutational studies. [3, 4, 6] Earlier solution NMR studies on HA3fp20 supported a helical structure at both the N- and C-terminuses at pH 5. However, at pH 7.4 the N-terminal helix is preserved but there is an extended structure at C-terminus. [13] In contrast, HA3fp20 is helical at both the N- and C-terminus at both pHs in the membranes containing PC:PG in 4:1 mole ratio. [19] However, the longer peptide HA1fp23, adopts a closed helical hairpin structure at both the pHs in detergents due to the presence of the additional residues at the C-terminus. [14] In the present study we investigated the structure of both the 20- and the 23-residue peptide at both pHs for both the H1- and H3 subtype of HAfp.

The present solid state NMR results confirm that for both the HAfp constructs are helical at both N- and C-terminuses at both pH 5 and pH 7. This result is in contrast with an earlier study of HA3fp20 in detergents, where HA3fp20 had an extended structure at pH 7.4. [27, 28] However, our results are consistent with the earlier study in detergents where HA1fp23 was helical at both pHs. Our results are also consistent with an earlier study of HA3fp20 in membranes. [19]

The REDOR dephasing buildups fits well to a single closed/semiclosed model which suggests that both the HAfp constructs have very similar structures in membranes and is not consistent with the earlier solution NMR studies of the HA1fp23 and HA3fp20 in detergents. The fittings of the REDOR buildups yield the $r_{cG} \approx 3.9$ Å and $r_{cA} \approx 5.5$ Å, and are consistent with the earlier closed structure of HA1fp23 in detergents. The semiclosed structure, $r_{sG} \approx 5.4$ Å and $r_{sA} \approx 8.2$ Å

is observed only in membranes. Because $(\Delta S/S_0)^{open} \approx 0$, the models that include open structure result in a greater fraction closed structure relative to the closed/semi-closed model. The lowest χ^2_{min} is obtained for the closed/semi-closed model and this model is also statistically reasonable based on χ^2_{min} close to ν_f. Much higher χ^2_{min}'s are obtained for the other models that include open structure and the $\chi^2_{min} >> \nu_f$. The closed/semi-closed model is therefore considered most likely. The significant differences between the structures in the membranes vs detergents are: (1) presence vs absence of the semiclosed structure; (b) absence vs presence of the open structure; and (3) mixture of closed and semiclosed structures for both HA3fp20 and HA1fp23 vs predominant open structure for HA3fp20 and the closed structure for HA1fp23.

Relative to HA3fp20, there is a larger fraction of the closed structure for HA1fp23 in membranes probably due to the stabilization of the tight N-helix/C-helix packing via the longer C-helix containing the additional Trp, Tyr and Gly residues. For both the HA3fp20 and HA1fp23, there is a larger semiclosed fraction at pH 5 relative to at pH 7. The larger fraction of semiclosed structure at low pH can be correlated to the protonation of Glu-11 present at the turn region. This result qualitatively agrees with an earlier MD simulation of HA3fp20 in implicit membranes. [29] In this study it was shown that the protonation of Glu-11 opened the structure of HA3fp20.

Earlier solution NMR studies suggested that HA1fp23 adopts ~20% open structures at low pH [16](figure 3.1d) and HA3fp20 adopts ~ 90% open at pH 7.4.[17] However, we never observed any open structures in membranes. In fact, including any open structure in our model made the fitting worse resulting in higher $\chi^2_{\min}$ values (Table 3.7). One possible reason why we never observed any open structures could be due to the high curvature of detergent micelle. The high curvature of the micelle probably matches better with the highly curved hydrophobic surface of the open structure (Figure 3.1b). In contrast, the planar hydrophobic face of the closed and the

semiclosed structure matches with the planar bilayer surface (Figures 4.3a and 4.3b). The present study shows that the structure of HAfp is different in membranes and in detergent micelles. There are very few examples where it was shown that the curvature of the micelle has an effect on the structure of a protein/peptide. For example, α-Synuclein forms a bent-helix when bound to detergents whereas it forms an elongated helix when bound to large unilamellar vesicles.[30, 31] These results highlight the influence of the membrane curvature on the structure of membrane proteins/peptides and emphasize the role of membrane curvature in determining the structure of the membrane proteins/peptides.

REFERENCES

REFERENCES

1. Dimitrov, D.S., *Cell Biology Of Virus Entry.* Cell, 2000. **101**(7): p. 697-702.

2. Eckert, D.M. and P.S. Kim, *Mechanisms Of Viral Membrane Fusion And Its Inhibition.* Annual Review of Biochemistry, 2001. **70**: p. 777-810.

3. Steinhauer, D.A., et al., *Studies Using Double Mutants Of The Conformational Transitions In Influenza Hemagglutinin Required For Its Membrane Fusion Activity.* Proceedings of the National Academy of Sciences of the United States of America, 1996. **93**(23): p. 12873-12878.

4. Qiao, H., et al., *A Specific Point Mutant At Position 1 Of The Influenza Hemagglutinin Fusion Peptide Displays A Hemifusion Phenotype.* Molecular Biology of the Cell, 1999. **10**(8): p. 2759-2769.

5. Gething, M.J., K. McCammon, and J. Sambrook, *Expression Of Wild-Type And Mutant Forms Of Influenza Hemagglutinin - The Role Of Folding In Intracellular-Transport.* Cell, 1986. **46**(6): p. 939-950.

6. Steinhauer, D.A., et al., *Studies Of The Membrane-Fusion Activities Of Fusion Peptide Mutants Of Influenza-Virus Hemagglutinin.* Journal of Virology, 1995. **69**(11): p. 6643-6651.

7. Cross, K.J., et al., *Studies On Influenza Haemagglutinin Fusion Peptide Mutants Generated By Reverse Genetics.* Embo Journal, 2001. **20**(16): p. 4432-4442.

8. Luneberg, J., et al., *Structure And Topology Of The Influenza-Virus Fusion Peptide In Lipid Bilayers.* Journal of Biological Chemistry, 1995. **270**(46): p. 27606-27614.

9. Gray, C., et al., *Effect Of The N-Terminal Glycine On The Secondary Structure, Orientation, And Interaction Of The Influenza Hemagglutinin Fusion Peptide With Lipid Bilayers.* Biophysical Journal, 1996. **70**(5): p. 2275-2286.

10. Macosko, J.C., C.H. Kim, and Y.K. Shin, *The Membrane Topology Of The Fusion Peptide Region Of Influenza Hemagglutinin Determined By Spin-Labeling EPR.* Journal of Molecular Biology, 1997. **267**(5): p. 1139-1148.

11. Wasniewski, C.M., et al., *Solid-State Nuclear Magnetic Resonance Studies Of HIV And Influenza Fusion Peptide Orientations In Membrane Bilayers Using Stacked Glass Plate Samples.* Chemistry and Physics of Lipids, 2004. **132**(1): p. 89-100.

12. Han, X. and L.K. Tamm, *pH-Dependent Self-Association Of Influenza Hemagglutinin Fusion Peptides In Lipid Bilayers.* Journal of Molecular Biology, 2000. **304**(5): p. 953-965.

13. Han, X., et al., *Membrane Structure And Fusion-Triggering Conformational Change Of The Fusion Domain From Influenza Hemagglutinin.* Nature Structural Biology, 2001. **8**(8): p. 715-720.

14. Lorieau, J.L., J.M. Louis, and A. Bax, *The Complete Influenza Hemagglutinin Fusion Domain Adopts A Tight Helical Hairpin Arrangement At The Lipid:Water Interface.* Proceedings of the National Academy of Sciences of the United States of America, 2010. **107**(25): p. 11341-11346.

15. Nobusawa, E., et al., *Comparison Of Complete Amino-Acid-Sequences And Receptor-Binding Properties Among 13 Serotypes Of Hemagglutinins Of Influenza A-Viruses.* Virology, 1991. **182**(2): p. 475-485.

16. Lorieau, J.L., et al., *pH-triggered, Activated-State Conformations Of The Influenza Hemagglutinin Fusion Peptide Revealed By NMR.* Proceedings of the National Academy of Sciences of the United States of America, 2012. **109**(49): p. 19994-19999.

17. Lorieau, J.L., J.M. Louis, and A. Bax, *Impact Of Influenza Hemagglutinin Fusion Peptide Length And Viral Subtype On Its Structure And Dynamics.* Biopolymers, 2013. **99**(3): p. 189-195.

18. Du, T., L. Jiang, and M. Liu, *NMR Structures Of Fusion Peptide From Influenza Hemagglutinin H3 Subtype And Its Mutants.* Journal of Peptide Science, 2014. **20**(4): p. 292-297.

19. Sun, Y. and D.P. Weliky, *C-13-C-13 Correlation Spectroscopy Of Membrane-Associated Influenza Virus Fusion Peptide Strongly Supports A Helix-Turn-Helix Motif And Two Turn Conformations.* Journal of the American Chemical Society, 2009. **131**(37): p. 13228-13229.

20. Morcombe, C.R. and K.W. Zilm, *Chemical Shift Referencing In MAS Solid State NMR.* Journal of Magnetic Resonance, 2003. **162**(2): p. 479-486.

21. Zhang, H.Y., S. Neal, and D.S. Wishart, *RefDB: A Database Of Uniformly Referenced Protein Chemical Shifts.* Journal of biomolecular nmr, 2003. **25**(3): p. 173-195.

22. Kricheldorf, H.R. and D. Muller, S*econdary Structure Of Peptides .8. C-13 NMR CP-MAS Investigation Of Solid Poly(l-leucines) And Poly(d-norvalines) Prepared From n-Carboxyanhydrides.* International Journal of Biological Macromolecules, 1983. **5**(3): p. 171-178.

23. Gullion, T. and J. Schaefer, *Rotational-Echo Double-Resonance NMR.* Journal of Magnetic Resonance, 1989. **81**(1): p. 196-200.

24. Yang, J., et al., *Solid State NMR Measurements Of Conformation And Conformational Distributions In The Membrane-Bound Hiv-1 Fusion Peptide.* Journal of Molecular Graphics & Modelling, 2001. **19**(1): p. 129-135.

25. Mueller, K.T., *Analytic Solutions For The Time Evolution Of Dipolar-Dephasing NMR Signals.* Journal of Magnetic Resonance Series A, 1995. **113**(1): p. 81-93.

26. Bak, M., J.T. Rasmussen, and N.C. Nielsen, *SIMPSON: A General Simulation Program For Solid-State NMR Spectroscopy.* Journal of Magnetic Resonance, 2000. **147**(2): p. 296-330.

27. Ghosh, U., L. Xie, and D.P. Weliky, *Detection Of Closed Influenza Virus Hemagglutinin Fusion Peptide Structures In Membranes By Backbone 13CO-15N Rotational-Echo Double-Resonance Solid-State NMR.* Journal of Biomolecular NMR, 2013. **55**(2): p. 139-146.

28. Ghosh, U., et al., *Closed And Semiclosed Interhelical Structures In Membrane Vs Closed And Open Structures In Detergent For The Influenza Virus Hemagglutinin Fusion Peptide And Correlation Of Hydrophobic Surface Area With Fusion Catalysis.* Journal of the American Chemical Society, 2015. **137**(24): p. 7548-7551.

29. Panahi, A. and M. Feig, *Conformational Sampling Of Influenza Fusion Peptide In Membrane Bilayers As A Function Of Termini And Protonation States.* Journal of Physical Chemistry B, 2010. **114**(3): p. 1407-1416.

30. Trexler, A.J. and E. Rhoades, *alpha-Synuclein Binds Large Unilamellar Vesicles As An Extended Helix.* Biochemistry, 2009. **48**(11): p. 2304-2306.

31. Middleton, E.R. and E. Rhoades, *Effects Of Curvature And Composition On Alpha-Synuclein Binding To Lipid Vesicles.* Biophysical Journal, 2010. **99**(7): p. 2279-2288.

Chapter 4

Structure - Function Correlation and Modeling of Membrane Associated Influenza Fusion Peptide

4.1 Introduction

This chapter describes how the structural models of the membrane associated HAfp was done using the experimentally determined chemical shifts and from the pdb coordinates of HA1fp23 (2KXA). [1] The best-fit distances from the ^{13}C-^{15}N REDOR dephasing buildups are:

Table 4.1. Interhelical distances of HAfp in membranes and in detergents

Labeling Scheme	Detergents HA1fp23	Membranes HA1fp23 and HA3fp20	
	Closed (Å)	Closed (Å)	Semiclosed (Å)
G16c-F9n	3.90	3.89	5.38
A5c-M17n	5.50	5.40	8.25

The closed structure observed in membranes is similar to the closed structure previously observed in detergents for HA1fp23 because:

1. The observed G16c-F9n and A5c-M17n distances for the closed structure in membranes are in very good agreement with the distances of the closed structure of HA1fp23 in detergents.

2. The chemical shifts of Ala-5 and Gly-16 ^{13}CO are 179 ppm and 177 ppm respectively at both pH 5 and pH 7. [2] These ^{13}CO chemical shifts further confirm that both the N- and C-terminal helices of HAfp are helical like HA1fp23 in detergents.

Therefore, the closed structure in detergent is similar to the closed structure of HAfp in membranes. The dihedral angles of the closed structure (2KXA) were used to model the closed structure of HAfp in membranes. Although the pdb coordinates of the closed structure was

available, we modeled the closed structure to cross-check the method used to model the semiclosed structure.

4.2 Modeling of the closed structure

The dihedral angles of the closed structure were obtained by using the VADAR (Volume Area Dihedral Angle Reporter). [3] VADAR is a knowledge based database and accepts Protein Data Bank (pdb) formatted files or pdb accession numbers and determines the backbone and side chain torsion angles (phi, psi, omega and chi angles) from the Cartesian coordinates. In VADAR, the φ angle is defined as the angle between the planes consists of CO.0 – N.1 and CA.1 – CO.1 and the ψ angles is defined as the angle between the N.1 – CA.1 and CO.1 – N.2 planes. The dihedral angles are calculated by $\cos\varphi = \frac{a_1a_2 + b_1b_2 + c_1c_2}{\sqrt{a_1^2+b_1^2+c_1^2}\sqrt{a_2^2+b_2^2+c_2^2}}$, where the planes are described by the equations $a_1x+b_1y+c_1z+d_1=0$ and $a_2x+b_2y+c_2z+d_2=0$. The calculated φ, ψ angles are then compared to a set of standards using Ramachandran plot and then a score is assigned based on the likelihood of the φ/ψ combination which indicates the quality of the structure. VADAR gives the consensus averages and the standard deviations for the dihedral angles for a given number of structures. For the closed structure, the φ and ψ angles for the residues Gly-1 to Gly-23 are based on the average values with standard deviations obtained from the 10 lowest energy structures. The PDB file for the closed structure was generated in the following steps:

1. Torsion angles were obtained from the VADAR program.
2. A closed.ang file was created using the backbone phi and psi angles.
3. The closed.ang file was given as input to the MOLMOL software. [4]
4. Once the closed.ang file was read by MOLMOL software, then the closed.pdb file was obtained as output.
5. The newly created closed.pdb was energy minimized using YASARA energy minimization program. [5] YASARA combines the AMBER all atom force field equation with the knowledge based potentials for the energy minimization with a consistent set of force field parameters. To start the minimization, YASARA first cleans the structure so the force field parameters can be assigned. For example, during the cleaning process YASARA adds missing atoms, correct H-bonds, reassign bond orders etc. After the cleaning step, energy minimization is done. During the minimization process a temporary water shell is added so that all the force fields parameters that are optimized for use with explicit solvent can be used.
6. Figure 4.2 shows the superimposition of the created closed.pdb and the deposited pdb file (2KXA) with a backbone RMSD of 0.40 Å.
7. The final pictures were done using PYMOL software.

```
# Structure of Closed HAfp,
  1 GLY   PHI    999.999 PSI   -107.800
  2 LEU   PHI    -64.600 PSI    -50.600
  3 PHE   PHI    -63.000 PSI    -38.000
  4 GLY   PHI    -64.000 PSI    -42.000
  5 ALA   PHI    -66.000 PSI    -37.000
  6 ILE   PHI    -68.000 PSI    -45.000
  7 ALA   PHI    -62.000 PSI    -40.000
  8 GLY   PHI    -62.000 PSI    -39.000
  9 PHE   PHI    -67.000 PSI    -37.000
 10 ILE   PHI    -63.000 PSI    -42.000
 11 GLU   PHI    -69.000 PSI    -27.000
 12 ASN   PHI    -96.000 PSI      8.000
 13 GLY   PHI     87.000 PSI     10.000
 14 TRP   PHI    -40.000 PSI    -42.000
 15 GLU   PHI    -53.000 PSI    -33.000
 16 GLY   PHI    -70.000 PSI    -18.000
 17 MET   PHI    -98.000 PSI    -11.000
 18 ILE   PHI    -71.000 PSI    -46.000
 19 ASP   PHI    -42.000 PSI    151.000
 20 GLY   PHI     78.000 PSI    999.999
```

Figure 4.1. Example of .ang file.

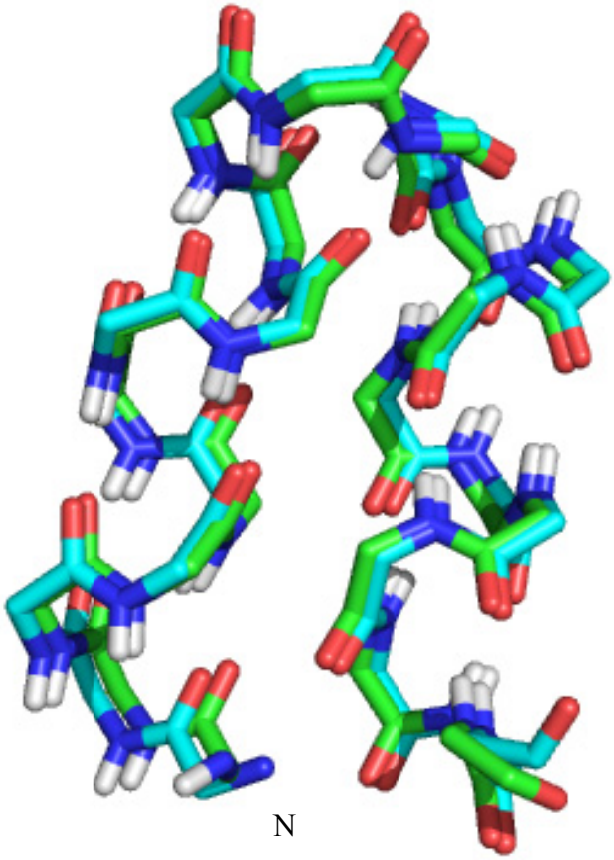

Figure 4.2. Superimposed backbone closed structures of HA1fp23 obtained by the method described in the section 4.1 (green) and the PDB coordinates of the 2KXA (cyan), fitting from Gly-1 to Gly-23. The RMSD is 0.40 Å. Here the alignment was done only for C-alpha atoms.

4.3 Modeling of the semiclosed structure

The semiclosed structure is based on the earlier solid state NMR data of HA3fp20 in membranes and solution state NMR data of HA1fp23 in detergents.[6] Both the N- and C- terminus of HA1fp23 and HA3fp20 at both pHs are helical (see section 3.2). The semiclosed structure is helical from residues Gly-1 to Glu-11 (N-helix) and from Trp-14 to Gly-20 or Gly-23 (C-helix). Previously, two different chemical shifts were observed for Glu-11 of HA3fp20 in membranes corresponding to two different turn conformations. [7] The ^{13}CO chemical shift of Glu-11 correlating to helical conformation, 178.7 ppm, was used for the semiclosed structure.[8] The dihedral angles for the residues Glu-11 and Asn-12/Gly-12 in the semiclosed structure were obtained from the TALOS analysis of the ^{13}CO chemical shift of HA3fp20 in membranes. TALOS is a knowledge based protein structural database which uses chemical shift and sequence information to predict the protein backbone φ and ψ angles.[9] TALOS uses chemical shift for the three consecutive residues and make dihedral angle predictions for the central residue in the triplet and searches its database for the 10 best matches for the triplet. The dihedral angle predictions are considered as good when the 10 best matches falls in the consistent region of the Ramachandran plot. TALOS uses their averages and standard deviations as predictions. The TALOS database has 200 high resolution proteins and uses more than 24,000 triplets for predictions. The predicted dihedral angles for Glu-11 and Asn-12 were used to build the semiclosed structure. For both the constructs, the greater fraction of the semiclosed structure at pH 5 correlates with the protonation of the Glu-11 ($pK_a \approx 5.9$) present adjacent to the turn region. [10] Stabilization of the closed structure by Glu-11 $–COO^-$ and the semiclosed structure by –COOH correlates with the stable structures observed in MD of HA3fp20 in implicit membranes.[11] Therefore, the side chains of the semiclosed structure were modeled using the

earlier structure of HA3fp20 (F1 structure) obtained from MD simulation in implicit membranes. The F1 structure was chosen because the Glu-11 of the F1 structure is protonated. The side chains from the residues Gly-1 to Gly-20 was modeled because the MD simulation was done on the 20- residue HAfp. Therefore, the semiclosed structure with the side chains was modeled only for HA3fp20 although the backbone structure was modeled for both the HA3fp20 and HA1fp23. Next the semiclosed structure for both the constructs was energy minimized using YASARA energy minimization program.

Table 4.2 lists the φ and ψ angles for the closed and semiclosed structures of HAfp. The φ and ψ angles for the residues Gly-1 to Gly-23 in closed structure are based on the average values with standard deviations obtained from 10 lowest energy structures. The dihedral angles for the open structure determined by solution NMR are also listed in Table 4.2. The φ and ψ angles of the open structure were obtained from VADAR program using the pdb accession number 1IBN. [12] Like the closed structure, the φ and ψ angles for the residues Gly-1 to Gly-20 in open structure are the average values with standard deviations obtained from 20 lowest minimum energy structures. The dihedral angles of the residues from Leu-2 to Ile-10 and Trp-14 to Tyr-22 and or Ile-18 are generally consistent with the helix structure. The set of dihedral angles given in Table 4.2 were used to build semiclosed structure of HAfp in MOLMOL and the final figures were done in PYMOL. The semiclosed backbone was stable under energy minimization and Table 4.3 lists the dihedral angles of the semiclosed structure after energy minimization. For the semiclosed structure, the φ = -59° and ψ = -42° for Glu-11 agreed with the helical conformation and φ = -83° and ψ = 8° for Asn-12 did not agree with either helical or beta-sheet conformation.

Figure 4.3a and 4.3b shows the backbone closed and semiclosed structure of membrane-associated HA1fp23. The interhelical angle in the closed and the semiclosed structure are 158°

and 146°. The interhelical angle was measured using the QHELIX program and the interhelical angle is defined as the angle between the two vectors, where each helix axis is represented as a vector from N- to C-terminus.[13] Figures 4.3a and 4.3b shows the lateral view of the closed and the energy minimized semiclosed structure with the side chains. Hydrophobic side chains are drawn in yellow, polar side chains in green and acidic side chains in red. In both the closed and the semiclosed structure, one side of the helical backbone is completely covered with hydrophobic residues and the opposite side exposes the polar side chains of Glu-11, Thr-15 and Asp-19 in the closed structure and Glu-11, Asn-12, Glu-15 and Asp-19 in the semiclosed structure. Therefore, both the closed and the semiclosed structure are amphipathic and have a distinct hydrophobic and hydrophilic face. The packing of the closed structure is favored by the packing of the eight Gly residues that line the inner faces of the N- and C-terminal helices as shown in Figure 4.4c. The closed and the semiclosed structure of HAfp are very similar but there are few differences between them:

1. The turn in the closed structure consists of only Gly-13 whereas in the semiclosed structure the turn consists of two residues, Asn-12 and Gly-13.
2. The semiclosed structure is more open than the closed structure as evident from the interhelical angles.
3. The semiclosed structure has both a hydrophobic face and a hydrophobic pocket consisting of Phe-9 and Met-17 whereas the closed structure has only a hydrophobic face.
4. The position of the Phe-9 ring is very different in the closed and the semiclosed structure. In the semiclosed structure the Phe-9 ring is inserted in between the N- and C-terminal helices but in the closed structure the Phe-9 ring is pointed downwards as shown in Figure 4.3a.

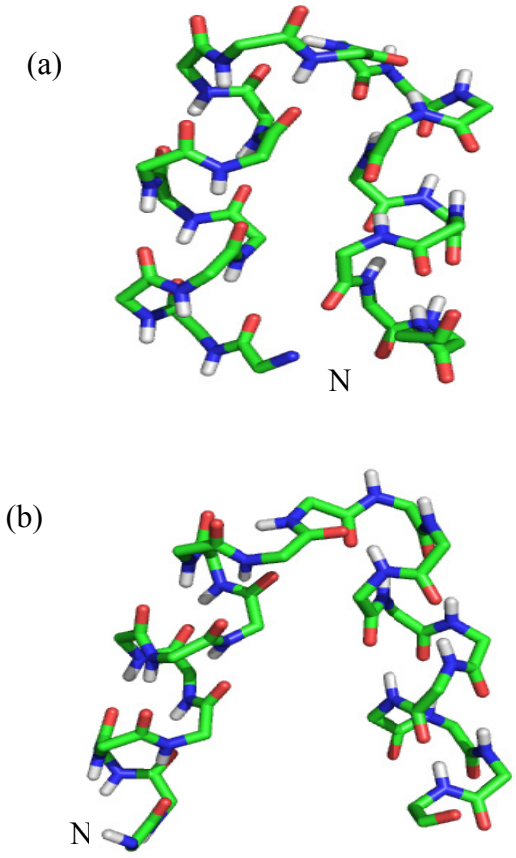

Figure 4.3. Heavy atom backbone structural models of membrane associated HA1fp23 from the residues Gly-1 to Gly-23. The amino terminus is marked as N. Longitudinal view of the (a) closed and (b) the semiclosed structure. C-atoms are represented by green vertices, N-atoms by blue vertices and the O-atoms by red vertices. (a) The interhelical angle between the helix A (residues 2-12) and helix B (residues 14-22) is 158°. (b) The interhelical angle between the helix A (residues 2-11) and helix B (residues 14-22) is 146°.

Table 4.2. φ/ψ angles in degrees of residues Gly-1 to Gly-23 for closed and semiclosed structure of HAfp. φ/ψ angles in degrees of residues Gly-1 to Gly-20 for open structure of HA3fp20 in detergents at pH 5. Standard deviations are given in parenthesis.[2]

Residue	Closed/Semiclosed		Open	
	ϕ	φ	ϕ	φ
G1	ND	-107.8 (97.2)	-	-160.1 (0.3)
L2	-64.6 (2.3)	-50.6 (2.6)	-46.7 (1.1)	-43.7 (0.1)
F3	-64.2 (0.9)	-46.5 (1.6)	-51.9 (1.6)	-34.9 (0.5)
G4	-56.9 (1.0)	-32.8 (0.8)	-67.6 (0.6)	-34.7 (2.5)
A5	-68.8 (1.3)	-46.4 (0.9)	-72.3 (2.2)	-36.4 (2.6)
I6	-60.9 (0.9)	-52.1 (0.8)	-57.9 (1.1)	-40.6 (1.1)
A7	-65.9 (0.8)	-42.2 (0.4)	-65.6 (1.3)	-35.1 (4.6)
G8	-63.3 (0.5)	-34.8 (0.8)	-53.5 (5.1)	-52.1 (5.7)
F9	-64.8 (0.9)	-44.3 (0.6)	-61.4 (4.6)	-44.2 (4.3)
I10	-66.4 (1.1)	-28.1 (0.9)	-48.7 (3.1)	-32.2 (9.7)
	Closed		Semiclosed		Open	
	ϕ	φ	ϕ	φ	ϕ	φ
E11	-91.6 (1.2)	-48.4 (1.3)	-69.0 (11.0)	-27.0 (13.0)	-98.3 (12.6)	-2.5 (3.7)
G12/N12	-112.7 (1.2)	-29.3 (1.4)	-96.0 (13.0)	-8.0 (12.0)	-135.5 (23.7)	32.9 (37.9)
	Closed/Semiclosed		Open	
	ϕ	φ	ϕ	φ
G13	44.3 (1.0)	-145.6 (1.2)	27.3 (117.5)	5.3 (14.2)
W14	-50.5 (0.4)	-61.4 (1.1)	-39.9 (3.3)	-41.6 (3.5)
T15/E15	-49.3 (0.9)	-33.1 (1.1)	-52.6 (3.8)	-33.2 (4.2)
G16	-69.8 (1.5)	-37.1 (0.6)	-70.2 (5.9)	-18.4 (8.5)
M17	-59.4 (1.2)	-46.7 (2.3)	-97.7 (10.8)	-10.7 (3.6)
I18	-62.4 (0.9)	-50.5 (1.2)	-70.7 (5.5)	-45.6 (8.9)
D19	-53.9 (2.7)	-43.5 (1.7)	-35.9 (44.7)	95.5 (89.7)
G20	-68.1 (2.2)	-34.4 (1.1)	63.1 (64.1)	-41.6 (58.7)
W21	-62.8 (1.3)	-48.8 (2.5)		
Y22	-75.8 (2.7)	-31.3 (2.8)		
G23	47.0 (51.6)	30.1 (86.0)		

Table 4.3. φ/ψ angles in degrees of residues Gly-1 to Gly-20 for semiclosed structure of HAfp after YASARA energy minimization.

Residue	Semiclosed	
	Φ	ψ
G1	0.0	-171.9
L2	-67.7	-47.8
F3	-49.5	-39.9
G4	-63.2	-37.5
A5	-72.3	-48.1
I6	-61.1	-48.4
A7	-75.0	-32.3
G8	-73.8	-49.4
F9	-46.8	-39.5
I10	-57.8	-43.7
E11	-58.9	-42.8
N12	-82.9	8.5
G13	44.1	-138.8
W14	-57.9	-58.0
E15	-51.6	-31.0
G16	-70.1	-40.7
M17	-56.9	-48.8
I18	-60.0	-36.4
D19	-65.2	-33.1
G20	-78.9	0.0

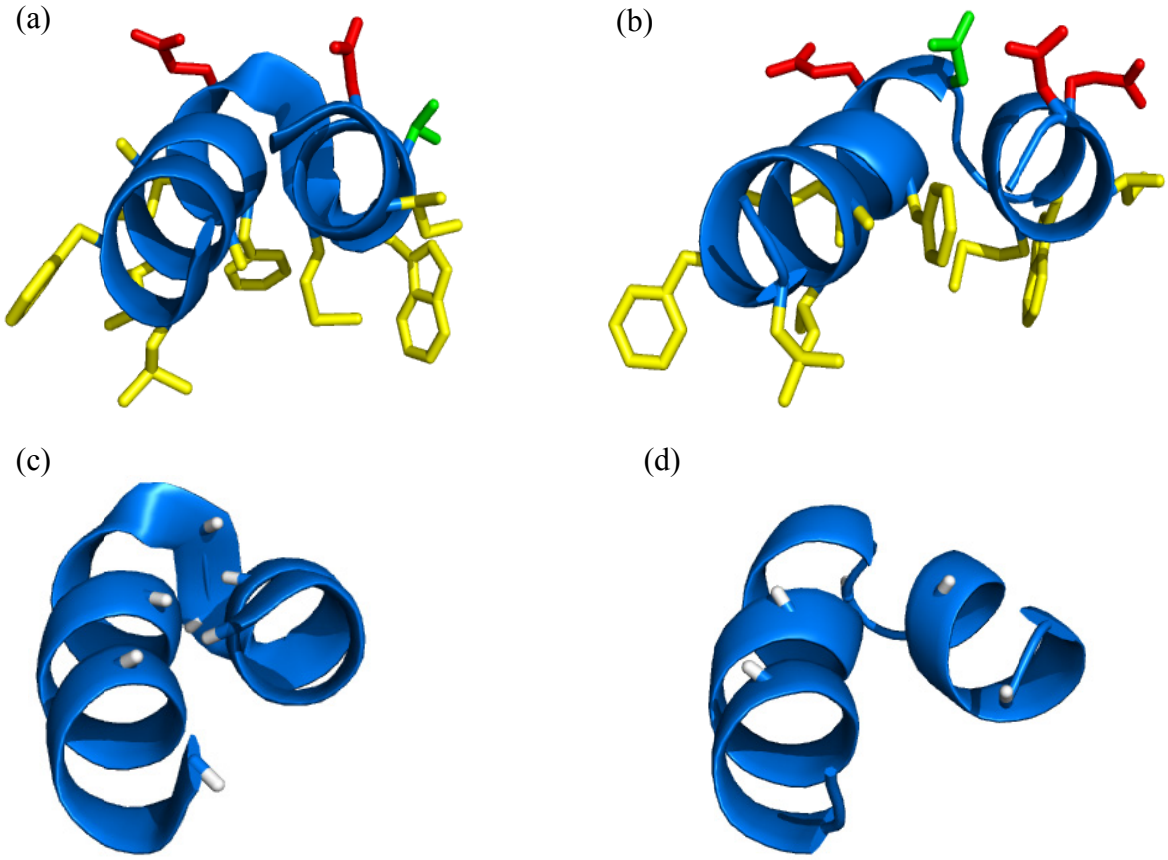

Figure 4.4. Structure of membrane associated HAfp from the residues Gly-1 to Gly-20. Lateral view of the (a) closed structure of HA1fp20 and (b) the semiclosed structure of HA3fp20. Hydrophobic side chains are represented in yellow, polar side chains in green and acidic side chains in red. Cartoon structures showing the orientation of the Gly residues in the (c) closed and the (d) semiclosed structures. (c) Gly-4, Gly-8, Gly-16 and Gly-20 in the closed structure are present at the inner faces of the N- and C-terminal helices. (d) Position of the Gly residues in the semiclosed structure.

4.4 Linewidth Analysis

Table 4.4. Typical linewidths of the HAfp spectra labeled at Gly-16 and Ala-5.

Labeling	HA1fp23 pH 5 FWHM (ppm)	HA1fp23 pH 7 FWHM (ppm)	HA3fp20 pH 5 FWHM (ppm)	HA3fp20 pH 7 FWHM (ppm)	Dephasing time (ms)
G16c-F9n	2.3	2.6	4.6	3.8	2
	2.7	2.8	4.3	2.7	40
A5c-M17n	1.3	1.0	2.0	1.6	2
	1.3	1.1	1.7	1.5	40

The experimental linewidths can be explained in terms of the population and the structure of the closed and the semiclosed structure. The above table shows that HA3fp20 pH 5 G16c-F9n samples have the biggest linewidth and the HA1fp23 pH 7 A5c-M17n sample has the least linewidth. The results of the Table 4.4 show that the typical linewidths for the Gly ^{13}CO labeled samples are bigger compared to the Ala ^{13}CO labeled samples. Generally due to the lack of the of side chain, Gly is the least restricted residue and this is apparent in the Ramachandran plot in which the allowable region for the Gly is considerably larger. This means that Gly can have a wide range of φ and ϕ values. The closed structure has two helices that are tightly packed forming a hairpin structure. The hairpin structure is stabilized by the interhelical H-bonds. In contrast, the semiclosed structure is more open and interhelical H-bonds are present. Therefore,

the closed structure has less conformational flexibility as compared to the semiclosed structure. In the closed structure, the Glys are present at the inner face of the closed structure (Figure 4.3c) and forms interhelical aliphatic H-bonds. As a result, the Glys have restricted conformational flexibility in the closed structure than in the semiclosed structure. Therefore, the linewidths of the Gly labeled samples are bigger. The best-fit values show that HA3fp20 at pH 5 has the largest semiclosed fraction and hence the biggest linewidth of ~ 5 ppm. On the other hand, Ala - 5 sits at the bottom of the closed structure and does not contribute in forming the helical hairpin structure. As a result one would expect to have the similar conformational flexibility of Ala-5 in the closed and the semiclosed structure. This is also evident in Table 4.4, where the linewidths of all the Ala labeled samples are similar.

The above table also indicates that the linewidths for the 20 residue peptides are typically larger than the 23 residue peptides. This is because the 23 residue peptide form more closed structure than the 20 residue peptide. Since the closed structure is more compact, the variation in the φ and ϕ values of Gly and Ala are less, giving rise to comparatively narrower peaks.

4.5 Insertion of Phe-9 in the semiclosed structure and the stabilization of the semiclosed structure

The Phe-9 ring in the semiclosed structure is inserted in between the N- and C-terminal helices and the Phe-9 ring is pointed downwards from the N-helix in the closed structure. The calculated G16^{13}CO – F9D$_5$ ring center distance is ~ 5 Å in the semiclosed structure and ~ 8 Å in the closed structure. The position of the Phe-9 in the semiclosed structure was probed by ^{13}CO - ^{2}H REDOR. Both the HAfp constructs have higher semiclosed structure at lower pH, however HA3fp20 sample at pH 5 has the highest semiclosed fraction. So HA3fp20 was used for ^{13}CO - ^{2}H REDOR experiment. HA3fp20 have 0.65 and 0.45 mole fraction of semiclosed structure at pH 5 and at pH 7 respectively. Therefore, HA3fp20 at pH 5 will have higher dephasing than at pH 7.

Figure 4.5 shows the insertion of the Phe-9 ring in the semiclosed structure. The ^{1}Hs of the Phe-9 ring were substituted by ^{2}Hs and the Gly-16 was ^{13}CO labeled. Figure 4.6a and 4.6b displays representative spectra of HA3fp20 at pH 5 and at pH 7 in DTPC and DTPG in 4:1 ratio. The chemical shift of the Gly-16 is 177 ppm which correlates with the helical conformation. Figure 4.6c shows experimental plots of ($\Delta S/S_0$) vs τ at both pH 5 (violet) and pH 7 (red). HA3fp20 at pH 5 shows higher dephasing than at pH 7. The ^{13}CO-^{2}H REDOR dephasing buildups at pH 5 were semi-quantitatively fitted to a single ^{13}CO-^{2}H distance.

Figure 4.6d displays fitting of the $(\Delta S/S_0)^{exp}$ buildup of HA3fp20 at pH 5 with G16 ^{13}CO and Phe-9 ring ^{2}H labeling. The fitting model was: (1) closed and semiclosed structures with $f_c = 0.35$ and $f_s = 0.65$; (2) ^{13}CO-^{2}H $d_{cD} \approx 0$ which reflects $r_{CD} > 8$ Å in the closed structure because the Phe-9 ring points away from the *C*-helix; and (3) fitting parameter d_{sD} that reflects ^{13}CO-^{2}H proximity in the semiclosed structure because of the Phe-9 ring location in the interhelical space.

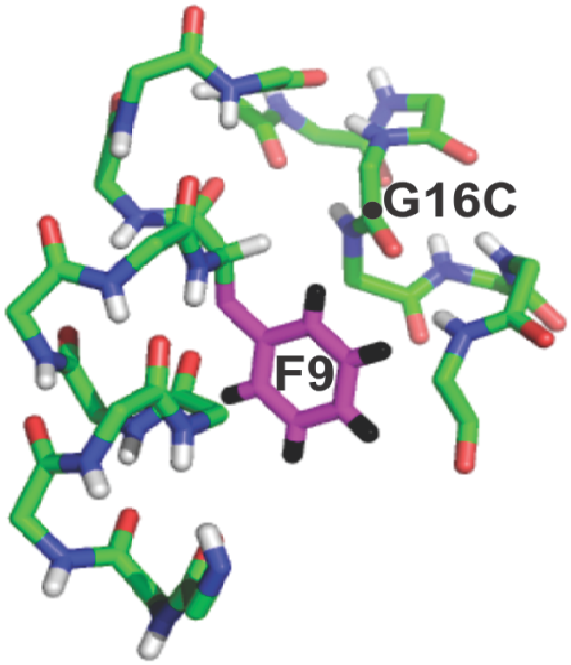

Figure 4.5. Insertion model of Phe-9 ring in the semiclosed structure. The ^{1}H's of the Phe-9 are replaced by ^{2}H's and are shown in black.

The buildup of $(\Delta S/S_0)^{exp}$ was fitted to $[0.65 \times (\Delta S/S_0)^{sim}]$ where the $(\Delta S/S_0)^{sim}$ are for isolated ^{13}CO-^{2}H spin pairs with a single value of d_{sD} and the $(\Delta S/S_0)^{sim}$ are calculated using the SIMPSON program which incorporates the 10 kHz MAS frequency, ^{13}C and ^{2}H pulse fields and durations, and ^{13}CO and ^{2}H anisotropies.[14] The best-fit d_{sD} =19(2) Hz corresponds to r_{sD} = 6.2(3) Å. The fitting model is semi-quantitative because of uncertainties which include: (1) five ring ^{2}H's so that the$(\Delta S/S_0)^{exp}$ reflect five somewhat different r_{sD}'s as well as a small contribution from the five different r_{cD}'s; (2) the calculated r_{SD} = 6.2 Å is based on rigid ^{13}CO-^{2}H spin pairs but would be smaller if there were motional averaging of ^{13}CO-^{2}H dipolar coupling from rotation of the F9 ring; and (3) fitting with $(\Delta S/S_0)^{lab}$ rather than $(\Delta S/S_0)^{exp}$ would likely lead to ~20% larger best-fit d_{SD} and ~5% smaller r_{sD} (The best-fit distance ~ 6 Å suggests that the Phe-9 ring is inserted in between the N- and C-terminal helices).

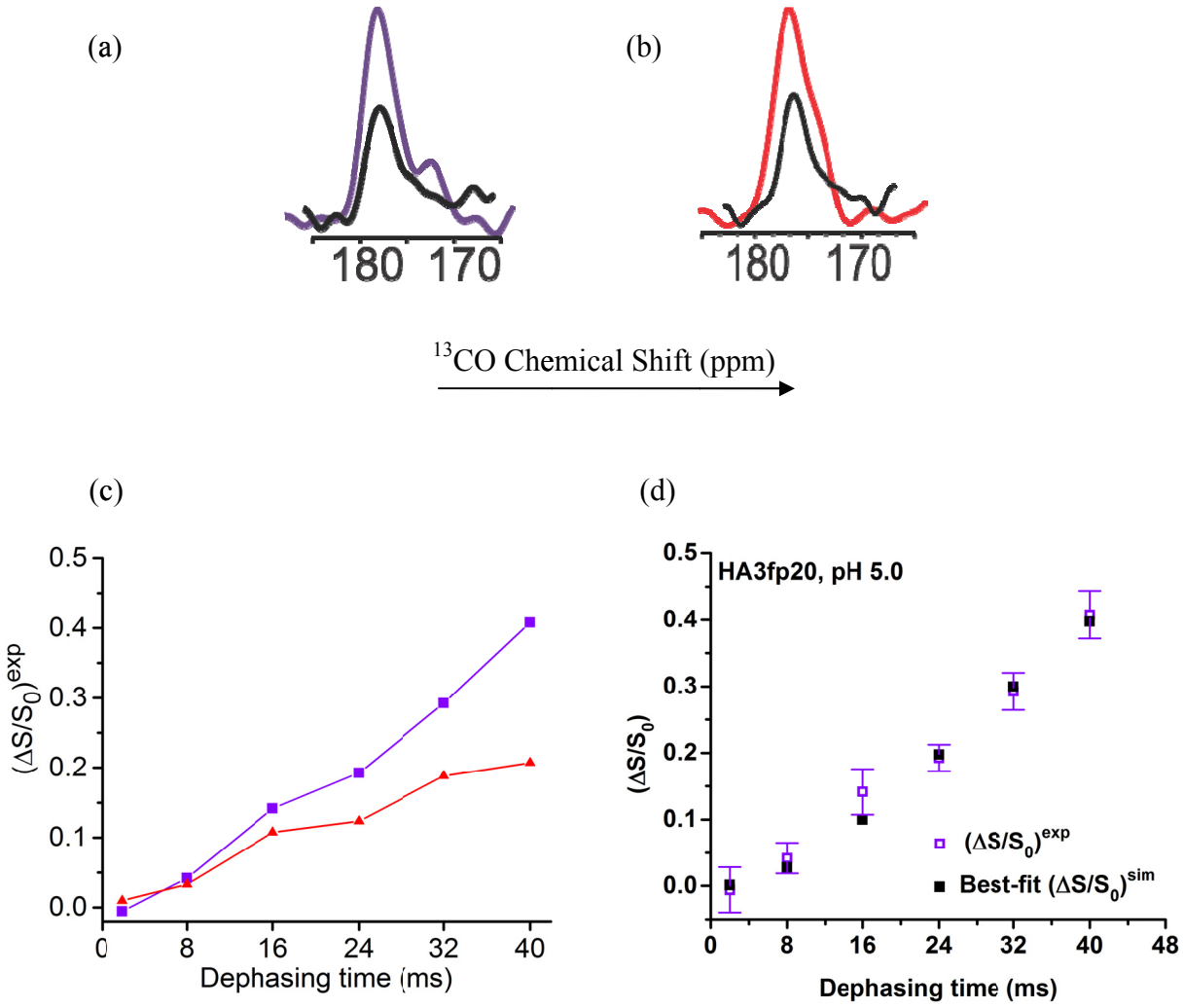

Figure 4.6. ^{13}C detect ^{2}H dephased REDOR spectra of membrane-associated HA3fp20 at 40 ms dephasing time. S_0 (color) and S_1 (black) spectra of HA3fp20 in DTPC:DTPG at (a) pH 5, and (b) pH 7. The chemical shift of Gly-16^{13}CO is 177 ppm which correlates with a helical structure. (c) Experimental dephasing building for HA3fp20 samples with G16^{13}CO/F9 ring ^{2}H labeling. The typical uncertainty is 0.02. (d) ^{13}CO-^{2}H $(\Delta S/S_0)^{exp}$ and best-fit [0.65 x $(\Delta S/S_0)^{exp}$] buildups with d_{sD} = 19 Hz.

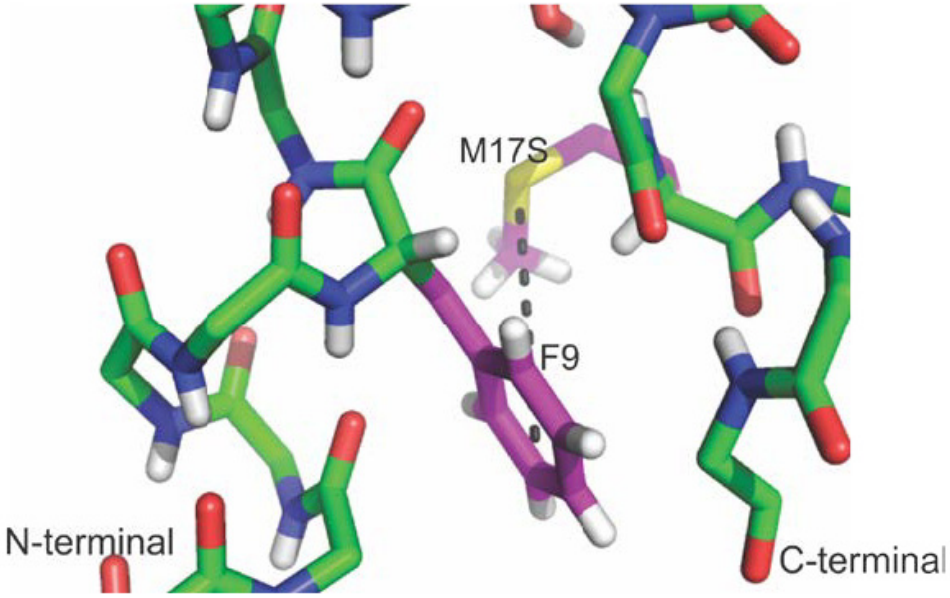

Figure 4.7. View of the Met-17 S – Phe-9 ring hydrophobic interaction in the energy minimized HA3fp20 structure.

The insertion of the Phe-9 ring in the interhelical cavity of the semiclosed structure places the Met-17 S (shown in yellow color in the Figure 4.6) is ~ 4.5 Å away from the Phe-9 ring. There might be a potential hydrophobic interaction between the Phe-9/Met-17 S that could stabilize the semiclosed structure. The distance between the Phe-9 ring centre and the methyl group (not shown in the figure) is ~ 5 Å which might lead to a possible hydrophobic interaction.

4.6 Correlation of the structure of HAfp with vesicle fusion

The structure-function correlation of HAfp was correlated using vesicle fusion assays under the similar condition used for NMR experiments.[15] Figure 4.8 shows the percent vesicle fusion for two different HAfp constructs at both the fusogenic pH (pH 5) and physiological pH (pH 7). All the samples showed significant fusion. The extent of vesicle fusion is ordered:

HA1fp23, pH 5 > HA1fp23, pH 7 > HA3fp20, pH 5 > HA3fp20, pH 7. The observed vesicle fusion trend is consistent with the previous studies.

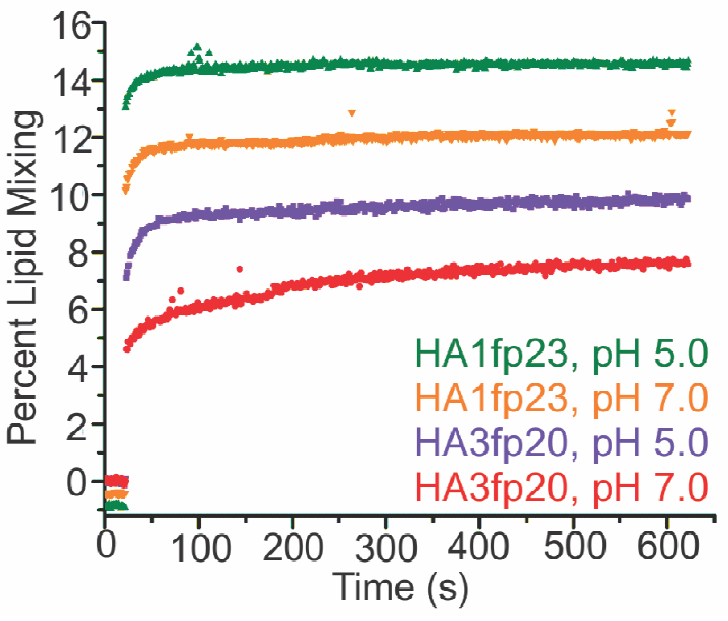

Figure 4.8. HAfp induced vesicle fusion for 1:50 peptide to lipid mole ratio in DTPC:DTPG (4:1) membrane at 37°C.

Relative to HA3fp20, the higher vesicle fusion of HA1fp23 supports the contribution of the addition of Trp, Tyr and Gly at C-terminus. For either HA3fp20 or HA1fp23, there is higher fusion at pH 5 than at pH 7 which correlates to the larger population of the semiclosed structure and smaller closed population at lower pH. The higher vesicle fusion at lower pH correlates with the larger semiclosed fraction at pH 5 which supports a contribution of the hydrophobic

interaction between the HAfp and the membrane to the fusion catalysis. Both the closed and the semiclosed structure (Figures 4.4a and 4.4b) have a distinct hydrophobic surface. The most usual or the general location for the amphipathic peptides is the membrane –interface location, where the hydrophobic face interacts with the hydrophobic core of the membrane as shown in Figure 4.9.

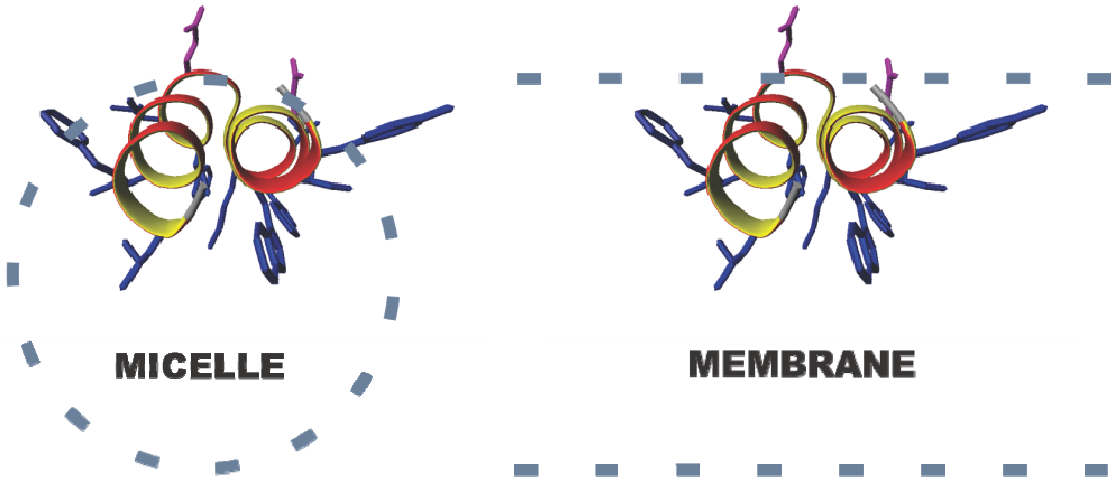

Figure 4.9. Models of the location of the closed structure of the HA1fp23 in detergent micelles and membranes. Dashed lines represent the hydrophobic core.

The hydrophobic interaction is represented by hydrophobic surface area. The mechanism is reduction in activation energy because the perturbed bilayer of the HAfp/membrane complex resembles the fusion transition state. The calculated HAfp hydrophobic surface area (S_a) is the quantity used to represent this hydrophobic interaction. The term S_a represents the hydrophobic contribution to the total accessible surface area of the entire protein/peptide which is available for intermolecular hydrophobic interactions. The S_a of the closed and the semiclosed structures were calculated using parameter optimized surfaces (POPS) program.[16] POPS calculates both the hydrophobic and hydrophilic contributions to the total solvent accessible surface area (SASA). An empirical parametrizable analytical equation is used for the calculation of solvent accessible areas. The parameters used in the calculations are optimized from a database containing ~ 90 proteins and nucleic acids of different sizes and known topologies. The SASA of the atoms of these proteins and nucleic acids in the database were evaluated using Naccess program (NACS). POPS can calculate the atomic (POPS-A) and the residue (POPS-R) level solvent accessibilities for proteins and nucleic acids. In POPS-R, the residue areas are simulated with a single sphere centered on C-α of each amino acid. In POPS-A the SASA of the atoms in a given dataset were fitted to the NACS SASAs with a minimization of variance of POPS-A from NACS areas. For our calculations, we used atomic-level calculations. The radius of the surface probe was 1.4 Å for the calculation. The S_a of HA1fp23 is larger than HA3fp20 because of the additional Trp, Tyr and Gly residues at the C-terminus of HA1fp23. The S_a of semiclosed structure is greater than the closed structure because of the more open interhelical geometry of the semiclosed structure. The S_a of the closed and the semiclosed structure was calculated from the POPS program. The S_a of each peptide was calculated as a weighted average using

experimentally solid state NMR derived closed and semiclosed fractions. Table 4.5 shows the total hydrophobic S_a of each sample and the extent of vesicle fusion.

Table 4.5. Average hydrophobic surface areas of HAfp and extent of vesicle fusion. Uncertainties are given in parenthesis and were obtained by repeating the experiments twice.

Sample	Vesicle fusion	Hydrophobic Surface Area ($Å^2$)
HA1fp23, pH 5	15.0 (0.7)	1316
HA1fp23, pH 7	12.0 (2.2)	1298
HA3fp20, pH 5	10.0 (5.1)	1169
HA3fp20, pH	8.0 (0.5)	1150

Table 4.5 shows that the ordering of the S_a is same as the extent of vesicle fusion. The importance of the S_a in vesicle fusion is also shown in larger HA2 constructs. One example is the ~185 residue FHA2, the extraviral domain of the HA2 which contains HAfp. The calculated S_a of FHA2: S_a of HA1fp23 ≈ 5 and FHA2 is much better fusion catalyst than HA1fp23.[17]

4.7. Discussion

The ~ 23 residue HAfp region of the HA2 subunit of the influenza hemagglutinin protein plays a critical role in the viral membrane fusion process and has been studied widely. Previous studies have shown that HAfp adopts mainly alpha helical structure in the membranes lacking cholesterol. [7] At higher peptide:lipid mole ratio (~0.1), a fraction of beta-strand HAfp was also observed at pH 7.4. [18] In detergents, HA3fp20 adopts helical structure at both N- and C-terminus at pH 5 with an open interhelical geometry (Figure 3.1a). However, at pH 7.4, the same peptide was helical at N-terminus and an extended structure at C-terminus (Figure 3.1b). [12] On the contrary, HA1fp23 adopts helical structure at both the N- and C-terminus at both pH 4 and pH 7.4 in detergents with a closed interhelical geometry (Figure 3.1c). [1] In the membranes containing PC:PG in the mole ration 4:1, the HA3fp20 forms majorly alpha helical structure (Figures 3.1e and 3.1f). [7] Although it was shown that in membranes, both the N- and C-terminus was helical at both the pHs, there was no information regarding the interhelical geometry of the HAfp. The present study shows that both the HA1fp23 and HA3fp20 are helical at both N- and C-terminus in membranes.

This chapter also presents the detailed study of the conformation of the HAfp in membranes. As discussed previously in the chapter 3, ^{13}C-^{15}N REDOR spectroscopy and selectively ^{13}CO and ^{15}N HAfps were used to investigate the interhelical geometry of the HAfp. The chemical shifts derived from the spectra confirmed that Gly-16 present at the C-terminus and the Ala-5 at the N-terminus are helical at both pHs for both the HA1fp23 and HA3fp20. As mentioned in the previous chapter, two different structures for each HAfp sample were observed in membranes containing PC:PG in 4:1 mole ratio – closed and semiclosed structure. The closed structure of HAfp was previously observed in detergents but the semiclosed structure is newly observed in

membranes. The overall secondary structure of the closed and the semiclosed structure is helix/turn/helix structure, but they differ in the interhelical geometry. The interhelical angle of the closed and the semiclosed structure is 158° and 146° respectively. The interhelical angle of the previously observed open structure of HA3fp20 in detergents was ~100°. Therefore, the semiclosed structure is more closed than the open structure and resembles the closed structure of HA1fp23 that was observed in detergents at both pHs. The closed structure is helical from the residues Leu-2 to Gly-12 and Trp-14 to Gly-23 with the turn in the residue Gly-13. The semiclosed structure is helical from Leu-2 to Glu-11 and from Trp-14 to Asp-19/Tyr-22 with the turn region around Asn-12 and Gly-13. Our observation of the HAfp helix/turn/helix structure of HAfp in membranes is consistent with the earlier helix/turn/helix structure of HAfp in detergents. However, the significance of our study is highlighted by the fact that the HAfp induces fusion between the membranes but not between the detergent micelles and therefore has more biological relevance. Additionally, the structure of HAfp was sequence-length dependent in detergents but sequence-length independent in membranes.

The HAfp induces much greater vesicle at pH 5 than at pH 7 and on lowering the pH from 7.4 to 5, additional fusion can be triggered. Han and coworkers proposed that the formation of the C-helix at pH 5 as opposed to the C-terminus extended structure at pH 7 was the major structural change of HA3fp20 that leads to the higher fusion at lower pH. [12] On the other hand, HA1fp23 interacts with the alkyl chains of the micelle through the hydrophobic face of the closed amphipathic structure.[1] Although a lot of studies have been done on the HAfp regarding the structure and the function, there is no general consensus regarding the structure-function correlation. In the present study we propose that the hydrophobic interaction between the peptide and the membrane is an underlying factor in the fusion catalysis. This proposal is based

on the hypothesis that once the peptide is bound to the membrane, the peptide alters the bilayer packing. During this process, the lipid molecules have to rearrange from the lamellar phase to the final step of the pore formation. In case of both HA1fp23 and HA3fp20, we observed a higher population of the semiclosed structure and lower fraction of the closed structure at lower fusogenic pH than at pH 7. The vesicle fusion assay probes the distance between the donor and the quencher as a result of the mixing of the lipid molecules after the addition of the peptide/protein. Since in the vesicle fusion assay there is only lipid mixing and no content mixing, this assay closely resembles hemifusion state, a state in which there is only lipid mixing but no content mixing. The closed and the semiclosed structure interact with the hydrocarbon core of the membrane with the hydrophobic face containing the non-polar residues. However, the semiclosed structure is more open than the closed structure and hence has a larger hydrophobic surface area. The larger surface area of the semiclosed structure can perturb more lipid molecules and eventually can promote higher lipid mixing than the closed structure. This is suggestive that the larger semiclosed fraction at lower pH causes HAfp more fusogenic than at pH 7. This is consistent with the one of the earlier study done by Epand and co-workers. In this study it was shown using ^{31}P NMR that the wild type HAfp was more membrane disrupting and promotes viral fusion at lower pH than at pH 7.[19]

How the semiclosed and the closed structure do contribute in the membrane fusion process:

The process of membrane fusion requires the rearrangement of the lipid molecules between the fusing bilayers. One of the important steps of the membrane fusion process is the stalk formation. A fusion stalk (Figure 4.10a) is hourglass shaped stalk formed from the two bilayers proceeding to the hemifusion step and finally pore formation. [20, 21] The stalk has a negative curvature at one side and positive along the other side. [22] Experiments incorporating negative curvature lipids, like DOPE stabilize the negative curvature of the stalk which finally promotes the rate of membrane fusion.[23-25] On the contrary, micelle-forming lipids like lysophosphatidylcholines when placed in the contacting monolayers reduce the rate of the membrane fusion by destabilizing the fusion stalk.[23, 26] Similarly, the fusion domains also promote and stabilize the negative curvature in the cis-monolayer and will facilitate the stalk formation or the hemifusion step. At low lipid:peptide ratio (~0.1 – 0.3 %), HA3fp20 decreases the thermal transition temperature of DPoPE lipid at low pH to stabilize the H_{II} phase with a negative curvature (Figure 4.10b). [19]

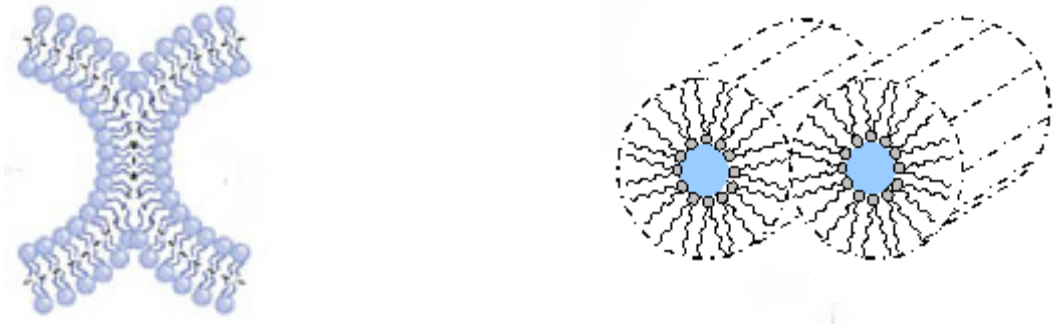

Figure 4.10. (a) Schematic representation of a hemifusion stalk. (b) Schematic representation showing the hexagonal phase (H_{II}) of the lipid. The lipids with a small polar head group also induces a negative curvature strain and favor the organization of the membrane into inverted micelle (H_{II}) structures.

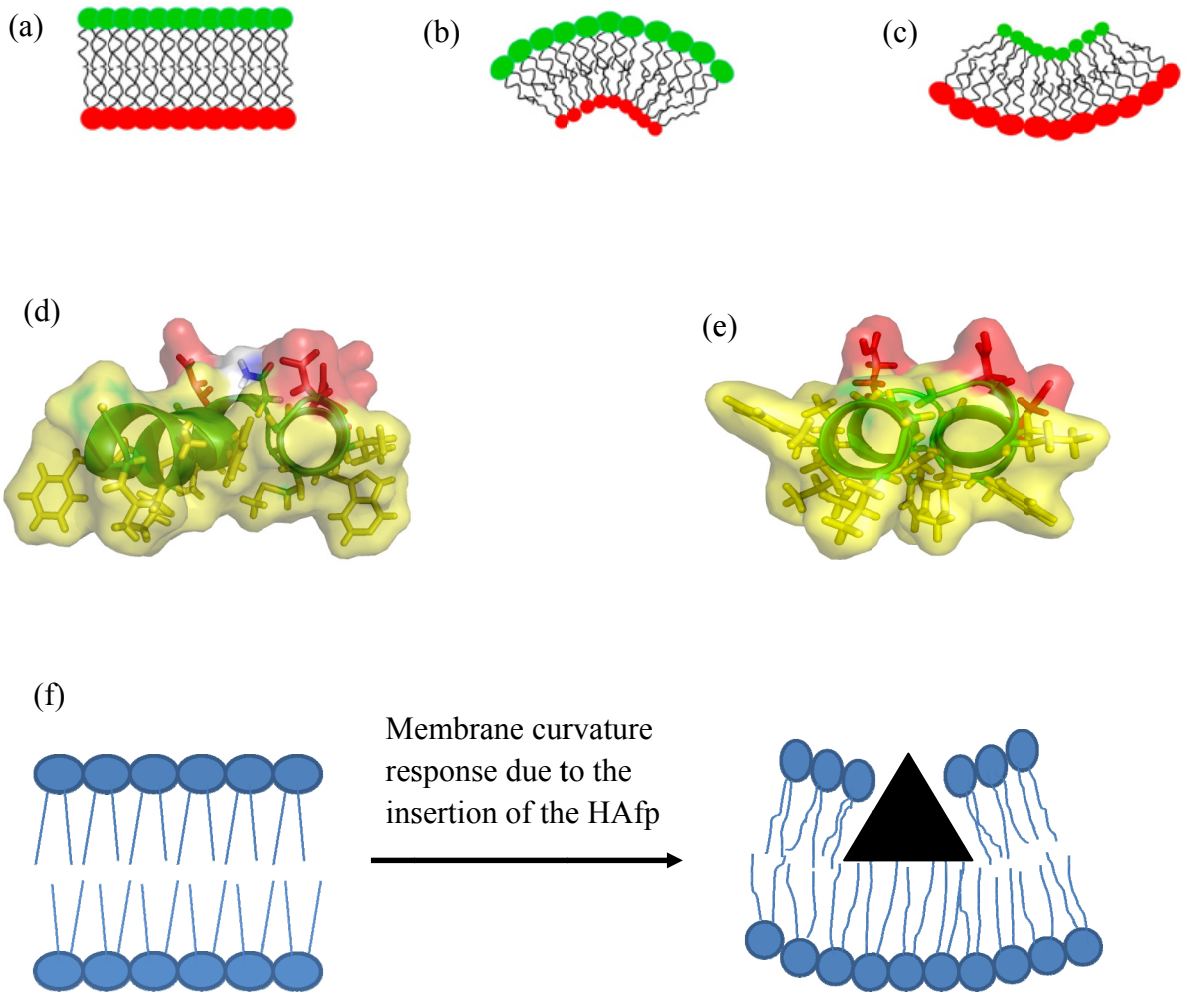

Figure 4.11. Top row shows different membrane curvature (a) zero, (b) positive and (c) negative curvature. Space-filling representation of (d) the semiclosed and (e) the closed structures with the hydrophobic (yellow), hydrophilic (red) and basic amino (blue) groups. (f) HAfp can introduce an amphipathic helical structure into one leaflet of the membrane. This "inverted wedge" displaces lipids and can cause the membrane to bend towards itself thereby creating a negative curvature. This mechanism is referred to as wedging mechanism.

Mutant HAfp domain increases the transition temperature of the lipid, thereby showing a reduced propensity for negative curvature structures and exhibit reduced fusion activity. This suggests that there is a correlation between the fusion activity and membrane curvature. Figures 4.11a, 4.11b and 4.11c show the different curvatures of the membrane. Additionally, the molecular shape of the amphipathic peptides has an impact on the curvature of the membrane. [27-29] Class A amphipathic helices have a wedge shape and induce positive curvature of the membrane. The class A amphipathic helices have a wedge shape with a larger hydrophilic cross-sectional area compared to the hydrophobic face. [28] For example, the N-terminus of BAR domains folds into amphipathic helices when interacts with the membrane and induces positive membrane curvature (Figure 4.11b).[29] In contrast, class L peptides or the lytic peptides induce negative membrane curvature (Figure 4.11c) and destabilizing the planar bilayer and stabilize some form of concave inverted lipid structure. The cross sectional shape of the L- amphipathic helices is an inverted wedge with its apex at the polar face and the bulkier base at the non-polar or the hydrophobic face.[28] Figure 4.11d and 4.11e represents the space filling models of the semiclosed and the closed structures. Both the closed and the semiclosed structures are amphipathic. However, the semiclosed structure has a larger hydrophobic base compared to the closed structure.

Table 4.6. Ratio of the hydrophobic to the hydrophilic surface areas

	Closed structure	Semiclosed structure
HA1fp23	2.4	3.7
HA3fp20	2.8	4.2

In case of the membrane fusion, the initial stalk formation requires that the membrane acquires a negative curvature. One common property of many viral fusion peptides is that they induce and stabilize negative membrane curvature.[24, 25, 30] As discussed previously, HAfp lowers the transition temperature of many lipids and stabilizes H_{II}-phase which has a high degree of negative curvature at low pH. Like the L-amphipathic helices, the HAfp have a bulky hydrophobic base which induces and stabilizes the negative membrane curvature of the fusion stalk. However, due to the smaller hydrophobic base, the closed structure induces the negative membrane curvature to a lesser extent than the semiclosed structure. Figure 4.11f shows a schematic diagram how the membrane responds and adjusts to the shape of the fusion peptide.

REFERENCES

REFERENCES

1. Lorieau, J.L., J.M. Louis, and A. Bax, *The Complete Influenza Hemagglutinin Fusion Domain Adopts A Tight Helical Hairpin Arrangement At The Lipid:Water Interface.* Proceedings of the National Academy of Sciences of the United States of America, 2010. **107**(25): p. 11341-11346.

2. Ghosh, U., et al., *Closed And Semiclosed Interhelical Structures In Membrane Vs Closed And Open Structures In Detergent For The Influenza Virus Hemagglutinin Fusion Peptide And Correlation Of Hydrophobic Surface Area With Fusion Catalysis.* Journal of the American Chemical Society, 2015. **137**(24): p. 7548-7551.

3. Willard, L., et al., *VADAR: A Web Server For Quantitative Evaluation Of Protein Structure Quality.* Nucleic Acids Research, 2003. **31**(13): p. 3316-3319.

4. Koradi, R., M. Billeter, and K. Wuthrich, *MOLMOL: A Program For Display And Analysis Of Macromolecular Structures.* Journal of Molecular Graphics, 1996. **14**(1): p. 51-&.

5. Krieger, E., et al., *Improving Physical Realism, Stereochemistry, And Side-Chain Accuracy In Homology Modeling: Four Approaches That Performed Well In CASP8.* Proteins-Structure Function and Bioinformatics, 2009. **77**: p. 114-122.

6. Ghosh, U., L. Xie, and D.P. Weliky, *Detection Of Closed Influenza Virus Hemagglutinin Fusion Peptide Structures In Membranes By Backbone ^{13}CO-^{15}N Rotational-Echo Double-Resonance Solid-State NMR.* Journal of Biomolecular NMR, 2013. **55**(2): p. 139-146.

7. Sun, Y. and D.P. Weliky, *C-13-C-13 Correlation Spectroscopy of Membrane-Associated Influenza Virus Fusion Peptide Strongly Supports a Helix-Turn-Helix Motif and Two Turn Conformations.* Journal of the American Chemical Society, 2009. **131**(37): p. 13228-13229.

8. Zhang, H.Y., S. Neal, and D.S. Wishart, *RefDB: A Database Of Uniformly Referenced Protein Chemical Shifts.* Journal of Biomolecular Nmr, 2003. **25**(3): p. 173-195.

9. Shen, Y., et al., *TALOS+: A Hybrid Method For Predicting Protein Backbone Torsion Angles From Nmr Chemical Shifts.* Journal of Biomolecular NMR, 2009. **44**(4): p. 213-223.

10. Chang, D.K., et al., *Self-Association Of Glutamic Acid-Rich Fusion Peptide Analogs Of Influenza Hemagglutinin In The Membrane-Mimic Environments: Effects Of Positional Difference Of Glutamic Acids On Side Chain Ionization Constant And Intra- And Inter-Peptide Interactions Deduced From NMR And Gel Electrophoresis Measurements.* Biochimica Et Biophysica Acta-Biomembranes, 2005. **1712**(1): p. 37-51.

11. Panahi, A. and M. Feig, *Conformational Sampling of Influenza Fusion Peptide in Membrane Bilayers as a Function of Termini and Protonation States.* Journal of Physical Chemistry B, 2010. **114**(3): p. 1407-1416.

12. Han, X., et al., *Membrane Structure And Fusion-Triggering Conformational Change Of The Fusion Domain From Influenza Hemagglutinin.* Nature Structural Biology, 2001. **8**(8): p. 715-720.

13. Lee, H.S., J. Choi, and S. Yoon, *QHELIX: A Computational Tool for the Improved Measurement of Inter-Helical Angles in Proteins.* The Protein Journal, 2007. **26**(8): p. 556-561.

14. Bak, M., J.T. Rasmussen, and N.C. Nielsen, *SIMPSON: A General Simulation Program for Solid-State NMR Spectroscopy.* Journal of Magnetic Resonance, 2000. **147**(2): p. 296-330.

15. Struck, D.K., D. Hoekstra, and R.E. Pagano, *Use Of Resonance Energy-Transfer To Monitor Membrane-Fusion.* Biochemistry, 1981. **20**(14): p. 4093-4099.

16. Cavallo, L., J. Kleinjung, and F. Fraternali, *POPS: A Fast Algorithm For Solvent Accessible Surface Areas At Atomic And Residue Level.* Nucleic Acids Research, 2003. **31**(13): p. 3364-3366.

17. Curtis-Fisk, J., et al., *Solid-state NMR Structural Measurements On The Membrane-Associated Influenza Fusion Protein Ectodomain.* Journal of the American Chemical Society, 2007. **129**(37): p. 11320-+.

18. Wasniewski, C.M., et al., *Solid-State Nuclear Magnetic Resonance Studies Of Hiv And Influenza Fusion Peptide Orientations In Membrane Bilayers Using Stacked Glass Plate Samples.* Chemistry and Physics of Lipids, 2004. **132**(1): p. 89-100.

19. Epand, R.M. and R.F. Epand, *Relationship Between The Infectivity Of Influenza-Virus And The Ability Of Its Fusion Peptide To Perturb Bilayers.* Biochemical and Biophysical Research Communications, 1994. **202**(3): p. 1420-1425.

20. Chernomordik, L.V. and M.M. Kozlov, *Membrane Hemifusion: Crossing A Chasm In Two Leaps.* Cell, 2005. **123**(3): p. 375-382.

21. Yang, L. and H.W. Huang, *Observation Of A Membrane Fusion Intermediate Structure.* Science, 2002. **297**(5588): p. 1877-1879.

22. Tenchov, B.G., R.C. MacDonald, and B.R. Lentz, *Fusion Peptides Promote Formation of Bilayer Cubic Phases in Lipid Dispersions. An X-Ray Diffraction Study.* Biophysical Journal, 2013. **104**(5): p. 1029-1037.

23. Chernomordik, L., *Non-Bilayer Lipids And Biological Fusion Intermediates.* Chemistry and Physics of Lipids, 1996. **81**(2): p. 203-213.

24. Chernomordik, L., et al., *The Hemifusion Intermediate And Its Conversion To Complete Fusion - Regulation By Membrane-Composition.* Biophysical Journal, 1995. **69**(3): p. 922-929.

25. Epand, R.M., et al., *Promotion Of Hexagonal Phase Formation And Lipid Mixing By Fatty-Acids With Varying Degrees Of Unsaturation.* Chemistry and Physics of Lipids, 1991. **57**(1): p. 75-80.

26. Chernomordik, L.V., et al., *The Shape Of Lipid Molecules And Monolayer Membrane-Fusion.* Biochimica Et Biophysica Acta, 1985. **812**(3): p. 643-655.

27. Epand, R.M., et al., *Mechanisms For The Modulation Of Membrane Bilayer Properties By Amphipathic Helical Peptides.* Biopolymers, 1995. **37**(5): p. 319-338.

28. Tytler, E.M., et al., *Reciprocal Effects Of Apolipoprotein And Lytic Peptide Analogs On Membranes - Cross-Sectional Molecular Shapes Of Amphipathic-Alpha Helixes Control Membrane Stability.* Journal of Biological Chemistry, 1993. **268**(29): p. 22112-22118.

29. Mim, C., et al., *Structural Basis of Membrane Bending by the N-BAR Protein Endophilin.* Cell, 2012. **149**(1): p. 137-145.

30. Ellens, H., et al., *Membrane-Fusion And Inverted Phases.* Biochemistry, 1989. **28**(9): p. 3692-3703.

Chapter 5

Development of Cross-Polarization with Quadrupolar Echo (cpquecho) and ^{2}H-NMR Studies of Protein Dynamics

5.1 Introduction

^{2}H NMR is extensively used to study the structure and dynamics of lipid membranes. ^{2}H-NMR is used to study the hydrophobic core of the membrane by substituting the fatty acyl chain 1Hs with ^{2}H. Two types of ^{2}H enrichment can be used; (1) site specific labeling with ^{2}H to observe a particular lipid in a complex, and (2) all the ^{1}Hs in the lipid acyl chain are replaced by ^{2}H to observe the overall effect on the lipid in presence of peptides/ proteins (Figure 5.1). ^{2}H is a spin 1 quadropolar nucleus. A detailed discussion of the orientational dependence on ^{2}H quadrupolar energy is given in chapter 1, quadrupolar interaction section. As mentioned earlier, the doublet nature of the ^{2}H powder pattern arises due to two allowed spin transitions and the doublet resonances for a particular molecular orientation are separated by quadrupolar splitting ($\Delta\nu_Q$) (Figure 5.2b). Local structural information about the bilayer can be obtained from the Pake doublet. [1] The motionally averaged $\Delta\nu_Q$ for each bilayer orientation with respect to $\mathbf{B_0}$ field is given by; $\Delta\nu_Q = \frac{3}{2}\chi_Q S_{CD}\frac{\left(3\cos^2\theta - 1\right)}{2}$ 5.1

Where, $\chi_Q = \frac{3(e^2qQ)}{4h}$ = Quadrupolar coupling constant in Hz and is ~ 170 kHz for the aliphatic C-^{2}H bond. [2, 3] θ is the angle between the bilayer normal and $\mathbf{B_0}$ field. S_{CD} describes the bond order and is given by $S_{CD} = \frac{1}{2}\left\langle 3\cos^2\beta - 1\right\rangle$ and the angle β is defined in Figure 5.3b.[4, 5]

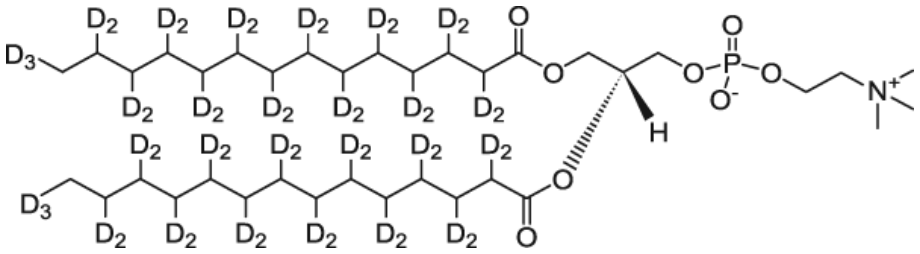

Figure 5.1. Chemical structure of DMPC-d54 lipid.

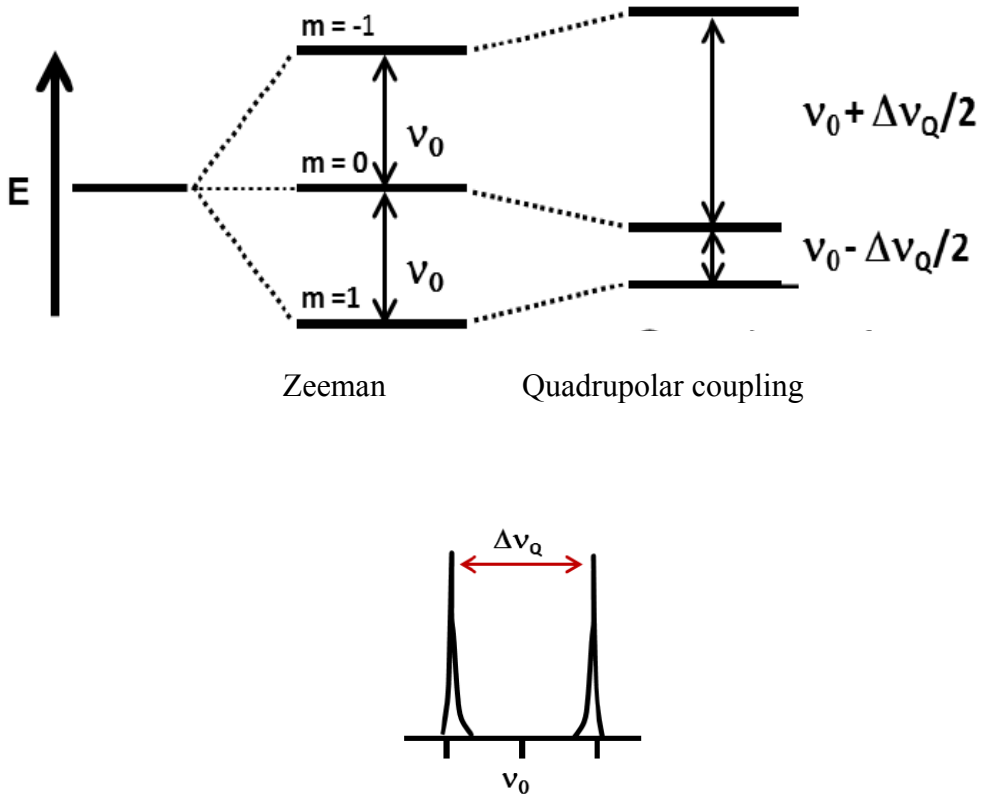

Figure 5.2. (a) Energy level diagram of ^{2}H. The Zeeman Hamiltonian ($\hat{H}_z$) is perturbed in presence of the quadrupolar Hamiltonian ($\hat{H}_Q$). Due to the quadrupolar interaction, the two spin energy levels are no longer equal. (b) Due to the two spin transitions, doublets of resonances are observed in the ^{2}H spectrum separated by the quadrupolar splitting $\Delta\nu_Q$.

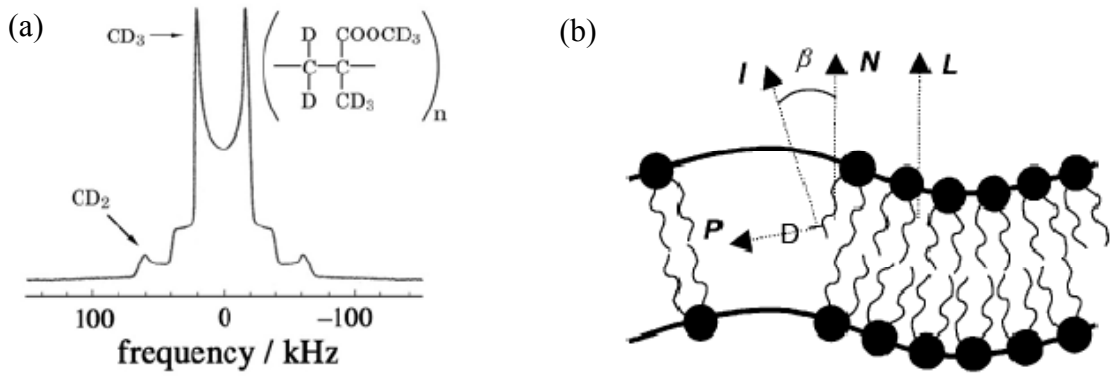

Figure 5.3. (a) Representative ^{2}H NMR powder spectrum of unoriented powdered plexiglass, PMMA-d8.The contributions of methyl and methylene groups are shown in the figure, and the methyl group undergoes threefold motion. (b) Different frames used in S_{CD} analysis. L represents the laboratory frame and is defined by the $\mathbf{B_0}$ field, N represents the bilayer normal frame, I designate the internal frame and P represents the principal axis frame. The L is parallel to N for a 0° oriented bilayer sample. For methylene groups, the z-axis of the internal frame, I, is perpendicular to the D-C-D plane.

Figure 5.3a shows the ^{2}H powder pattern for a randomly oriented PMMA-d8 powder sample. [6] In the figure 5.3a the outer splitting is ± 60 kHz and is due to the methylene groups (-C $^2H_2$-) of PMMA-d8. For the –C $^2H_2$- groups, the motion is nearly absent on the ^{2}H NMR timescale and hence the static coupling is observed. The ± 60 kHz splitting in the experimental ^{2}H NMR spectrum (large peaks) represents the $\theta = 90°$ orientation for which the $3\chi/4 = 127$ kHz $\Rightarrow \chi = \sim$ 170 kHz in case of less mobile –C $^2H_2$- groups. The weak peaks corresponding to $\theta = 0°$ orientation are not so evident in figure 5.3a. The large narrow central splitting ± 20 kHz, is due to the methyl groups (-C$^2H_3$). The threefold rotation of the –C $^2H_3$ groups about the methyl axes, means axially symmetric motion ($\eta_Q = 0$) and the largest principal value will be reduced by a

factor of (1/3). Therefore for $\theta = 90°$, the C^2H_3 splitting is $(3\chi/4) \times (1/3) = 42.5$ kHz and is in good agreement with the experimental spectrum of ~ 40 kHz. For the weaker shoulder corresponding to $\theta = 0°$, $\Delta\nu_Q = \chi/2 = 85$ kHz and is also in good agreement with the experimental ^2H powder spectrum in figure 5.3a. Therefore, according to the above experiment we can read off the $\Delta\nu_Q$ from the NMR spectrum and can calculate the segmental order parameters S_{CD} according to equation 5.1.

The order parameter describes the amplitudes of the angular excursions of the C-^{2}H bond and is related to the average structure of the lipid. [7] The time averaged order parameter depends on the conformational fluctuations of the C-^{2}H bond and the fluctuations increase towards the bilayer center. The two extremum of order parameter is 0 and 1. These extremas represent the rapid isotropic motion and or completely rigid system i.e. no motion. An order parameter of zero represents an unordered system or the isotropic system. An order parameter of 1 describes an ordered system. In general, order decreases from the lipid interface to the bilayer center. The lipid samples used in this dissertation have multiple ^2H sites, and the ^2H spectrum is much more complex as there are contributions from every ^2H along the lipid acyl chain. Each pair of ^2H at a particular carbon has a specific quadrupolar coupling and the powder spectrum is the superposition of the powder spectrum of the individual C-^{2}H (Figure 5.4a). As the motion increases, $\Delta\nu_Q$ decreases and the acyl chain order decreases. Once $\Delta\nu_Q$ is determined from the experimental spectra, S_{CD} values can be calculated for that particular methylene peak. The ^2Hs at the terminal position of the acyl chain (also bilayer center) will have more motion and has the lowest S_{CD}. Additionally, the terminal methyl ^2Hs will have ~ 1.5 times more signal due to the additional ^2H than the other methylene ^2Hs. From the Figure 5.4a we can see that the ^2H powder pattern is very complex and is difficult to assign specific peak frequencies. To get the ^2H peak

frequencies or $\Delta\nu_Q$ the powder pattern is deconvoluted or de-Paked to obtain highly resolved subspectra corresponding to $\theta = 0°$. [8, 9] In the de-Paked spectrum, $\Delta\nu_Q$ is calculated according to equation 5.1 using $\theta = 0°$. In the de-Paked spectrum, the average bilayer normal is the parallel to the laboratory frame. An example de-Paked spectrum is shown in Figure 5.4b.

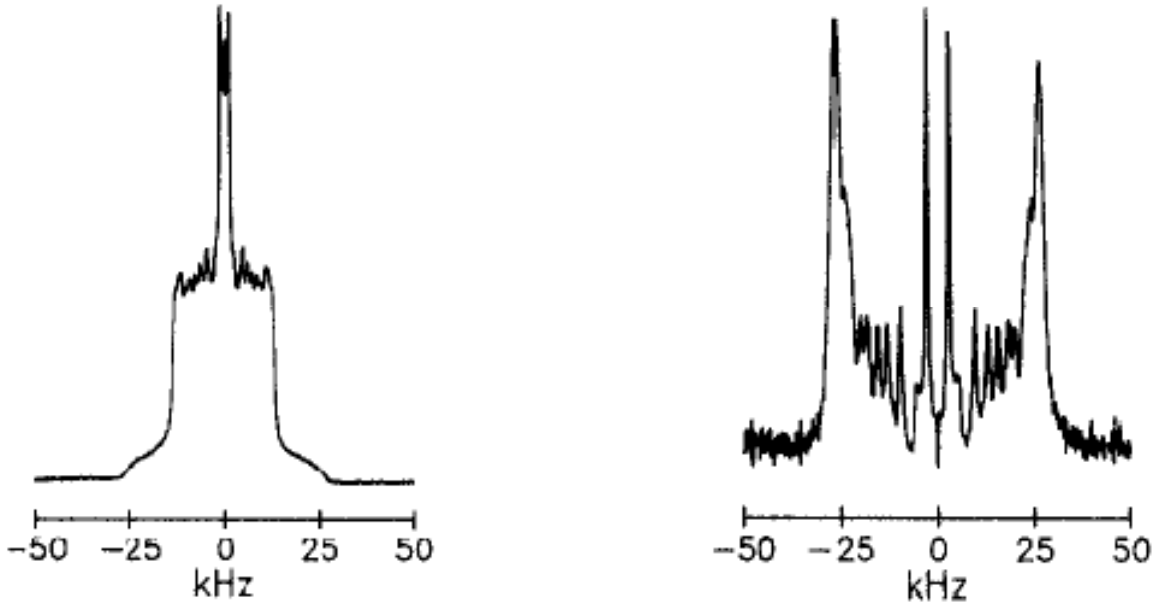

Figure 5.4. ^2H NMR spectrum of a multilamellar dispersion of 50 wt % [$^2H_{31}$] 16:0 – 18:1 PC at 22°C. (a) Powder spectrum, and (b) de-Paked spectrum.

^2H NMR spectroscopy have been widely used to study the membrane lipids. ^2H NMR has been also used to study the effect of peptides on the lipid membranes. Additionally, ^2H NMR spectroscopy is also used to study the molecular motion. This is because ^2H has a relatively small quadrupole moment and the quadrupolar coupling constants are in the range 140 – 220 kHz in most organic compounds. Therefore, the ^2H powder patterns are relatively easier to observe and are also sensitive to molecular motion with correlation times in the range 10^{-4} – 10^{-6} s. [10] In this research we are applying ^2H NMR to study the effect of the fusion peptides on the

membranes. To have a better understanding of the fusion process it is important to study the peptide-lipid interaction i.e. how the peptides perturb the host cell membrane to make it fuse more rapidly with the viral membrane. ^{2}H NMR has previously been applied by our group to understand changes in bulk structural and motional properties of lipid molecules in membranes with bound fusion peptide by measuring the $\Delta\nu_Q$ of the Pake doublet. [11] ^{2}H-NMR was also applied to study lipid/peptide interactions, studies in membrane proteins.[12-17] Almost all these studies utilize solid echo experiment to investigate the properties of the lipid molecules which reflects the total change in the system. These bulk changes are small and not very informative about fusion. We hypothesize that the changes are small because they are the average over lipid molecules far from and close to the fusion peptide. The distant lipids are likely not affected at all by the presence of the peptide whereas the close lipids may experience large changes (i.e. much greater motion) and fusion may therefore be localized at least initially near these close lipids.

In order to do so, we developed a new method "cross polarization with quadrupolar echo" (cpquecho). The new method is based on the two existing methods; (1) cross polarization (CP; described in chapter 1) and (2) solid echo (also described in chapter 1). As mentioned in chapter 1, CP is a widely used method to transfer the magnetization from the abundant to the rare nuclei for easier detection of the rare nuclei. The magnetization transfer process depends on the heteronuclear dipolar coupling and in turn depends on the internuclear distance between the spins engaged in the transfer. In contrast, in cpquecho experiment we are transferring the magnetization from the abundant to the rare nuclei. Since ^{2}H line-shapes are sensitive to motion, we choose ^{2}H as our detecting nucleus and ^{2}H enriched lipids were used. ^{1}Hs are naturally abundant and generally we have ^{1}Hs in our sample, we choose ^{1}Hs as our rare nuclei. So in

cpquecho experiment we are transferring magnetization from $^1H \rightarrow {}^2H$ with ^2H detection. Therefore, the real NMR sample contains lipids and water with near complete substitution of ^1H's for ^2H's in the acyl chain, so the only population of ^1H's is in the fully protonated peptide. One spectrum will be of all of the ^2H nuclei in the sample, i.e. a bulk lipid spectrum. The other will be a spectrum of ^2H nuclei within ~5 Å of a ^1H nucleus, i.e. a spectrum of lipid molecules next to the fusion peptide. The distance 5 Å is based on the heteronuclear dipolar coupling between the ^1H and ^2H nucleus. The ^1H -^2H dipolar coupling = $18568/r^3$. For 5 Å internuclear separations, $^1H - {}^2H$ dipolar coupling is ~ 148 Hz. Therefore, the rate of CP is ~ 0.74. The cross-polarization transfer expression is (chapter 1, equation 1.70):[18]

$$\mathbf{I}_y \xrightarrow{(\hat{S}_z\hat{I}_z + \hat{S}_x\hat{I}_x)} \mathbf{I}_y \frac{1}{2}(1+\cos\omega_{HX}t) + \mathbf{S}_y \frac{1}{2}(1-\cos\omega_{HX}t) + (\mathbf{S}_z\mathbf{I}_x - \mathbf{S}_x\mathbf{I}_z)\sin\omega_{HX}t$$

Where the term $\mathbf{S_y}$ (1-cos ω_{HX}.t) term represents the magnetization transfer from $\mathbf{I} \rightarrow \mathbf{S}$ spins. One of the major factors for the CP transfer is the strength of the dipolar coupling between I and S spins or ω_{HX}. 't" denotes the contact time between the I and S spins. The CP transfer is inefficient when the cosine term ≈ 0. The CP transfer is maximum when the cosine term ≈ π/2. The typical contact time in our experiments is ~ 5 ms. Therefore, the maximum CP transfer can be obtained when $^1H - {}^2H$ is ~ 157 Hz (which gives the rate of CP transfer ~ 0.78). So the rate of CP transfer for 5 Å is comparable to the maximum CP transfer for 5 ms contact time.

5.1.1 Relaxation measurements

The approach of a system to thermal equilibrium is known as relaxation. Following a pulse, the magnetization **M** returns to the equilibrium with different time constants T_1 and T_2:[19]

$$M_z(t) - M_z(0) = [M_z(0) - M_0]\exp(-\frac{t}{T_1}) \qquad 5.2$$

$$M_x(t) = M_x(0)\exp(-\frac{t}{T_2}); M_y(t) = M_y(0)\exp(-\frac{t}{T_2}) \qquad 5.3$$

T_1 is known as "spin-lattice" or "longitudinal" relaxation and T_2 is known as "spin-spin" or "transverse" relaxation process. The T_1 relaxation process in ^2H NMR is only sensitive to "spectral densities", $J(\omega)$, of the fluctuating quadrupolar interactions at $\omega = \omega_0$ where $f_0 = \omega_0/2\pi$ is the nuclear Larmor frequency. The T_2 processes are affected by $J(0)$. The dependence of T_2 on the low frequency components of $J(\omega)$ means that the T_2 processes are sensitive to slow-motions with correlation times $\tau_C >> \omega_0^{-1}$. [20]

5.2 Probe design

To do the cpquecho experiment I built a double resonance $^{1}H - ^{2}H$ probe tuned to ^{1}H and ^{2}H frequency. In NMR probe, each channel is considered as a tank circuit or LC circuit because of the presence of capacitors and inductors. When a rf pulse is applied to a LC circuit the inductive reactance X_L, the capacitive reactance X_C and the total impedance Z experienced by the rf pulse is given by;

$$X_C = -\left(\frac{i}{2\pi\nu C}\right) \quad 5.4$$

$$X_L = (i2\pi\nu L) \quad 5.5$$

$$Z = X_C + X_L = (i2\pi\nu C) - \left(\frac{i}{2\pi\nu C}\right) \quad 5.6$$

Where C is the capacitance of the capacitor, L is the inductance of the coil, and ν is the frequency of the rf pulse. During the resonance condition Z = 0 and the resonance frequency of the LC circuit is given by;

$$\nu = \frac{1}{2\pi\sqrt{LC}} \quad 5.7$$

The total impedance Z experienced by the rf pulse can be minimized by using specific components like plug-ins, using correct length of the tune tube so that the capacitance and the inductance fulfill the resonance condition. Generally the tuning configuration of a probe is given by the manufacturer. However, the configuration of a probe that finally works might be different from the configuration provided. In my case, I built a double resonance probe means there are two channels; ^{1}H and ^{2}H. Since there was no double resonance probes in our laboratory, I configured a triple resonance probe to a double resonance probe. The tuning configuration for the 7050 the $^{1}H - ^{2}H$ probe is:

62 pf series plug in

SC trap plug in

SC Low channel receiver platform

36 Mid channel receiver platform

6.7” Low tune tube (Y- channel)

Where pf represents picofarad, unit of capacitance; SC represents the short circuit. The tuning rod contains a top copper part and a bottom dielectric plastic attached to a copper tube. 3.9” refer to the top copper part. Since I am using only two channels in a probe, I used a sc trap. Additionally, I left the mid-channel empty to achieve shorter 90° pulses.

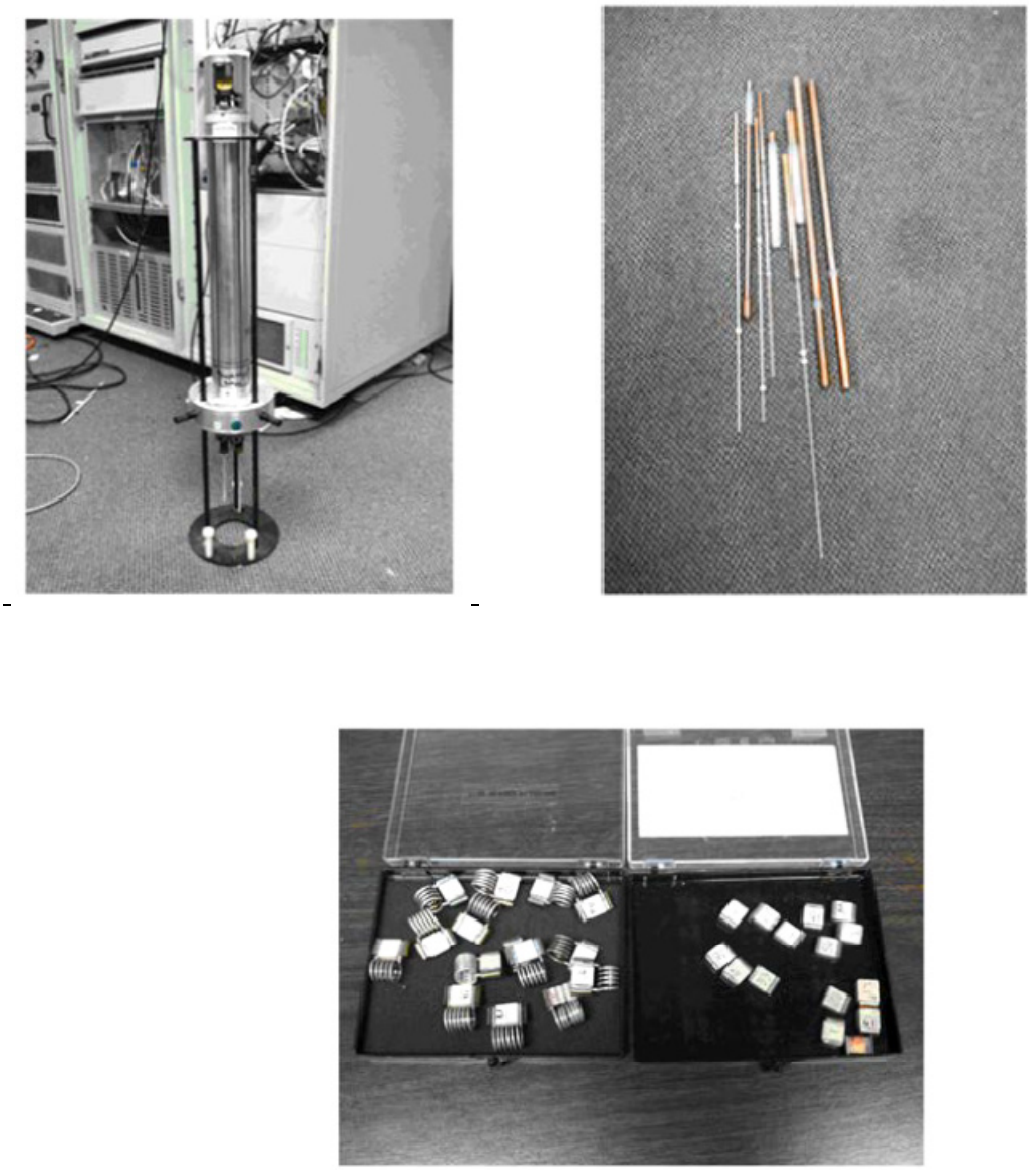

Figure 5.5. (a) Solid state NMR bprobe. (b) Tuning tube and tuning rods. (c) Series plug-ins (left) and traps (right) used in solid state NMR probes.

5.2.1 Tuning of a NMR probe

In order to efficiently deliver rf power to the sample and to detect the transverse magnetization, the probe circuit must be well tuned so that the resonant frequency, $\nu = \frac{1}{2\pi\sqrt{LC}}$ of the circuit is same as the rf frequency. By adjusting the match, we are matching the impedance of the LC circuit. The tuning and the matching are performed by adjusting the capacitors present in the probe circuit. The coil is driven by rf input and the response is observed by measuring the reflected power. The capacitors are adjusted interactively to optimize the response i.e. to minimize the reflected power, V_r. Generally two methods are used to tune and match the probe; (1) using sweep generator configuration or low power tuning and (2) using rf source or high power tuning. The first step of building a probe is to get the desired channels tunable e.g in a 400 MHz spectrometer, the ^2H channel should be tunable at 62 MHz. To do so low power tuning is done because the tuning and the matching responses can be monitored independently. In low power no rf pulses are applied to the probe. Figure 5.6 illustrates a schematic representation of the connections of the cable used during low power tuning. Additionally, the Sec/Div menu on the oscilloscope needs to be adjusted and the time scale is changed to "CH1X" to observe all the resonance peaks at different frequencies on the oscilloscope. When a channel is tunable, a response similar to Figure 5.7 is observed on the oscilloscope when the probe is connected to the sweep generator. Once the probe is well tuned and matched, high power tuning is done. The high power tuning is done in presence of the rf pulses. A probe is considered as well tuned when the ration of the forward voltage (V_f) to the reflected voltage (V_r) is ~10:1.

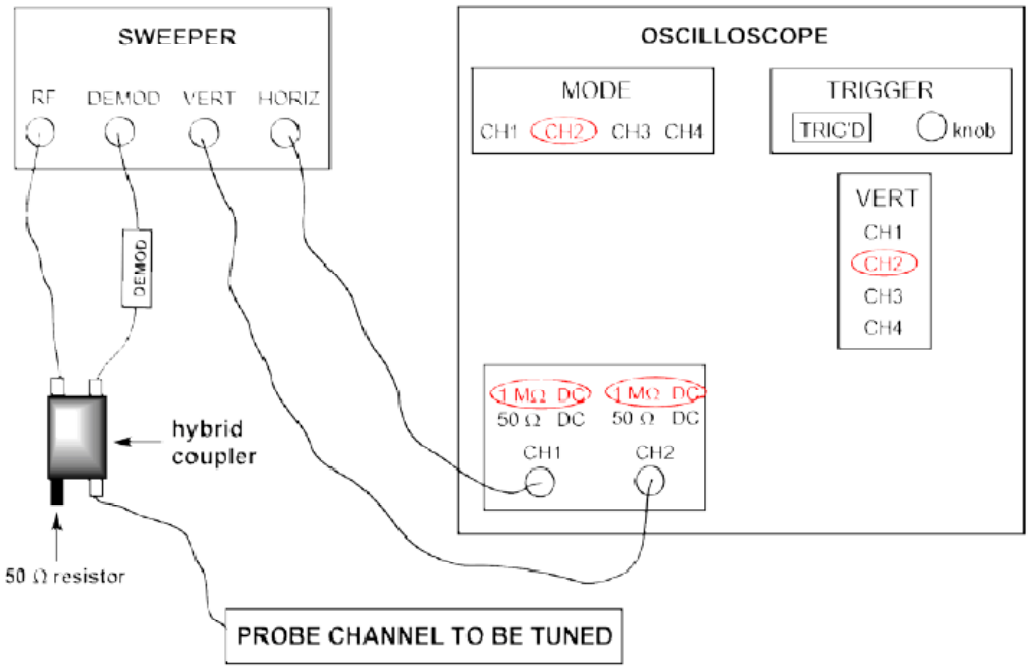

Figure 5.6. Schematic representation for the cable connections used for low power tuning.

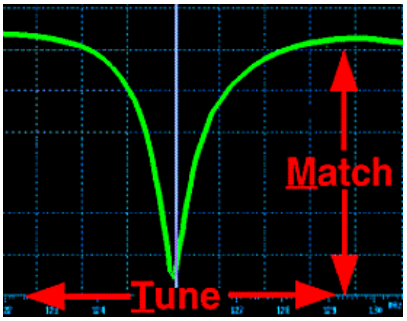

Figure 5.7. The response on the oscilloscope when the probe is connected to the sweep generator for a well tuned and well matched probe. The tune rod changes the frequency while the match adjusts the depth of the peak. The horizontal axis position of the dip indicates the resonance frequency of the coil; the depth of the dip is a measure of the match between the impedance of the circuit and the 50 Ohm load.

5.3 Pulse sequence programming

P-code language is used to program the pulse sequence. The main code for the pulse program with the phase cycling is stored as source code file (.s file extension). Every pulse program is associated with acqpars (acquisition parameters) file that enables Spinsight to display the list of parameters in the acquisition panel. The acqpars file also contains the minimum and the maximum value of each parameter. Next the source code file is compiled by using the command "pcomp", where pcomp is the command that runs P-code compiler. If the pulse program is free of syntac errors, the P-code compiler compiles the source code file and creates the executable files that run on the CPC boards.

Figure 5.8 shows the cpquecho pulse sequence. At the beginning, the cpquecho sequence is similar to the ramped CP sequence. But after the contact pulse, a 90° pulse is applied on the ^{2}H channel after time τ_1. Similar to the solid echo experiment, there is another delay τ_2 before acquisition. Ideally $\tau_1$should be equal to τ_2, but in practice τ_2 is made smaller than τ_1.

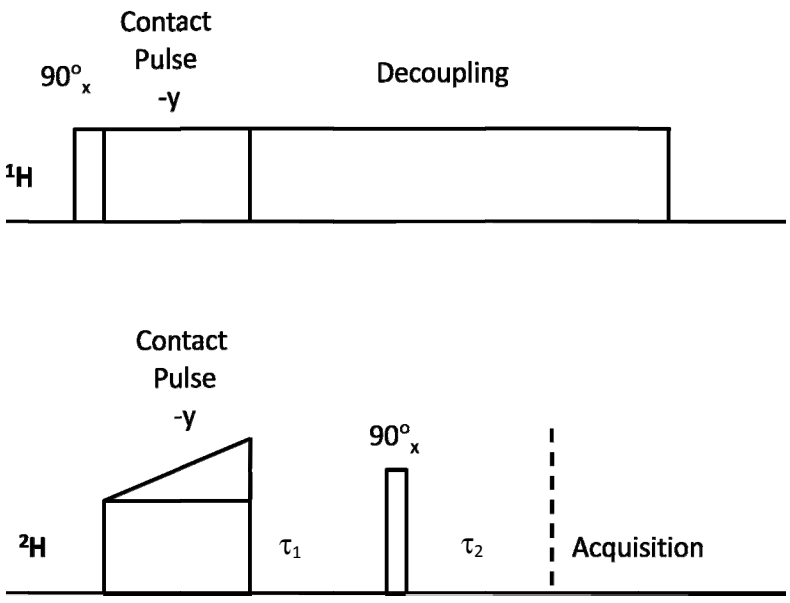

Figure 5.8. Pulse sequence of cpquecho. The effect of the CP pulse is to transfer the magnetization from the rare (^{1}H) spins to the abundant (^{2}H) spins followed by ^{2}H detection. Here ramped CP is used to increase the efficiency of the matching conditions.

5.3.1 Phase cycling

The main purpose of phase cycling is to select the desired signals and to remove the unwanted signals and the artifacts. The phase cycling was based on the phase cycling of the solid or quecho experiment. The density operator is given by: [18]

$$\hat{\rho}(2\tau)=\hat{U}(2\tau)\hat{I}_y\hat{U}^{-1}(2\tau)=\hat{I}_y$$

On the basis $\left[3\hat{I}_y{}^a\hat{I}_y{}^b-\hat{\mathbf{I}}^a\bullet\hat{\mathbf{I}}^b,\hat{I}_y\right]=0$

Where $\hat{U}(2\tau)=\exp\omega_\theta(3\hat{I}_y{}^a\hat{I}_y{}^b-\hat{\mathbf{I}}^a\bullet\hat{\mathbf{I}}^b)\tau\exp(i\frac{\pi}{2}\hat{I}_y)$

In quecho experiment, the final magnetization before the application of the second 90° pulse is $\mathbf{I_y}$ and then a second 90° pulse is applied which is 90° out of phase of the first pulse. So there is no

net rotation of the ^{2}H magnetization. For cpquecho experiment, eight phase cycling was applied. H90 refers to the first 90° pulse on the ^{1}H channel, Hmix refers to the spin lock pulse applied to the ^{1}H channel. Xmix refers to the spin-lock pulse on the ^{2}H channel, X90 refers to the second 90° pulse used for refocusing the magnetization. The phase cycling of cpquecho pulse sequence is given below:

Table 5.1. Phase cycling of the cpquecho experiment

H90	Hmix	Xmix	X90	Receiver Phase
0	90	270	270	3
180	90	270	90	1
0	90	180	180	2
180	90	180	0	0
0	90	270	90	3
180	90	270	270	1
0	90	180	0	2
180	90	180	180	0

0, 1, 2, 3 refers to x, y,-x, and –y or 0, 90, 180, and 270 phase of the pulse.

5.4 Setup compound(s)

To test the new pulse program a proper setup is required. The criteria for an ideal setup compound can be listed as follows:

1. An ideal setup compound should have the same nucleus as the observed nucleus. The NMR samples to be studied for the above-mentioned experiments are isotopically labeled with ^{2}H, therefore the set compound should also contain ^{2}H as detecting nucleus.
2. An ideal set up compound should have good signal to noise.
3. Preferably an ideal setup compound should be similar to the real NMR samples. For example, the samples to be studied are the lipids and the peptide-bound lipids. Therefore it is preferable to have a setup compound that is made of lipid molecules.

For my experiments, I used three different setup compounds to optimize different parts of the experiment. The different setup compounds used for the experiments are:

(1) Deuterium oxide (D_2O) for ^{2}H 90° pulse width and the amplitude of the pulse optimization. D_2O was used because D_2O gives a sharp narrow peak to 0 ppm and only 4-8 scans is required to have a good signal to noise. D_2O was difficult to pack in 4 mm solid state NMR rotor. Therefore, D_2O was packed in a 4 mm clear glass tube with a rubber cap.

(2) To test the new pulse program we needed a compound that contains both the ^{1}Hs and the ^{2}Hs. The ^{1}Hs should be close to the ^{2}Hs in order to transfer the ^{1}H magnetization to the ^{2}Hs. But at the same time the compound should have small quadrupolar anisotropy in order to observe the ^{2}H within the spectral window. For this reason we started with deuterated glycine, COO^{-} - CH_2 - ND_3^{+}, where the amino ($–NH_3^{+}$) group of the glycine is deuterated ($-ND_3^{+}$). However, we never observed any cross polarization signal from the

$^1H \rightarrow {}^2H$. This could be due to the threefold motion of the $–NH_3$ group about the -NH axis. This threefold motion averages the heteronuclear dipolar coupling and hence no cross polarization signal was observed. Therefore, we used glycine-d_2 where the $–CH_2$ group is deuterated (COO^- - CD_2 - NH_3^+). The $–CD_2$ have larger quadrupolar anisotropy relative to $–CD_3$ because of the rigidity of $–CD_2$ group. Since $–CD_2$ is less mobile, we were able to observe the cross polarization signal from the ^{1}Hs of $–CD_3 \rightarrow {}^2$Hs of $–CD_2$. Pure crystalline glycine-d_2 was directly packed into 4 mm MAS rotor.

(3) Finally for cpquecho experiment optimization, DMPC-d54 lipids were used. The chemical structure of DMPC-d54 is shown in Figure 5.1. This lipid was chosen because all the ^{1}Hs in the acyl chain are per-deuterated. All the NMR samples to be studied were made with DMPC-d54 lipid. For the standard sample, 44 μmoles of pure DMPC-d54 lipid was used. The lipid sample was suspended in either pH 5 or pH 7 buffer, followed by 10 freeze-thaw cycles. Large unilamellar vesicles were prepared by repeated extrusion through a 100 nm polycarbonate filter. The lipid pallet was lyophilized overnight. The lipid sample was packed with 5 μL of either pH 5 or pH 7 buffer. The amount of buffer added to all the NMR samples used for H-D experiments were kept constant.

5.5 Pulse sequence optimization

The optimization procedure for the cpquecho pulse sequence is described as follows:

5.5.1 ^{2}H 90° pulse optimization

Both the cpquecho and quecho pulse sequences utilize 90° ^{2}H pulse; in quecho sequence, ^{2}H 90° pulses are used as excitation and refocusing ^{2}H magnetization, while in cpquecho experiment ^{2}H 90° pulse is used only for refocusing ^{2}H magnetization. ^{2}H 90° (pw90X) pulse was set using D_2O.

Pulse program = 1 pulse with phase cycle x, -x, y, -y, ^{2}H transmitter frequency = 61.5207824 MHz, static sample, temperature 25°C. After setting the above mentioned parameters in Spinsight interface, we need to tune the ^{2}H channel. Once the desired channel is well tuned, we start the acquisition process where we array the pw90X for particular pulse power (aXrf ampl).

The Rabi frequency for the ^{2}H 90° pulse is; $\frac{\gamma B_1}{2\pi} = \frac{1}{4 \times \text{pw90X}} = 154.32$ kHz. The pulse flip angle is $\gamma B1 \times$ (pw90X) = 90°. An alternate way of setting 90°pulse is to fix the pw90X and array the aXrf ampl.

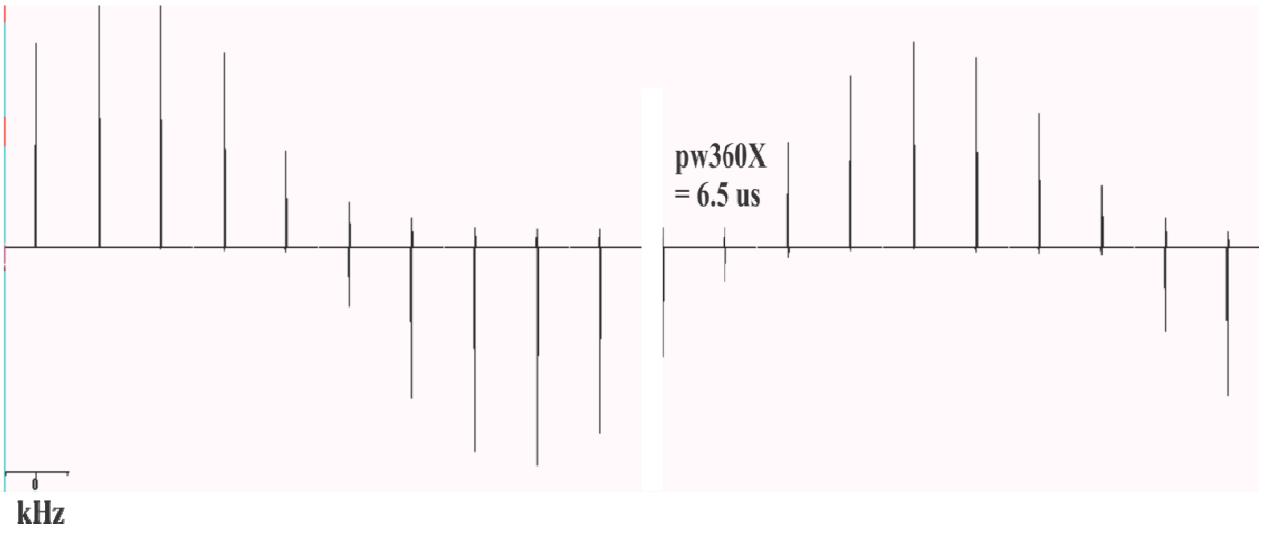

Figure 5.9. ^{2}H spectra of D_2O static sample at 25°C. pw90X arrayed from 1.0 µs to 10.5 µs with an increment of 0.5 µs, aXrf ampl = 0.7, number of scans = 8. The best optimized pw90X is $\frac{\text{pw360X}}{4}$.

5.5.2 Transmitter frequency setup

Setting the transmitter frequency for the quecho and cpquecho is very crucial and the transmitter frequency for these experiments should be either on resonance or the resonance offset field should be very small (± ~ 0.5 kHz offset). This is because in these experiments we are observing the relaxation and not the precession of the magnetization around some fictitious frequency. The. fictitious frequency is not intrinsic to the sample. This is called transmitter beating. Figure 5.10 shows a case where the ^{2}H-signal is not decaying exponentially rather we can see an oscillations of the signal

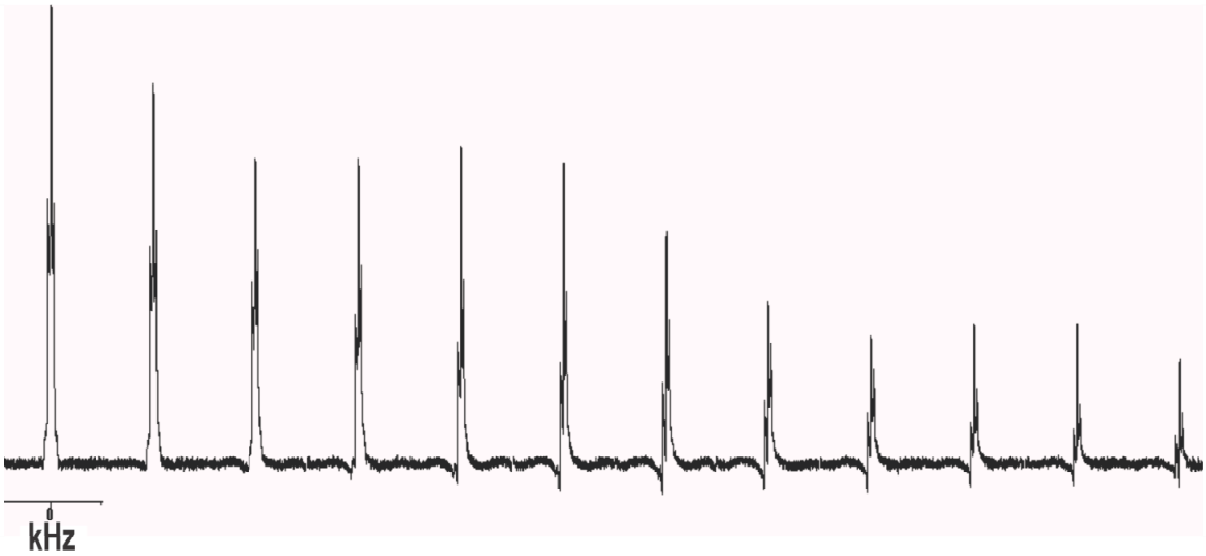

Figure 5.10. ^{2}H spectra of DMPC-d54 with HAfp in the ratio 25:1 at pH 7. The delay between the two 90° pulses in the solid echo experiment are arrayed from τ_1 = 30 μs, τ_1 = 11 μs to τ_1 = 415 μs, τ_1 = 396 μs for static sample at temperature 35°C. In the above figure we can see that the decay is not fully exponential but there is an echo at some other frequency ~ 3 kHz.

We can check the oscillations are not intrinsic to the sample and are coming from amplifier by changing the transmitter frequency. In the Figure 5.10, the resonance offset field is ~ 2 kHz. So we can change the transmitter frequency by ~ 2 kHz. If the frequency of the oscillation changes, then the oscillations are not intrinsic to the sample and is coming from the transmitter and is shown in the Figure 5.11.

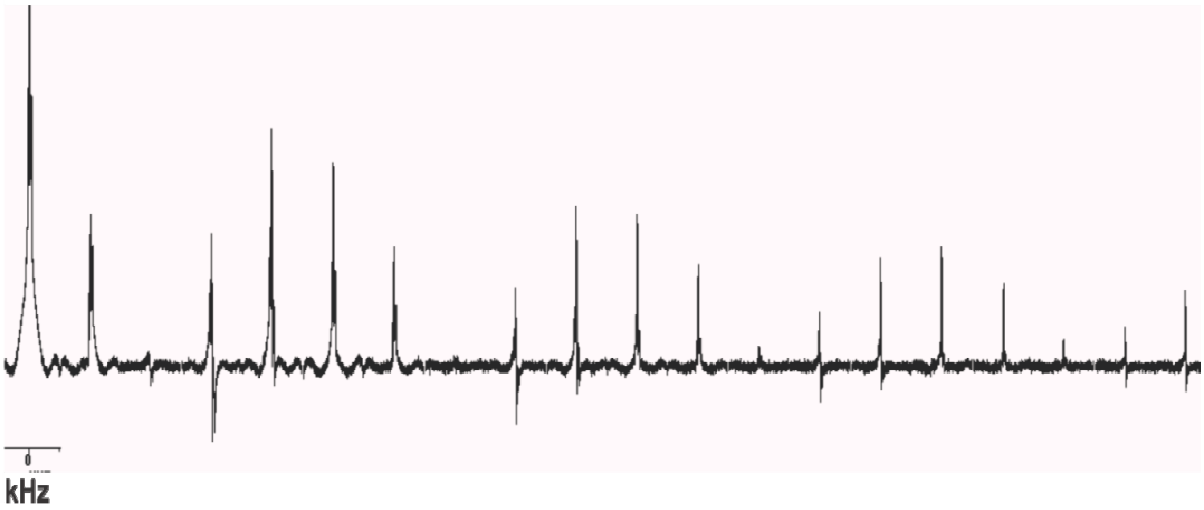

Figure 5.11. ^{2}H spectra of DMPC-d54 lipid with HIV-fusion peptide in the ratio 25:1. The spectra were recorded with the transmitter frequency of 61.204 MHz. As we can see from the above figure that the echo point changed and the resonance offset is ~ 2 kHz. So the transmitter frequency is changed by 2 kHz.

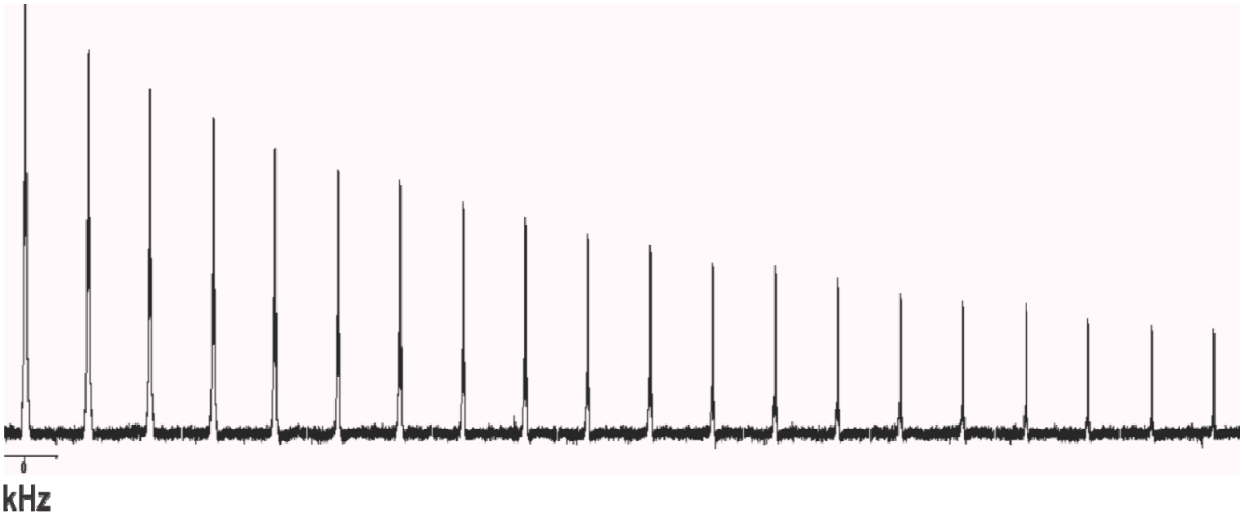

Figure 5.12.^{2}H-spectra of DMPC-d54 lipid with HIV fusion peptide acquired with the corrected transmitter frequency. The transmitter frequency for ^{2}H was 61.5207824 MHz was used for all of the ^{2}H-NMR experiments.

5.5.3 CP optimization

The CP optimization was done on two samples, Glycine-d_2 and DMPC-d54.

Step 1: ^{1}H 90° pulse optimization

The ^{1}H 90° pulse is the first pulse in the cpquecho experiment which rotates the ^{1}H z- axis magnetization to the xy-plane. We first set the ^{1}H 90° pulse width to 4 μs and then array the pulse power (aHrf ampl) and identify the maximum ^{2}H signal. The maximum ^{2}H signal corresponds to the optimized aHrf ampl. Alternatively, we could also set pw90H to 8 μs and array the aHrf ampl and look for the zero ^{2}H signal which also corresponds to the best aHrf ampl.

The Rabi frequency for the ^{1}H 90° pulse = $\frac{\gamma B_1}{2\pi} = \frac{1}{4 \times \text{pw90X}} = 65.79$ kHz.

Step -2: ^{1}H and ^{2}H CP pulse optimization

The next step is to optimize the ^{1}H CP power (aHcp). Generally we set the aHcp same as aHrf ampl although they both could be different. In cpquecho experiment, I set pw90H different than aHrf ampl to higher value. After setting the aHcp, the next step is to array the ^{2}H CP pulse power (aXcp) and then identifying the value of aXcp that produces the maximum ^{2}H signal intensity. Next, the ramp on the CP pulse in the ^{2}H channel is optimized by arraying aXcpmod. By including the ramp we maximizing the magnetization transfer from $^1\text{H} \rightarrow {}^2\text{H}$.

Step-3: Contact time optimization

The last step of CP optimization is optimizing the contact time (ct). Contact time is time during which the contact pulse or spin-lock pulse is applied to both the ^{1}H and ^{2}H channel. If the ct is too short then there will be an incomplete magnetization transfer from $^1\text{H} \rightarrow {}^2\text{H}$. If the ct is too long, the ^{2}H intensity will also decrease because of ^{1}H $T_{1\rho}$ relaxation. $T_{1\rho}$ relaxation is the decay

of ^{1}H magnetization under spin-lock field and is described in chapter 1. Figure 5.14 shows that the ^{2}H signal builds up with increasing ct but later with increasing ct the ^{2}H signal decreases

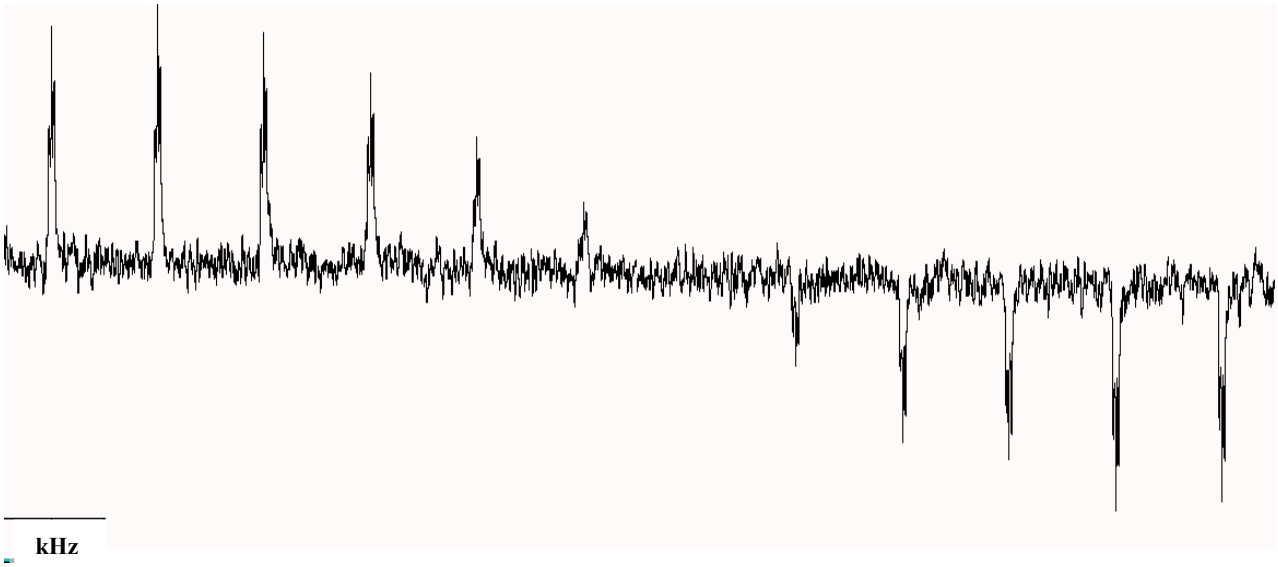

Figure 5.13. ^{2}H spectra of DMPC-d54 for pw90H array from 3 μs to 11.8 μs with an increment of 0.8 μs, for 360 scans, aHrf ampl = 0.65, static sample, temperature = 35°C.

.

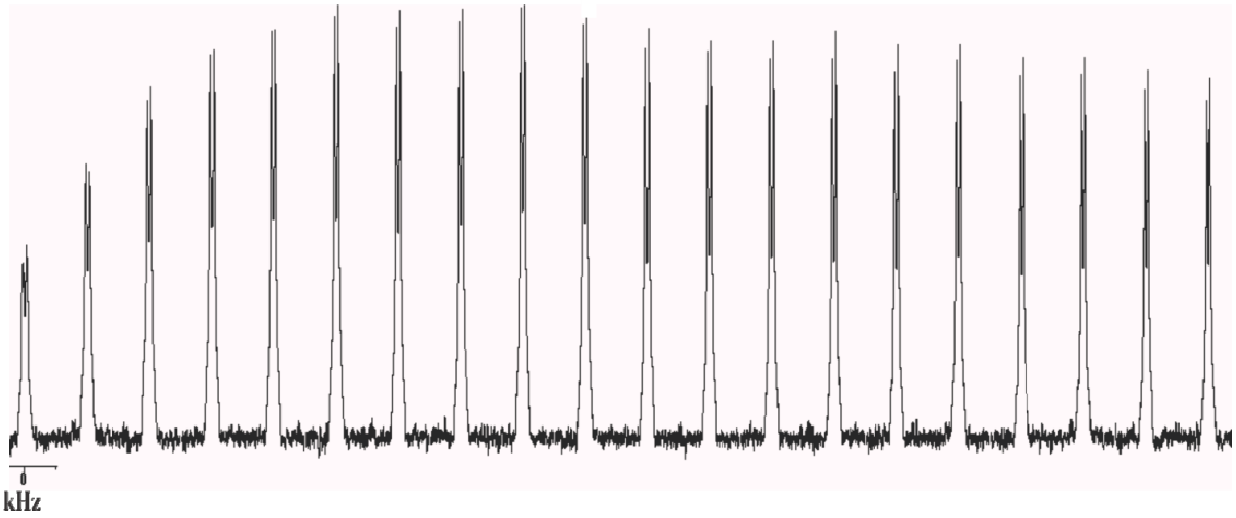

Figure 5.14. ^{2}H spectra of DMPC-d54 at 30°C. Contact time is arrayed from 1 ms to 10.5 ms with 0.5 ms increment, number of scans is 2000, pw90H = 3.8 μs, aHrf ampl = 0.8, aHcp = 0.9, pw90X = 1.6 μs, aXrf ampl = 0.56, aXcp = 0.25, aXcpmod = 0.1, dwell time = 2 μs.

5.6 Testing a new pulse sequence

The new pulse sequence was tested in couple different ways to check if the pulse program is working properly.

1. The first method is to check the signal in the oscilloscope while pulsing the cpquecho pulse program in the spectrometer.

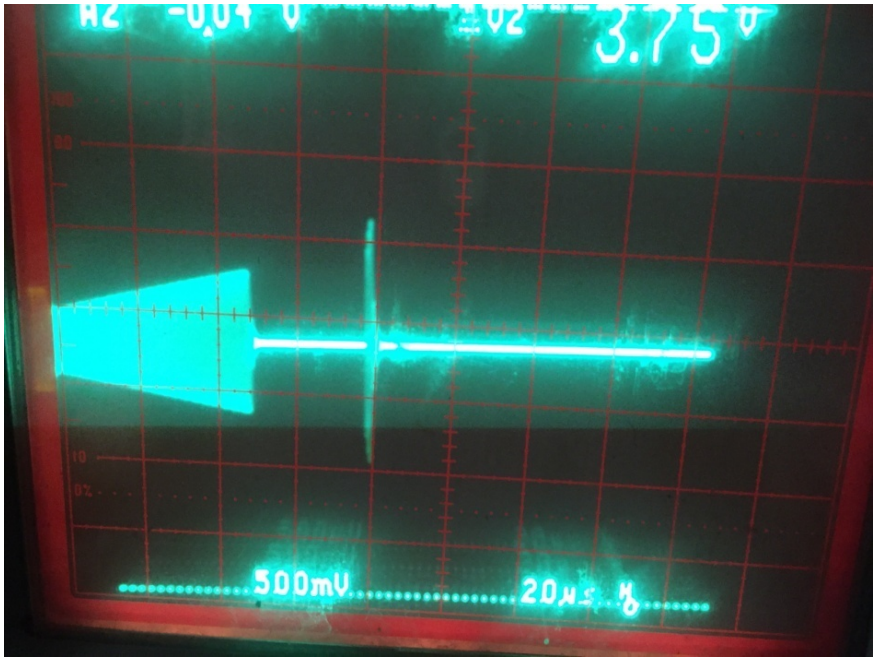

Figure 5.15. Voltage response in the oscilloscope due to the application of the pulse in the spectrometer. The first signal shows the ramped spin-locked pulse and the last component represents the ^{2}H 90° pulse.

2. The next method is to vary the pw90H and monitor the ^{2}H signal. Since in CP experiment, the magnetization developed in the ^{2}H nucleus is essentially the ^{1}H magnetization that has been transferred to ^{2}H, we can monitor the ^{2}H signal as a function of the pw90H. Figure 5.16 show change in the ^{2}H signal intensity as a function of pw90H. The zero ^{2}H signal appears at pw180H 7.8 μs and the maximum ^{2}H signal at pw90H = 7.8/2 = 3.9 μs.

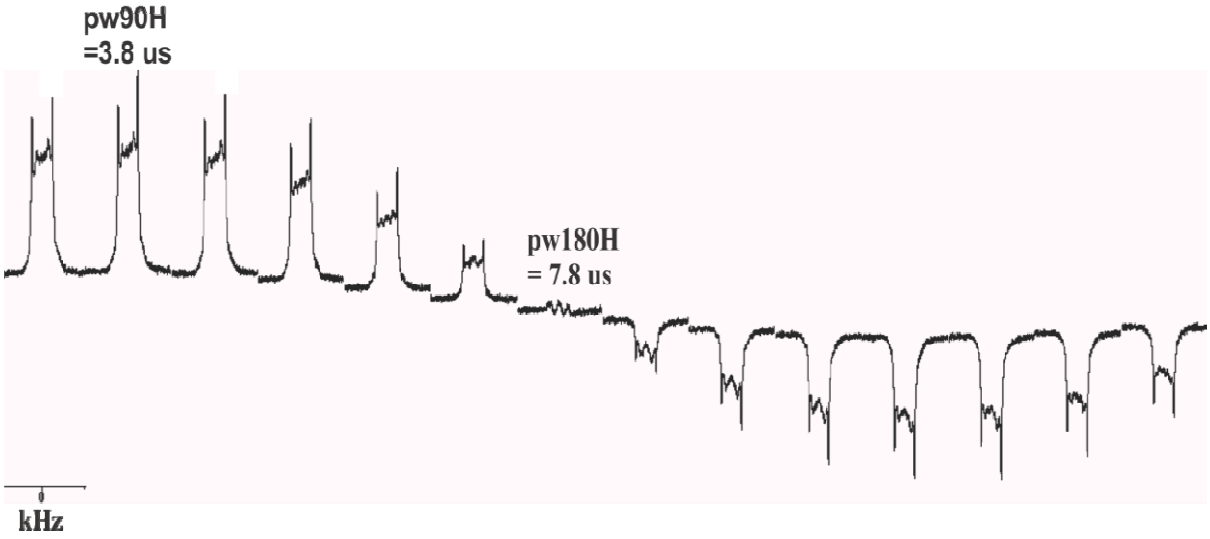

Figure 5.16. ^{2}H spectra of Gly-d2 for pw90H array from 3.0 μs to 13.4 μs with 0.8 μs increament at 23°C, static sample, 360 scans.

3. After making the ^{1}H CP contact pulse (aHcp) zero, no ^{2}H signal was observed (Figure 5.17a). Figure 5.17a shows the FID of Gly-d2 after ~ 250 scans whereas for the same sample, ^{2}H signal was observed when the ^{1}H contact pulse was applied for ~ 350 scans (Figure 5.17b).

(a)

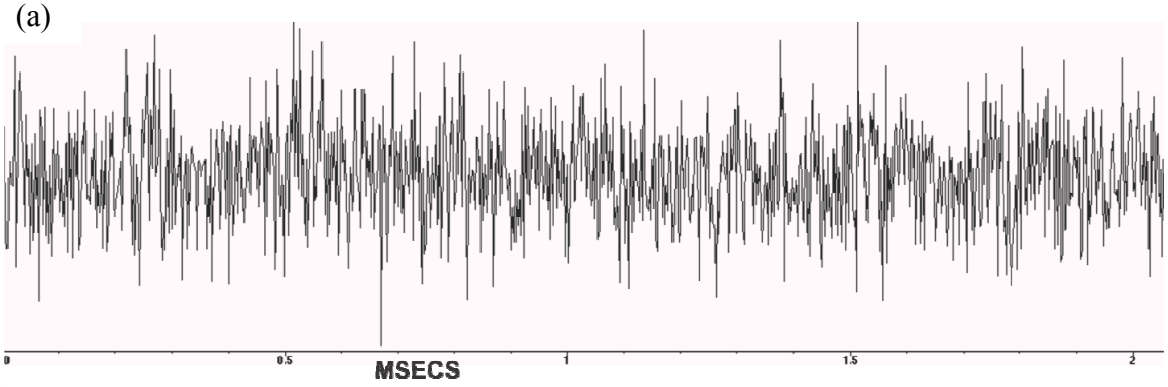

(b)

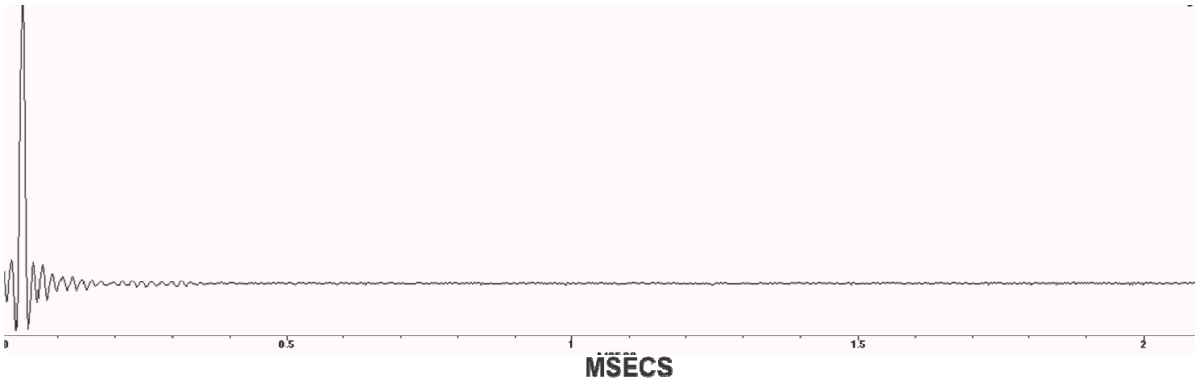

Figure 5.17. ^{2}H FID of Gly-d2 for **(a)** aHcp = 0, and (b) aHcp = 0.9 at 23°C for static sample. The number of scans in case of (a) is 250 and in (b) is 350. Comparison of the above two figure shows that the there is no ^{2}H sgnal when the ^{1}H contact pulse is turned off.

5.7 Experimental conditions

The variable temperature ^{2}H NMR spectrum were obtained using both solid echo (quecho) and cross polarization with quadrupolar echo (cpquecho) experiment. The pulse sequences of quecho and cpquecho experiments are shown below:

(a)

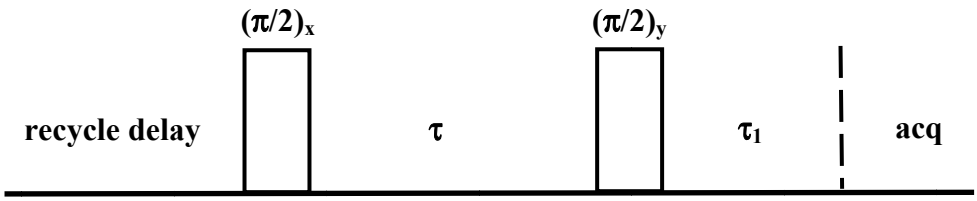

(b)

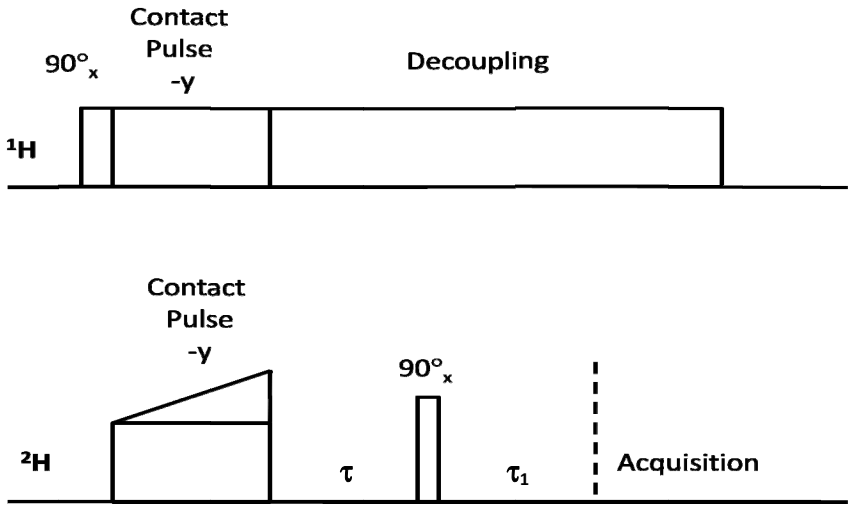

Figure 5. 18. (a) pulse sequence of quecho experiment, and (b) cpquecho experiment.

The experimental conditions of quecho experiment are described in chapter 2 section 2.6 under static NMR spectroscopy. The typical experimental parametrs for the cpquecho experiment included 3.8 μs ^{1}H 90° pulse, 75 kHz ^{1}H CP, (70 – 75) kHz ramped ^{2}H CP, 33 kHz ^{1}H decoupling, 1.62 μs ^{2}H 90°-pulse. The typical duration for the CP contact time is ~ 5 ms. The spectra were typically processed with -10 or -11 data shift, ~1000 Hz Gaussian line broadening and polynomial baseline correction. For the variable temperature study, ^{2}H spectra were obtained by keeping τ = 30 μs and τ_1 = 11 μs. This is because when τ = 30 μs and τ_1 = 11 μs, the ^{2}H signal intensity was found to be maximum. Each sample was equlibrated for ~15 – 20 minutes at each temperature before data collection and this was done by keeping the rotor inside the probe while mainting the temperature. For relaxation studies, ^{2}H spectra were accquired for different τ and τ_1 values and keeping the delay increments constant.

In cpquecho experiment, ~ 30kHz decoupling was used. This is because, if we apply decoupling the signal to noise of the ^{2}H spectum increases by a factor of 1.13 without any narrowing effect on the ^{2}H spectra. Figure 5.19 show the comparison of ^{2}H cpquecho spectra of glycine-d_2 under different decoupling conditions. The $\Delta\nu_Q$ for each spectrum is ~ 116 kHz.

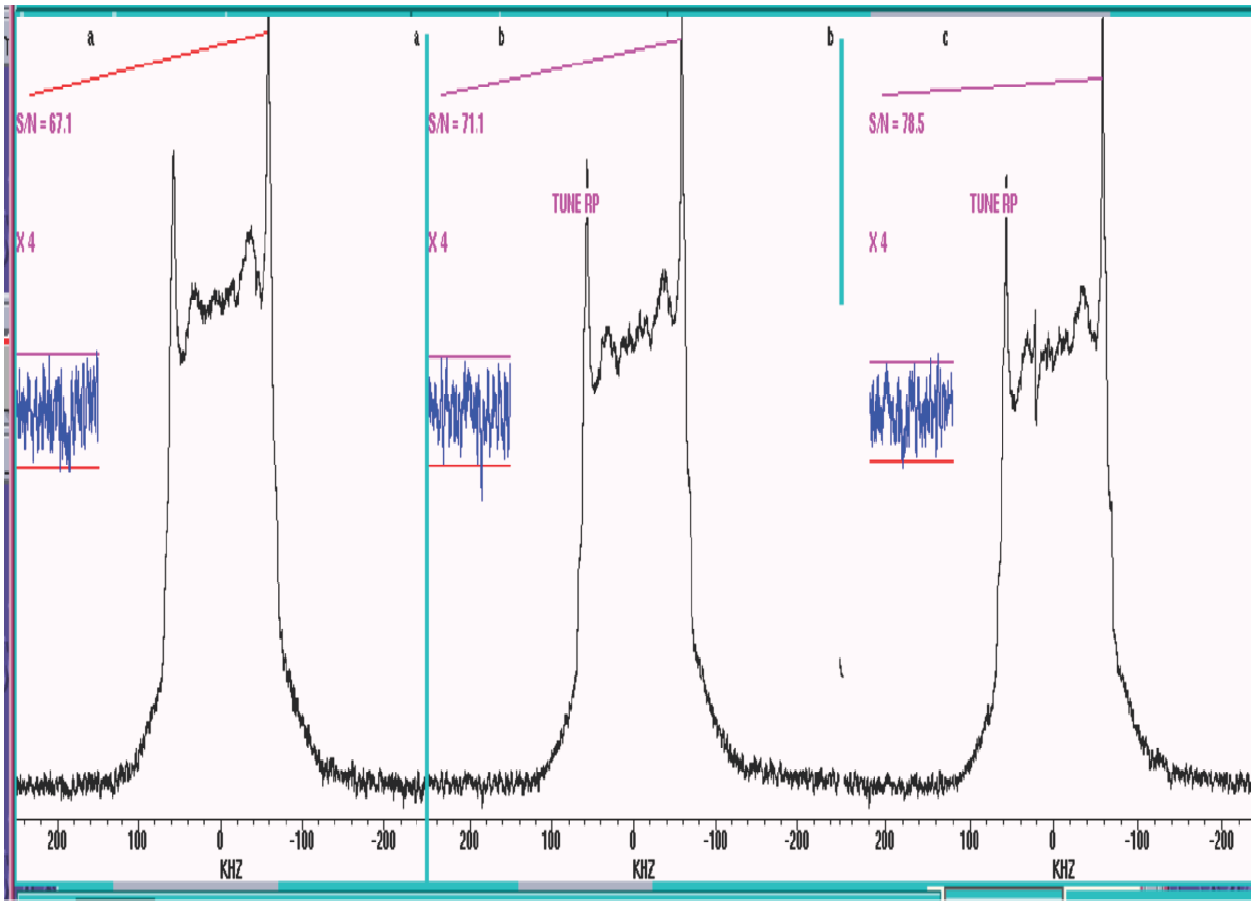

Figure 5.19. "cpquecho" ^{2}H NMR spectrum of Glycine-d_2 under static condition at 23°C. The first, second and third panel shows the cpquecho ^{2}H spectra acquired when ^{1}H decoupling = 0, ^{1}H decoupling = ~ 15 kHz and ^{1}H decoupling = ~ 30 kHz respectively. Each spectrum was processed with 500 Hz line broadening, -19 data shift. The number of scans for each spectrum was 360.

5.8 Results

5.8.1 Secondary structure of HFP and HAfp in DMPC-d54

The quecho and the cpquecho experiments were done with both the HAfp and also with the HIV-fusion peptide. The 23 N-terminal residues of the HIV gp41 protein are known as HIV fusion peptide and is represented as HFP in this dissertation. Earlier work showed that the HFP adopts a predominantly β-sheet structure in DMPC-d54 lipids. To confirm the secondary structure of HAfp in DMPC-d54, a separate HAfp sample was prepared in DMPC-d54 lipid. The HAfp was ^{13}CO labeled at Ala-5 position, and the peptide to lipid ratio was 1:25. Figure 5.20 shows the secondary structure of HAfp in DMPC-d54.The ^{13}CO chemical shift of Ala-5 ^{13}CO is 180.3 ppm which confirms that the HA3fp20 is helical at pH 5 in DMPC-d54 lipid.

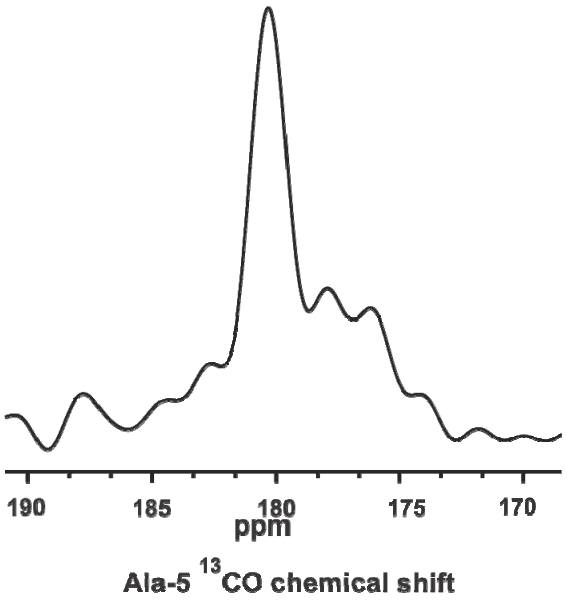

Figure 5.20. Ala-5 ^{13}CO NMR spectrum of HAfp in DMPC-d54 in the ratio 1:25 at pH 7. The spectrum was acquired using a ramped cross polarization pulse sequence. Experimental conditions include: 3000 scans, 8 kHz MAS and -50°C. 5. The chemical shift of Ala-^{13}CO is 180.3 ppm which confirms that HAfp is helical in DMPC-d54 lipid.

5.8.2 Solid echo or quecho experimental results

5.8.2.1 Variable temperature ^{2}H NMR

To obtain molecular level view of how the HIV-fusion peptide and the HAfp modulates lipid organization and mixing, solid state ^{2}H NMR spectra of saturated lipid mixtures containing HFP and HAfp at different temperatures were obtained and analyzed. Figure 5.21 shows the stack plots of ^{2}H NMR data obtained for DMPC-d54 lipid at different temperatures. In absence of any peptide the phase transition temperature of DMPC-d54 is ~ 23°C and is evident from the figure 5.21, where the ^{2}H spectra changes its shape from 20°C - 25°C. Below the transition temperature the lipid is in gel phase and due to the less motion of C-^{2}H bond, the ^{2}H spectra is broad and is not well-resolved. Above the transition temperature, the lipid is in fluid phase. As a result, there is an increased motion of the C-^{2}H bond giving rise to the well-resolved ^{2}H spectra. For this reason the ^{2}H spectra at 20°C is broader and not well resolved as compared to higher temperatures. Figure 5.22 shows the effect of addition of 4 mole % HIV fusion peptide (HFP) in DMPC-d54 at different temperatures. By comparing the ^{2}H spectra at 20°C of DMPC-d54 with and without HFP (Figures 5.21 and 5.22), we can see that the shape of the ^{2}H spectra changes in presence of HFP at 20°C. This observation suggests that HFP lowers the phase transition temperature of the DMPC-d54. Figure 5.23 and 5.24 shows the effect of the addition of 4 mole % HAfp at different temperatures. In Figures 5.21 and 5.23, the shapes of the ^{2}H spectra of DMPC-d54 at 20°C are very similar which suggests that HAfp has no effect on the transition temperature of DMPC-d54. However, at pH 7 the ^{2}H spectra of DMPC-d54 with and without the HAfp are not similar which suggests that the HAfp has an effect on the phase transition temperature of DMPC-d54.

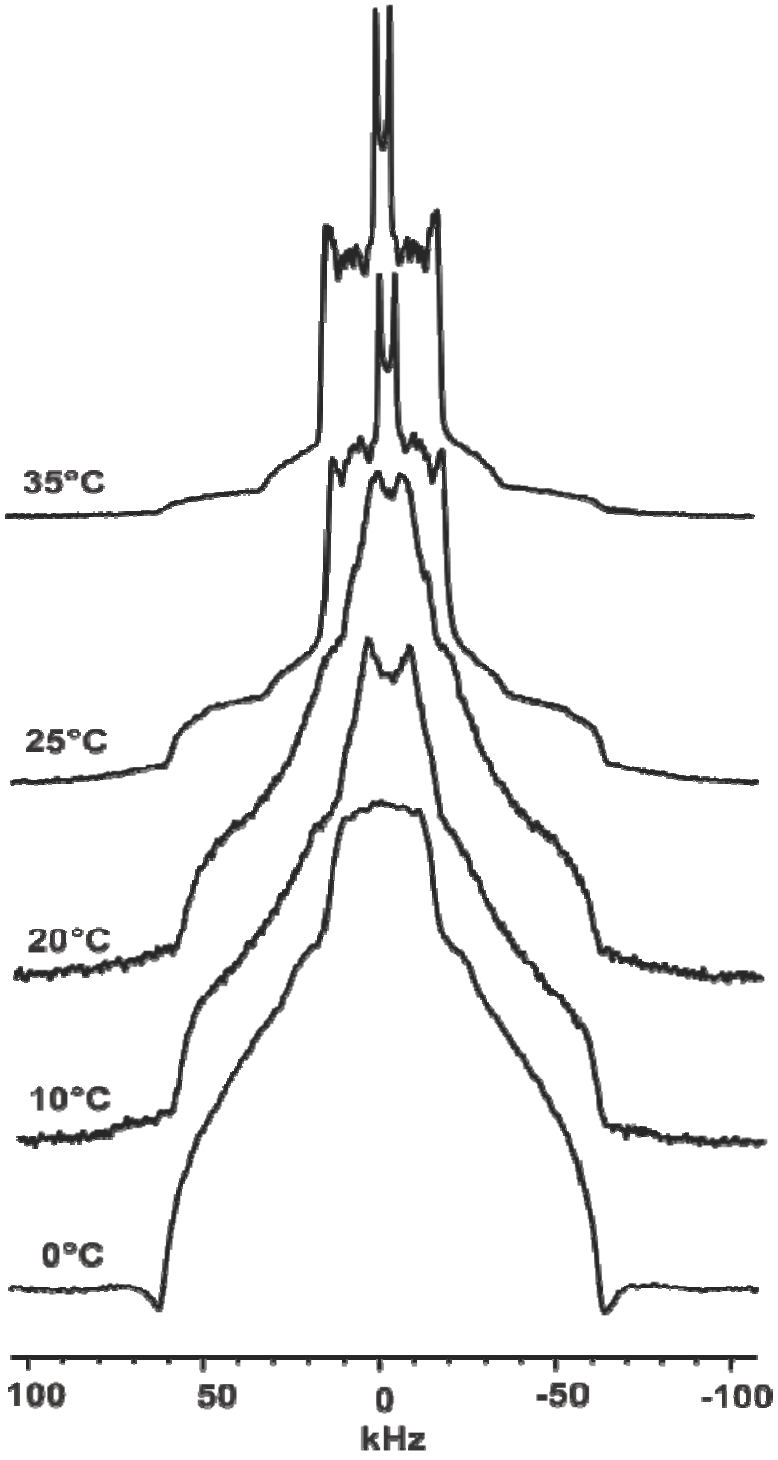

Figure 5.21. ^{2}H NMR spectra of DMPC-d54 taken at different temperatures.

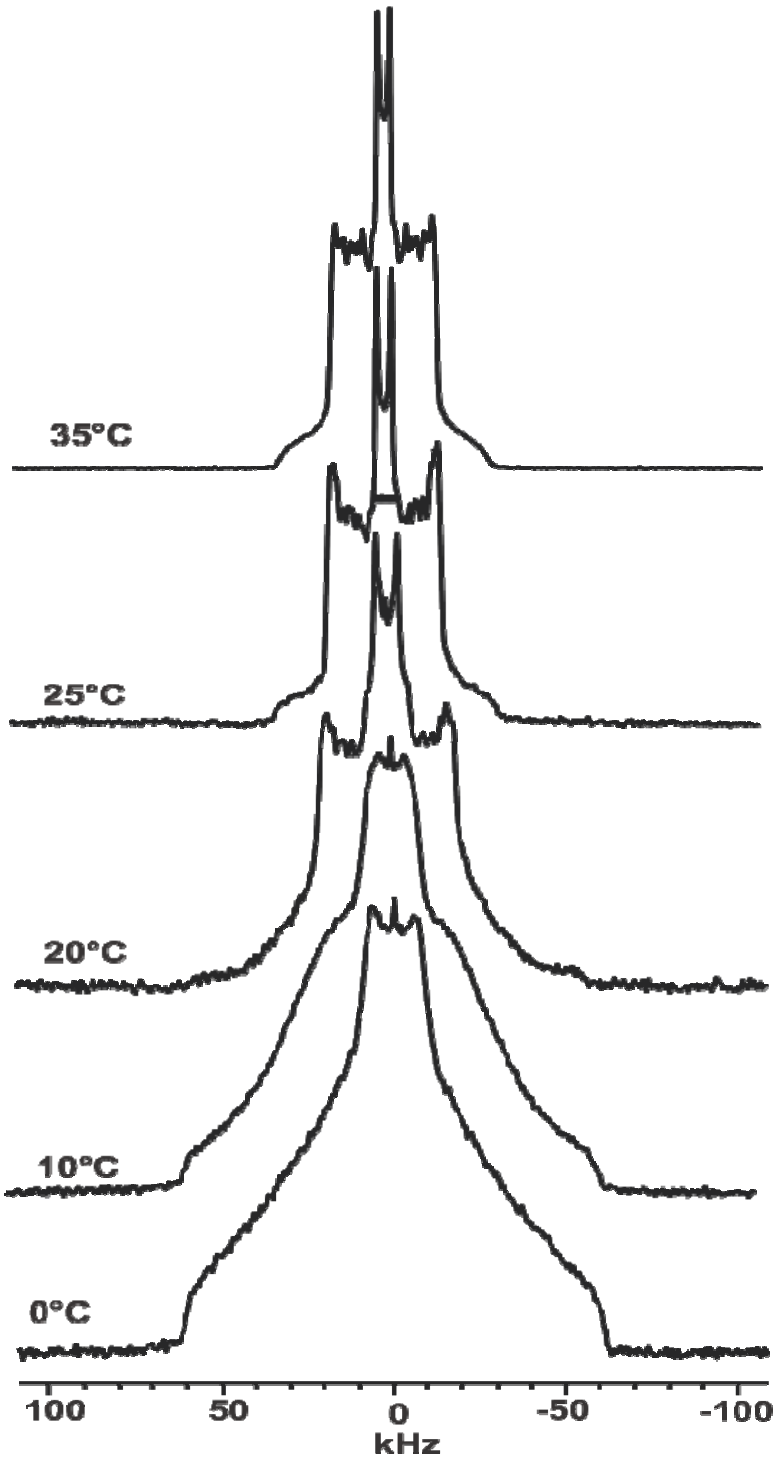

Figure 5.22. ^{2}H NMR spectra as a function of temperature of DMPC-d54 with HFP.

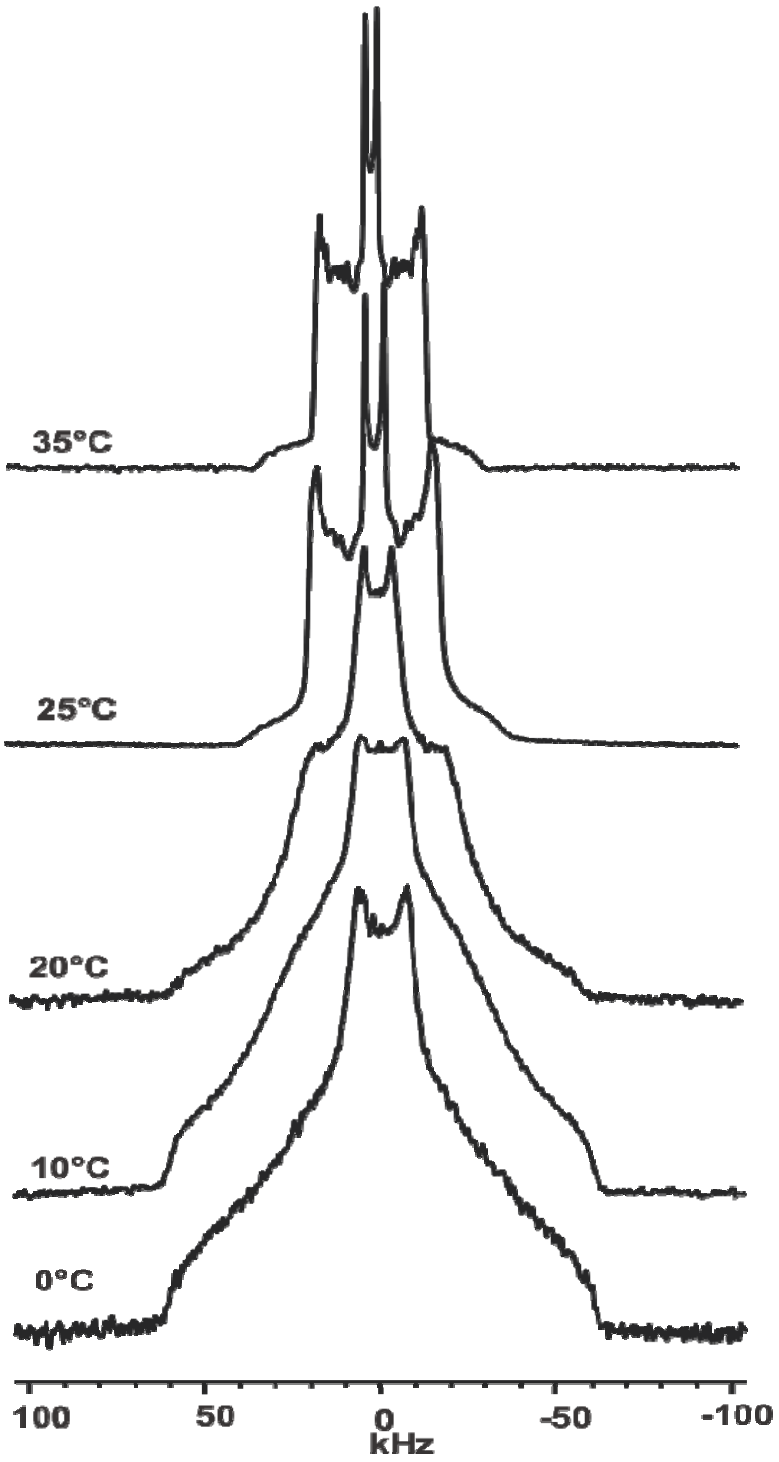

Figure 5.23. ^{2}H NMR spectra of DMPC-d54 with HAfp at pH 5 taken at different temperatures.

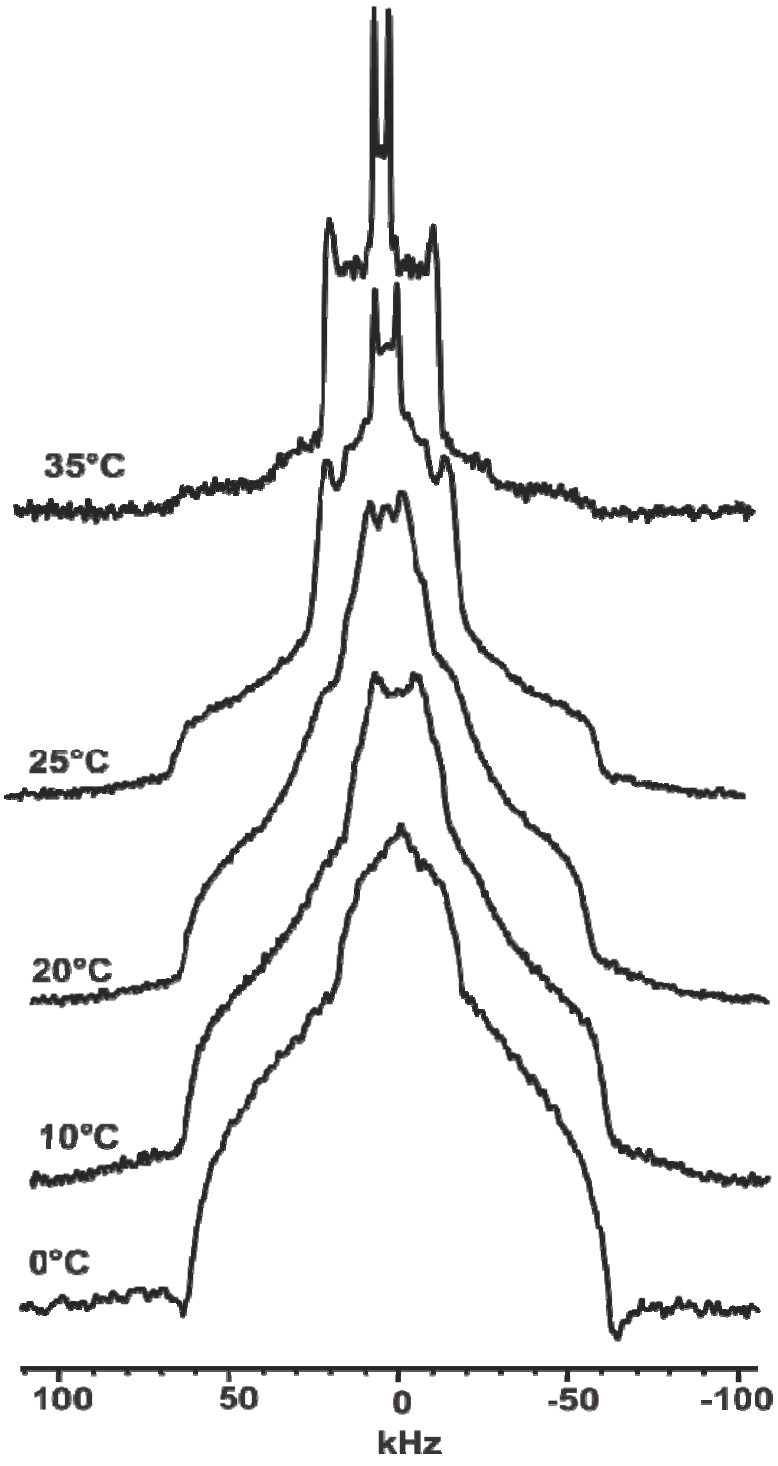

Figure 5.24. ^{2}H NMR spectra of DMPC-d54 with HAfp at pH 7 taken at different temperatures.

5.8.2.2 Segmental order parameters

The spectra of DMPC-d54 in the fluid phase consisted of superimposed powder doublets with the maximum quadrupole anisotropy not exceeding 31.8 kHz at 35°C. After addition of 4 mole % HFP, the quadrupolar anisotropy was reduced to ~27.7 kHz at 35°C. This reduction of quadrupolar splitting in presence of HFP indicates that the peptide causes disordering of the acyl chain. Similarly in case of HAfp, the quadrupolar splitting of DMPC-d54 lipid reduces to ~30.1 kHz at pH 5 at 35°C indicating the disorder of the acyl chain. In contrast at pH 7, the quadrupolar splitting of DMPC-d54 increases to ~ 34 kHz which indicates an increase in the order of the acyl chain. The increase in the order of the lipid acyl chain at pH 7 could reflect in the lower fusion activity of HAfp at pH 7.

As mentioned earlier that the ^{2}H spectrum obtained for a perdeuterated lipid molecule is complex because it contains contributions of all the deuterons along the acyl chain. Therefore it is difficult to assign specific frequencies to each peak in the ^{2}H lineshape without deconvoluting the spectra. The process of deconvoluting is called de-Paking and it transforms the complicated broad lineshapes to individual frequencies to make the assignment easier. de-Paking generates a oriented spectrum from an un-oriented spectrum. Figure 5.25 shows the ^{2}H powder spectrum of the DMPC-d54 lipid with and without peptide. Figure 5.26 shows the de-Paked spectrum of the lipid and lipid/peptide mixtures.

By analyzing the ^{2}H NMR spectra of the lipids above their phase transition temperature, one can monitor the effect of the peptide on the dynamics of the lipid acyl chain. From this effect, we can infer the partitioning depth of the peptide into lipid bilayers. For this reason the order parameters were determined. Figure 5.27 illustrate the effect of HFP and HAfp on the order parameters of

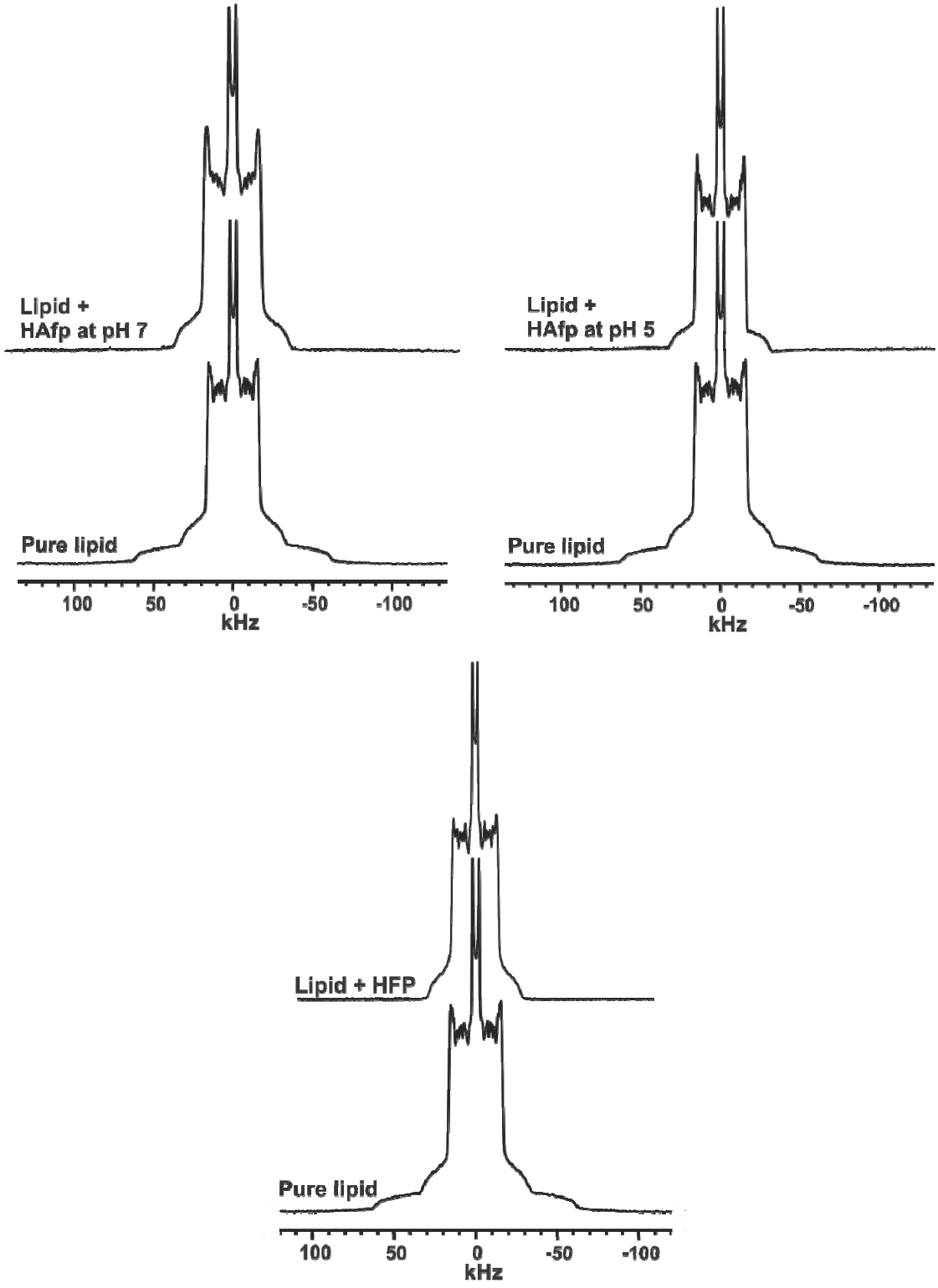

Figure 5.25. ^{2}H NMR spectra of DMPC-d54 with and without peptide at 35°C.

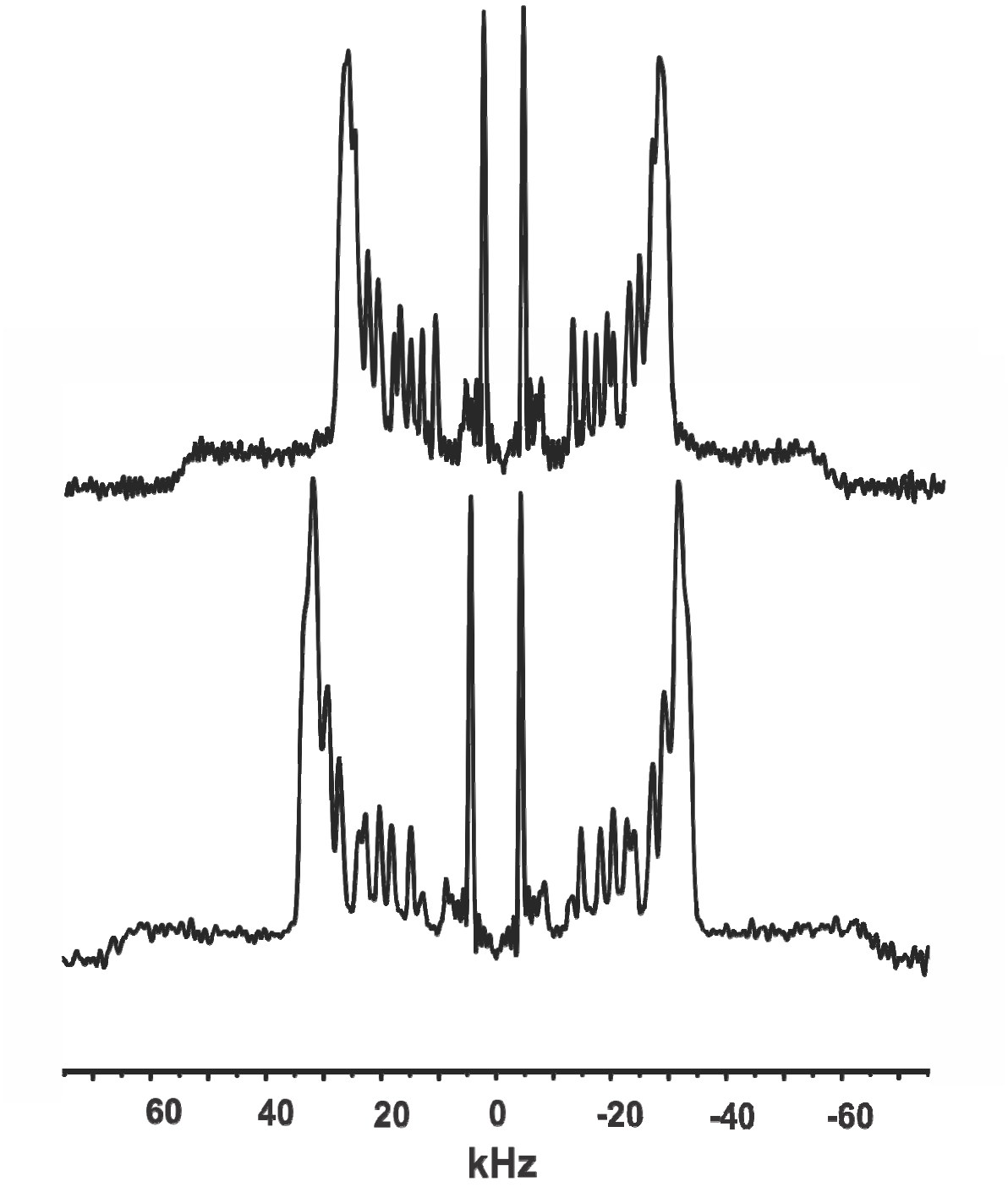

Figure 5.26a. de-Paked spectra of DMPC-d54 (bottom) and DMPC-d54 containing HAfp (top) at pH 5. The $\Delta\nu_Q$ in case of the lipid containing HAfp is smaller than the neat lipid.

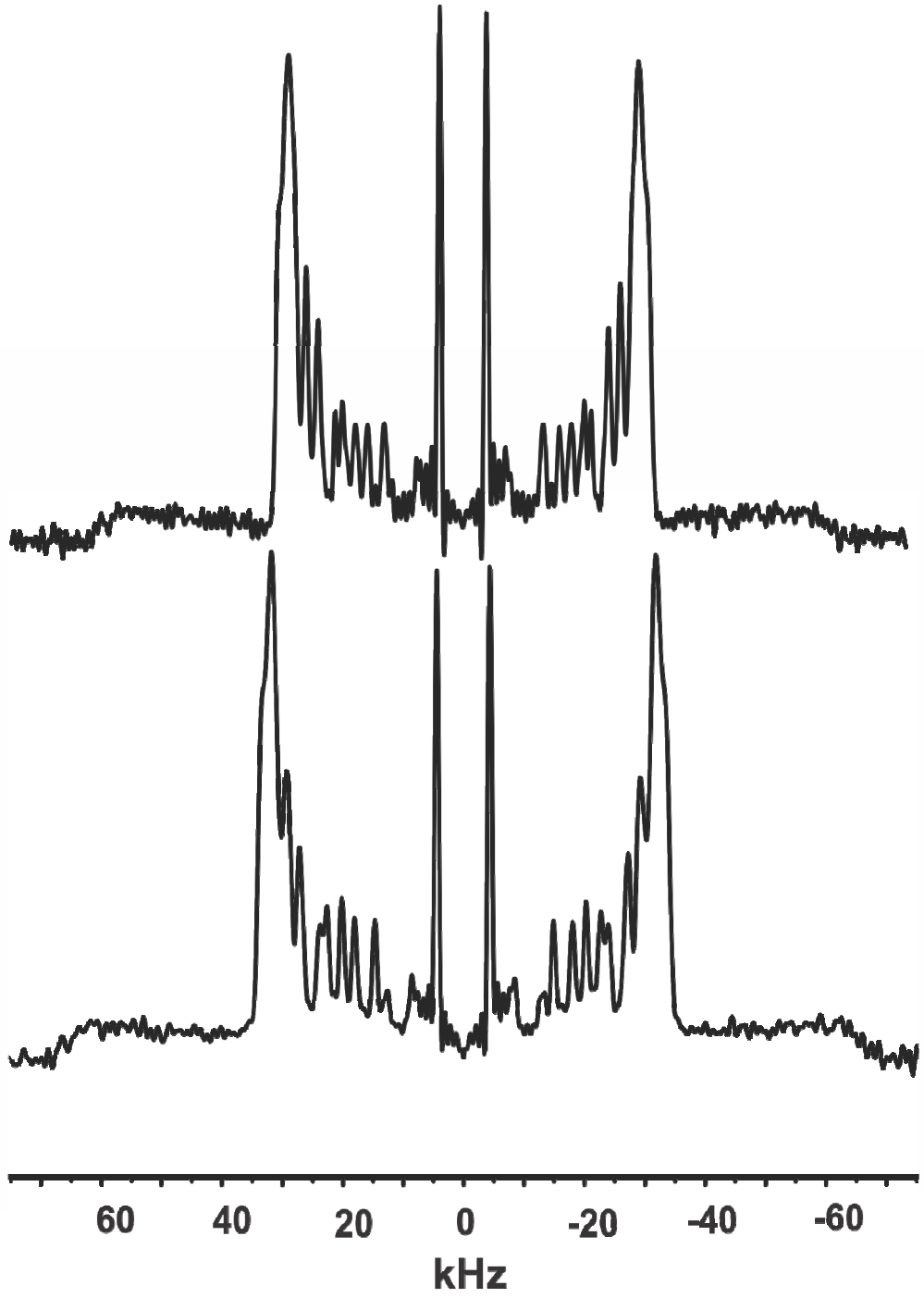

Figure 5.26b. de-Paked spectra of DMPC-d54 (bottom) and DMPC-d54 containing HAfp (top) at pH 7. The $\Delta\nu_Q$ in case of the lipid containing HAfp is larger than the neat lipid.

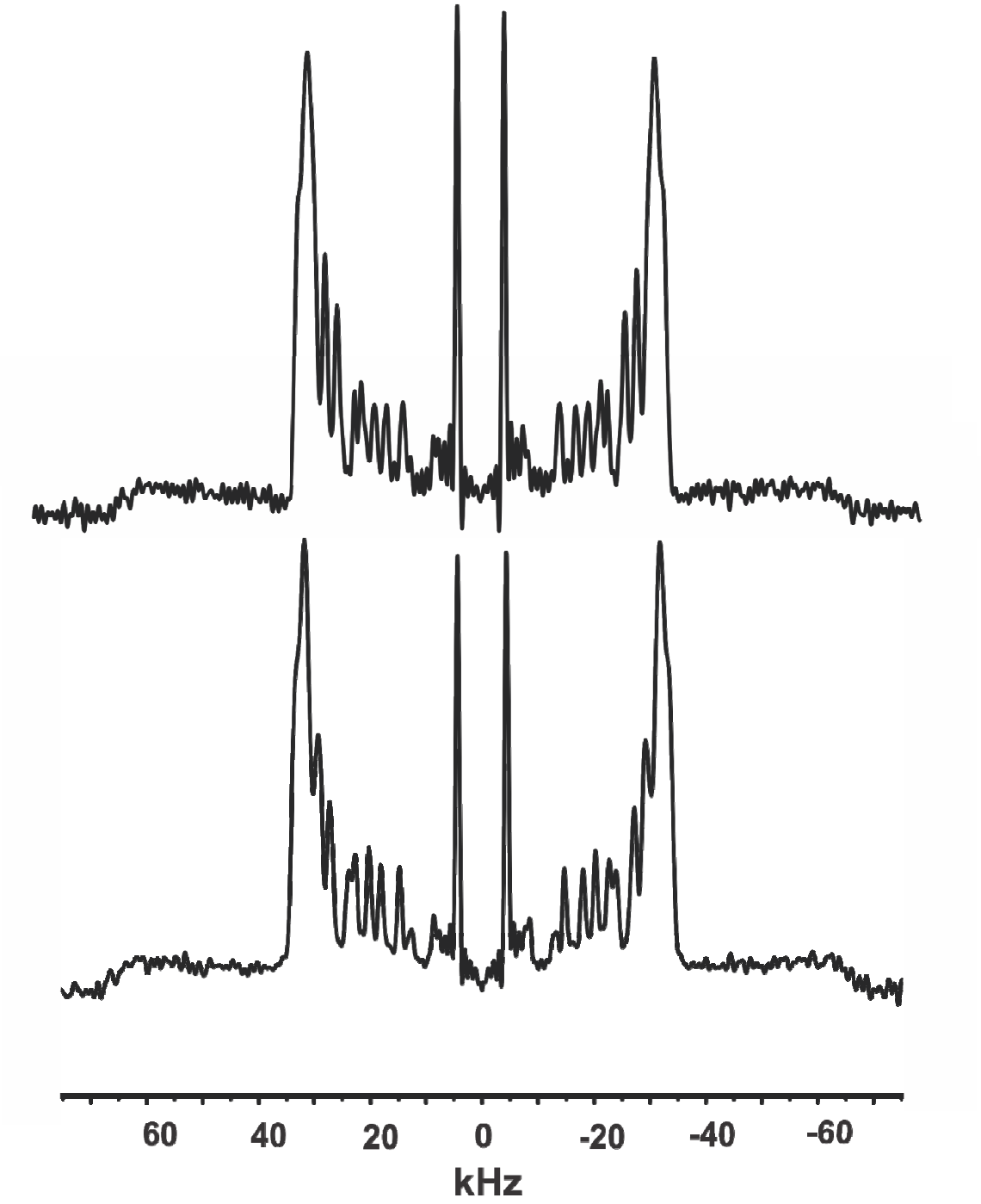

Figure 5.26c. de-Paked spectra of DMPC-d54 (bottom) and DMPC-d54 containing HFP (top) at pH 7. The $\Delta\nu_Q$ in case of the lipid containing HFP is smaller than the neat lipid.

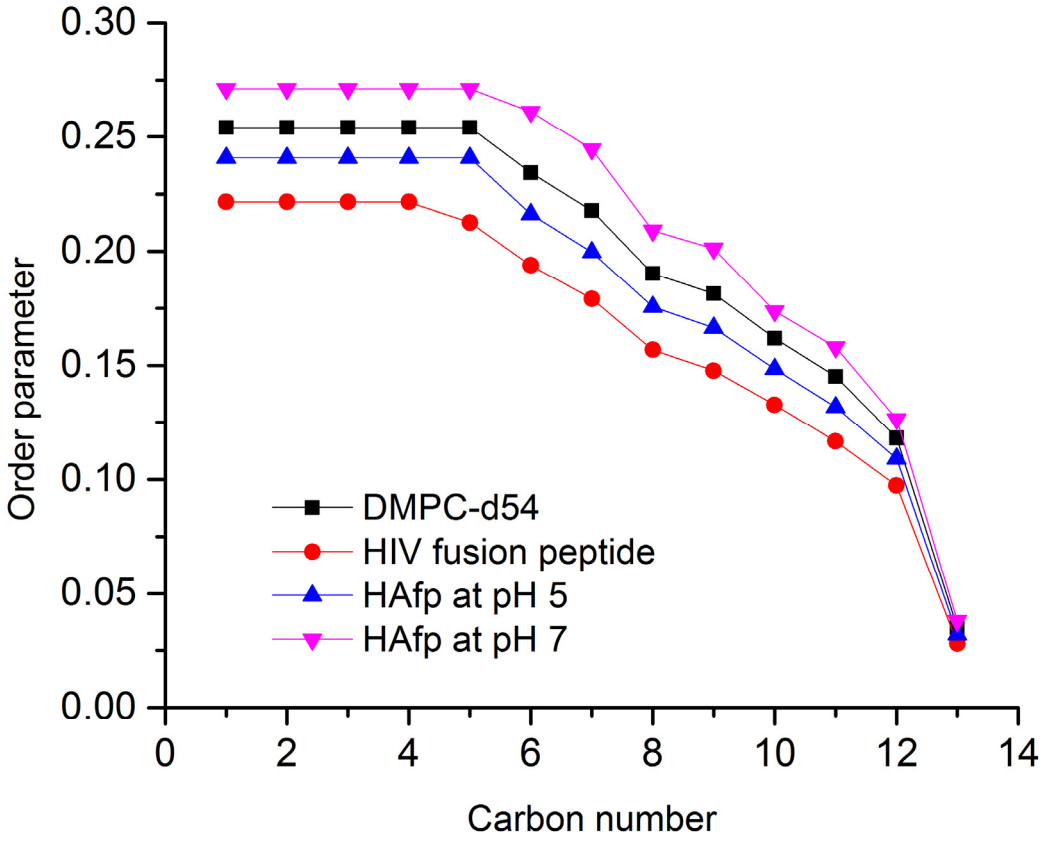

Figure 5.27. Effect of HFP and HAfp on the order parameters profile of DMPC-d54 at 35°C. HFP and HAfp at pH 5 decreases the order parameters along the acyl chain of the lipid compared to the pure DMPC-d54 lipid. In contrast, HAfp at pH 7 increases the order parameters compared to pure lipid.

DMPC-d54 at 35°C. From the order parameters it can be seen that the methylenes towards the center of the bilayer are more affected than those at the plateau region.

5.8.2.3 Transverse relaxation studies

The transverse relaxation or spin-spin relaxation (T_2 relaxation) was investigated by quecho experiment at 10°C, 20°C, 25°C, 30°C and 35°C under static conditions. For relaxation studies τ and τ_1 were arrayed using fixed delay increments. Figures 5.29 – 5.31 show the representative stack plots of ^2H spectra for all the samples at different temperatures. In the figures we can see that the T_2 relaxation follows exponential decay.

Data fitting

The relaxation data was fitted in two different ways:

1. Integrated area of the whole spectrum: above the phase transition temperature, for all the samples, the ^2H spectra have two horns around ± ~ 30 kHz (Figures 5.21 – 5.24). The integrated intensity was calculated by integrating the whole ^2H spectrum over a ~10 kHz integration range. When the T_2s are obtained in this way, we get an average T_2 value. This is because the full ^2H spectrum has contributions from the $–CD_2$ deuterons as well as the $–CD_3$ deuterons. Therefore the integrated intensity represents the average T_2's for all the deuterons present in the acyl chain of the lipid. Below the phase transition temperature, the ^2H spectra were integrated in the similar way with a ± ~ 10 kHz integrating range.
2. Fitting $–CD_2$ intensity: Since all the samples above the phase transition temperature showed well resolved $–CD_2$ horns, this fitting method was applied to the ^2H relaxation data only at temperatures 25°C, 30°C and 35°C (see Figure 5.28) [11].

Since the integrated ^2H intensity and the $–CD_2$ intensity was exponential, a single exponential function was used to fit all the ^2H data. The data were fitted with:

$$I(2\tau)=I(0)\times\exp(-2\tau/T_2) \qquad 5.8$$

Where I(2τ) is the measured echo intensity,

2τ is the total echo time and is given by $2\tau = \tau + \tau_1$ + (data shift × dwell time), and I(0) and T_2 are the fitting parameters. The outer component in the Figure 5.28 represents the $–CD_2$ deuterons and the intensity of the CD_2 deuterons were fitted as a function of 2τ. [11]

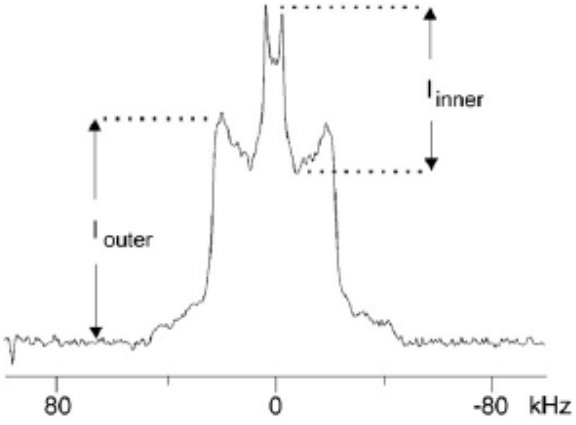

Figure 5.28. ^{2}H-NMR spectrum of LM3-DMPC dac sample. Measurement of the outer feature or the $–CD_2$ intensity. The outer component is measured between the outer $–CD_2$ peaks of the Pake doublet and the spectrum baseline.

Figures 5.29 - 5.31 displays an array of ^{2}H NMR spectra with varied τ and τ_1 for four different samples. Figures 5.32 - 5.35 displays some representative best fit plots of the $–CD_2$ or the outer feature for the four samples. Table 5.2 displays the best-fit T_2 values for all four samples obtained by using the two different fitting methods as described above.

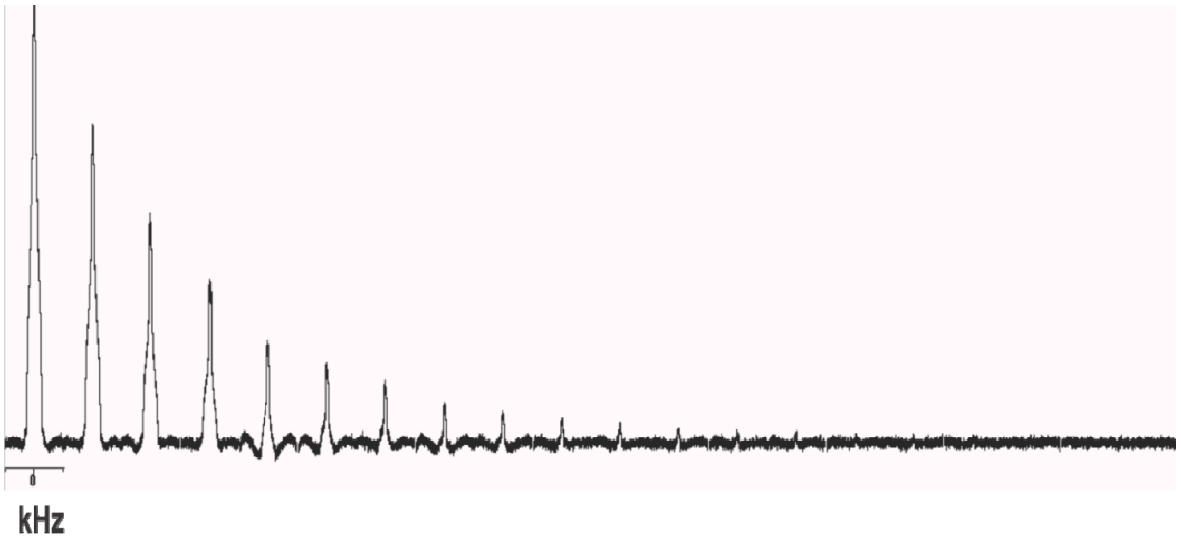

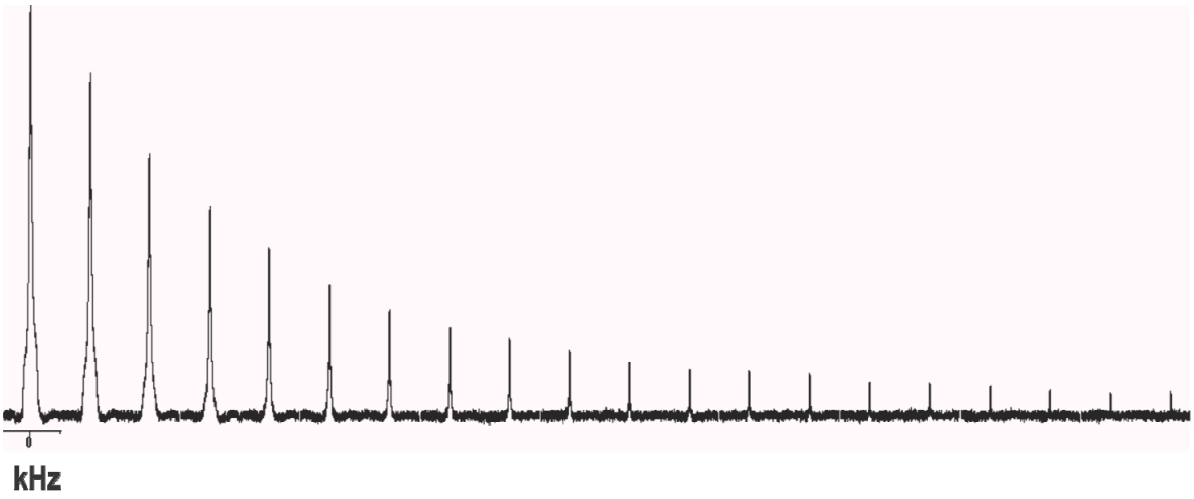

Figure 5.29. Representative stacked plots DMPC-d54 at 10°C (top) and 25°C (bottom). The ^{2}H spectra were obtained by varying τ and τ_1. For each τ and τ_1, the number of scans was 500. All spectra were processed with 500 Hz line broadening, data shift = -11, and baseline correction of the order 5.

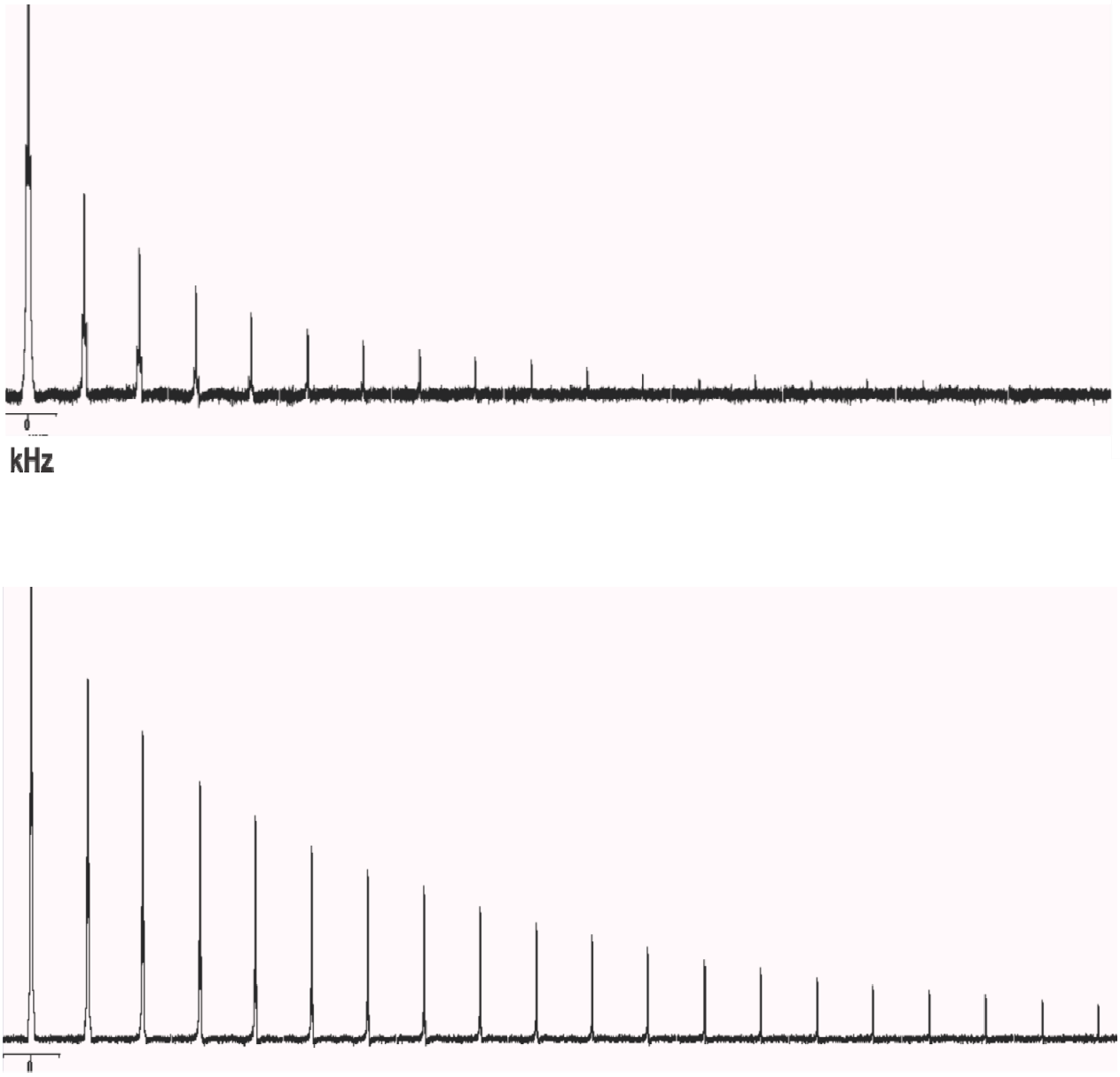

Figure 5.30. Representative stacked plots of HFP in DMPC-d54 in the ratio 1:25 at 20°C (top) and 35°C (bottom). The ^{2}H stacked plots were obtained by varying τ and τ_1. For each τ and τ_1, the number of scans was 200. All spectra were processed with 500 Hz line broadening, data shift = -11, and baseline correction of the order 3.

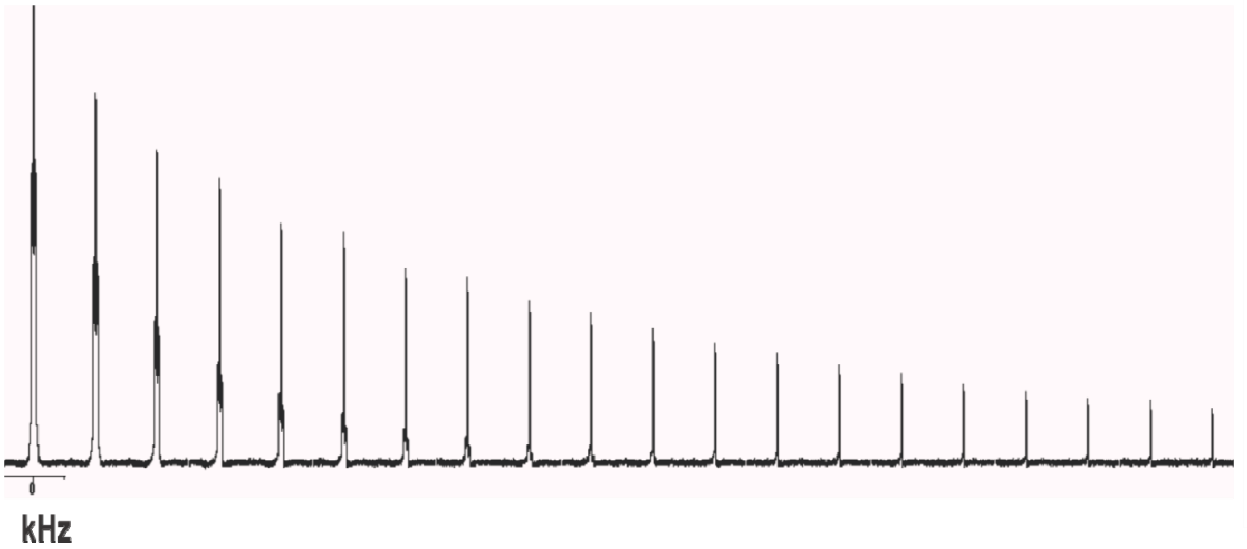

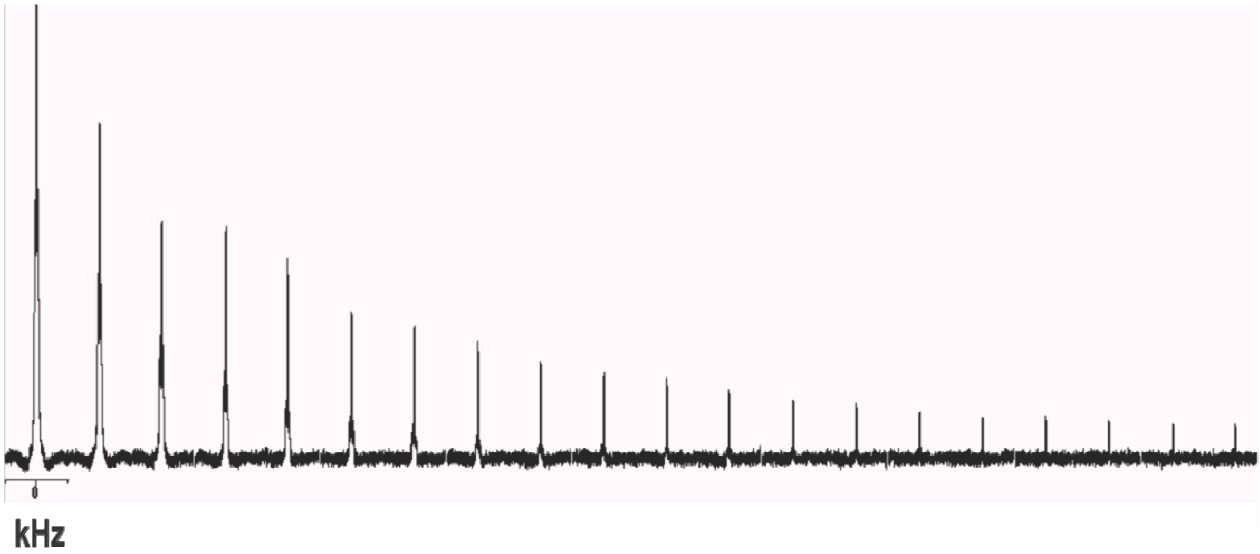

Figure 5.31. Representative stacked plots of HAfp in DMPC-d54 in the ratio 1:25 at 25°C (top, pH 5) and 35°C (bottom, pH 7). The ^{2}H spectra were obtained by varying τ and τ_1. For each τ and τ_1, the number of scans was 1000 (top) and 400 (bottom). All spectra were processed with 500 Hz line broadening, data shift = -11, and baseline correction of the order 3.

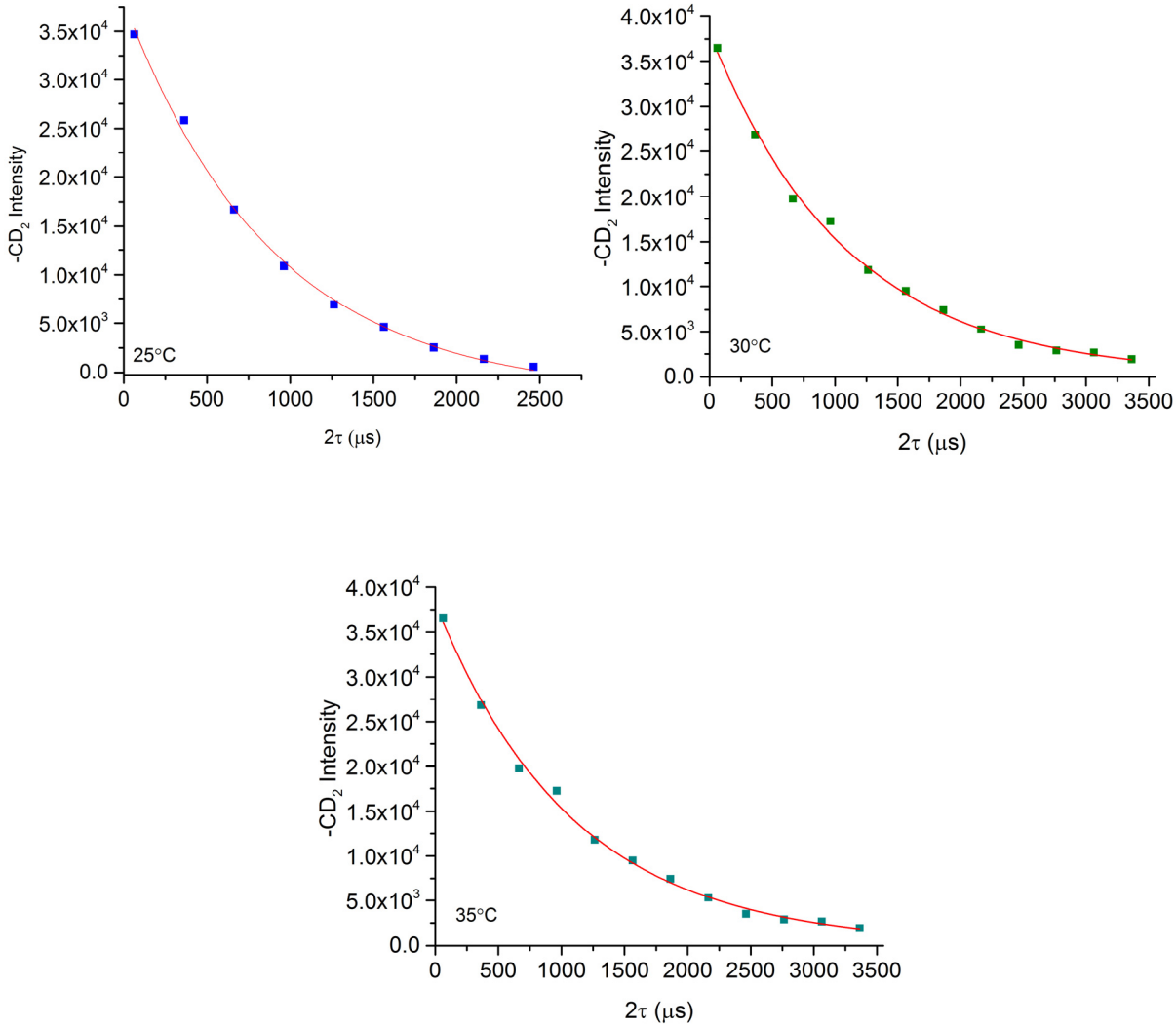

Figure 5.32. Quecho experimental (colored squares) and best fit (red lines) plots of -CD_2 intensity vs 2τ under static conditions for DMPC-d54 lipid at different temperatures. The fitting equation is $I(2\tau)=I(0)\times\exp(-2\tau/T_2)$.

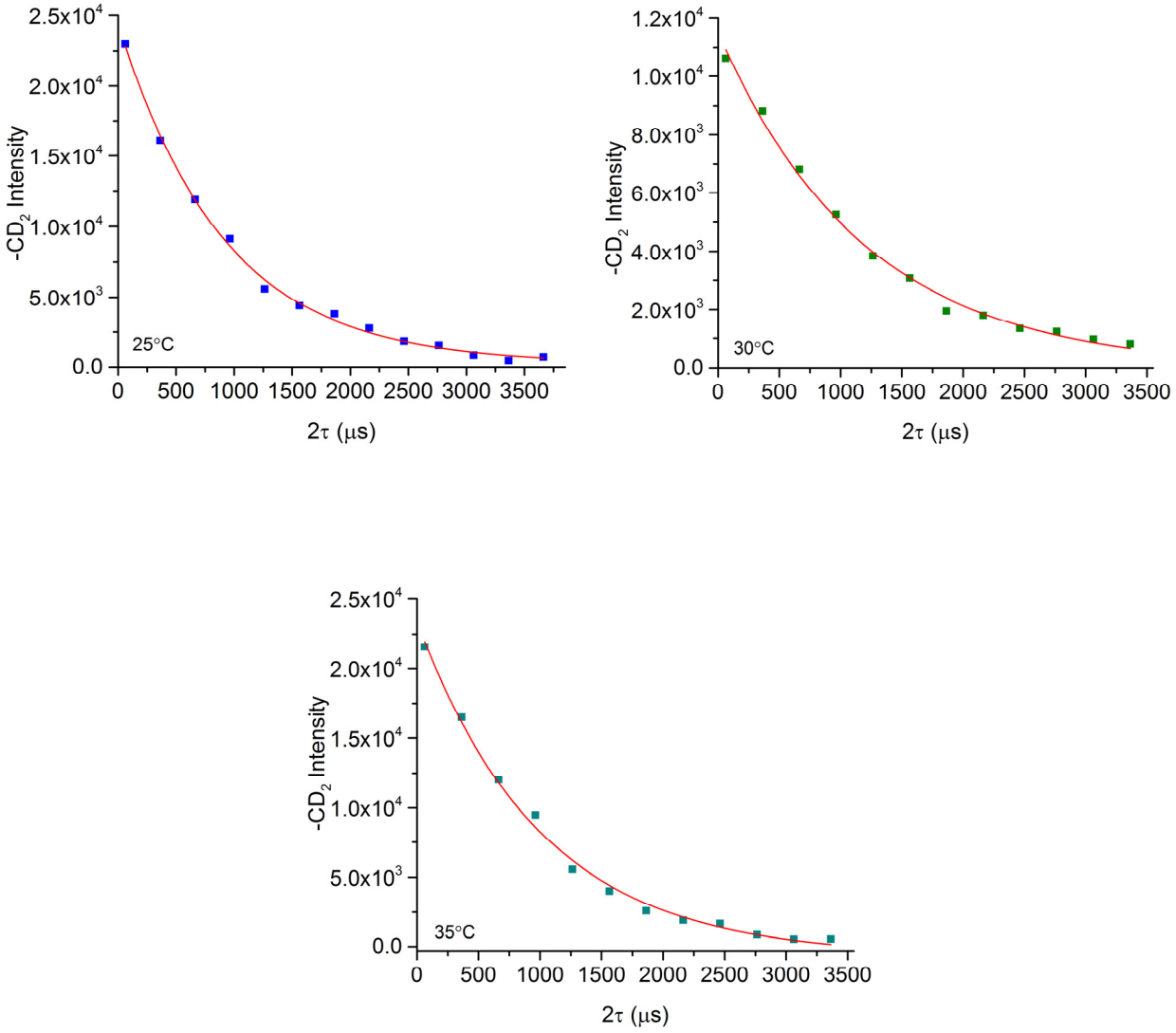

Figure 5.33. Quecho experimental (colored squares) and best fit (red lines) plots of -CD_2 intensity vs 2τ under static conditions for HFP in DMPC-d54 in the ratio 1:25 at different temperatures. The fitting equation is $I(2\tau)=I(0)\times\exp(-2\tau/T_2)$.

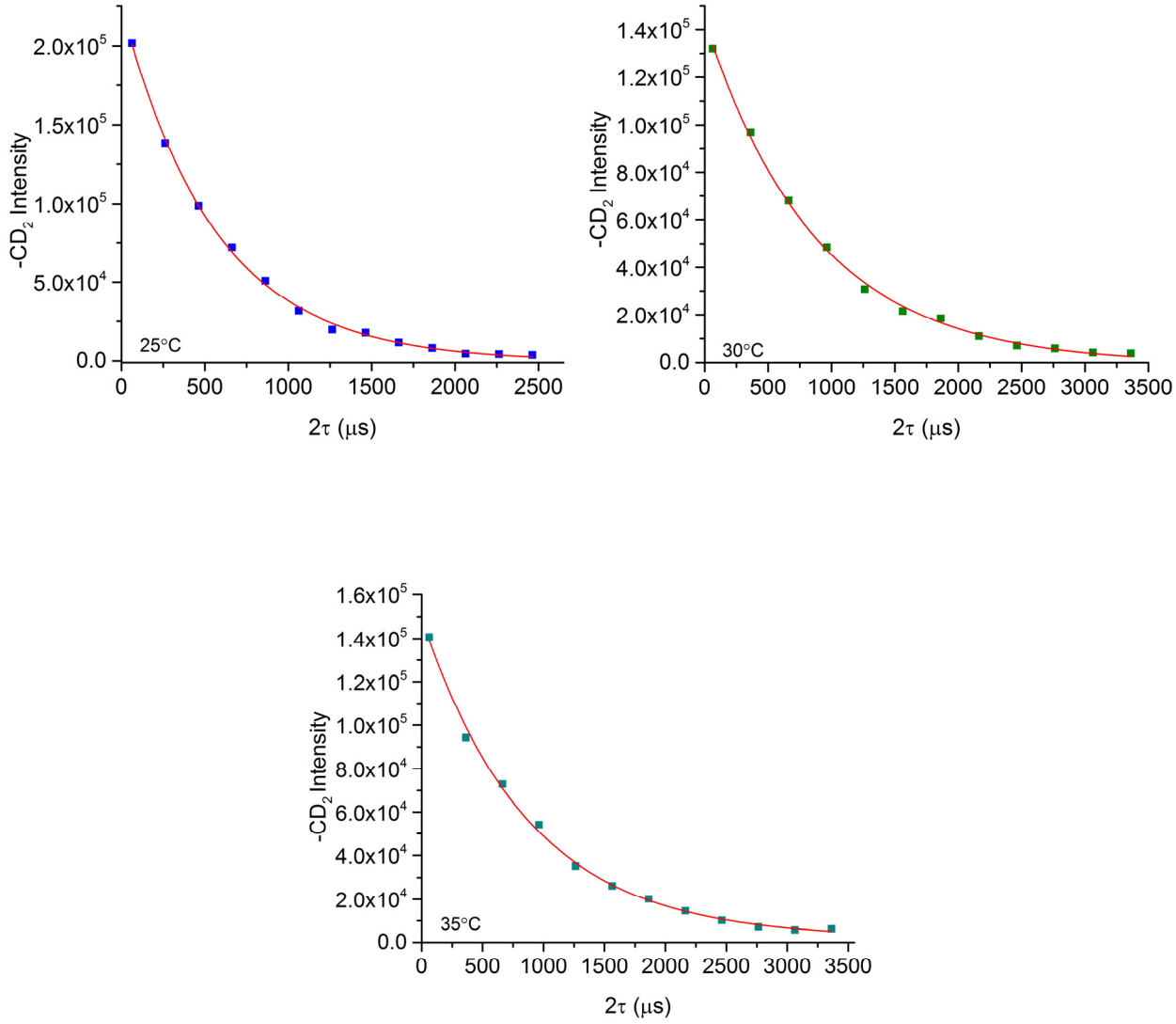

Figure 5.34. Quecho experimental (colored squares) and best fit (red lines) plots of -CD_2 intensity vs 2τ under static conditions for HAfp in DMPC-d54 in the ratio 1:25 at different temperatures. The fitting equation is $I(2\tau)=I(0)\times\exp(-2\tau/T_2)$. The pH of the NMR sample was 5.

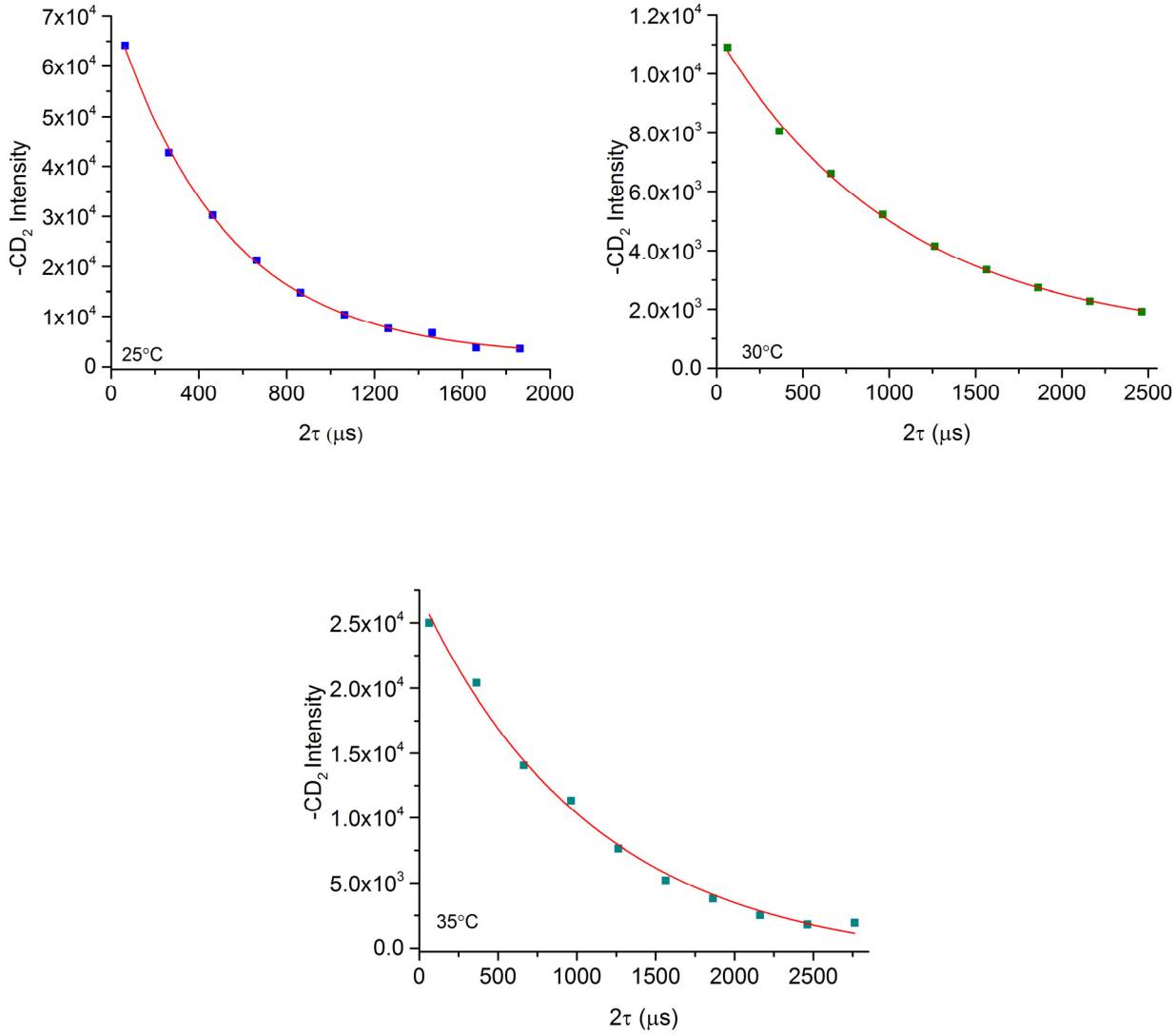

Figure 5.35. Quecho experimental (colored squares) and best fit (red lines) plots of -CD_2 intensity vs 2τ under static conditions for HAfp in DMPC-d54 in the ratio 1:25 at different temperatures. The fitting equation is $I(2\tau)=I(0)\times\exp(-2\tau/T_2)$. The pH of the NMR sample was 7.

Table 5.2. Best-fit ^2H T_2 (μs) measured using quecho experiment. The uncertainties are in parenthesis and is given by standard error. The T_2 values obtained by fitting the $–CD_2$ intensity are listed in the column intensity.

Temperature (°C)	DMPC-d54	HFP/D54	HAfp/D54 pH 5	HAfp/D54, pH 7
25	885(56)	750(37)	563(14)	627(8)
30	996(72)	950(11)	876(30)	1062(36)
35	1090(63)	942(10)	875(38)	1109(108)

5.8.3 Cpquecho experimental results

Like the quecho experiment, cpquecho experiment was also run at different temperatures. However, the ^{2}H cpquecho spectrum does not show the similar features like the quecho spectrum. Figures 5.36 - 5.39 represents some ^{2}H cpquecho spectra for all the samples at two different temperatures.

5.8.3.1 DMPC-d54 cpquecho spectra

The ^{2}H cpquecho spectrum DMPC-d54 has two horns. The magnetization transfer in the cross polarization experiment relies on the internuclear distance between the spins. The ^{1}Hs present in the glycerol headgroup are close to the carbon-2 of the lipid acyl chain. Therefore, most likely we are observing the signals from the ^{2}Hs closest to the ^{1}Hs present in the glycerol headgroup.

Figure 5.36 show representative ^{2}H cpquecho spectra of DMPC-d54. At lower temperature only two peaks were observed. But above the phase transition temperature, an additional set of peaks were also observed. The splitting of the additional peaks is ~ 40 kHz. However, the additional set of peaks was not observed in any other samples.

The ^{2}H powder patterns for all the samples with the peptides have two horns. The two horns represent the $–CD_2$ groups of the lipid acyl chain. The spectral features that were observed in the ^{2}H spectra in the quecho experiment were absent in the cpquecho experiment.

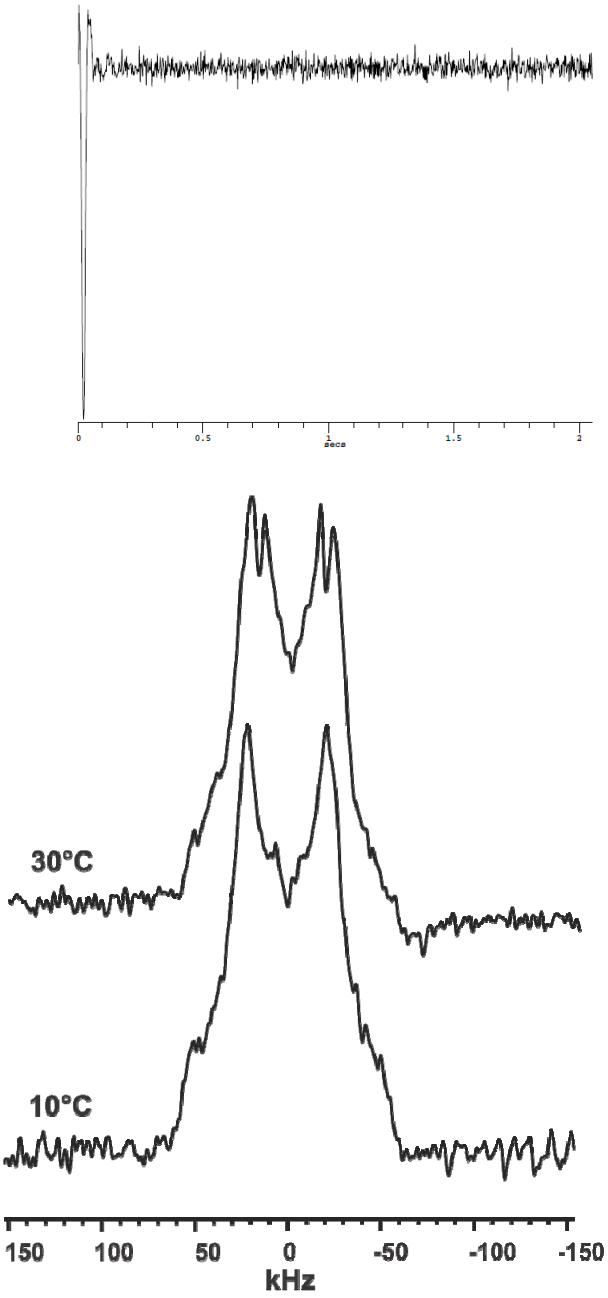

Figure 5.36. "cpquecho" experiments of DMPC-d54 at variable temperature under static conditions for 3000 scans. Top: ^{2}H FID for τ = 30 μs and τ_1 = 12 μs at 30°C. Bottom: ^{2}H cpquecho spectra for τ = 30 μs and τ_1 = 12 μs. Each spectrum was processed with 2000 Hz Gaussian line broadening, and -10 data shift.

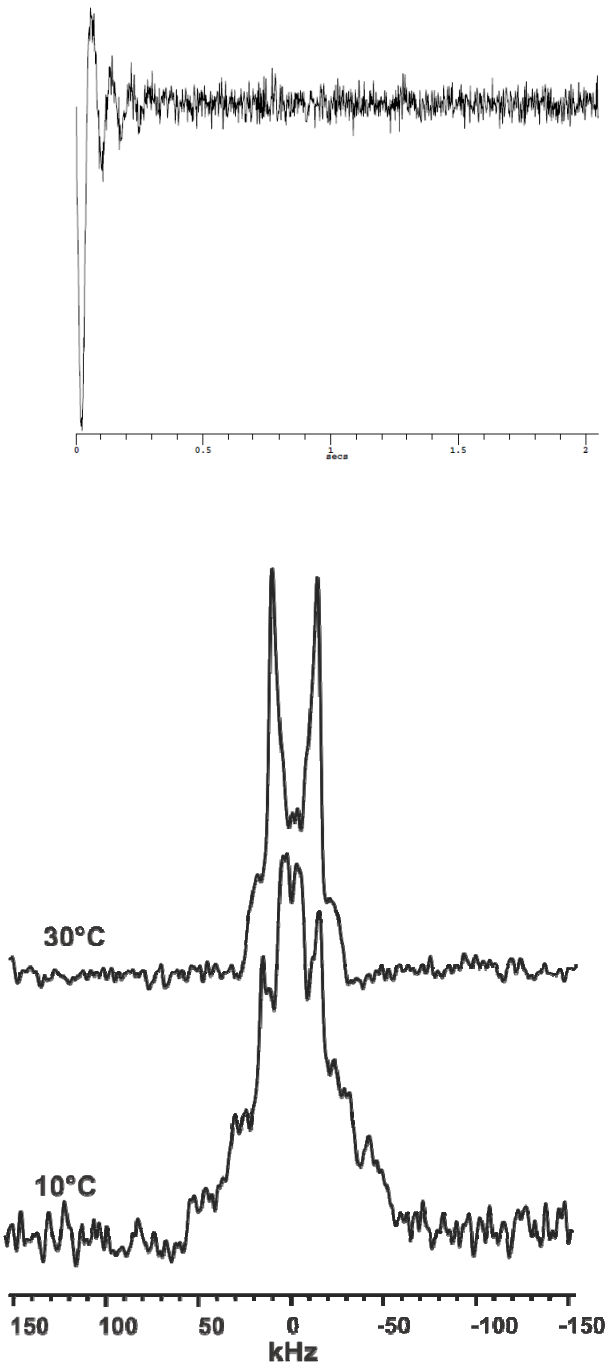

Figure 5.37. "cpquecho" experiments of HFP with DMPC-d54 (1:25 ratio) at variable temperature under static conditions. Top: ^{2}H FID for τ = 30 μs and τ_1 = 12 μs at 30°C. Bottom: ^{2}H cpquecho spectra for τ = 30 μs and τ_1 = 12 μs. Each spectra were processed with 2000 Hz Gaussian line broadening, -10 data shift. The number of scans for each spectrum was 6000.

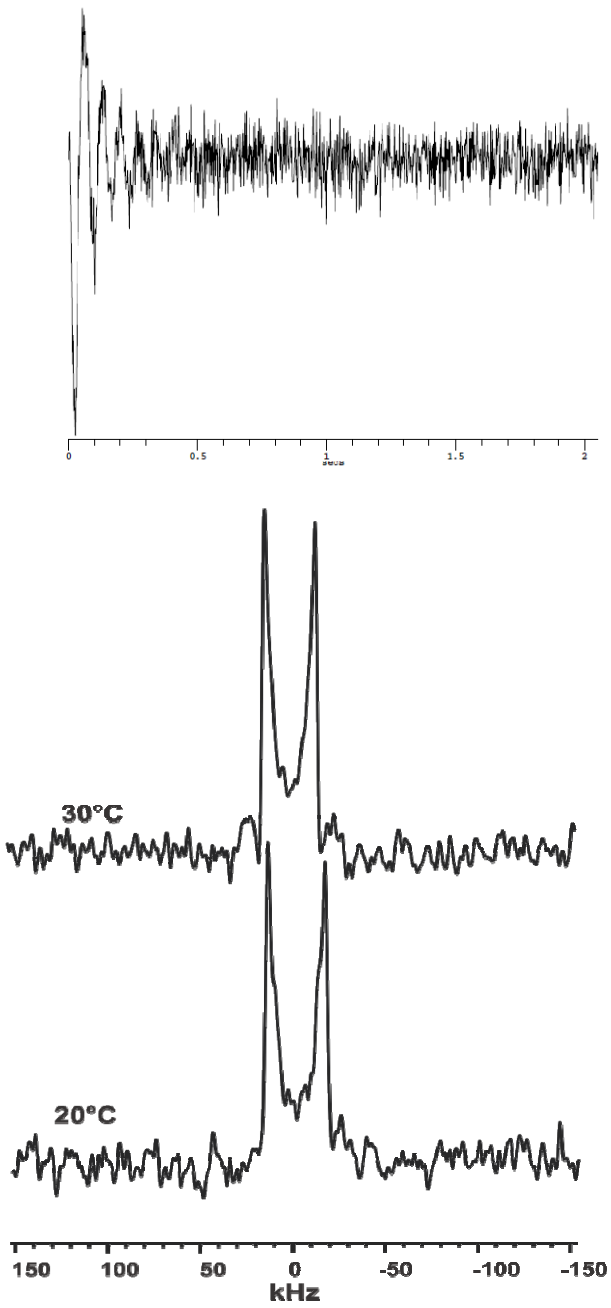

Figure 5.38. "cpquecho" experiments of HAfp with DMPC-d54 (1:25 ratio) at variable temperature under static conditions at pH 5. Top: ^{2}H FID for τ = 30 μs and τ_1 = 12 μs at 30°C. Bottom: ^{2}H cpquecho spectra for τ = 30 μs and τ_1 = 12 μs. Each spectrum was processed with 2000 Hz Gaussian line broadening, -10 data shift. The number of scans for each spectrum was 3000.

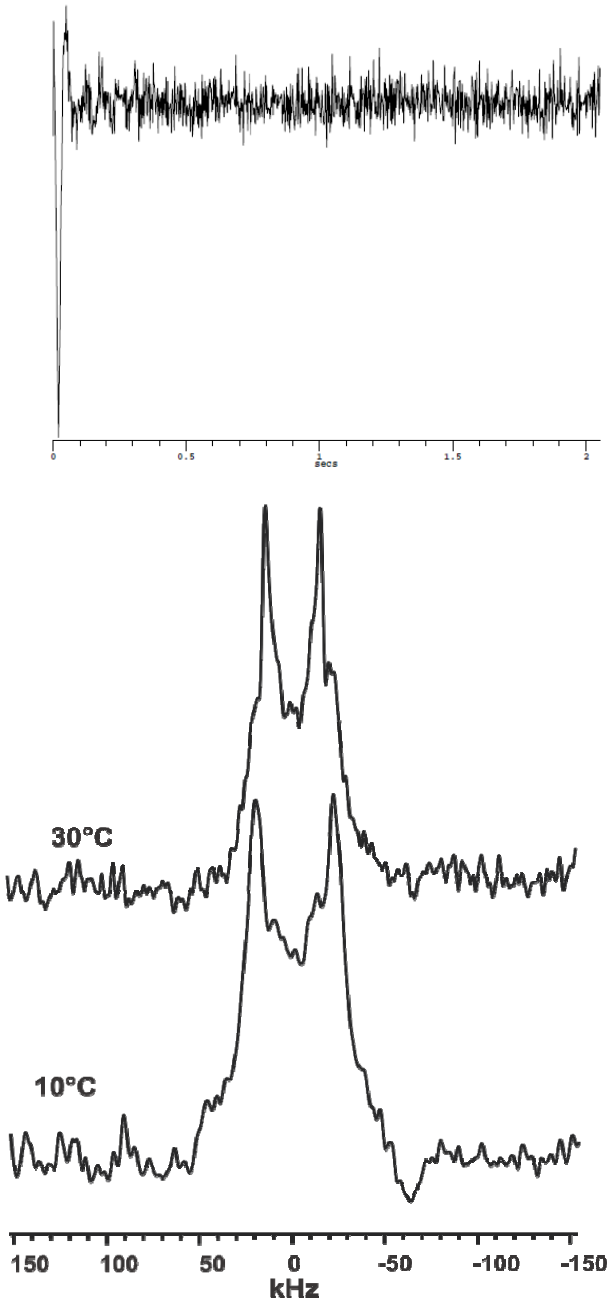

Figure 5.39. "cpquecho" experiments of HAfp with DMPC-d54 (1:25 ratio) at variable temperature under static conditions at pH 7. Top: ^{2}H FID for τ = 30 μs and τ_1 = 12 μs at 30°C. Bottom: ^{2}H cpquecho spectra for τ = 30 μs and τ_1 = 12 μs. Each spectrum was processed with 2000 Hz Gaussian line broadening, -10 data shift. The number of scans for each spectrum was 3000.

5.8.3.2 HFP/DMPC-d54 cpquecho spectra

In Figure 5.40, the $\Delta\nu_Q$ in the bottom quecho spectrum matches with the $\Delta\nu_Q$ of the top cpquecho spectrum at 10°C. Therefore we can conclude that the doublets with $\Delta\nu_Q \sim 7$ kHz arises from the $-CD_3$ groups of the lipid acyl chain. In the Figure 5.37, the small narrow central quadrupolar splitting of ~ 6.6 kHz at 30°C (top spectrum) and the large narrow central splitting ~ 7.2 kHz of the bottom spectrum is due to the CD_3 groups. The $-CD_3$ peaks are also observed at higher temperatures but the intensity of the peaks are low as shown in Figure 5.37. One possible reason for the low intensity could be due to the motion of the $-CD_3$ group about the C-D axes. Due to the increased motion, the CP transfer is not very efficient and the signal intensity is less. Since at low temperatures, the overall motion gets attenuated, the intensity of the $-CD_3$ peaks is higher as compared to the $-CD_2$ peaks and the effect is illustrated in the Figure 5.37. Additionally, the decay of the observed $-CD_3$ peaks are also very slow due to the motion which is a characteristic of the $-CD_3$ groups. In the ^2H quecho spectrum, we observed a longer T_2's for $-CD_3$ as compared to the $-CD_2$ groups. The typical measured T_2's of the HFP sample for $-CD_3$ and $-CD_2$ groups are ~ 1.9 ms and ~ 0.9 ms respectively.

5.8.3.3 HAfp/DMPC-d54 cpquecho spectra

HAfp/DMPC-d54 spectra only have two horns from the $-CD_2$ groups. The quadrupolar splitting in HAfp/DMPC-d54 sample at pH 7 is bigger than the pH 5 sample. This is consistent with our earlier observation of the quecho experiment where HAfp at pH 7 increases the order of the membrane.

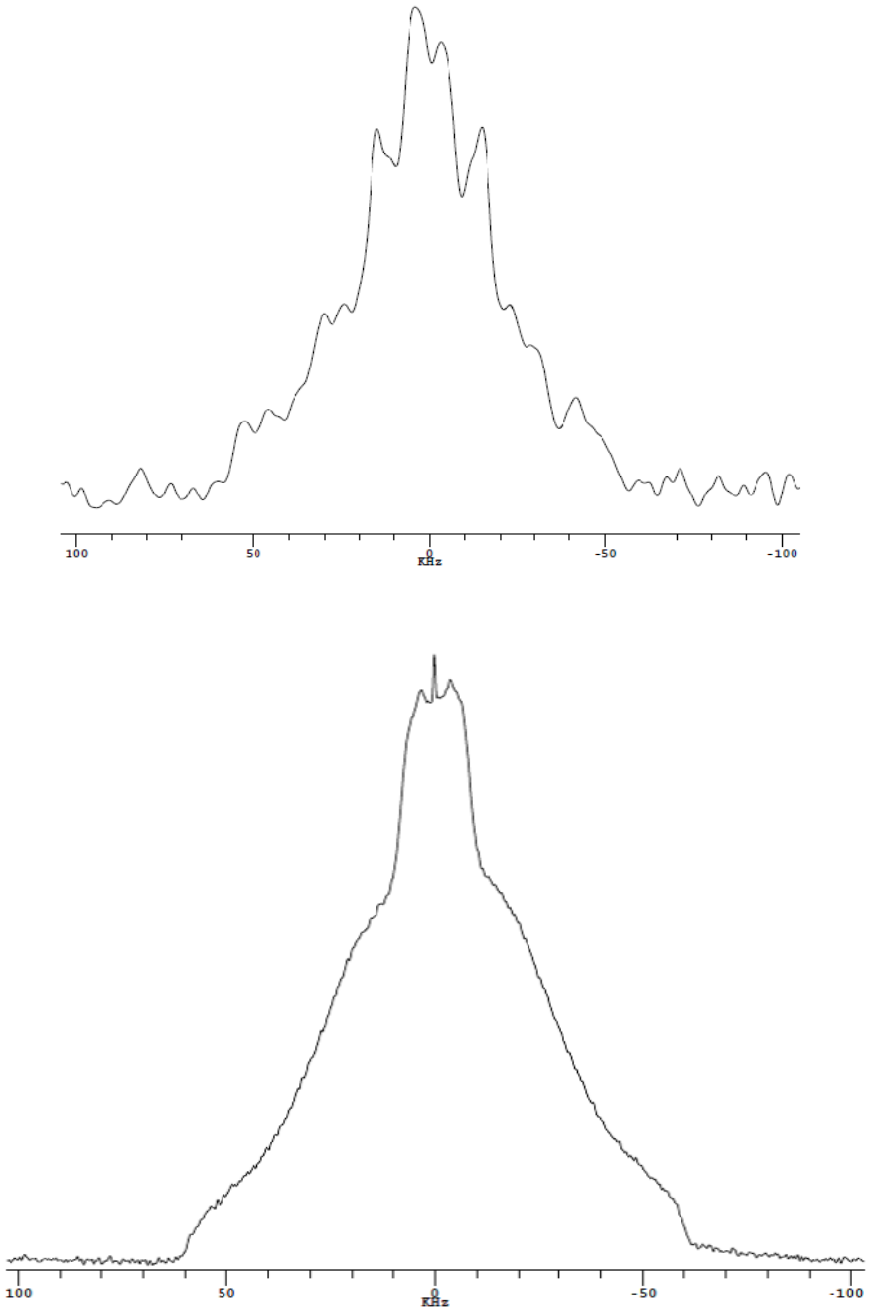

Figure 5.40. Comparison of the ^{2}H NMR spectrum of HFP/DMPC-d54 for cpquecho (top) and quecho (bottom) experiment at 10°C. Each spectrum was processed with -10 data shift and polynomial baseline correction of the order 5. The top and the bottom spectra were processed with 2000 and 500 Hz Gaussian line broadening.

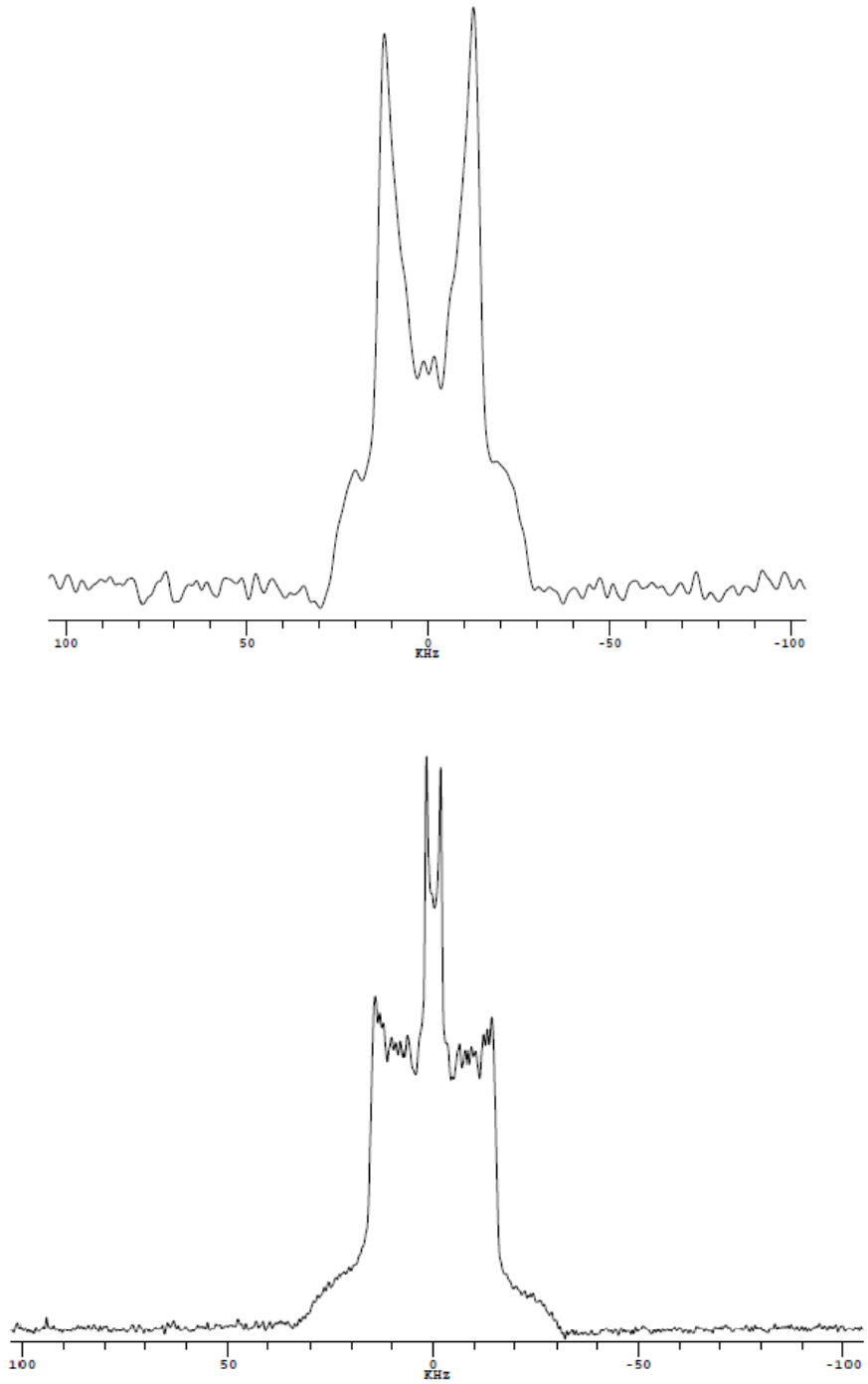

Figure 5.41. Comparison of the ^{2}H NMR spectrum of HFP/DMPC-d54 for cpquecho (top) and quecho (bottom) experiment at 30°C. The processing parameters are similar to the ones as described in figure 5.31. The 2τ for the top and bottom spectrum is 64 μs.

5.8.3.4 Quadrupolar splitting

Like the ^{2}H quecho powder pattern, the cpquecho powder pattern also gets narrower at higher temperatures. Table 5.3 lists the ^{2}H quadrupolar splitting determined from both the quecho and the cpquecho experiment at three different temperatures.

Table 5.3. ^{2}H quadrupolar splitting of DMPC-d54 with and without peptide at different temperatures. The numbers in italics represent the quadropolar splitting determined from the quecho experiment. Below the phase transition temperature, the quadrupolar splitting was not determined because of the lack of the well resolved $-CD_2$ resonances.

Temperature (°C)	DMPC-d54 (kHz)	HFP/d54 pH 7.0 (kHz)	HAfp/d54 pH 5.0 (kHz)	HAfp/d54 pH 7.0 (kHz)
10	46.4 (-)	30.7 (-)	-	43.6
20	39.4 *35.4*	- *33.9*	30.7 *35.2*	38.9 *39.6*
25	30.4 *31.8*	26.6 *30.9*	28.6 *31.6*	31.6 *34.2*
30	30.4 *30.8*	25.1 *28.3*	26.9 *30.4*	29.7 *33.1*
35	29.5 *30.4*	24.1 *26.5*	26.1 *28.8*	28.6 *30.6*

The quadrupolar splitting for each sample decreases with an increase in temperature. As the temperature increases, the motion averages out the quadrupolar anisotropy because of the dependence of $(3\cos^2\theta - 1)$ term on the quadrupolar anisotropy. After the inclusion of the HFP and HAfp at pH 5, the quadrupolar anisotropy decreases in both the cases. However, the decrease in the anisotropy is greater for HFP than HAfp at pH 5. In contrast, the quadrupolar anisotropy of DMPC-d54 gets broader after the addition of HAfp at pH 7. In case of cpquecho experiment, the quadrupolar splitting is always less than the splitting measured by quecho experiment.

5.8.3.5 Transverse relaxation studies

Transverse relaxation studies were also done using cpquecho experiment. Representative stacked ^2H spectra as a function of 2τ are shown below. In the ^2H cpquecho spectra for all the samples, two intense $-CD_2$ peaks were observed. Therefore, only the $-CD_2$ peak intensities were fitted to obtain the T_2 values. For each sample the $-CD_2$ intensity was fitted to;

$$I(2\tau) = I(0) \times \exp(-2\tau / T_2)$$

Where $I(2\tau)$ is the measured echo intensity,

2τ is the total echo time and is given by $2\tau = \tau + \tau_1 +$ (data shift × dwell time), and $I(0)$ and T_2 are the fitting parameters.

Figure 5.42 – 5.43 shows the representative ^2H NMR cpquecho stacked plots for four samples with varying τ and τ_1. Figure 5.44 – 5.47 displays the best fit plots for the $-CD_2$ fitting or the outer feature for the four samples at three different temperatures. Best-fit T_2 values are presented in Table 5.4.

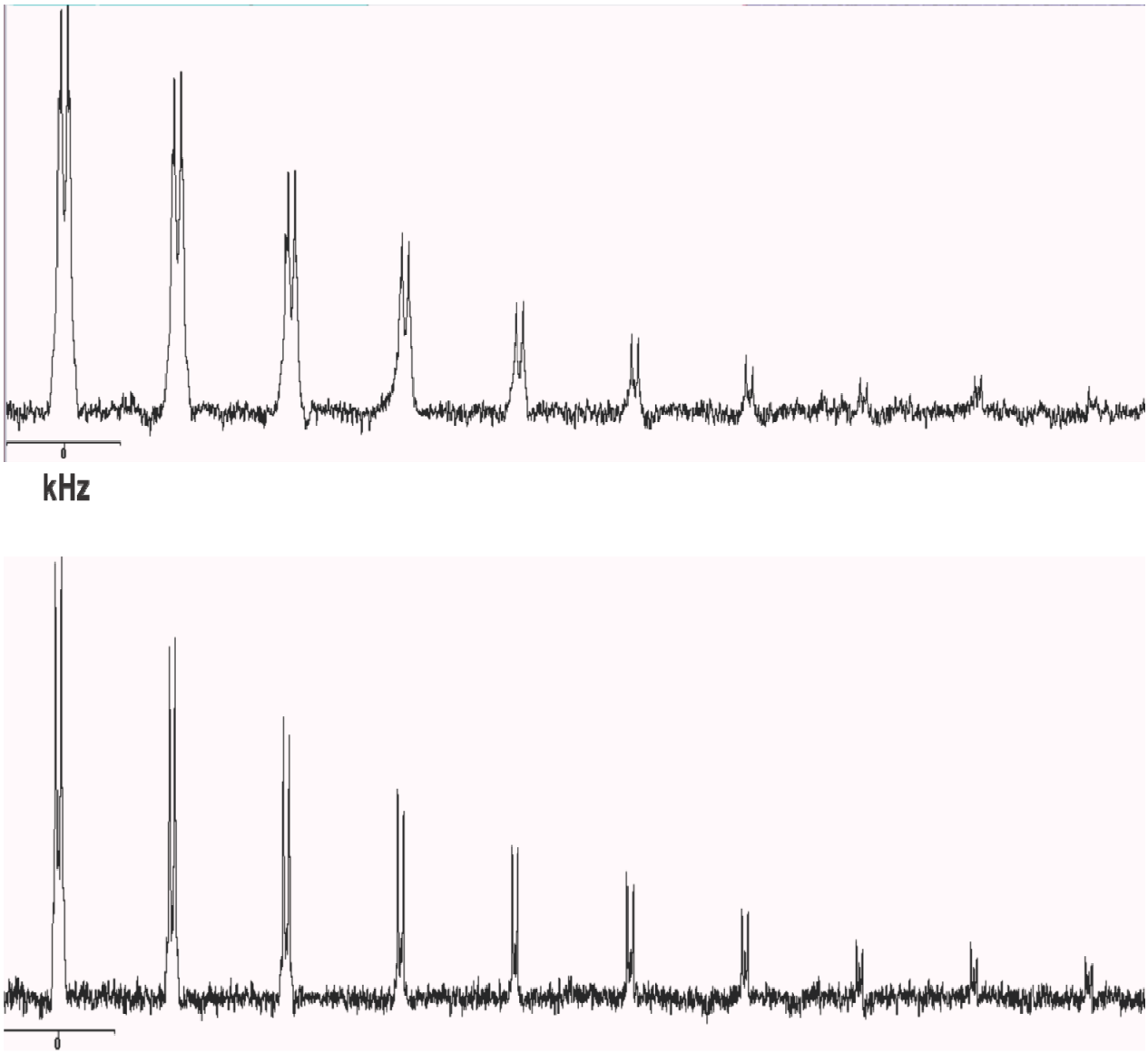

Figure 5.42. Representative "cpquecho" stacked plots DMPC-d54 at 35°C (top) and HFP/DMPC-d54 at 30°C (bottom). The ^2H spectra were obtained by varying τ and τ_1. For each τ and τ_1, the number of scans was ~ 4000. All spectra were processed with 1000 Hz line broadening, data shift = -11, and baseline correction of the order 5.

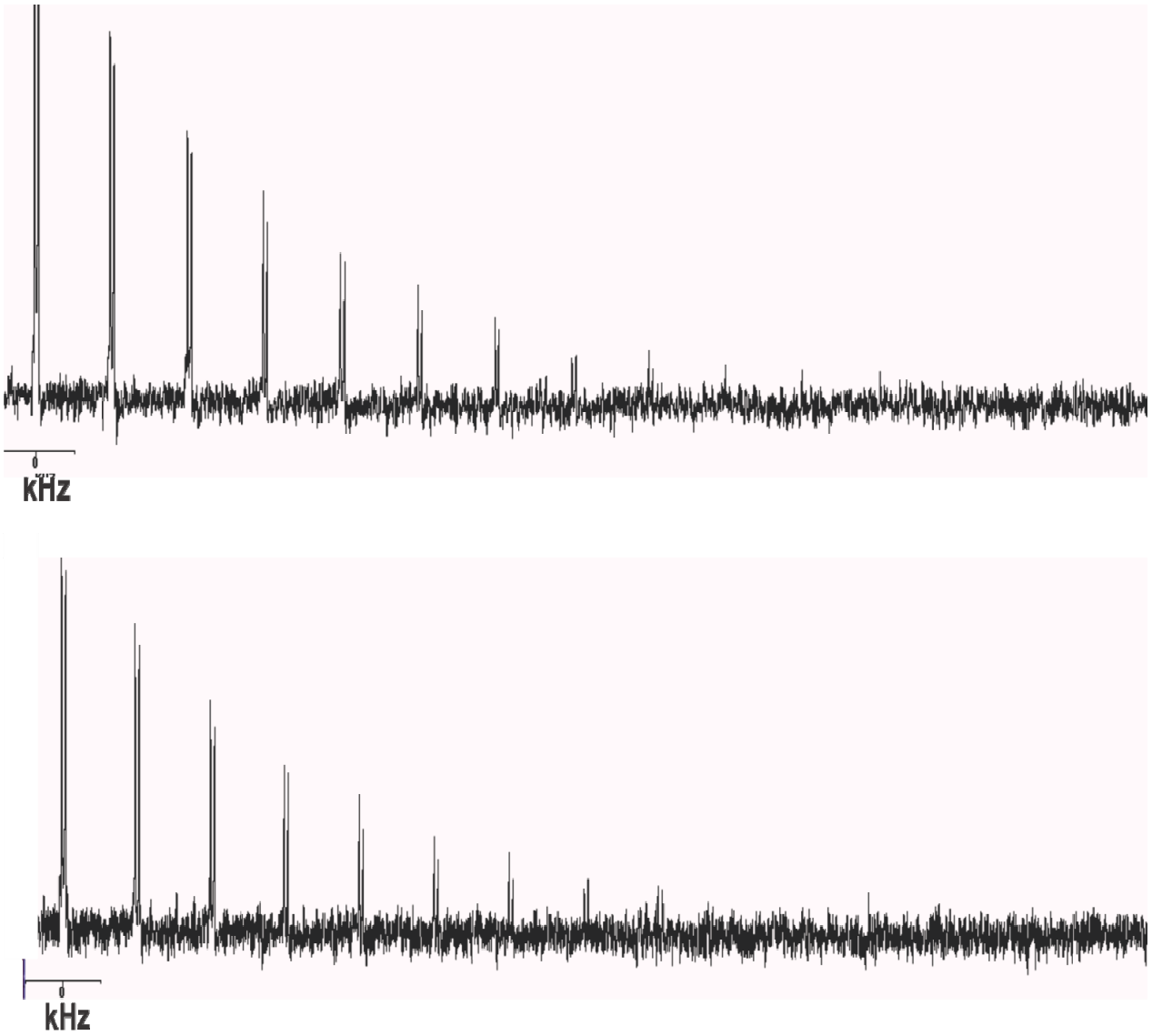

Figure 5.43. Representative "cpquecho" stacked plots HAfp/DMPC-d54-pH 5 sample at 35°C (top) and HAfp/DMPC-d54-pH 7 at 30°C (bottom). The ^{2}H spectra were obtained by varying τ and τ_1. For each τ and τ_1, the number of scans was ~ 2000. All spectra were processed with 1000 Hz line broadening, data shift = -11, and baseline correction of the order 5.

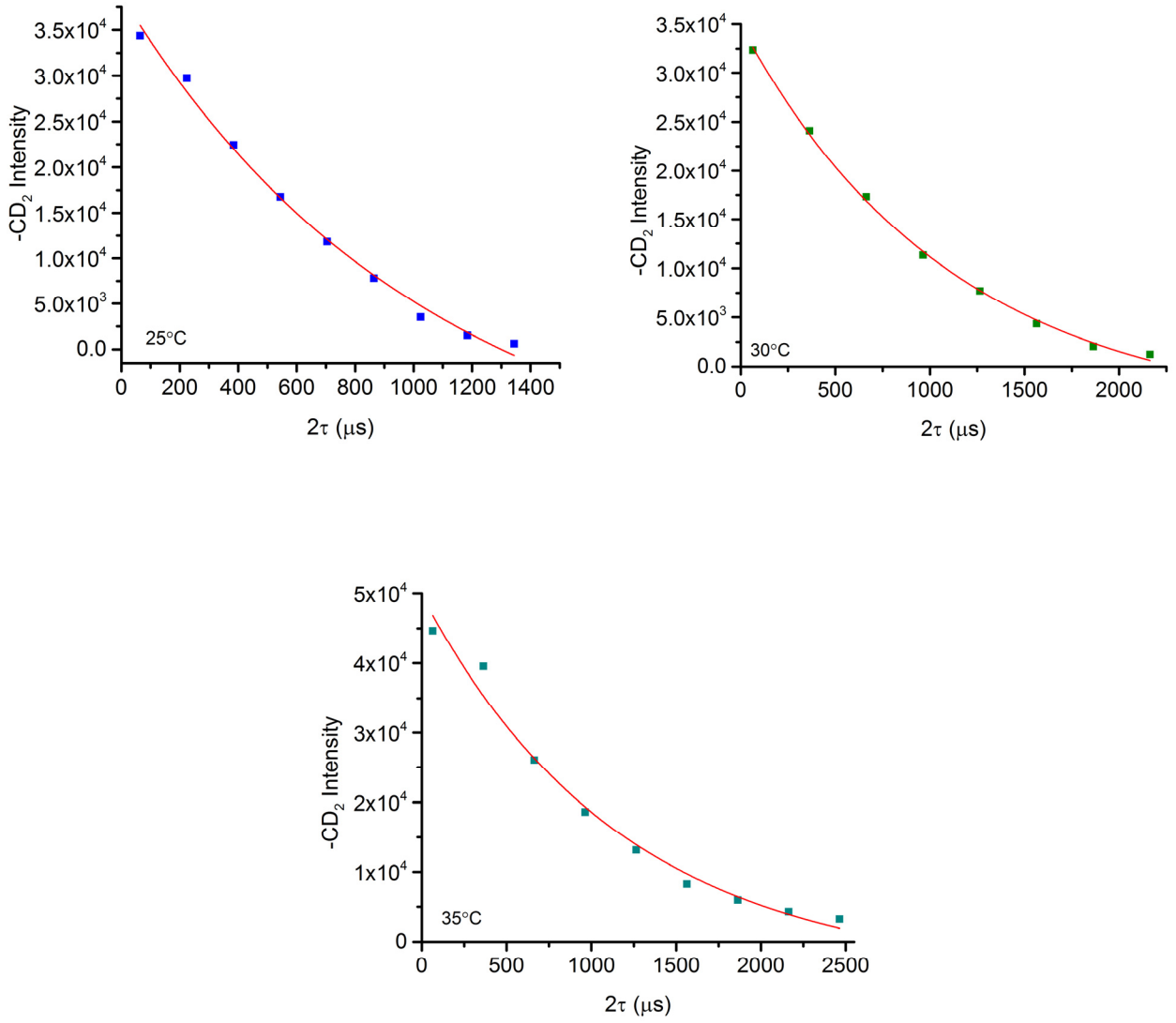

Figure 5.44. "cpquecho" experimental (colored squares) and best fit (red lines) plots of -CD_2 intensity vs 2τ under static conditions for DMPC-d54 lipid at different temperatures. The fitting equation is $I(2\tau)=I(0)\times\exp(-2\tau/T_2)$.

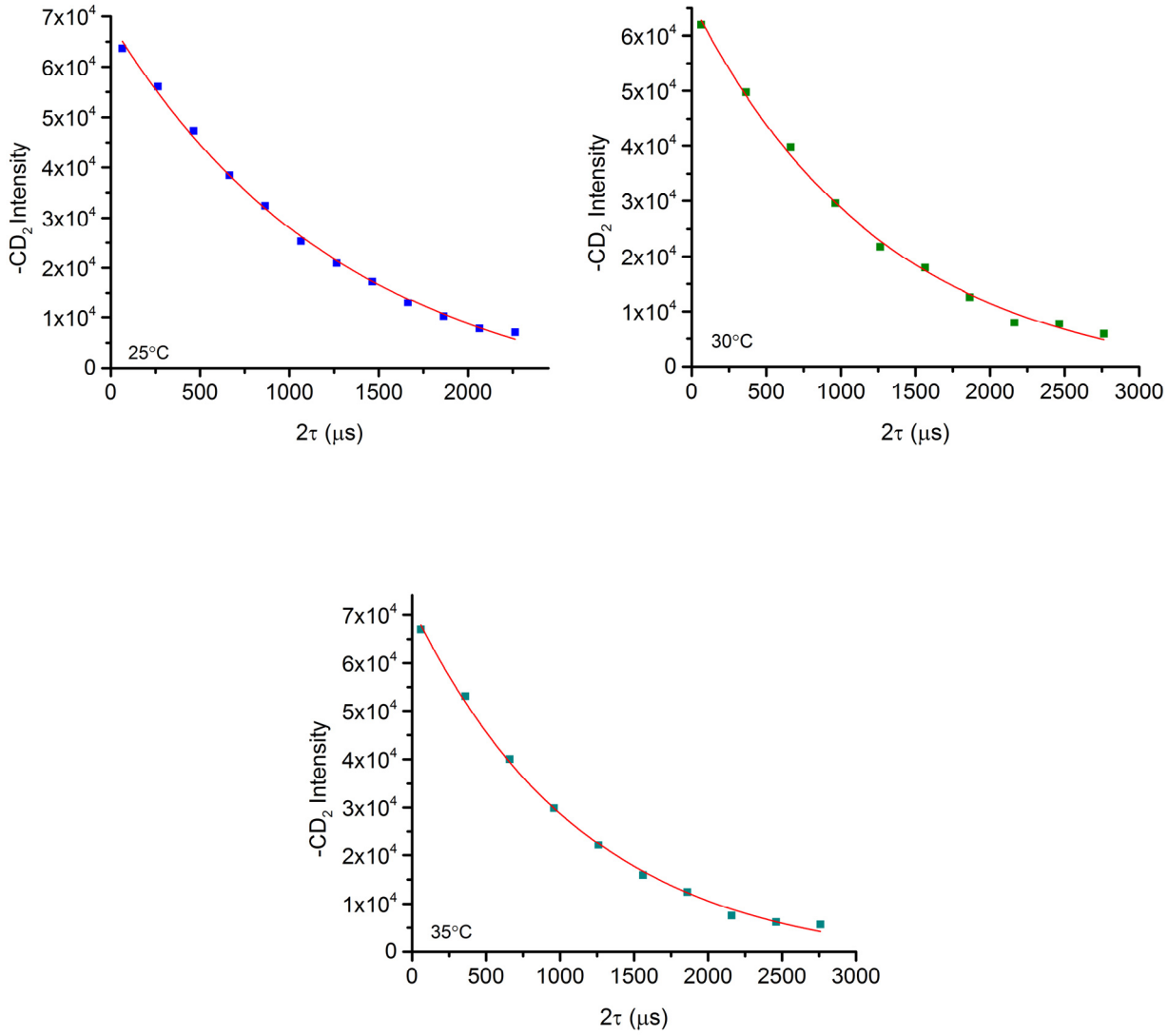

Figure 5.45. "cpquecho" experimental (colored squares) and best fit (red lines) plots of -CD_2 intensity vs 2τ under static conditions for HFP/DMPC-d54 lipid at different temperatures. The pH of the sample was 7. The fitting equation is $I(2\tau)=I(0)\times\exp(-2\tau/T_2)$.

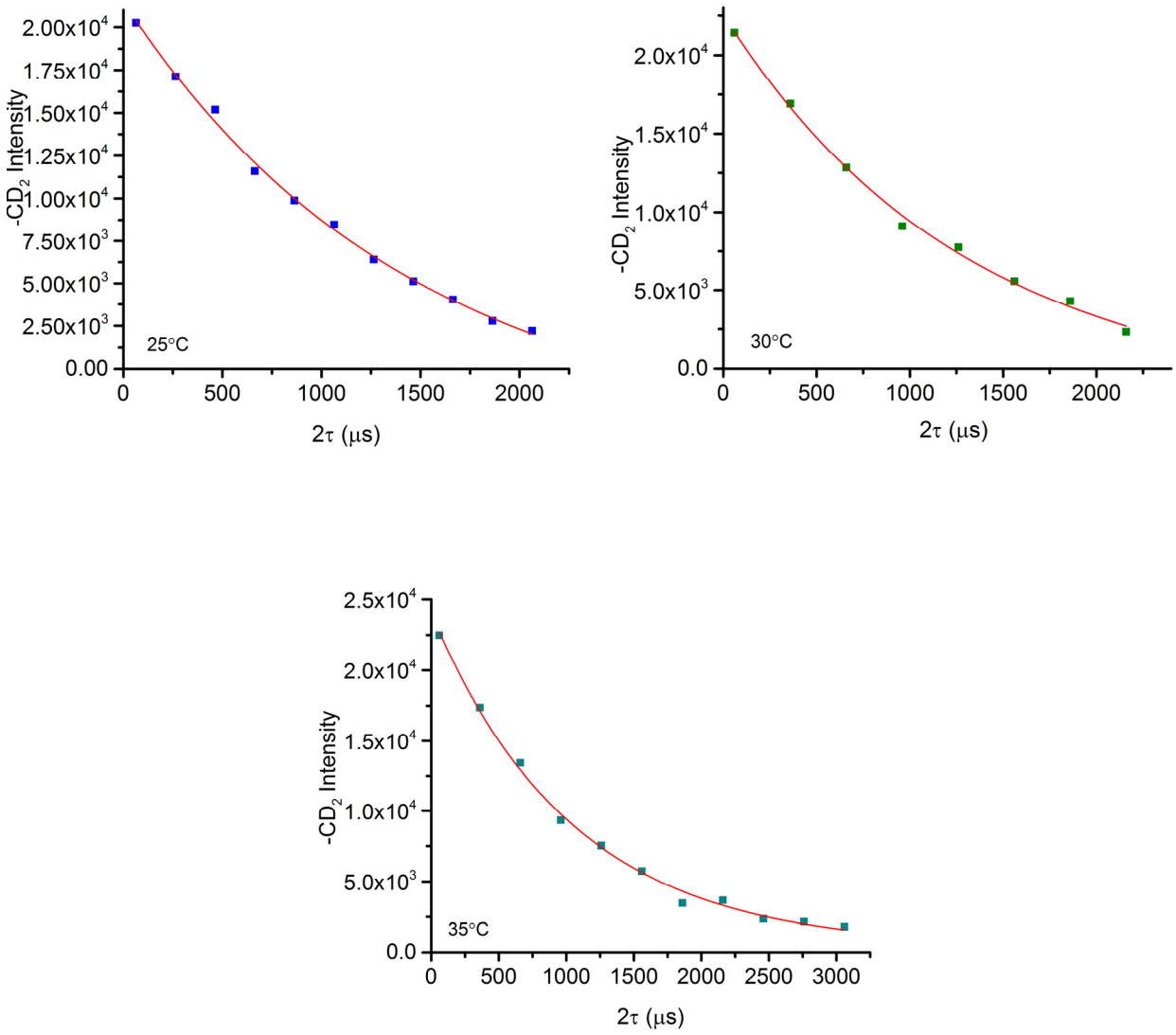

Figure 5.46. "cpquecho" experimental (colored squares) and best fit (red lines) plots of -CD_2 intensity vs 2τ under static conditions for HAfp in DMPC-d54 in the ratio 1:25 at different temperatures. The fitting equation is $I(2\tau)=I(0)\times\exp(-2\tau/T_2)$. The pH of the NMR sample was 5.

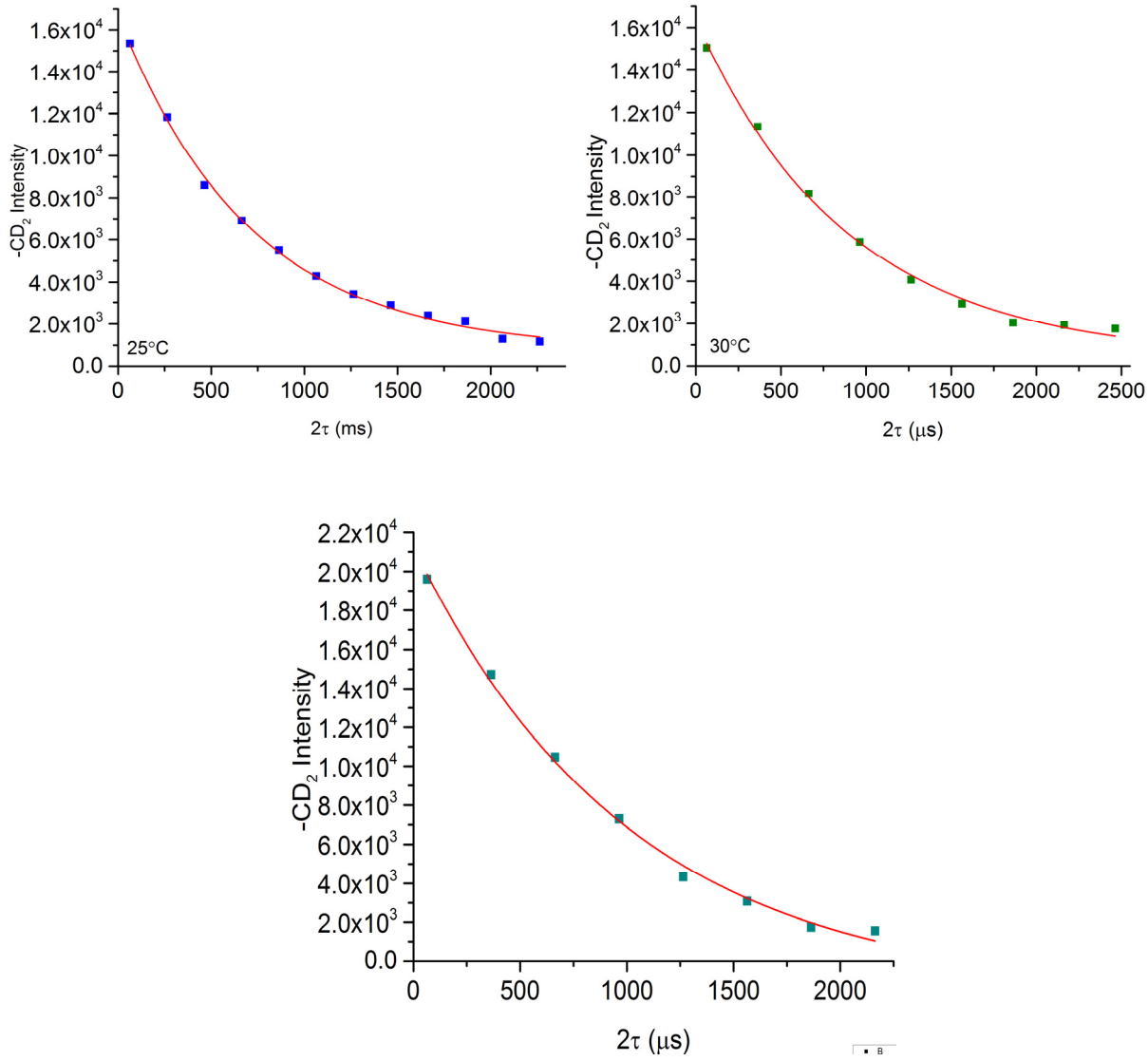

Figure 5.47. "cpquecho" experimental (colored squares) and best fit (red lines) plots of -CD_2 intensity vs 2τ under static conditions for HAfp in DMPC-d54 in the ratio 1:25 at different temperatures. The fitting equation is $I(2\tau)=I(0)\times\exp(-2\tau/T_2)$. The pH of the NMR sample was 7.

Table 5.4. Best-fit ^2H T_2 values in μs of DMPC-d54 lipid with and without peptide. The uncertainties are given in parenthesis. The T_2 values are obtained by fitting the $–CD_2$ intensities.

Temperature (°C)	DMPC-d54	HFP/DMPC-d54	HAfp/DMPC-d54 pH 5	HAfp/DMPC-d54 pH 7
25	1050(200)	1350(99)	1462(146)	804(30)
30	1110(70)	1301(88)	1311(158)	896(60)
35	1179(56)	1160(156)	1024(64)	890(56)

5.9 Discussion

The experiments performed in this study had two major purposes. The first was to study the dynamics of the PC lipids in presence of peptide; the other was to develop a NMR method which will only probe the local dynamics of the lipids to better understand the mechanism of the membrane fusion process. In prior work we have shown that the HAfp adopts a closed and a semiclosed structure in DTPC: DTPG membranes in the ratio 4:1. The larger surface area of the semiclosed structure was correlated with higher vesicle fusion because of the ability to perturb more lipid bilayer. The central unanswered question for the fusion peptides including HAfp is how they perturb the lipid bilayer of the host cell membrane to make it fuse more rapidly with the viral membrane. In the present study, we aim to learn the lipid/peptide interactions via ^{2}H NMR.

5.9.1 HFP and HAfp disrupts acyl chain packing

In the present study we have used perduterated lipid acyl chain to monitor the effect of adding a fusion peptide to a neutrally charged membrane. From Figures 5.22 – 5.24, it is evident that the overall shape of the ^{2}H NMR spectra remains similar upon peptide addition. This indicates that addition of HFP and HAfp to DMPC lipid does not change the lamellar membrane phase. This observation is consistent with the earlier works by Gabrys. Also, worth noting is the effect of HFP on the transition temperature of DMPC-d54. Figure 5.22 shows the spectra of HFP/DMPC-d54 taken at different temperatures. At 20°C, the flat base and the sharp cut off signal indicate that the sample is in the liquid phase. Therefore, HFP reduces the phase transition temperature of DMPC-d54 where the phase transition temperature of DMPC is ~ 23°C. However, no such effect was observed in case of HAfp.

Using the fully deuteriated DMPC-d54 and the spectral de-Paking procedure, we have obtained ^{2}H NMR spectra of DMPC and DMPC / peptide. Although the assignment of each of the resonance peaks to a specific methylene groups on either of the chain is ambiguous, comparisons with the spectra of specifically deuteriated DMPC lipids allow us to make most of the resonances unequivocal. The peak having the smallest $\Delta\nu_Q$ of ~ 4.2 kHz arises from the terminal methyl group of the lipid acyl chain. The broad peak with the largest $\Delta\nu_Q$ of ~ 31 kHz arises from about five methylene groups near the bilayer surface (Figure 5.21). This region is called as the plateau region. Some of the well resolved peaks having an intermediate $\Delta\nu_Q$ values are coming from methylene groups near the center of the bilayer. The deuterons at the C-2 position have anomalously small $\Delta\nu_Q$ values determined by Oldfield. [21] The C-2 deuterons are also resolved in our DMPC ^{2}H NMR spectrum. Generally, larger splitting indicates that the methylene groups are further from terminal methyl groups. The cpquecho ^{2}H NMR spectra have two horns and most likely the horns arise from the methylene groups. This is because the $\Delta\nu_Q$ of the horns in the cpquecho is similar to $\Delta\nu_Q$'s of the methylene groups obtained in the quecho experiment.

As seen from the Figures 5.22 and 5.25, the $\Delta\nu_Q$ decreases after the addition of the HFP peptide to DMPC membrane. The $\Delta\nu_Q$ of the methylene groups decreases to from ~31 kHz to ~ 27 kHz and the $\Delta\nu_Q$ of the terminal methyl group decreases to ~ 3.5 kHz from ~ 4.2 kHz at 35°C. Similar decrease on $\Delta\nu_Q$ are also observed for the intermediate methylene positions. Similar effects were also observed in case of HAfp/DMPC-d54. The $\Delta\nu_Q$ of DMPC-d54 decreases by ~ 1.1 kHz in presence of HAfp at pH 5. The $\Delta\nu_Q$ decrease for the methyl groups was ~ 0.2 kHz. In contrast, upon addition of HAfp at pH 7, $\Delta\nu_Q$ of DMMPC increases by ~ 2.5 kHz. By comparing the $\Delta\nu_Q$ s of DMPC in presence of HFP and HAfp at pH 5, it can be concluded that these two peptides

decrease the order of the lipid acyl chain whereas the addition of HAfp at pH 7 increases the order of the lipid acyl chain.

The $\Delta\nu_Q$ of the DMPC/peptide also depends on the concentration of the peptide. Figure 5.48 shows the narrowing of the $\Delta\nu_Q$ in presence of higher HFP concentration.

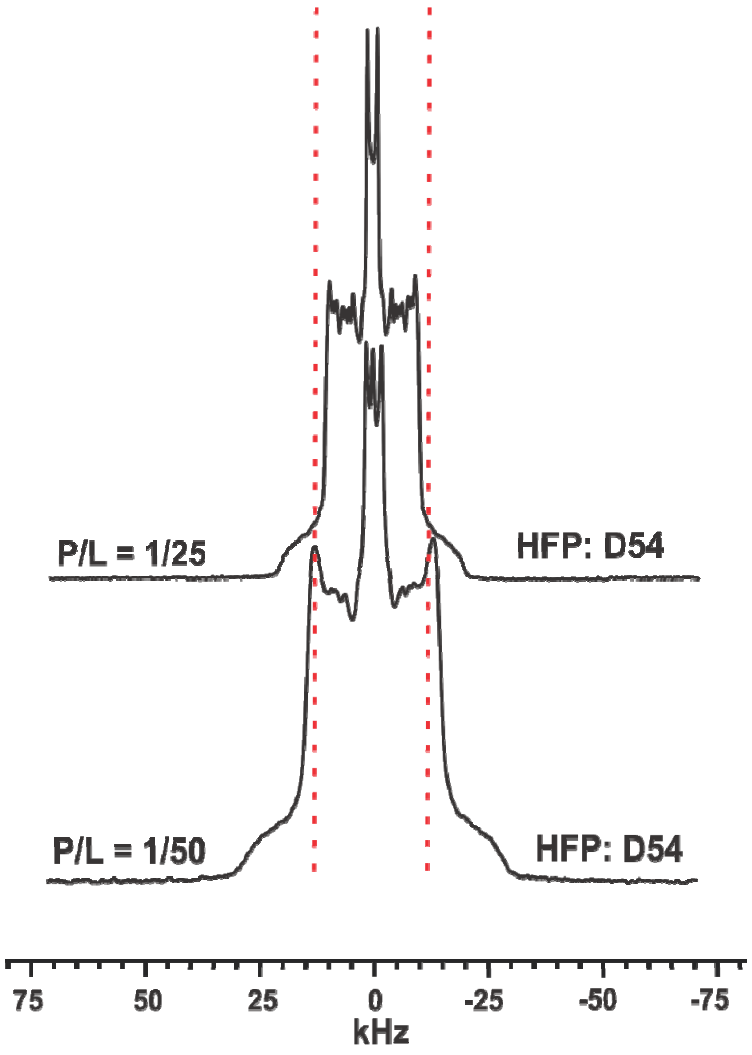

Figure 5.48. Effect of the peptide concentration on quadrupolar splitting. ^{2}H quecho NMR spectra of HFP/DMPC at 35°C.

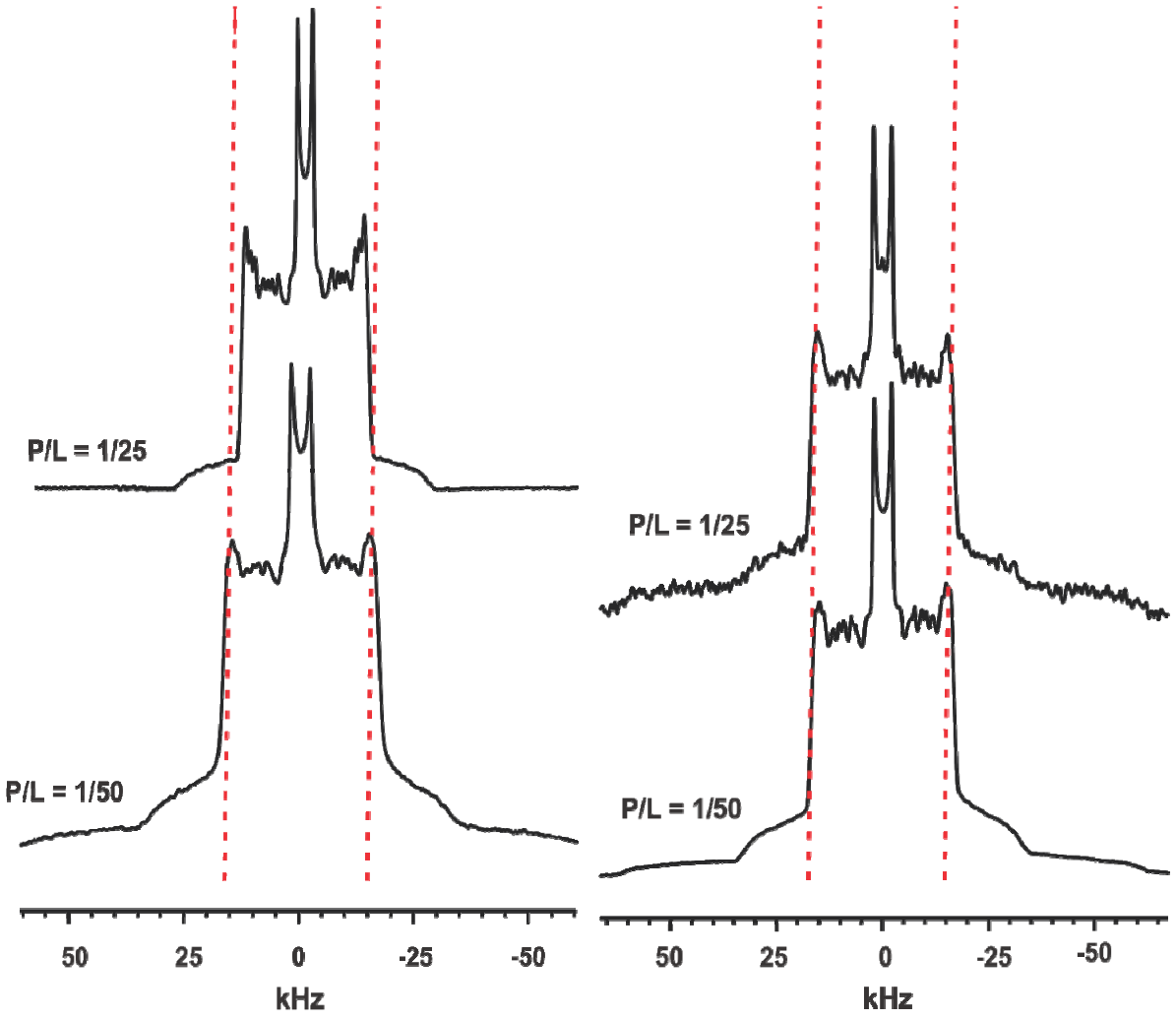

Figure 5.49. ^{2}H quecho NMR spectra of HAfp/DMPC at 35°C. (a) at pH 5 and (b) at pH 7. In case of pH 5, at higher peptide concentration the quadrupolar splitting gets narrower. In contrast, at pH 7, the quadrupolar splitting at higher and lower peptide concentration are similar.

5.9.2 Insertion of the peptides into the hydrophobic core of the membrane

Details on the depth at which the peptides are inserted or sit on the membrane can be obtained from the ^2H NMR results. The addition of the peptides, HFP and HAfp (pH 5), results in a decrease in the magnitude of the order parameters in both lipid environments as shown in Figure 5.27. To distinguish the effect of the peptide on the different parts of the lipid acyl chain, difference order profiles were calculated by subtracting the $|S_{CD}|$ values of the peptide/lipid samples from the $|S_{CD}|$ values of the same acyl chain position. Therefore, a positive value of ΔS_{CD} represents an increase in the disorder and negative value indicates the increase in the order. However, the ΔS_{CD} order profiles are complicated by the intrinsic decrease as the magnitude of the S_{CD} along the acyl chain. For this reason ΔS_{CD} order profiles are normalized relative to the pure lipid. These profiles show the fractional order parameter change after the addition of the peptide. These order parameters also show the extent of the acyl chain disordering upon binding of the peptide to the lipid membranes. Figure 5.43 shows the normalized order parameter profiles for the DMPC-d54 lipid acyl chain upon addition of the HFP and HAfp peptide. As shown below, the extent of disorder is divided into two distinct sections for all the samples – the more disordered segment and the less disordered segment. The upper half of the chain C2 - C7 is disordered by HFP and HAfp (at pH 5), but the disordering effect is greater in the lower half of the lipid acyl chain (C8 – C13). In case of HAfp at pH 7, there is an increase in the order for all the acyl chain positions. Also worth noting in the plot 5.43 is the ΔS_{CD} of the terminal methyl group for HFP and HAfp at pH 5. In case of HFP, the ΔS_{CD} for the terminal methyl group is larger than that of HAfp (pH 5). This observation suggests that the HFP in inserted more deeply (~ at the center of the bilayer) inside the bilayer as compared to the HAfp at pH 5. Additionally, the ΔS_{CD} values for the HFP at all the lipid acyl chain positions are larger than the HAfp at pH 5.

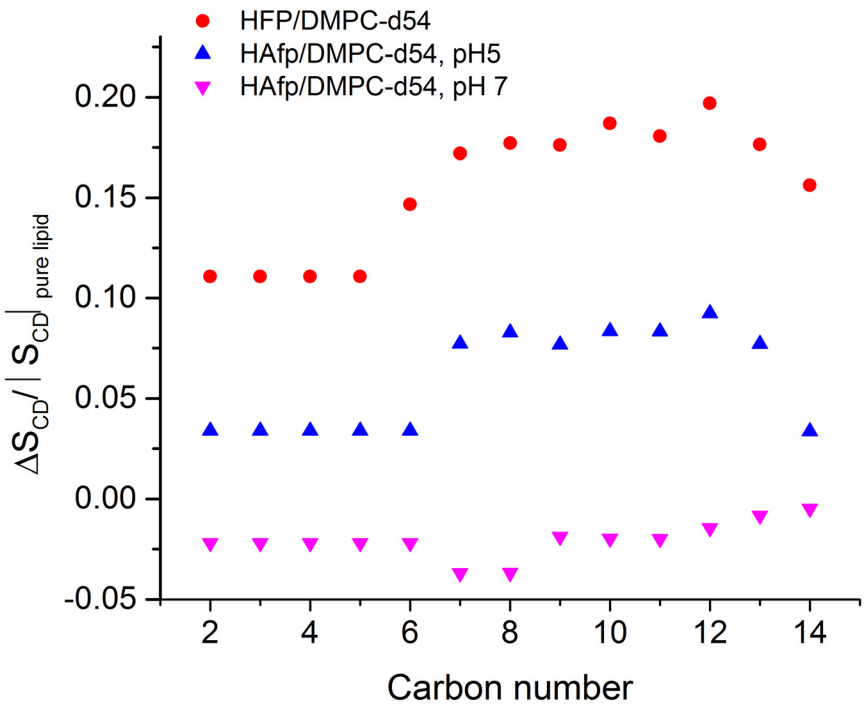

Figure 5.50. Normalized order parameter profiles of DMPC-d54 after the addition of the 0.04 mole % peptides. The normalized order parameter profiles are calculated at 35°C. The plot shows the fractional change in the order parameters at each acyl chain position. The positive value indicates an increase in the disorder and a negative value indicates an increase in the order of the acyl chain.

As stated earlier, in cpquecho experiment we see the ^{2}H signal due to the terminal CD_3 groups. This suggests that the HFP peptide is in contact with the methyl groups and therefore the magnetization is transferred from the peptide ^{1}Hs to the lipid ^{2}Hs which eventually gave rise to the methyl signals. At shorter dephasing time, the ^{2}H signals of the methylene deuterons are very strong as compared to the methyl deuterons. But at longer dephasing time as the ^{2}H signals from the methylene deuterons gets attenuated the ^{2}H signals from the methyl deuterons gets stronger. This is because due to the fast axial rotation of the methyl group, the T_2's are longer and therefore the methyl peaks gets are more prominent at longer dephasing times. This effect is

shown figure 5.51 below. However, the methyl peaks are absent in the cpquecho spectra of HAfp at both the pHs which suggests that the HAfp (pH 5) peptide might not be inserted into the center of the bilayer. The methyl peaks are also absent in the cpquecho spectra of DMPC-d54. In the pure lipid sample the only ^{1}Hs available for CP transfer are the ^{1}Hs present in the glycerol head group. The distance of the methyl deuterons from the glycerol ^{1}Hs are ~ 12 Å The dipolar coupling corresponding to ~ 12 Å is ~ 11 Hz and the rate of CP transfer is ~ 0.055. Therefore no CP transfer will be observed. Hence the CP transfer will be restricted to the deuterons present on the C2 to ~ C4 deuterons and only two peaks were observed.

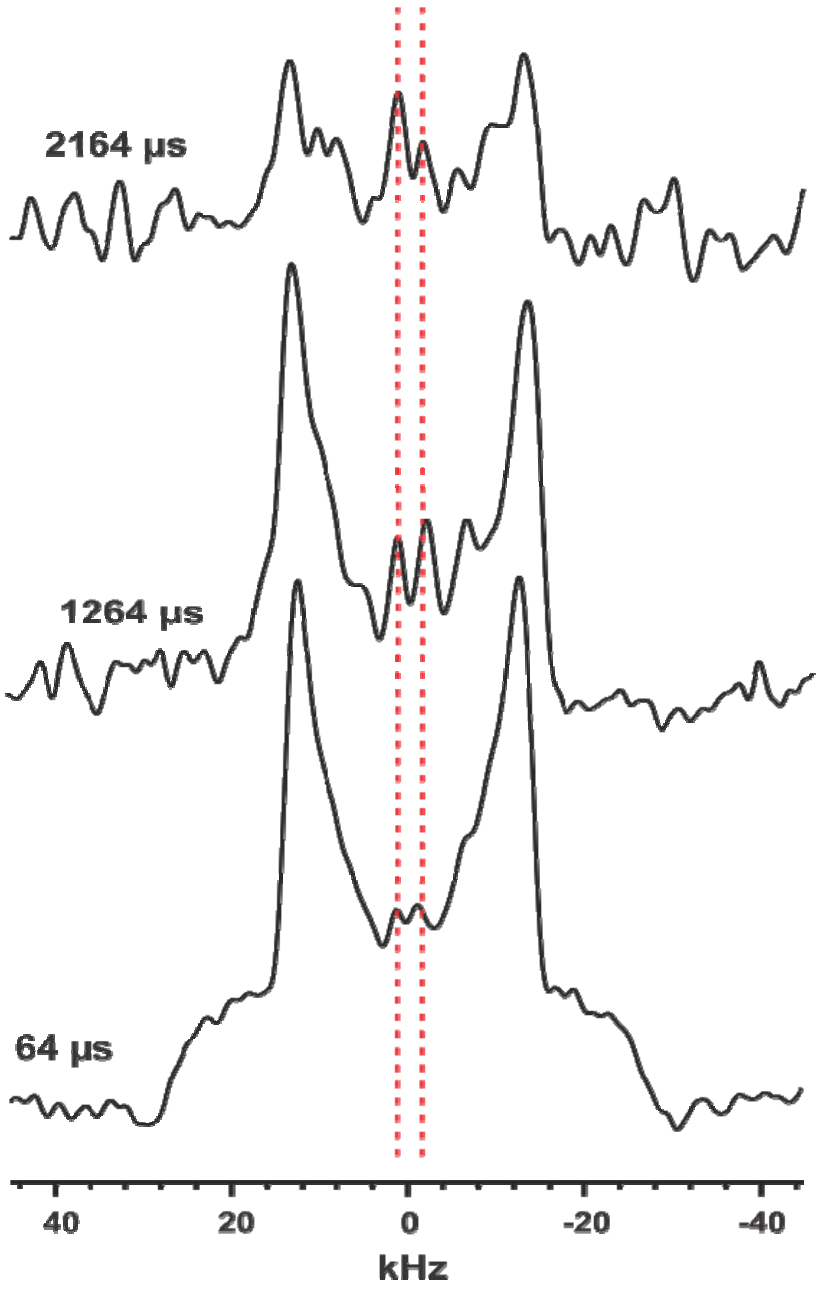

Figure 5.51. "cpquecho" ^{2}H NMR spectra of HFP/DMPC-d54 at 35°C at different dephasing times. The $\Delta\nu_Q$ for the methyl group is ~ 3.1 kHz. The splitting is consistent with the methyl group splitting of 3.5 kHz at 35°C obtained from the quecho experiment.

5.9.3 Spin-spin relaxation studies

Table 5.5 lists the best-fit T_2 values for the outer feature for four samples measured using quecho and cpquecho experiment. The T_2 values at 10°C for quecho experiment were obtained by integrating full ^2H NNMR spectrum.

Table 5.5. Best-fit T_2 (μs) values at different temperatures. Uncertainties are in parenthesis.

Temperature (°C)	DMPC-d54	HFP/d54	HAfp/d54-pH 5	HAfp/d54-pH 7	Experiment
10	521(24)	216(15)	210(14)	507(28)	Quecho
	498(35)	244(37)	315(30)	552(30)	Cpquecho
25	885(56)	900(37)	563(14)	627(14)	Quecho
	1050(200)	1350(99)	1308(146)	804(65)	Cpquecho
30	996(72)	950(11)	876(30)	1010(36)	Quecho
	1110(75)	1301(102)	1311(150)	896(60)	Cpquecho
35	1090(63)	942(10)	875(30)	1109(108)	Quecho
	1185(56)	1160(66)	1024(64)	1013(90)	Cpquecho

In case of pure lipid, there was no peptide present in the sample. Therefore the T_2 values obtained from the two experiments should be similar because we are measuring the T_2 for the deuterons attached to the ~ C2 – C5 position of the acyl chain. The T_2 values listed in the Table 5.5 measured using the quecho experiment are obtained by fitting the $–CD_2$ intensity (except at 10°C). Therefore most likely the T_2 should be similar. One of the important differences between the quecho and the cpquecho experiment is the decoupling present in the cpquecho pulse sequence. In absence of the ~ 30 kHz decoupling the T_2 value for DMPC-d54, HFP/d54,

HAfp/d54 at pH 5 and HAfp/d54 at pH 7 are 898 (200) μs at 25°C, 790 (45) at 35°C, 651 (84) at 35°C and 869 (51) at 35°C respectively. Therefore T_2s were measured for each sample at 35°C under no decoupling are scaled by a factor of ~ 1.3 ± 0.2 times. So we can see that T_2s values after scaling are very similar at higher temperatures except at 10°C.

5.9.4 Alternative fitting method

Both the quecho and cpquecho data were also fitted using the echo intensity as a function of total echo time 2τ. The data were fitted to $I(2\tau)=I(0)\times\exp(-2\tau/T_2)$ where I (2τ) is the measured echo intensity and I (0) and T_2 are fitting parameters.

Table 5.6. Best-fit T_2 (μs) values at different temperatures obtained by fitting of the tip of the echo as a function of 2τ. Uncertainties are in parenthesis.

Temperature (°C)	DMPC-d54	HFP/d54	HAfp/d54-pH 5	HAfp/d54-pH 7	Experiment
0	490(20)	180(7)	240(13)	544(13)	Quecho
	412(15)	150(3)	171(15)	400(16)	Cpquecho
10	531(9)	260(9)	253(4)	595(7)	Quecho
	474(16)	175(17)	204(17)	410(13)	Cpquecho
25	861(30)	720(25)	735(4)	658(12)	Quecho
	587(20)	637(30)	662(50)	560(40)	Cpquecho
35	890(25)	806(21)	868(13)	697(7)	Quecho
	494(26)	547(25)	573(14)	430(29)	Cpquecho

(a)

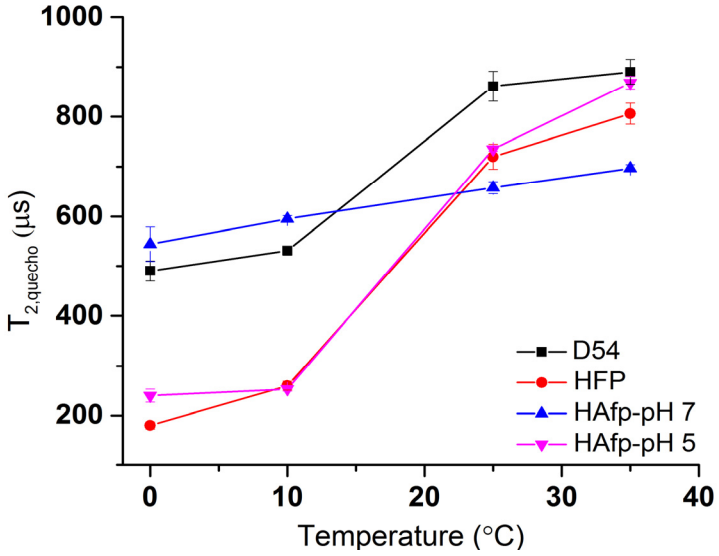

(b)

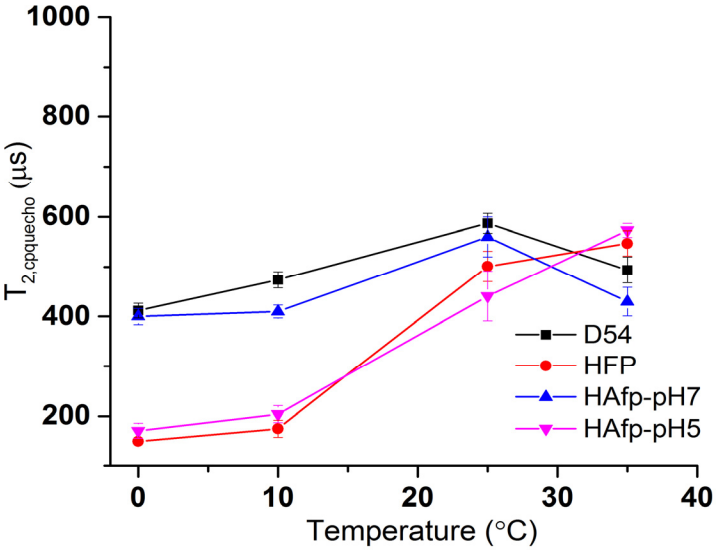

Figure 5.52. Plots of best-fit T_2 values at different temperatures obtained from (a) quecho experiment and (b) cpquecho experiment.

At 10°C, there is a substantial difference between the T_2 values for the samples HFP and HAfp at pH 5. The lipids containing HFP and HAfp at pH 5, the T_2 values decreases by a factor of 2, but for HAfp at pH 7 the T_2 value is comparable to that of the pure lipid. This suggests that the HAfp peptide at pH 5 and HFP is inserted in the membranes. The T_2 values increases with an increase in the temperature and this is consistent with the T_2 expression given by Abragam,

$$1/T_2 = (1/90)\Omega_Q^2 [9j(0) + 15j(\omega_0) + 6j(2\omega_0)] \quad 5.9$$

where $\Omega_Q = ¾(e^2qQ/h)$ or the quadrupolar coupling,

j(0) is the spectral density at the zero frequency,

$j(\omega_0)$ is the spectral density at Larmor frequency.

It is worth noting that the T_2 values measured using the cpquecho experiment slightly decreases with the increase in the temperature. This might be due to the increase in the lateral diffusion of the lipids with the increase in temperature. Since the diffusion of the lipids increases with the temperature, the cross polarization efficiency decreases.

The decrease in the T_2 values can be correlated with the curvature induced by the fusion peptide upon insertion in the membrane. As mentioned earlier, that the T_2 processes reflect the slow motions. The best-candidate for this kind of motion is the molecular diffusion of the lipid along the curved membrane surface.[20] The deuterons present in the C-D bond will experience some fluctuation in the quadrupolar field as a result of the molecular diffusion. This is because the quadrupolar field varies with the C-D bond angle with respect to the external magnetic field. If the lipid moves along the surface of the planar membrane, there will be a little variation in the angle between the C-D bond and the external magnetic field. As a result there will very less fluctuation between in the quadrupolar field resulting in slower relaxation. If the lipid diffuses along the curved surface, there will be greater change in the angle between the C-D bond and the

external magnetic field resulting in the greater fluctuation in the quadrupolar field experienced by the deuterons. Therefore, the greater fluctuation in the quadrupolar field will cause faster relaxation. Therefore there is a correlation between the curvature and the fluctuation of the quadrupolar field which in turn has an effect on the relaxation process. The movement of the lipids along the curved surface can be correlated as the movement of the lipids along the fusion stalk. Since pH 7 is not the fusion pH of influenza, the slight decrease in T_2 could be due to the inability of the HAfp to perturb membrane at pH 7.

APPENDICES

APPENDIX A

NMR File Location

Figure 3.2

(a) /home/hapi0/mb4c/data/Ujjayini/IFP_061312 (G16c-F9n pH 5)

(b) /home/hapi0/mb4c/data/Ujjayini/IFP_062512 (G16c-F9n pH 7)

(c) /home/khafre0/mb4b/data/Ujjayini/IFP_102113_Ph5 (G16c-F9n)

(d) /home/khafre0/mb4b/data/Ujjayini/IFP_103013_7.0 (G16c-F9n)

(e) /home/khafre0/mb4b/data/Ujjayini/13C15N/IFP20_020415_PH5 (A5c-M17n)

(f) /home/khafre0/mb4b/data/Ujjayini/13C15N/IFP20_021715_pH7 (A5c-M17n)

(g) /home/khafre0/mb4b/data/Ujjayini/13C15N/IFP23_030315_pH5 (A5c-M17n)

(h) /home/khafre0/mb4b/data/Ujjayini/13C15N/IFP23_031215_pH7 (A5c-M17n)

Figure 3.3

The same file locations as those for figures 3.2.

Figure 3.4

The same file locations as those for figures 3.2.

Figure 3.5

The same file locations as those for figures 3.2.

Figure 3.6

The same file locations as those for figures 3.2.

Figure 3.7

/home/khafre0/mb4b/data/Ujjayini/13C15N/IFP23_040915_pH7 (A5c-M17n, -20°C)

Figure 4.5

(a) /home/hapi0/mb4c/data/Ujjayini/IFP20_pH5_022715 (G16c-F9d_5A5ch_3)

(b) /home/hapi0/mb4c/data/Ujjayini/IFP20_pH7_030615 (G16c-F9d_5A5ch_3)

Figure 5.9

/home/khafre0/mb4b/data/Ujjayini/H_D_061216/setup/pw90X_4_061416_real_trans

Figure 5.10

/home/khafre0/mb4b/data/Ujjayini/H_D_032516/IFP_1_25/032816_quecho_35C

Figure 5.11

/home/khafre0/mb4b/data/Ujjayini/H_D_061216/setup/Quecho_1_061416_1

Figure 5.12

/home/khafre0/mb4b/data/Ujjayini/H_D_061216/setup/Quecho_1_061416_real_transmitter

Figure 5.13

/home/khafre0/mb4b/data/Ujjayini/1H2H/D54_35/082114_pw90H

Figure 5.14

/home/khafre0/mb4b/data/Ujjayini/H_D_061216/D54_setup/cpq_062616_ct

Figure 5.16

/home/khafre0/mb4b/data/Ujjayini/1H2D/Glycine_d2/081214_pw90H_array

Figure 5.17

(a) /home/khafre0/mb4b/data/Ujjayini/1H2D/Glycine_d2/081214_aHcp_zero

(b) /home/khafre0/mb4b/data/Ujjayini/1H2D/Glycine_d2/081214_aHdec_zero

Figure 5.19

/home/khafre0/mb4b/data/Ujjayini/1H2D/Glycine_d2/081214_aHdec_zero

/home/khafre0/mb4b/data/Ujjayini/1H2D/Glycine_d2/081214_aHdec_0.2

/home/khafre0/mb4b/data/Ujjayini/1H2D/Glycine_d2/081214_aHdec_0.4

Figure 5.20

/home/khafre0/mb4b/data/Ujjayini/H_D_071715/SecStructure/IFP23_071915

Figure 5.21

/home/khafre0/mb4b/data/Ujjayini/H_D_061216/D54

Figure 5.22

/home/khafre0/mb4b/data/Ujjayini/H_D_061216/HFP_1_25

Figure 5.23

/home/khafre0/mb4b/data/Ujjayini/H_D_061216/IFP_1_25_ph5

Figure 5.24

/home/khafre0/mb4b/data/Ujjayini/H_D_061216/IFP_1_25_7

Figure 5.25

The same file locations as those for figures 5.21 – 5.24.

Figure 5.29

The same file location as those for figures 5.21.

Figure 5.30

The same file location as those for figures 5.22.

Figure 5.31

The same file locations as those for figures 5.23 – 5.24.

Figure 5.36

/home/khafre0/mb4b/data/Ujjayini/H_D_061216/D54_cpq

Figure 5.37

/home/khafre0/mb4b/data/Ujjayini/H_D_061216/HFP_1_25_CPQ

Figure 5.38

/home/khafre0/mb4b/data/Ujjayini/H_D_061216/IFP_1_25_ph5_CPQ

Figure 5.39

/home/khafre0/mb4b/data/Ujjayini/H_D_061216/IFP_1_25_PH7_CPQ

Figure 5.40

(a) /home/khafre0/mb4b/data/Ujjayini/H_D_061216/HFP_1_25_CPQ

(b) /home/khafre0/mb4b/data/Ujjayini/H_D_061216/HFP_1_25

Figure 5.41

The same file locations as those for figure 5.40.

Figure 5.42

The same file locations as those for figures 5.36 and 5.37.

Figure 5.43

The same file locations as those for figures 5.38 and 5.39.

Figure 5.48

/home/khafre0/mb4b/data/Ujjayini/H_D_061216/D54

/home/khafre0/mb4b/data/Ujjayini/H_D_061216/HFP_1_25

/home/khafre0/mb4b/data/Ujjayini/H_D_061216/HFP_1_50

Figure 5.49

same as the locations for the figures 5.23 – 5.24.

Figure 5.51

/home/khafre0/mb4b/data/Ujjayini/H_D_061216/HFP_1_25_CPQ/cpquecho_35C_080116_array

Figure F1

(a) /home/khafre0/mb4b/data/Ujjayini/13C-15N_050416/IP23_A5CM17N_5

(b) /home/khafre0/mb4b/data/Ujjayini/13C-15N_050416/IP23_A5CM17N_7

APPENDIX B

Solid Phase Peptide Synthesis (SPPS)

B1. Peptide synthesis:

The experiments in my research utilized peptide sequences of 27 and 30 amino acids in length and the peptides were synthesized either by Fmoc or t-Boc SPPS synthesis before reconstitution with the lipids. HA3fp20 was synthesized using Fmoc synthesis and HA1fp23 was synthesized using t-Boc synthesis. The main objective of the SPPS is to couple the C-terminus of one amino acid to N-terminus of another amino acid until the desired sequence was obtained. The peptide chains were built on small insoluble resin beads that are covalently attached to the linkers that keeps the peptide immobilized on the solid phase during the washings, de-protecting, and coupling. The protocol for the Fmoc synthesis is described below:

1. The first Fmoc protected amino acid is attached to the resin by the linker.
2. The Fmoc protecting group is removed with the de-protecting solution.
3. The next Fmoc protected amino acid is coupled to the amino acid linker support. The coupling reactions times vary with the type of amino acids, e.g. amino acids having large aromatic side chains are coupled for at least ~ 4-5 hrs or longer, but for the residues like Gly, Lys ~ 2-3 hours coupling times are adequate.
4. After the desired coupling reaction time, the resin is washed with the capping solution to cap any unreacted amino acid.
5. The capping/deprotection/coupling cycle is repeated several times until the desired peptide is synthesized.
6. The linker/resin support and the sidechain protecting groups are cleaved with TFA yielding the free peptide. The peptide is purified with reverse phase HPLC and the purity is checked by MALDI-TOF.

The dealied composition of the solutions used in Fmoc SPPS can be found in Li Xie;s PhD Thesis.

HA1fp23 was synthesised with t-Boc synthesis and the resin used was Boc-Gly-PAM resin. The basic outline of the Boc SPPS is stated below:

1. Sequences of the steps are same for all the residues except the first coupling and are listed in the initial coupling section.
2. The appropriate amount of resin is weighed out and swelled in DCM for ~ 4-5 hrs.
3. The resin is washed 5 x 2 mins with DCM.
4. The t-Boc protecting group is removed by the deprotecting solution containing 50 % TFA, 48 % DCM and 2 % Anisole. Deprotection washes are done two times: 1 x 1 min and 1 x 12 mins.
5. The resin is washed 5 x 1 min with DCM.
6. The resin is neutralized with the neutralization solution containing 5 % DIEA in DCM. The neutralization washes are done 3 x 2 mins.
7. The coupling solution is added to the resin.

Initial Coupling

- The first amino acid is double coupled.
- The first amino acid is added in 10 x molar excess of the amino acid.
- The minimum coupling time for the first residue is ~ 3 hrs.
- The amino acids are added 5 x molar excess of the amino acid.

Coupling Conditions for DEPBT

- 2 x molar equivalent of DEPBT with respect to amino acids are used.
- The amino acid is dissolved in THF to a final concentration of 0.35 – 0.4 M.
- The coupling solution is allowed to pre-react in dark for ~ 1 hr while we are preparing the resin for the coupling reaction.
- The coupling times are atleast ~ 2-3 hrs roughly. β-branched amino acids and bulky side chains containing amino acids takes longer time.

Calculations

- mg of DEPBT = 2 x (moles/residue) x (300 g DEPBT/mol) x (1000 mg /1g)
- µL of DIEA = 2 x (moles/residue) x (1L/5.9 moles DIEA) x (10^6 µL/1L)
- µL of THF

  = (moles/residue) x (10^6 µL/0.35 moles) - (mg of residue) – (µL THF) – (mg of DEPBT)

B2. $^{13}C/^{15}N$ labeled amino acid synthesis

Synthesis of ^{13}CO labeled Fmoc- protected Alanine

The ^{13}CO and ^{15}N labels used in the research were synthesized in the laboratory. This method can be used to synthesize either the ^{13}CO labeled or the ^{15}N labeled Fmoc protected amino acids. The steps for the synthesis of Fmoc-Alanine are:

1. 4 mmol of L-Alanine was weighed ≈ 356 mg of Alanine.
2. The Alanine was dissolved in 20 ml 9% sodium carbonate solution. The flask containing the Alanine was placed in an ice bath with continuous stirring.
3. 4 mmol of Fmoc-Osu (≈ 1.35 g) was weighed and dissolved in 30 ml DMF.
4. The Fmoc-Osu solution was added dropwise to the Alanine solution in an ice-bath.
5. The solution was stirred in the ice bath for ~ 5 hrs and then stirred overnight at room temperature.
6. The solution was transferred to a separating funnel. Distilled water was added to the solution until the solid precipitate dissolved.
7. The solution was extracted with ~ 30 – 70 ml diethyl ether. Save the aqueous layer.
8. The aqueous layer was extracted 2 x with 20 ml ethyl acetate. After each extractions save the aqueous layer.
9. The pH of the aqueous layer was adjusted to 1.5 - 2.0 with 1N HCl while checking thefinal pH with a pH paper. This step is very critical and has to be done very carefully and slowly.
10. The aqueous layer was then extracted 5 x 30 ml ethyl acetate. The organic layer was saved from each extraction and then finally combined together.

11. The ethyl acetate layer was finally extracted 2 x 30 ml saturated sodium chloride solution.
12. Na_2SO_4 was added to the organic layer and kept for ~ 3-4 hrs.
13. The Na_2SO_4 was filtered off and the ethyl acetate layer was evaporated under the N_2 gas, and the beaker was stored in the vacuum desiccator overnight.

Synthesis of ^{13}CO labeled 274 mg t-Boc- protected Glycine

1. ^{13}CO Labeled unprotected Glycine required ≈ 118 mg.
2. The Glycine was dissolved in 50 % dioxane solution.
3. Used 329 µl of 5M NaOH to raise the pH.
4. Boc- anhydride was added every 10 mins while stirring.
5. 1.2 ml of 5M NaOH was added to raise the pH to ~ 11.
6. The reaction was stirred overnight.
7. 6.5 ml of distilled water was added to the reaction.
8. The solution was extracted 4 x 3 ml of ether. The bottom layer was saved.
9. The pH of the aqueous layer was adjusted to 1.5 – 2.0 with 1M H_2SO_4 in an ice-bath.
10. The aqueous layer was extracted with 4 x 6 ml of ethyl acetate. The organic layer was saved and then combined together.
11. The organic layer was extracted with 3 x 2 ml saturated sodium chloride solution.
12. The organic layer was dried over Na_2SO_4.
13. Na_2SO_4 was filtered off, and the organic layer was dried under N_2 gas and then stored in vacuum desiccator.

APPENDIX C

HPLC Program and Mass Spectra of the Purified Peptide

The HPLC program was used to purify the HAfp peptide using semi-prep C18 column is shown below. Solvent A is degassed distilled water with 0.1 % TFA. Solvent B is 90 % HPLC grade acetonitrile and 10 % degassed distilled water with 0.1 % TFA.

C1. HPLC program for the purification of HA3fp20 peptide using C18 column

```
 Title:      40 -80 in 37mins
 IFP Datasource: D1M6XV81_local
Location:   Ujjayini\40 - 80 IN 37 MINS IFP.SEQ    Created: 8/8/2013 12:45:29 PM by MICHIGAN STATE
Timebase:   Ultimate3000                           Changed: 8/8/2013 12:45:29 PM by MICHIGAN STATE
```

```
              Pressure.LowerLimit =              20 [psi]
              Pressure.UpperLimit =              5076 [psi]
              MaximumFlowRampDown =              3.000
              [ml/min²] MaximumFlowRampUp =      3.000
              [ml/min²]
              %A.Equate =                        "%A"
              %B.Equate =                        "%B"
              %C.Equate =                        "%C"c
              %D.Equate =                        "%D"
              Pump_Pressure.Step =               Auto
              Pump_Pressure.Average =            On
              Data_Collection_Rate =             2.5 [Hz]
              TimeConstant =                     0.60 [s]
              UV_VIS_1.Wavelength =              214 [nm]
              UV_VIS_2.Wavelength =              280 [nm]

   0.000      Autozero
              Flow =                             3.000 [ml/min]
              %B =                               40.0 [%]
              %C =                               0.0 [%]
              %D =                               0.0 [%]
              Wait                               Ready
              Inject
              Pump_Pressure.AcqOn
              UV_VIS_1.AcqOn
              UV_VIS_2.AcqOn
              Flow =                             3.000 [ml/min]
              %B =                               40.0 [%]
              %C =                               0.0 [%]
              %D =                               0.0 [%]

  30.000      Flow =                             3.000 [ml/min]
              %B =                               80.0 [%]
              %C =                               0.0 [%]
              %D =                               0.0 [%]
```

C1. HPLC program for the purification of HA3fp20 peptide using C18 column

```
33.000      Flow =                                  3.000 [ml/min]
            %B =                                    80.0 [%]
            %C =                                    0.0 [%]
            %D =                                    0.0 [%]

33.500      Flow =                                  3.000 [ml/min]
            %B =                                    40.0 [%]
            %C =                                    0.0 [%]
            %D =                                    0.0 [%]

37.000      Pump_Pressure.AcqOff
            UV_VIS_1.AcqOff
            UV_VIS_2.AcqOff
            Flow =                                  3.000 [ml/min]
            %B =                                    40.0 [%]
            %C =                                    0.0 [%]
            %D =                                    0.0 [%]


End
```

C2. HPLC program for the purification of HA1fp23 peptide using C18 semi-prep column

```
Title:       20 to 80 in 37 mins
Datasource: D1M6XV81_local
Location:   Ujjayini\20 to 80 in 37 mins.SEQ      Created: 7/25/2013 1:29:52 PM by MICHIGAN STATE
Timebase:   Ultimate3000                          Changed: 7/25/2013 1:29:52 PM by MICHIGAN STATE
```

```
            Pressure.LowerLimit =               20 [psi]
            Pressure.UpperLimit =               5076 [psi]
            MaximumFlowRampDown =               3.000
            [ml/min²] MaximumFlowRampUp =       3.000
            [ml/min²]
            %A.Equate =                         "%A"
            %B.Equate =                         "%B"
            %C.Equate =                         "%C"
            %D.Equate =                         "%D"
            Pump_Pressure.Step =                Auto
            Pump_Pressure.Average =             On
            Data_Collection_Rate =              2.5 [Hz]
            TimeConstant =                      0.60 [s]
            UV_VIS_1.Wavelength =               214 [nm]
            UV_VIS_2.Wavelength =               280 [nm]
```

C2. HPLC program for the purification of HA1fp23 peptide using C18 semi-prep column

```
Title:       20 to 80 in 37 mins
Datasource: D1M6XV81_local
Location:   Ujjayini\20 to 80 in 37 mins.SEQ      Created: 7/25/2013 1:29:52 PM by MICHIGAN STATE
Timebase:   Ultimate3000                          Changed: 7/25/2013 1:29:52 PM by MICHIGAN STATE
```

0.000	Autozero	
	Flow =	3.000 [ml/min]
	%B =	20.0 [%]
	%C =	0.0 [%]
	%D =	0.0 [%]
	Wait	Ready
	Inject	
	Pump_Pressure.AcqOn	
	UV_VIS_1.AcqOn	
	UV_VIS_2.AcqOn	
	Flow =	3.000 [ml/min]
	%B =	20.0 [%]
	%C =	0.0 [%]
	%D =	0.0 [%]
5.000	Flow =	3.000 [ml/min]
	%B =	40.0 [%]
	%C =	0.0 [%]
	%D =	0.0 [%]
25.000	Flow =	3.000 [ml/min]
	%B =	60.0 [%]
	%C =	0.0 [%]
	%D =	0.0 [%]
30.000	Flow =	3.000 [ml/min]
	%B =	80.0 [%]
	%C =	0.0 [%]
	%D =	0.0 [%]
37.000	Pump_Pressure.AcqOff	
	UV_VIS_1.AcqOff	
	UV_VIS_2.AcqOff	
	Flow =	3.000 [ml/min]
	%B =	40.0 [%]
	%C =	0.0 [%]
	%D =	0.0 [%]

End

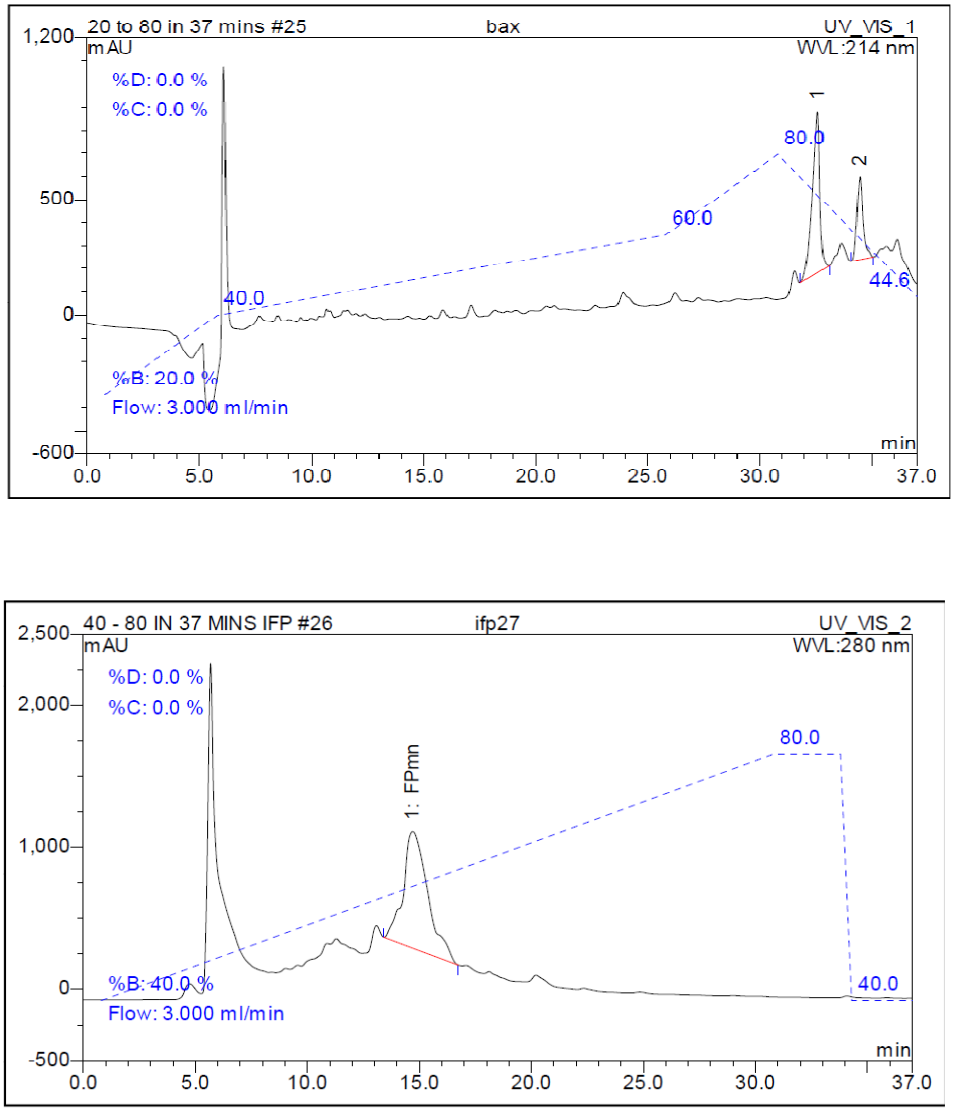

Figure C1. HPLC chromatogram of HA3fp20 (top row) and HA1fp23 (bottom row) purification. The peak at around ~ 15 mins in a was the diagnostic peak of HA3fp20 and the peak at around ~ 32 mins in b was the diagnostic peak of HA3fp20 based on the MALDI-TOF mass spectrum.

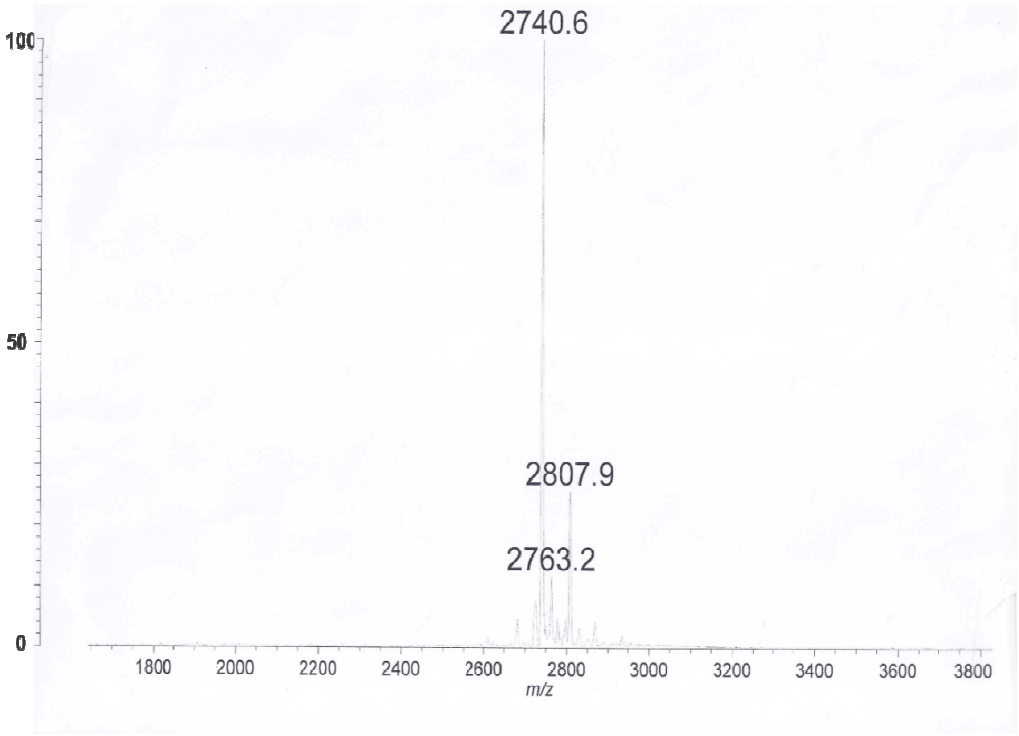

Figure C2. MALDI mass spectrum of HA3fp20 after purification. The theoretical molecular weight of HFP is 2738 Da.

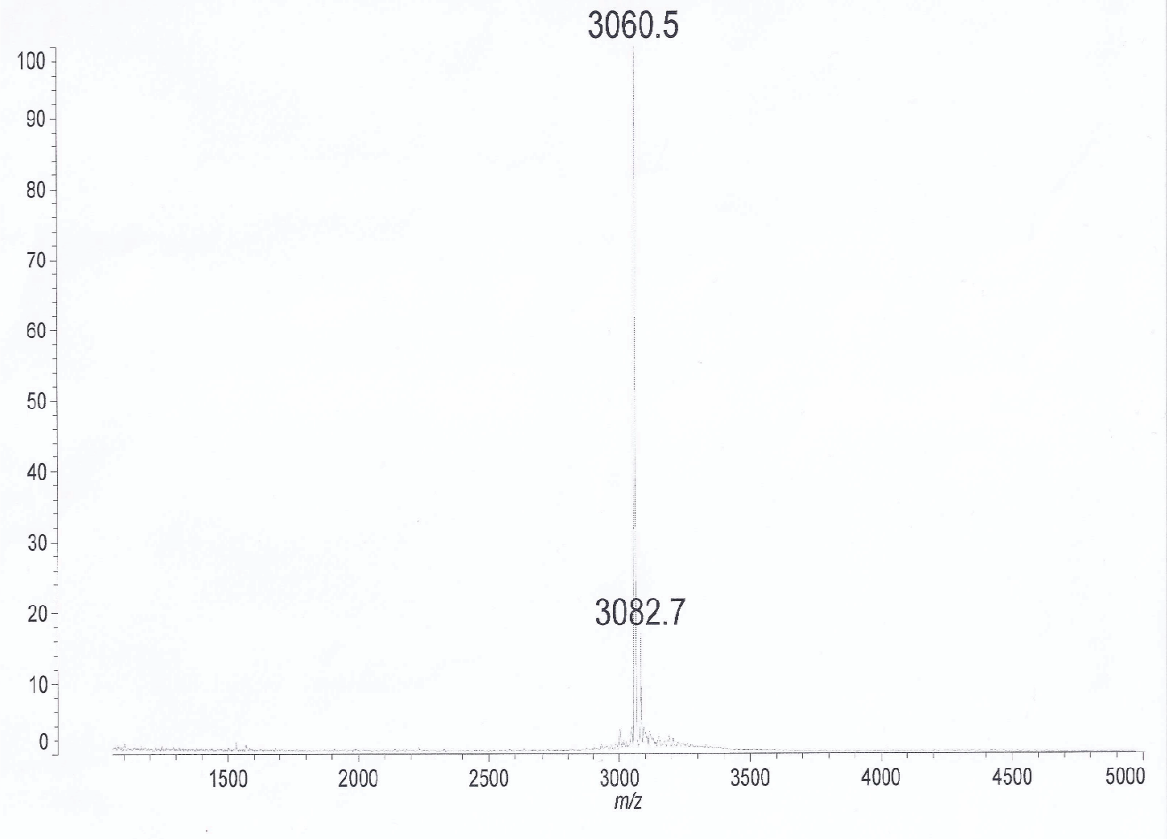

Figure C3. MALDI mass spectrum of HA1fp23 after purification. The theoretical molecular weight of HFP is 3060 Da

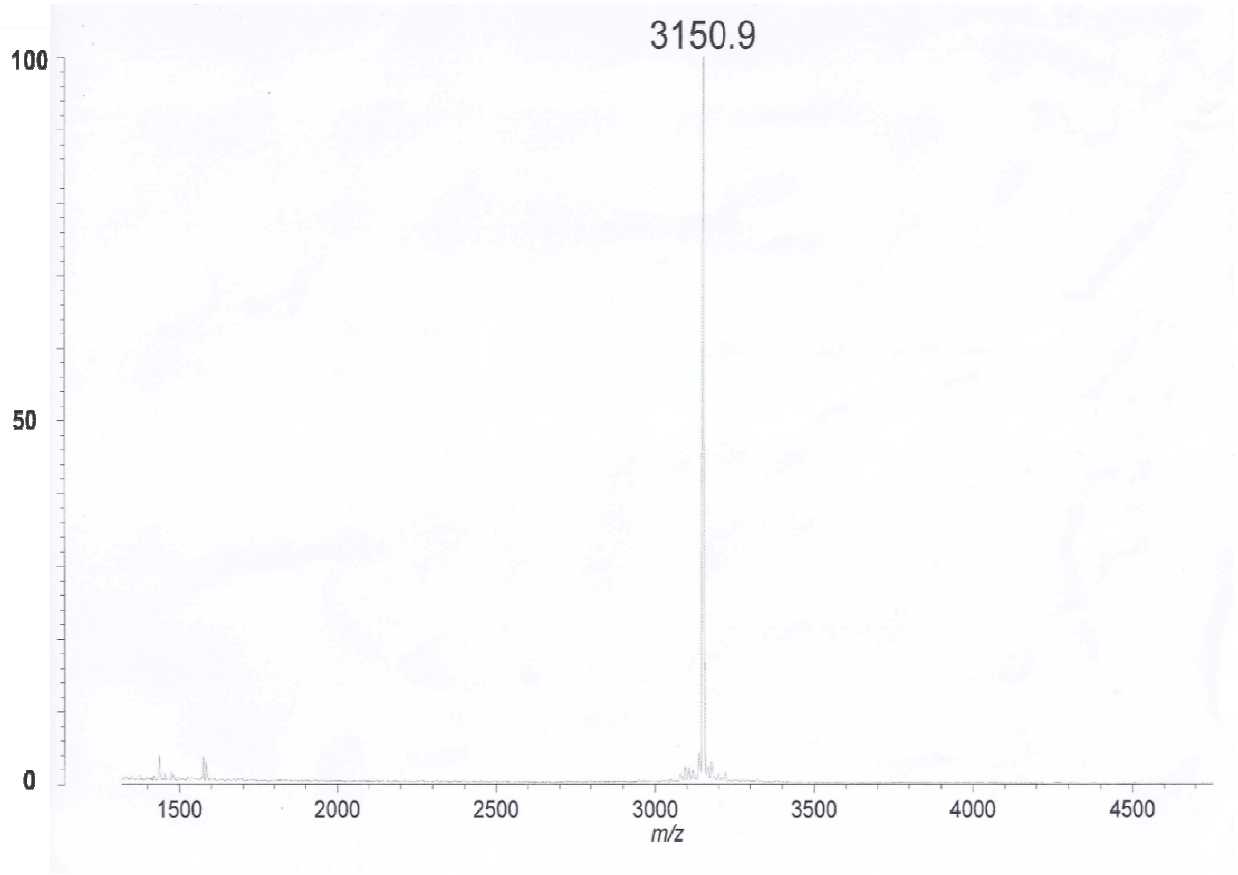

.

Figure C4. MALDI mass spectrum of HFP after purification. The theoretical molecular weight of HFP is 3150 Da.

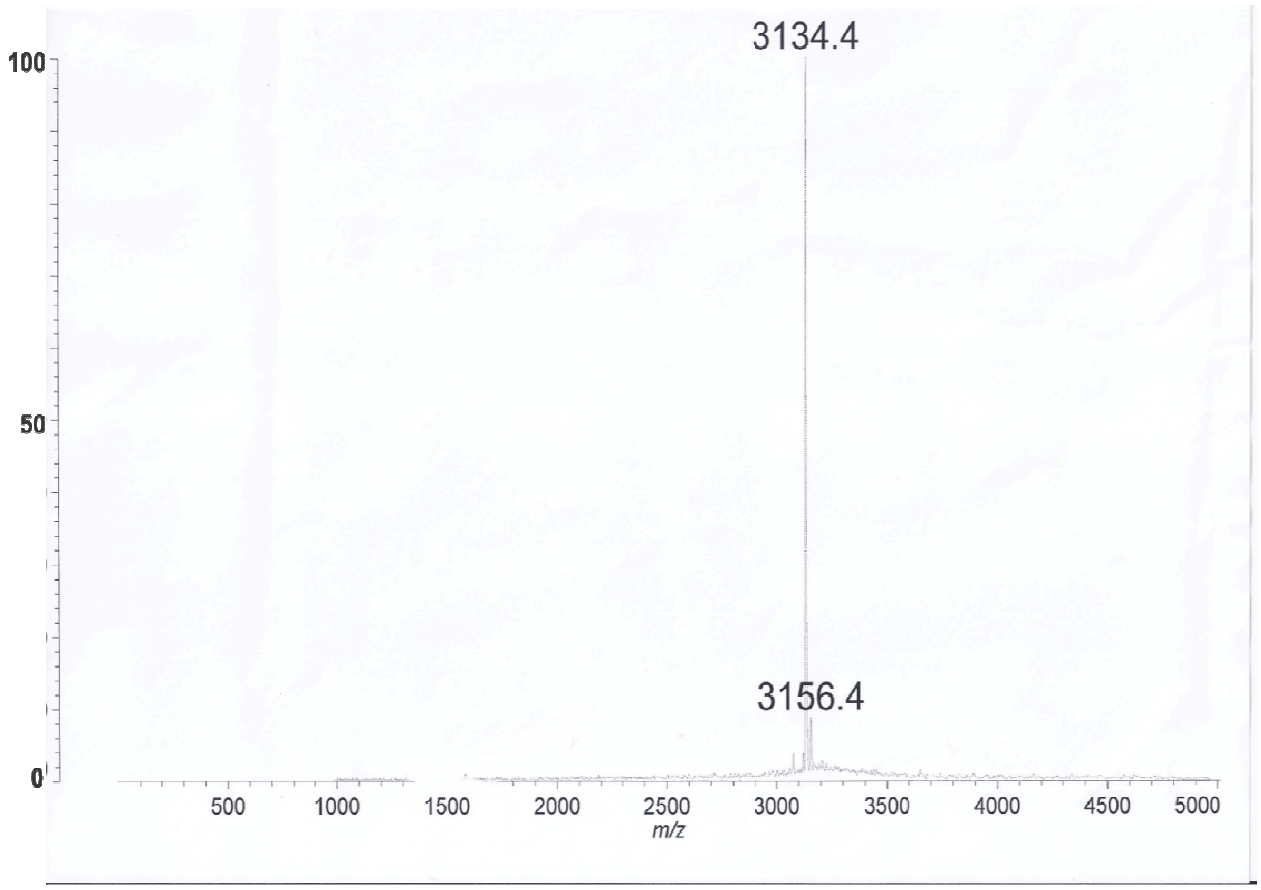

Figure C5. MALDI mass spectrum of HA1fp23 – G1E mutant after purification. The theoretical molecular weight is 3132 Da.

APPENDIX D

Mathematica Algorithm for the Global Fitting of the $^{13}CO - ^{15}N$ REDOR Data

D1. Source code for the array of distances/dipolar couplings:

```
OpenWrite["2msph5onefirst"]
OutputStream[2msph5onefirst,71]
Do[done=3066/deltaone^3;tau=0.002;sone=-(BesselJ[0,Sqrt[2]*done*tau])^2+2
Sum[(BesselJ[k,Sqrt[2]*done*tau])^2/(16*k^2-1),{k, 1, 5}];Do[Write["2msph5onefirst",fone*
(1+sone)],{fone,0.36,0.36,0.01}];Clear[ done, tau, sone], {deltaone, 3.8875,3.8875,0.0125}]
Close["2msph5onefirst"]
2msph5onefirst

OpenWrite["8msph5onefirst"]
OutputStream[8msph5onefirst,84]
Do[done=3066/deltaone^3;tau=0.008;sone=-(BesselJ[0,Sqrt[2]*done*tau])^2+2
Sum[(BesselJ[k,Sqrt[2]*done*tau])^2/(16*k^2-1),{k, 1, 5}];Do[Write["8msph5onefirst",fone*
(1+sone)],{fone,0.36,0.36,0.01}];Clear[ done, tau, sone], {deltaone, 3.8875,3.8875 ,0.0125}]
Close["8msph5onefirst"]
8msph5onefirst

OpenWrite["16msph5onefirst"]
OutputStream[16msph5onefirst,86]
Do[done=3066/deltaone^3;tau=0.016;sone=-(BesselJ[0,Sqrt[2]*done*tau])^2+2
Sum[(BesselJ[k,Sqrt[2]*done*tau])^2/(16*k^2-1),{k, 1, 5}];Do[Write["16msph5onefirst",fone*
(1+sone)],{fone,0.36,0.36,0.01}];Clear[ done, tau, sone], {deltaone, 3.8875,3.8875 ,0.0125}]
Close["16msph5onefirst"]
16msph5onefirst

OpenWrite["24msph5onefirst"]
OutputStream[24msph5onefirst,88]
Do[done=3066/deltaone^3;tau=0.024;sone=-(BesselJ[0,Sqrt[2]*done*tau])^2+2
Sum[(BesselJ[k,Sqrt[2]*done*tau])^2/(16*k^2-1),{k, 1, 5}];Do[Write["24msph5onefirst",fone*
(1+sone)],{fone,0.36,0.36,0.01}];Clear[ done, tau, sone], {deltaone, 3.8875,3.8875 ,0.0125}]
Close["24msph5onefirst"]
24msph5onefirst

OpenWrite["32msph5onefirst"]
OutputStream[32msph5onefirst,90]
Do[done=3066/deltaone^3;tau=0.032;sone=-(BesselJ[0,Sqrt[2]*done*tau])^2+2
Sum[(BesselJ[k,Sqrt[2]*done*tau])^2/(16*k^2-1),{k, 1, 5}];Do[Write["32msph5onefirst",fone*
(1+sone)],{fone,0.36,0.36,0.01}];Clear[ done, tau, sone], {deltaone, 3.8875,3.8875 ,0.0125}]
Close["32msph5onefirst"]
32msph5onefirst

OpenWrite["40msph5onefirst"]
OutputStream[40msph5onefirst,92]
```

```
Do[done=3066/deltaone^3;tau=0.040;sone=-(BesselJ[0,Sqrt[2]*done*tau])^2+2
Sum[(BesselJ[k,Sqrt[2]*done*tau])^2/(16*k^2-1),{k, 1, 5}];Do[Write["40msph5onefirst",fone*
(1+sone)],{fone,0.36,0.36,0.01}];Clear[ done, tau, sone], {deltaone, 3.8875,3.8875 ,0.0125}]
Close["40msph5onefirst"]
40msph5onefirst

OpenWrite["48msph5onefirst"]
OutputStream[48msph5onefirst,94]
Do[done=3066/deltaone^3;tau=0.048;sone=-(BesselJ[0,Sqrt[2]*done*tau])^2+2
Sum[(BesselJ[k,Sqrt[2]*done*tau])^2/(16*k^2-1),{k, 1, 5}];Do[Write["48msph5onefirst",fone*
(1+sone)],{fone,0.36,0.36,0.01}];Clear[ done, tau, sone], {deltaone, 3.8875,3.8875 ,0.0125}]
Close["48msph5onefirst"]
48msph5onefirst
**************************************************************************
**********ph5_1 (1-f1)d2
OpenWrite["2msph5twofirst"]
OutputStream[2msph5twofirst,96]
Do[dtwo=3066/deltatwo^3;tau=0.002;stwo=-(BesselJ[0,Sqrt[2]*dtwo*tau])^2+2
Sum[(BesselJ[k,Sqrt[2]*dtwo*tau])^2/(16*k^2-1),{k, 1, 5}];Do[Write["2msph5twofirst",(1-
fone)
*(1+stwo)],{fone,0.36,0.36,0.01}];Clear[ dtwo, tau, stwo], {deltatwo, 5.425,5.425 ,0.0125}]
Close["2msph5twofirst"]
2msph5twofirst

OpenWrite["8msph5twofirst"]
OutputStream[8msph5twofirst,98]
Do[dtwo=3066/deltatwo^3;tau=0.008;stwo=-(BesselJ[0,Sqrt[2]*dtwo*tau])^2+2
Sum[(BesselJ[k,Sqrt[2]*dtwo*tau])^2/(16*k^2-1),{k, 1, 5}];Do[Write["8msph5twofirst",(1-
fone)*(1+stwo)],{fone,0.36,0.36,0.01}];Clear[ dtwo, tau, stwo], {deltatwo, 5.425,5.425
,0.0125}]
Close["8msph5twofirst"]
8msph5twofirst

OpenWrite["16msph5twofirst"]
OutputStream[16msph5twofirst,100]
Do[dtwo=3066/deltatwo^3;tau=0.016;stwo=-(BesselJ[0,Sqrt[2]*dtwo*tau])^2+2
Sum[(BesselJ[k,Sqrt[2]*dtwo*tau])^2/(16*k^2-1),{k, 1, 5}];Do[Write["16msph5twofirst",(1-
fone)*(1+stwo)],{fone,0.36,0.36,0.01}];Clear[ dtwo, tau, stwo], {deltatwo, 5.425,5.425
,0.0125}]
Close["16msph5twofirst"]
16msph5twofirst

OpenWrite["24msph5twofirst"]
OutputStream[24msph5twofirst,102]
```

```
Do[dtwo=3066/deltatwo^3;tau=0.024;stwo=-(BesselJ[0,Sqrt[2]*dtwo*tau])^2+2
Sum[(BesselJ[k,Sqrt[2]*dtwo*tau])^2/(16*k^2-1),{k, 1, 5}];Do[Write["24msph5twofirst",(1-
fone)*(1+stwo)],{fone,0.36,0.36,0.01}];Clear[ dtwo, tau, stwo], {deltatwo, 5.425,5.425,0.0125}]
Close["24msph5twofirst"]
24msph5twofirst

OpenWrite["32msph5twofirst"]
OutputStream[32msph5twofirst,104]
Do[dtwo=3066/deltatwo^3;tau=0.032;stwo=-(BesselJ[0,Sqrt[2]*dtwo*tau])^2+2
Sum[(BesselJ[k,Sqrt[2]*dtwo*tau])^2/(16*k^2-1),{k, 1, 5}];Do[Write["32msph5twofirst",(1-
fone)*(1+stwo)],{fone,0.36,0.36,0.01}];Clear[ dtwo, tau, stwo], {deltatwo, 5.425,5.425
,0.0125}]
Close["32msph5twofirst"]
32msph5twofirst

OpenWrite["40msph5twofirst"]
OutputStream[40msph5twofirst,106]
Do[dtwo=3066/deltatwo^3;tau=0.040;stwo=-(BesselJ[0,Sqrt[2]*dtwo*tau])^2+2
Sum[(BesselJ[k,Sqrt[2]*dtwo*tau])^2/(16*k^2-1),{k, 1, 5}];Do[Write["40msph5twofirst",(1-
fone)*(1+stwo)],{fone,0.36,0.36,0.01}];Clear[ dtwo, tau, stwo], {deltatwo, 5.425,5.425
,0.0125}]
Close["40msph5twofirst"]
40msph5twofirst

OpenWrite["48msph5twofirst"]
OutputStream[48msph5twofirst,108]
Do[dtwo=3066/deltatwo^3;tau=0.048;stwo=-(BesselJ[0,Sqrt[2]*dtwo*tau])^2+2
Sum[(BesselJ[k,Sqrt[2]*dtwo*tau])^2/(16*k^2-1),{k, 1, 5}];Do[Write["48msph5twofirst",(1-
fone)*(1+stwo)],{fone,0.36,0.36,0.01}];Clear[ dtwo, tau, stwo], {deltatwo, 5.425,5.425,0.0125}]
Close["48msph5twofirst"]
48msph5twofirst
**********************************************************************
**********************************************ph7_1 f2d1
OpenWrite["2msph7onefirst"]
OutputStream[2msph7onefirst,110]
Do[done=3066/deltaone^3;tau=0.002;sone=-(BesselJ[0,Sqrt[2]*done*tau])^2+2
Sum[(BesselJ[k,Sqrt[2]*done*tau])^2/(16*k^2-1),{k, 1, 5}];Do[Write["2msph7onefirst",ftwo*
(1+sone)],{ftwo,0.55,0.55,0.01}];Clear[ done, tau, sone], {deltaone, 3.8875,3.8875,0.0125}]
Close["2msph7onefirst"]
2msph7onefirst

OpenWrite["8msph7onefirst"]
OutputStream[8msph7onefirst,112]
Do[done=3066/deltaone^3;tau=0.008;sone=-(BesselJ[0,Sqrt[2]*done*tau])^2+2
Sum[(BesselJ[k,Sqrt[2]*done*tau])^2/(16*k^2-1),{k, 1, 5}];Do[Write["8msph7onefirst",ftwo*
(1+sone)],{ftwo,0.55,0.55,0.01}];Clear[ done, tau, sone], {deltaone, 3.8875,3.8875,0.0125}]
```

```
Close["8msph7onefirst"]
8msph7onefirst

OpenWrite["16msph7onefirst"]
OutputStream[16msph7onefirst,114]
Do[done=3066/deltaone^3;tau=0.016;sone=-(BesselJ[0,Sqrt[2]*done*tau])^2+2
Sum[(BesselJ[k,Sqrt[2]*done*tau])^2/(16*k^2-1),{k, 1, 5}];Do[Write["16msph7onefirst",ftwo*
(1+sone)],{ftwo,0.55,0.55,0.01}];Clear[ done, tau, sone], {deltaone, 3.8875,3.8875 ,0.0125}]
Close["16msph7onefirst"]
16msph7onefirst

OpenWrite["24msph7onefirst"]
OutputStream[24msph7onefirst,116]
Do[done=3066/deltaone^3;tau=0.024;sone=-(BesselJ[0,Sqrt[2]*done*tau])^2+2
Sum[(BesselJ[k,Sqrt[2]*done*tau])^2/(16*k^2-1),{k, 1, 5}];Do[Write["24msph7onefirst",ftwo*
(1+sone)],{ftwo,0.55,0.55,0.01}];Clear[ done, tau, sone], {deltaone, 3.8875,3.8875 ,0.0125}]
Close["24msph7onefirst"]
24msph7onefirst

OpenWrite["32msph7onefirst"]
OutputStream[32msph7onefirst,118]
Do[done=3066/deltaone^3;tau=0.032;sone=-(BesselJ[0,Sqrt[2]*done*tau])^2+2
Sum[(BesselJ[k,Sqrt[2]*done*tau])^2/(16*k^2-1),{k, 1, 5}];Do[Write["32msph7onefirst",ftwo*
(1+sone)],{ftwo,0.55,0.55,0.01}];Clear[ done, tau, sone], {deltaone, 3.8875,3.8875 ,0.0125}]
Close["32msph7onefirst"]
32msph7onefirst

OpenWrite["40msph7onefirst"]
OutputStream[40msph7onefirst,120]
Do[done=3066/deltaone^3;tau=0.040;sone=-(BesselJ[0,Sqrt[2]*done*tau])^2+2
Sum[(BesselJ[k,Sqrt[2]*done*tau])^2/(16*k^2-1),{k, 1, 5}];Do[Write["40msph7onefirst",ftwo*
(1+sone)],{ftwo,0.55,0.55,0.01}];Clear[ done, tau, sone], {deltaone, 3.8875,3.8875 ,0.0125}]
Close["40msph7onefirst"]
40msph7onefirst

OpenWrite["48msph7onefirst"]
OutputStream[48msph7onefirst,122]
Do[done=3066/deltaone^3;tau=0.048;sone=-(BesselJ[0,Sqrt[2]*done*tau])^2+2
Sum[(BesselJ[k,Sqrt[2]*done*tau])^2/(16*k^2-1),{k, 1, 5}];Do[Write["48msph7onefirst",ftwo*
(1+sone)],{ftwo,0.55,0.55,0.01}];Clear[ done, tau, sone], {deltaone, 3.8875,3.8875 ,0.0125}]
Close["48msph7onefirst"]
48msph7onefirst
**********************************************************************
**********************************ph7_1 (1-f2)d2
OpenWrite["2msph7twofirst"]
OutputStream[2msph7twofirst,124]
```

```
Do[dtwo=3066/deltatwo^3;tau=0.002;stwo=-(BesselJ[0,Sqrt[2]*dtwo*tau])^2+2
Sum[(BesselJ[k,Sqrt[2]*dtwo*tau])^2/(16*k^2-1),{k, 1, 5}];Do[Write["2msph7twofirst",(1-
ftwo)*(1+stwo)],{ftwo,0.55,0.55,0.01}];Clear[ dtwo, tau, stwo], {deltatwo, 5.425,5.425
,0.0125}]
Close["2msph7twofirst"]
2msph7twofirst

OpenWrite["8msph7twofirst"]
OutputStream[8msph7twofirst,126]
Do[dtwo=3066/deltatwo^3;tau=0.008;stwo=-(BesselJ[0,Sqrt[2]*dtwo*tau])^2+2
Sum[(BesselJ[k,Sqrt[2]*dtwo*tau])^2/(16*k^2-1),{k, 1, 5}];Do[Write["8msph7twofirst",(1-
ftwo)*(1+stwo)],{ftwo,0.55,0.55,0.01}];Clear[ dtwo, tau, stwo], {deltatwo, 5.425,5.425
,0.0125}]
Close["8msph7twofirst"]
8msph7twofirst

OpenWrite["16msph7twofirst"]
OutputStream[16msph7twofirst,128]
Do[dtwo=3066/deltatwo^3;tau=0.016;stwo=-(BesselJ[0,Sqrt[2]*dtwo*tau])^2+2
Sum[(BesselJ[k,Sqrt[2]*dtwo*tau])^2/(16*k^2-1),{k, 1, 5}];Do[Write["16msph7twofirst",(1-
ftwo)*(1+stwo)],{ftwo,0.55,0.55,0.01}];Clear[ dtwo, tau, stwo], {deltatwo, 5.425,5.425
,0.0125}]
Close["16msph7twofirst"]
16msph7twofirst

OpenWrite["24msph7twofirst"]
OutputStream[24msph7twofirst,130]
Do[dtwo=3066/deltatwo^3;tau=0.024;stwo=-(BesselJ[0,Sqrt[2]*dtwo*tau])^2+2
Sum[(BesselJ[k,Sqrt[2]*dtwo*tau])^2/(16*k^2-1),{k, 1, 5}];Do[Write["24msph7twofirst",(1-
ftwo)*(1+stwo)],{ftwo,0.55,0.55,0.01}];Clear[ dtwo, tau, stwo], {deltatwo, 5.425,5.425
,0.0125}]
Close["24msph7twofirst"]
24msph7twofirst

OpenWrite["32msph7twofirst"]
OutputStream[32msph7twofirst,132]
Do[dtwo=3066/deltatwo^3;tau=0.032;stwo=-(BesselJ[0,Sqrt[2]*dtwo*tau])^2+2
Sum[(BesselJ[k,Sqrt[2]*dtwo*tau])^2/(16*k^2-1),{k, 1, 5}];Do[Write["32msph7twofirst",(1-
ftwo)*(1+stwo)],{ftwo,0.55,0.55,0.01}];Clear[ dtwo, tau, stwo], {deltatwo, 5.425,5.425
,0.0125}]
Close["32msph7twofirst"]
32msph7twofirst

OpenWrite["40msph7twofirst"]
OutputStream[40msph7twofirst,134]
```

```
Do[dtwo=3066/deltatwo^3;tau=0.040;stwo=-(BesselJ[0,Sqrt[2]*dtwo*tau])^2+2
Sum[(BesselJ[k,Sqrt[2]*dtwo*tau])^2/(16*k^2-1),{k, 1, 5}];Do[Write["40msph7twofirst",(1-
ftwo)*(1+stwo)],{ftwo,0.55,0.55,0.01}];Clear[ dtwo, tau, stwo], {deltatwo, 5.425,5.425
,0.0125}]
Close["40msph7twofirst"]
40msph7twofirst

OpenWrite["48msph7twofirst"]
OutputStream[48msph7twofirst,136]
Do[dtwo=3066/deltatwo^3;tau=0.048;stwo=-(BesselJ[0,Sqrt[2]*dtwo*tau])^2+2
Sum[(BesselJ[k,Sqrt[2]*dtwo*tau])^2/(16*k^2-1),{k, 1, 5}];Do[Write["48msph7twofirst",(1-
ftwo)*(1+stwo)],{ftwo,0.55,0.55,0.01}];Clear[ dtwo, tau, stwo], {deltatwo, 5.425,5.425
,0.0125}]
Close["48msph7twofirst"]
48msph7twofirst
**********************************************************************
**********************************************************ph5_2 f3d1
OpenWrite["2msph5onesecond"]
OutputStream[2msph5onesecond,138]
Do[done=3066/deltaone^3;tau=0.002;sone=-(BesselJ[0,Sqrt[2]*done*tau])^2+2
Sum[(BesselJ[k,Sqrt[2]*done*tau])^2/(16*k^2-1),{k, 1,
5}];Do[Write["2msph5onesecond",fthree*(1+sone)],{fthree,0.53,0.53,0.01}];Clear[ done, tau,
sone], {deltaone, 3.8875,3.8875 ,0.0125}]
Close["2msph5onesecond"]
2msph5onesecond

OpenWrite["8msph5onesecond"]
OutputStream[8msph5onesecond,140]
Do[done=3066/deltaone^3;tau=0.008;sone=-(BesselJ[0,Sqrt[2]*done*tau])^2+2
Sum[(BesselJ[k,Sqrt[2]*done*tau])^2/(16*k^2-1),{k, 1,
5}];Do[Write["8msph5onesecond",fthree*(1+sone)],{fthree,0.53,0.53,0.01}];Clear[ done, tau,
sone], {deltaone, 3.8875,3.8875 ,0.0125}]
Close["8msph5onesecond"]
8msph5onesecond

OpenWrite["16msph5onesecond"]
OutputStream[16msph5onesecond,142]
Do[done=3066/deltaone^3;tau=0.016;sone=-(BesselJ[0,Sqrt[2]*done*tau])^2+2
Sum[(BesselJ[k,Sqrt[2]*done*tau])^2/(16*k^2-1),{k, 1, 5}];Do[Write
["16msph5onesecond",fthree*(1+sone)],{fthree,0.53,0.53,0.01}];Clear[ done, tau, sone],
{deltaone, 3.8875,3.8875 ,0.0125}]
Close["16msph5onesecond"]
16msph5onesecond

OpenWrite["24msph5onesecond"]
OutputStream[24msph5onesecond,144]
```

```
Do[done=3066/deltaone^3;tau=0.024;sone=-(BesselJ[0,Sqrt[2]*done*tau])^2+2
Sum[(BesselJ[k,Sqrt[2]*done*tau])^2/(16*k^2-1),{k, 1, 5}];Do[Write
["24msph5onesecond",fthree*(1+sone)],{fthree,0.53,0.53,0.01}];Clear[ done, tau, sone],
{deltaone, 3.8875,3.8875 ,0.0125}]
Close["24msph5onesecond"]
24msph5onesecond

OpenWrite["32msph5onesecond"]
OutputStream[32msph5onesecond,146]
Do[done=3066/deltaone^3;tau=0.032;sone=-(BesselJ[0,Sqrt[2]*done*tau])^2+2
Sum[(BesselJ[k,Sqrt[2]*done*tau])^2/(16*k^2-1),{k, 1, 5}];Do[Write
["32msph5onesecond",fthree*(1+sone)],{fthree,0.53,0.53,0.01}];Clear[ done, tau, sone],
{deltaone, 3.8875,3.8875 ,0.0125}]
Close["32msph5onesecond"]
32msph5onesecond

OpenWrite["40msph5onesecond"]
OutputStream[40msph5onesecond,148]
Do[done=3066/deltaone^3;tau=0.040;sone=-(BesselJ[0,Sqrt[2]*done*tau])^2+2
Sum[(BesselJ[k,Sqrt[2]*done*tau])^2/(16*k^2-1),{k, 1, 5}];Do[Write
["40msph5onesecond",fthree*(1+sone)],{fthree,0.53,0.53,0.01}];Clear[ done, tau, sone],
{deltaone, 3.8875,3.8875 ,0.0125}]
Close["40msph5onesecond"]
40msph5onesecond

OpenWrite["48msph5onesecond"]
OutputStream[48msph5onesecond,150]
Do[done=3066/deltaone^3;tau=0.048;sone=-(BesselJ[0,Sqrt[2]*done*tau])^2+2
Sum[(BesselJ[k,Sqrt[2]*done*tau])^2/(16*k^2-1),{k, 1, 5}];Do[Write
["48msph5onesecond",fthree*(1+sone)],{fthree,0.53,0.53,0.01}];Clear[ done, tau, sone],
{deltaone, 3.8875,3.8875 ,0.0125}]
Close["48msph5onesecond"]
48msph5onesecond
**************************************************************************
**********************************************pH5_2; (1-f3)*d2
OpenWrite["2msph5twosecond"]
OutputStream[2msph5twosecond,152]
Do[dtwo=3066/deltatwo^3;tau=0.002;stwo=-(BesselJ[0,Sqrt[2]*dtwo*tau])^2+2
Sum[(BesselJ[k,Sqrt[2]*dtwo*tau])^2/(16*k^2-1),{k, 1, 5}];Do[Write["2msph5twosecond",(1-
fthree)*(1+stwo)],{fthree,0.53,0.53,0.01}];Clear[ dtwo, tau, stwo], {deltatwo, 5.425,5.425
,0.0125}]
Close["2msph5twosecond"]
2msph5twosecond

OpenWrite["8msph5twosecond"]
OutputStream[8msph5twosecond,154]
```

```
Do[dtwo=3066/deltatwo^3;tau=0.008;stwo=-(BesselJ[0,Sqrt[2]*dtwo*tau])^2+2
Sum[(BesselJ[k,Sqrt[2]*dtwo*tau])^2/(16*k^2-1),{k, 1, 5}];Do[Write["8msph5twosecond",(1-
fthree)*(1+stwo)],{fthree,0.53,0.53,0.01}];Clear[ dtwo, tau, stwo], {deltatwo, 5.425,5.425
,0.0125}]
Close["8msph5twosecond"]
8msph5twosecond

OpenWrite["16msph5twosecond"]
OutputStream[16msph5twosecond,156]
Do[dtwo=3066/deltatwo^3;tau=0.016;stwo=-(BesselJ[0,Sqrt[2]*dtwo*tau])^2+2
Sum[(BesselJ[k,Sqrt[2]*dtwo*tau])^2/(16*k^2-1),{k, 1, 5}];Do[Write["16msph5twosecond",(1-
fthree)*(1+stwo)],{fthree,0.53,0.53,0.01}];Clear[ dtwo, tau, stwo], {deltatwo, 5.425,5.425
,0.0125}]
Close["16msph5twosecond"]
16msph5twosecond

OpenWrite["24msph5twosecond"]
OutputStream[24msph5twosecond,158]
Do[dtwo=3066/deltatwo^3;tau=0.024;stwo=-(BesselJ[0,Sqrt[2]*dtwo*tau])^2+2
Sum[(BesselJ[k,Sqrt[2]*dtwo*tau])^2/(16*k^2-1),{k, 1, 5}];Do[Write["24msph5twosecond",(1-
fthree)*(1+stwo)],{fthree,0.53,0.53,0.01}];Clear[ dtwo, tau, stwo], {deltatwo, 5.425,5.425
,0.0125}]
Close["24msph5twosecond"]
24msph5twosecond

OpenWrite["32msph5twosecond"]
OutputStream[32msph5twosecond,160]
Do[dtwo=3066/deltatwo^3;tau=0.032;stwo=-(BesselJ[0,Sqrt[2]*dtwo*tau])^2+2
Sum[(BesselJ[k,Sqrt[2]*dtwo*tau])^2/(16*k^2-1),{k, 1, 5}];Do[Write["32msph5twosecond",(1-
fthree)*(1+stwo)],{fthree,0.53,0.53,0.01}];Clear[ dtwo, tau, stwo], {deltatwo, 5.425,5.425
,0.0125}]
Close["32msph5twosecond"]
32msph5twosecond

OpenWrite["40msph5twosecond"]
OutputStream[40msph5twosecond,162]
Do[dtwo=3066/deltatwo^3;tau=0.040;stwo=-(BesselJ[0,Sqrt[2]*dtwo*tau])^2+2
Sum[(BesselJ[k,Sqrt[2]*dtwo*tau])^2/(16*k^2-1),{k, 1, 5}];Do[Write["40msph5twosecond",(1-
fthree)*(1+stwo)],{fthree,0.53,0.53,0.01}];Clear[ dtwo, tau, stwo], {deltatwo, 5.425,5.425
,0.0125}]
Close["40msph5twosecond"]
40msph5twosecond

OpenWrite["48msph5twosecond"]
OutputStream[48msph5twosecond,164]
```

```
Do[dtwo=3066/deltatwo^3;tau=0.048;stwo=-(BesselJ[0,Sqrt[2]*dtwo*tau])^2+2
Sum[(BesselJ[k,Sqrt[2]*dtwo*tau])^2/(16*k^2-1),{k, 1, 5}];Do[Write["48msph5twosecond",(1-
fthree)*(1+stwo)],{fthree,0.53,0.53,0.01}];Clear[ dtwo, tau, stwo], {deltatwo, 5.425,5.425
,0.0125}]
Close["48msph5twosecond"]
48msph5twosecond
**********************************************************************
**********************************************pH 7_2: f4*d1
OpenWrite["2msph7onesecond"]
OutputStream[2msph7onesecond,166]
Do[done=3066/deltaone^3;tau=0.002;sone=-(BesselJ[0,Sqrt[2]*done*tau])^2+2
Sum[(BesselJ[k,Sqrt[2]*done*tau])^2/(16*k^2-1),{k, 1, 5}];
Do[Write["2msph7onesecond",ffour*(1+sone)],{ffour,0.68,0.68,0.01}];Clear[ done, tau, sone],
{deltaone, 3.8875,3.8875 ,0.0125}]
Close["2msph7onesecond"]
2msph7onesecond

OpenWrite["8msph7onesecond"]
OutputStream[8msph7onesecond,168]
Do[done=3066/deltaone^3;tau=0.008;sone=-(BesselJ[0,Sqrt[2]*done*tau])^2+2
Sum[(BesselJ[k,Sqrt[2]*done*tau])^2/(16*k^2-1),{k, 1, 5}];
Do[Write["8msph7onesecond",ffour*(1+sone)],{ffour,0.68,0.68,0.01}];Clear[ done, tau, sone],
{deltaone, 3.8875,3.8875 ,0.0125}]
Close["8msph7onesecond"]
8msph7onesecond

OpenWrite["16msph7onesecond"]
OutputStream[16msph7onesecond,170]
Do[done=3066/deltaone^3;tau=0.016;sone=-(BesselJ[0,Sqrt[2]*done*tau])^2+2
Sum[(BesselJ[k,Sqrt[2]*done*tau])^2/(16*k^2-1),{k, 1, 5}];
Do[Write["16msph7onesecond",ffour*(1+sone)],{ffour,0.68,0.68,0.01}];Clear[ done, tau, sone],
{deltaone, 3.8875,3.8875 ,0.0125}]
Close["16msph7onesecond"]
16msph7onesecond

OpenWrite["24msph7onesecond"]
OutputStream[24msph7onesecond,172]
Do[done=3066/deltaone^3;tau=0.024;sone=-(BesselJ[0,Sqrt[2]*done*tau])^2+2
Sum[(BesselJ[k,Sqrt[2]*done*tau])^2/(16*k^2-1),{k, 1, 5}];
Do[Write["24msph7onesecond",ffour*(1+sone)],{ffour,0.68,0.68,0.01}];Clear[ done, tau, sone],
{deltaone, 3.8875,3.8875 ,0.0125}]
Close["24msph7onesecond"]
24msph7onesecond

OpenWrite["32msph7onesecond"]
OutputStream[32msph7onesecond,174]
```

```
Do[done=3066/deltaone^3;tau=0.032;sone=-(BesselJ[0,Sqrt[2]*done*tau])^2+2
Sum[(BesselJ[k,Sqrt[2]*done*tau])^2/(16*k^2-1),{k, 1, 5}];
Do[Write["32msph7onesecond",ffour*(1+sone)],{ffour,0.68,0.68,0.01}];Clear[ done, tau, sone],
{deltaone, 3.8875,3.8875 ,0.0125}]
Close["32msph7onesecond"]
32msph7onesecond

OpenWrite["40msph7onesecond"]
OutputStream[40msph7onesecond,176]
Do[done=3066/deltaone^3;tau=0.040;sone=-(BesselJ[0,Sqrt[2]*done*tau])^2+2
Sum[(BesselJ[k,Sqrt[2]*done*tau])^2/(16*k^2-1),{k, 1, 5}];
Do[Write["40msph7onesecond",ffour*(1+sone)],{ffour,0.68,0.68,0.01}];Clear[ done, tau, sone],
{deltaone, 3.8875,3.8875 ,0.0125}]
Close["40msph7onesecond"]
40msph7onesecond

OpenWrite["48msph7onesecond"]
OutputStream[48msph7onesecond,178]
Do[done=3066/deltaone^3;tau=0.048;sone=-(BesselJ[0,Sqrt[2]*done*tau])^2+2
Sum[(BesselJ[k,Sqrt[2]*done*tau])^2/(16*k^2-1),{k, 1, 5}];
Do[Write["48msph7onesecond",ffour*
(1+sone)],{ffour,0.68,0.68,0.01}];Clear[ done, tau, sone], {deltaone, 3.8875,3.8875 ,0.0125}]
Close["48msph7onesecond"]
48msph7onesecond
**********************************************************************
**********************************************************pH 7_2: (1-f4)*d2
OpenWrite["2msph7twosecond"]
OutputStream[2msph7twosecond,180]
Do[dtwo=3066/deltatwo^3;tau=0.002;stwo=-(BesselJ[0,Sqrt[2]*dtwo*tau])^2+2
Sum[(BesselJ[k,Sqrt[2]*dtwo*tau])^2/(16*k^2-1),{k, 1, 5}];Do[Write["2msph7twosecond",(1-
ffour)*(1+stwo)],{ffour,0.68,0.68,0.01}];Clear[ dtwo, tau, stwo], {deltatwo, 5.425,5.425
,0.0125}]
Close["2msph7twosecond"]
2msph7twosecond

OpenWrite["8msph7twosecond"]
OutputStream[8msph7twosecond,182]
Do[dtwo=3066/deltatwo^3;tau=0.008;stwo=-(BesselJ[0,Sqrt[2]*dtwo*tau])^2+2
Sum[(BesselJ[k,Sqrt[2]*dtwo*tau])^2/(16*k^2-1),{k, 1, 5}];Do[Write["8msph7twosecond",(1-
ffour)*(1+stwo)],{ffour,0.68,0.68,0.01}];Clear[ dtwo, tau, stwo], {deltatwo, 5.425,5.425
,0.0125}]
Close["8msph7twosecond"]
8msph7twosecond

OpenWrite["16msph7twosecond"]
OutputStream[16msph7twosecond,184]
```

```
Do[dtwo=3066/deltatwo^3;tau=0.016;stwo=-(BesselJ[0,Sqrt[2]*dtwo*tau])^2+2
Sum[(BesselJ[k,Sqrt[2]*dtwo*tau])^2/(16*k^2-1),{k, 1, 5}];Do[Write["16msph7twosecond",(1-
ffour)*(1+stwo)],{ffour,0.68,0.68,0.01}];Clear[ dtwo, tau, stwo], {deltatwo, 5.425,5.425
,0.0125}]
Close["16msph7twosecond"]
16msph7twosecond

OpenWrite["24msph7twosecond"]
OutputStream[24msph7twosecond,186]
Do[dtwo=3066/deltatwo^3;tau=0.024;stwo=-(BesselJ[0,Sqrt[2]*dtwo*tau])^2+2
Sum[(BesselJ[k,Sqrt[2]*dtwo*tau])^2/(16*k^2-1),{k, 1, 5}];Do[Write["24msph7twosecond",(1-
ffour)*(1+stwo)],{ffour,0.68,0.68,0.01}];Clear[ dtwo, tau, stwo], {deltatwo, 5.425,5.425
,0.0125}]
Close["24msph7twosecond"]
24msph7twosecond

OpenWrite["32msph7twosecond"]
OutputStream[32msph7twosecond,188]
Do[dtwo=3066/deltatwo^3;tau=0.032;stwo=-(BesselJ[0,Sqrt[2]*dtwo*tau])^2+2
Sum[(BesselJ[k,Sqrt[2]*dtwo*tau])^2/(16*k^2-1),{k, 1, 5}];Do[Write["32msph7twosecond",(1-
ffour)*(1+stwo)],{ffour,0.68,0.68,0.01}];Clear[ dtwo, tau, stwo], {deltatwo, 5.425,5.425
,0.0125}]
Close["32msph7twosecond"]
32msph7twosecond

OpenWrite["40msph7twosecond"]
OutputStream[40msph7twosecond,190]
Do[dtwo=3066/deltatwo^3;tau=0.040;stwo=-(BesselJ[0,Sqrt[2]*dtwo*tau])^2+2
Sum[(BesselJ[k,Sqrt[2]*dtwo*tau])^2/(16*k^2-1),{k, 1, 5}];Do[Write["40msph7twosecond",(1-
ffour)*(1+stwo)],{ffour,0.68,0.68,0.01}];Clear[ dtwo, tau, stwo], {deltatwo, 5.425,5.425
,0.0125}]
Close["40msph7twosecond"]
40msph7twosecond

OpenWrite["48msph7twosecond"]
OutputStream[48msph7twosecond,192]
Do[dtwo=3066/deltatwo^3;tau=0.048;stwo=-(BesselJ[0,Sqrt[2]*dtwo*tau])^2+2
Sum[(BesselJ[k,Sqrt[2]*dtwo*tau])^2/(16*k^2-1),{k, 1, 5}];Do[Write["48msph7twosecond",(1-
ffour)*(1+stwo)],{ffour,0.68,0.68,0.01}];Clear[ dtwo, tau, stwo], {deltatwo, 5.425,5.425
,0.0125}]
Close["48msph7twosecond"]
48msph7twosecond
**********************************************************************
**********************************************************************
```

D2. Source code for the global chisquare fitting:

```
ms2ph5onefirst=ReadList["2msph5onefirst",Number];ms8ph5onefirst=ReadList["8msph5onefirs
t",Number];ms16ph5onefirst=ReadList["16msph5onefirst",Number];ms24ph5onefirst=ReadList[
"24msph5onefirst",Number];ms32ph5onefirst=ReadList["32msph5onefirst",Number];ms40ph5o
nefirst=ReadList["40msph5onefirst",Number];ms48ph5onefirst=ReadList["48msph5onefirst",Nu
mber];

ms2ph5twofirst=ReadList["2msph5twofirst",Number];ms8ph5twofirst=ReadList["8msph5twofir
st",Number];ms16ph5twofirst=ReadList["16msph5twofirst",Number];ms24ph5twofirst=ReadLis
t["24msph5twofirst",Number];ms32ph5twofirst=ReadList["32msph5twofirst",Number];ms40ph
5twofirst=ReadList["40msph5twofirst",Number];ms48ph5twofirst=ReadList["48msph5twofirst",
Number];

ms2ph5onesecond=ReadList["2msph5onesecond",Number];ms8ph5onesecond=ReadList["8msp
h5onesecond",Number];ms16ph5onesecond=ReadList["16msph5onesecond",Number];ms24ph5
onesecond=ReadList["24msph5onesecond",Number];ms32ph5onesecond=ReadList["32msph5o
nesecond",Number];ms40ph5onesecond=ReadList["40msph5onesecond",Number];ms48ph5one
second=ReadList["48msph5onesecond",Number];

ms2ph5twosecond=ReadList["2msph5twosecond",Number];ms8ph5twosecond=ReadList["8msp
h5twosecond",Number];ms16ph5twosecond=ReadList["16msph5twosecond",Number];ms24ph5
twosecond=ReadList["24msph5twosecond",Number];ms32ph5twosecond=ReadList["32msph5t
wosecond",Number];ms40ph5twosecond=ReadList["40msph5twosecond",Number];ms48ph5tw
osecond=ReadList["48msph5twosecond",Number];

ms2ph7onefirst=ReadList["2msph7onefirst",Number];ms8ph7onefirst=ReadList["8msph7onefirs
t",Number];ms16ph7onefirst=ReadList["16msph7onefirst",Number];ms24ph7onefirst=ReadList[
"24msph7onefirst",Number];ms32ph7onefirst=ReadList["32msph7onefirst",Number];ms40ph7o
nefirst=ReadList["40msph7onefirst",Number];ms48ph7onefirst=ReadList["48msph7onefirst",Nu
mber];

ms2ph7twofirst=ReadList["2msph7twofirst",Number];ms8ph7twofirst=ReadList["8msph7twofir
st",Number];ms16ph7twofirst=ReadList["16msph7twofirst",Number];ms24ph7twofirst=ReadLis
t["24msph7twofirst",Number];ms32ph7twofirst=ReadList["32msph7twofirst",Number];ms40ph
7twofirst=ReadList["40msph7twofirst",Number];ms48ph7twofirst=ReadList["48msph7twofirst",
Number];

ms2ph7onesecond=ReadList["2msph7onesecond",Number];ms8ph7onesecond=ReadList["8msp
h7onesecond",Number];ms16ph7onesecond=ReadList["16msph7onesecond",Number];ms24ph7
onesecond=ReadList["24msph7onesecond",Number];ms32ph7onesecond=ReadList["32msph7o
nesecond",Number];ms40ph7onesecond=ReadList["40msph7onesecond",Number];ms48ph7one
second=ReadList["48msph7onesecond",Number];
ms2ph7twosecond=ReadList["2msph7twosecond",Number];ms8ph7twosecond=ReadList["8msp
h7twosecond",Number];ms16ph7twosecond=ReadList["16msph7twosecond",Number];ms24ph7
```

```
twosecond=ReadList["24msph7twosecond",Number];ms32ph7twosecond=ReadList["32msph7t
wosecond",Number];ms40ph7twosecond=ReadList["40msph7twosecond",Number];ms48ph7tw
osecond=ReadList["48msph7twosecond",Number];

expph5one={0.03182,0.08195,0.27824,0.47615,0.59305,0.6155,0.69965}
{0.03182,0.08195,0.27824,0.47615,0.59305,0.6155,0.69965}
expph7one={0.04372,0.11534,0.34959,0.58337,0.76922,0.78422,0.84259}
{0.04372,0.11534,0.34959,0.58337,0.76922,0.78422,0.84259}
expph5oneprime={0.00139,0.16551,0.37006,0.5820,0.68427,0.75577,0.79702}
{0.00139,0.16551,0.37006,0.582,0.68427,0.75577,0.79702}
expph7oneprime={-0.01193,0.08124,0.39964,0.65278,0.80486,0.90073,0.87622}
{-0.01193,0.08124,0.39964,0.65278,0.80486,0.90073,0.87622}
sigmaph5one={0.01954,0.01449,0.01469,0.01059,0.01089,0.01596,0.01674}
{0.01954,0.01449,0.01469,0.01059,0.01089,0.01596,0.01674}
sigmaph7one={0.02968,0.02529,0.02702,0.02414,0.03966,0.03923,0.05159}
{0.02968,0.02529,0.02702,0.02414,0.03966,0.03923,0.05159}
sigmaph5oneprime={0.03776,0.02999,0.02157,0.02083,0.02769,0.01976,0.02095}
{0.03776,0.02999,0.02157,0.02083,0.02769,0.01976,0.02095}
sigmaph7oneprime={0.03611,0.04307,0.03207,0.02945,0.02992,0.02767,0.05458}
{0.03611,0.04307,0.03207,0.02945,0.02992,0.02767,0.05458}

OpenWrite["ms2ph5onetotal"]
OutputStream[ms2ph5onetotal,250]
Do[ms2ph5onetotal=ms2ph5onefirst[[a]]+ms2ph5twofirst[[a]];Write["ms2ph5onetotal",ms2ph5
onetotal],{a,1,1}]
Close["ms2ph5onetotal"]
ms2ph5onetotal

OpenWrite["ms8ph5onetotal"]
OutputStream[ms8ph5onetotal,252]
Do[ms8ph5onetotal=ms8ph5onefirst[[a]]+ms8ph5twofirst[[a]];Write["ms8ph5onetotal",ms8ph5
onetotal],{a,1,1}]
Close["ms8ph5onetotal"]
ms8ph5onetotal

OpenWrite["ms16ph5onetotal"]
OutputStream[ms16ph5onetotal,254]
Do[ms16ph5onetotal=ms16ph5onefirst[[a]]+ms16ph5twofirst[[a]];Write["ms16ph5onetotal",ms
16ph5onetotal],{a,1,1}]
Close["ms16ph5onetotal"]
ms16ph5onetotal

OpenWrite["ms24ph5onetotal"]
OutputStream[ms24ph5onetotal,256]
Do[ms24ph5onetotal=ms24ph5onefirst[[a]]+ms24ph5twofirst[[a]];Write["ms24ph5onetotal",ms
24ph5onetotal],{a,1,1}]
```

```
Close["ms24ph5onetotal"]
ms24ph5onetotal

OpenWrite["ms32ph5onetotal"]
OutputStream[ms32ph5onetotal,258]
Do[ms32ph5onetotal=ms32ph5onefirst[[a]]+ms32ph5twofirst[[a]];Write["ms32ph5onetotal",ms
32ph5onetotal],{a,1,1}]
Close["ms32ph5onetotal"]
ms32ph5onetotal

OpenWrite["ms40ph5onetotal"]
OutputStream[ms40ph5onetotal,260]
Do[ms40ph5onetotal=ms40ph5onefirst[[a]]+ms40ph5twofirst[[a]]-
0.02;Write["ms40ph5onetotal",ms40ph5onetotal],{a,1,1}]
Close["ms40ph5onetotal"]
ms40ph5onetotal

OpenWrite["ms48ph5onetotal"]
OutputStream[ms48ph5onetotal,262]
Do[ms48ph5onetotal=ms48ph5onefirst[[a]]+ms48ph5twofirst[[a]]-
0.02;Write["ms48ph5onetotal",ms48ph5onetotal],{a,1,1}]
Close["ms48ph5onetotal"]
ms48ph5onetotal
**********************************************************************
**********************************************************************
**********************************************************************
OpenWrite["ms2ph7onetotal"]
OutputStream[ms2ph7onetotal,264]
Do[ms2ph7onetotal=ms2ph7onefirst[[a]]+ms2ph7twofirst[[a]];Write["ms2ph7onetotal",ms2ph7
onetotal],{a,1,1}]
Close["ms2ph7onetotal"]
ms2ph7onetotal

OpenWrite["ms8ph7onetotal"]
OutputStream[ms8ph7onetotal,266]
Do[ms8ph7onetotal=ms8ph7onefirst[[a]]+ms8ph7twofirst[[a]];Write["ms8ph7onetotal",ms8ph7
onetotal],{a,1,1}]
Close["ms8ph7onetotal"]
ms8ph7onetotal

OpenWrite["ms16ph7onetotal"]
OutputStream[ms16ph7onetotal,268]
Do[ms16ph7onetotal=ms16ph7onefirst[[a]]+ms16ph7twofirst[[a]];Write["ms16ph7onetotal",ms
16ph7onetotal],{a,1,1}]
Close["ms16ph7onetotal"]
ms16ph7onetotal
```

```
OpenWrite["ms24ph7onetotal"]
OutputStream[ms24ph7onetotal,270]
Do[ms24ph7onetotal=ms24ph7onefirst[[a]]+ms24ph7twofirst[[a]];Write["ms24ph7onetotal",ms
24ph7onetotal],{a,1,1}]
Close["ms24ph7onetotal"]
ms24ph7onetotal

OpenWrite["ms32ph7onetotal"]
OutputStream[ms32ph7onetotal,272]
Do[ms32ph7onetotal=ms32ph7onefirst[[a]]+ms32ph7twofirst[[a]];Write["ms32ph7onetotal",ms
32ph7onetotal],{a,1,1}]
Close["ms32ph7onetotal"]
ms32ph7onetotal

OpenWrite["ms40ph7onetotal"]
OutputStream[ms40ph7onetotal,274]
Do[ms40ph7onetotal=ms40ph7onefirst[[a]]+ms40ph7twofirst[[a]];Write["ms40ph7onetotal",ms
40ph7onetotal],{a,1,1}]
Close["ms40ph7onetotal"]
ms40ph7onetotal

OpenWrite["ms48ph7onetotal"]
OutputStream[ms48ph7onetotal,276]
Do[ms48ph7onetotal=ms48ph7onefirst[[a]]+ms48ph7twofirst[[a]]+0.02;Write["ms48ph7onetota
l",ms48ph7onetotal],{a,1,1}]
Close["ms48ph7onetotal"]
ms48ph7onetotal
**********************************************************************
**********************************************************************
**********************************************************
OpenWrite["ms2ph5oneprimetotal"]
OutputStream[ms2ph5oneprimetotal,278]
Do[ms2ph5oneprimetotal=ms2ph5onesecond[[a]]+ms2ph5twosecond[[a]];Write["ms2ph5onepri
metotal",ms2ph5oneprimetotal],{a,1,1}]
Close["ms2ph5oneprimetotal"]
ms2ph5oneprimetotal

OpenWrite["ms8ph5oneprimetotal"]
OutputStream[ms8ph5oneprimetotal,280]
Do[ms8ph5oneprimetotal=ms8ph5onesecond[[a]]+ms8ph5twosecond[[a]];Write["ms8ph5onepri
metotal",ms8ph5oneprimetotal],{a,1,1}]
Close["ms8ph5oneprimetotal"]
ms8ph5oneprimetotal

OpenWrite["ms16ph5oneprimetotal"]
```

```
OutputStream[ms16ph5oneprimetotal,282]
Do[ms16ph5oneprimetotal=ms16ph5onesecond[[a]]+ms16ph5twosecond[[a]];Write["ms16ph5o
neprimetotal",ms16ph5oneprimetotal],{a,1,1}]
Close["ms16ph5oneprimetotal"]
ms16ph5oneprimetotal

OpenWrite["ms24ph5oneprimetotal"]
OutputStream[ms24ph5oneprimetotal,284]
Do[ms24ph5oneprimetotal=ms24ph5onesecond[[a]]+ms24ph5twosecond[[a]];Write["ms24ph5o
neprimetotal",ms24ph5oneprimetotal],{a,1,1}]
Close["ms24ph5oneprimetotal"]
ms24ph5oneprimetotal

OpenWrite["ms32ph5oneprimetotal"]
OutputStream[ms32ph5oneprimetotal,286]
Do[ms32ph5oneprimetotal=ms32ph5onesecond[[a]]+ms32ph5twosecond[[a]];Write["ms32ph5o
neprimetotal",ms32ph5oneprimetotal],{a,1,1}]
Close["ms32ph5oneprimetotal"]
ms32ph5oneprimetotal

OpenWrite["ms40ph5oneprimetotal"]
OutputStream[ms40ph5oneprimetotal,295]
Do[ms40ph5oneprimetotal=ms40ph5onesecond[[a]]+ms40ph5twosecond[[a]];Write["ms40ph5o
neprimetotal",ms40ph5oneprimetotal],{a,1,1}]
Close["ms40ph5oneprimetotal"]
ms40ph5oneprimetotal

OpenWrite["ms48ph5oneprimetotal"]
OutputStream[ms48ph5oneprimetotal,297]
Do[ms48ph5oneprimetotal=ms48ph5onesecond[[a]]+ms48ph5twosecond[[a]]+0.01;Write["ms4
8ph5oneprimetotal",ms48ph5oneprimetotal],{a,1,1}]
Close["ms48ph5oneprimetotal"]
ms48ph5oneprimetotal
**********************************************************************
**********************************************************************
**********************************************************************
**********
OpenWrite["ms2ph7oneprimetotal"]
OutputStream[ms2ph7oneprimetotal,299]
Do[ms2ph7oneprimetotal=ms2ph7onesecond[[a]]+ms2ph7twosecond[[a]];Write["ms2ph7onepri
metotal",ms2ph7oneprimetotal],{a,1,1}]
Close["ms2ph7oneprimetotal"]
ms2ph7oneprimetotal

OpenWrite["ms8ph7oneprimetotal"]
OutputStream[ms8ph7oneprimetotal,301]
```

```
Do[ms8ph7oneprimetotal=ms8ph7onesecond[[a]]+ms8ph7twosecond[[a]];Write["ms8ph7onepri
metotal",ms8ph7oneprimetotal],{a,1,1}]
Close["ms8ph7oneprimetotal"]
ms8ph7oneprimetotal

OpenWrite["ms16ph7oneprimetotal"]
OutputStream[ms16ph7oneprimetotal,303]
Do[ms16ph7oneprimetotal=ms16ph7onesecond[[a]]+ms16ph7twosecond[[a]];Write["ms16ph7o
neprimetotal",ms16ph7oneprimetotal],{a,1,1}]
Close["ms16ph7oneprimetotal"]
ms16ph7oneprimetotal

OpenWrite["ms24ph7oneprimetotal"]
OutputStream[ms24ph7oneprimetotal,305]
Do[ms24ph7oneprimetotal=ms24ph7onesecond[[a]]+ms24ph7twosecond[[a]]-
0.01;Write["ms24ph7oneprimetotal",ms24ph7oneprimetotal],{a,1,1}]
Close["ms24ph7oneprimetotal"]
ms24ph7oneprimetotal

OpenWrite["ms32ph7oneprimetotal"]
OutputStream[ms32ph7oneprimetotal,307]
Do[ms32ph7oneprimetotal=ms32ph7onesecond[[a]]+ms32ph7twosecond[[a]];Write["ms32ph7o
neprimetotal",ms32ph7oneprimetotal],{a,1,1}]
Close["ms32ph7oneprimetotal"]
ms32ph7oneprimetotal

OpenWrite["ms40ph7oneprimetotal"]
OutputStream[ms40ph7oneprimetotal,309]
Do[ms40ph7oneprimetotal=ms40ph7onesecond[[a]]+ms40ph7twosecond[[a]];Write["ms40ph7o
neprimetotal",ms40ph7oneprimetotal],{a,1,1}]
Close["ms40ph7oneprimetotal"]
ms40ph7oneprimetotal

OpenWrite["ms48ph7oneprimetotal"]
OutputStream[ms48ph7oneprimetotal,311]
Do[ms48ph7oneprimetotal=ms48ph7onesecond[[a]]+ms48ph7twosecond[[a]]+0.02;Write["ms4
8ph7oneprimetotal",ms48ph7oneprimetotal],{a,1,1}]
Close["ms48ph7oneprimetotal"]
ms48ph7oneprimetotal
**********************************************************************
**********************************************************************
**********************************************************************
ms2ph5one=ReadList["ms2ph5onetotal",Number];ms8ph5one=ReadList["ms8ph5onetotal",Nu
mber];ms16ph5one=ReadList["ms16ph5onetotal",Number];ms24ph5one=ReadList["ms24ph5on
etotal",Number];ms32ph5one=ReadList["ms32ph5onetotal",Number];ms40ph5one=ReadList["
ms40ph5onetotal",Number];ms48ph5one=ReadList["ms48ph5onetotal",Number];
```

```
ms2ph7one=ReadList["ms2ph7onetotal",Number];ms8ph7one=ReadList["ms8ph7onetotal",Nu
mber];ms16ph7one=ReadList["ms16ph7onetotal",Number];ms24ph7one=ReadList["ms24ph7on
etotal",Number];ms32ph7one=ReadList["ms32ph7onetotal",Number];ms40ph7one=ReadList["
ms40ph7onetotal",Number];ms48ph7one=ReadList["ms48ph7onetotal",Number];
ms2ph5oneprime=ReadList["ms2ph5oneprimetotal",Number];ms8ph5oneprime=ReadList["ms8
ph5oneprimetotal",Number];ms16ph5oneprime=ReadList["ms16ph5oneprimetotal",Number];ms
24ph5oneprime=ReadList["ms24ph5oneprimetotal",Number];ms32ph5oneprime=ReadList["ms3
2ph5oneprimetotal",Number];ms40ph5oneprime=ReadList["ms40ph5oneprimetotal",Number];
ms48ph5oneprime=ReadList["ms48ph5oneprimetotal",Number];
ms2ph7oneprime=ReadList["ms2ph7oneprimetotal",Number];ms8ph7oneprime=ReadList["ms8
ph7oneprimetotal",Number];ms16ph7oneprime=ReadList["ms16ph7oneprimetotal",Number];ms
24ph7oneprime=ReadList["ms24ph7oneprimetotal",Number];ms32ph7oneprime=ReadList["ms3
2ph7oneprimetotal",Number];ms40ph7oneprime=ReadList["ms40ph7oneprimetotal",Number];
ms48ph7oneprime=ReadList["ms48ph7oneprimetotal",Number];
**********************************************************************
**********************************************************************
**********************************************************************
***
OpenWrite["chisquarefit"]
OutputStream[chisquarefit,743]
Do[simph5oneprime={ms2ph5oneprime[[a]],ms8ph5oneprime[[a]],ms16ph5oneprime[[a]],ms24
ph5oneprime[[a]],ms32ph5oneprime[[a]],ms40ph5oneprime[[a]],ms48ph5oneprime[[a]]};simph
7oneprime={ms2ph7oneprime[[a]],ms8ph7oneprime[[a]],ms16ph7oneprime[[a]],ms24ph7onepri
me[[a]],ms32ph7oneprime[[a]],ms40ph7oneprime[[a]],ms48ph7oneprime[[a]]};simph5one={ms
2ph5one[[a]],ms8ph5one[[a]],ms16ph5one[[a]],ms24ph5one[[a]],ms32ph5one[[a]],ms40ph5one[
[a]],ms48ph5one[[a]]};simph7one={ms2ph7one[[a]],ms8ph7one[[a]],ms16ph7one[[a]],ms24ph7
one[[a]],ms32ph7one[[a]],ms40ph7one[[a]],ms48ph7one[[a]]};sumph5and7=Sum[(expph7one[[l
]]-simph7one[[l]])^2/sigmaph7one[[l]]^2,{l,1,7}]+Sum[(expph5oneprime[[l]]-
simph5oneprime[[l]])^2/sigmaph5oneprime[[l]]^2,{l,1,7}]+Sum[(expph7oneprime[[l]]-
simph7oneprime[[l]])^2/sigmaph7oneprime[[l]]^2,{l,1,7}]+Sum[(expph5one[[l]]-
simph5one[[l]])^2/sigmaph5one[[l]]^2,{l,1,7}];Write["chisquarefit",sumph5and7];Clear[simph7
one,simph5oneprime,simph7oneprime,simph5one],{a,1,1}]
Close["chisquarefit"]
chisquarefit
FilePrint["chisquarefit"]
34.61143757361456
```

APPENDIX E

Computer Program of the Cpquecho Experiment

E1. cpramp_echo_phase_2.s file: This file contains the main source code for the cpquecho pulse program.

```
name  "cp_ramp_quecho";
title "cross polarization with a ramp on X channel with solid echo";

!  COMPILED WITH OPTIMIZATION ON
!  $Header: /usr2/users/applab/CFR/I+/ppg/cp.s,v 1.2 2000/06/27 19:43:03
applab Exp $
!  InfinityPlus Compatible

!  modified from "cp" by Jun, 6/1/2002

      NMRchnls    RF: ch1 ch2; NMRacq;

! ----------------------------------------
! Define variables in .data section
! ----------------------------------------
! begin.data block

.data
        .time   autofix extern times[] TAU1;
        .time   autofix extern tau1 = 10.0u;

      .phase      list H90[]        = 0, 180;   !H90 phase list
      .phase  Hmix                  = 90;       !Hmix&decouple phase list

      .phase      list Xmix[]             = 270,270,180,180;           !X
phase list

      .time       TRI;                                          ! cp ramp
interval
      .ampl list ramp[20];
      .ampl extern aXcpmod          = 0.0;           ! cp ramp change

      .long list dummies[]          I = 0,
                              J = 0,
                              K = 0,
                              L = 0,
                              M = 0,
                              N = 0;
      .phase list X90[]        = 270, 90, 180, 0, 90, 270, 0, 180;
      .long extern list abph[]      = 3, 1, 2, 0, 3, 1, 2, 0;    !receiver
cycling


include "../includes/STANDARD_PARAMS";
include "../includes/1D.inc";

! ------------------------------------------------
! Define error codes specific to this pulse program
```

```
! ------------------------------------------------
define TAU_ERR 0x100
define TAU_ERROR_CODE USER_ERROR_BASE + TAU_ERR
comment "ERROR "TAU_ERROR_CODE "pw90X too long or tau too short";

define TAU1_ERR 0x100
define TAU1_ERROR_CODE USER_ERROR_BASE + TAU1_ERR
comment "ERROR "TAU1_ERROR_CODE "pw90X or rd too long or tau1 too short";


! end .data block


!-----------------------------------------
! update Spinsight with calculations.
!-----------------------------------------

.update "rb=1.30*sw";
.update "aqtm=(dw*al)";
.update "extm=(pw90H+ct+ad+rd+aqtm+tau+tau1+pd+pw90X)";
.update "txduty1=(pw90H+(2.0*ct)+ad+rd+aqtm+pw90X)/extm";
.update "time1d=((na+dp)*extm)/60.0";

!-----------------------------------------
!  Executed once at Start of Experiment
!-----------------------------------------

.program

dpc = dp;
TRI  = (0.05*ct);
for(I=0,I<20,I++)
      {
            ramp[I] = aXcp + (2.0*(I-10)*aXcpmod)/19.0;
      }

ramp = ramp.start;
abph = abph.start;
H90  = H90.start;
Xmix = Xmix.start;

TAU = (tau - (pw90X/2.0) - tMXP);
TAU1 = (tau1 - (pw90X/2.0) - rd);


txduty1=(pw90H+(2.0*ct)+tau+pw90X+tau1+ad+rd+aqtm)/extm;
if (txduty1 > 0.2) {error(TXDUTY_ERR);}            !Duty factor too large

! ----------------------------------------
! actual pulse prog. runtime loop
! ----------------------------------------

.start
      aqph=@abph++;
```

```
      ramp = ramp.start;

      out   time(3u)    ch1: SC(scX)           ch2: SC(scH);
      out   time(1u)    ch1: P(@Xmix++)        ch2: MX | AP(aH,@H90++);
      !preset phase, ampl.& MX
      out   pw90H       ch1: MX                ch2: TG;
      !output pi/2 pulse
!     out   ct          ch1: TG                ch2: TG | AP(aHcp,Hmix);
      !output CP pulse
      do (20)
      {
      out   time(TRI)   ch1: TG|A(@ramp++)     ch2: TG|AP(aHcp,Hmix);
      }

      out     TAU             ch1: A(aX)              ch2: TG | A(aHdec);
        out     tMXP            ch1: MX | P(@X90++)     ch2: TG;
        out     pw90X           ch1: TG                 ch2: MX;
        out     rd              ch1: TB                 ch2: TG;
! blank X, decouple H
        out     TAU1            ch1: RE | TB            ch2: TG;
        Acq     dw              ch1: RE | TB            ch2: TG;
! acquire
        scan pd;
.end
```

E2. cpramp_echo_phase_2.acq file: this file contains the list of the acquisition parameters and their respective minimum and the maximum values that enables Spinsight to display a list of parameters in the acquisition panel. The acqpars file does not need to list all of the parameters used in the pulse program; rather it shows all the parameters that the user needs to adjust to run the experiment.

```
# cp.acq ##############################################################
#  $Revision: 1.1 $  $Date: 1999/11/10 21:25:19 $
#  $Source: /usr2/users/applab/CFR/I+/ppg/cp.acq,v $
#  InfinityPlus Compatible
#
#   This section sets the initial cmx global parameters
#
#     The file format is as follows
#
#     si_name;long name;value;units;min;max;decimal pnts;user level;data
type
#
#   a - is a blank field.
#   tabs and spaces are allowed if you wish to seperate the fields a
little
#   but a line can be only 80 characters.
#
# first line = ppfn and na
#
na;# acq's (x 4);1;-;1;100000000;0;1;long
#
# Channel assignments
#
ch1;ppg ch1;1;-;1;4;0;1;long
sf1;ch1 spect freq;100.6;MHz;1.0;800.5;7;1;float
ch2;ppg ch2;2;-;1;4;0;1;long
sf2;ch2 spect freq;400.2;MHz;1.0;800.5;7;1;float
sf3;ch3 spect freq;50.0;MHz;1.0;800.5;7;1;float
sf4;ch4 spect freq;20.0;MHz;1.0;800.5;7;1;float
#
#
# timing variables
#
pw90H;H 90 pulse;4;u;.1;1000;2;1;float
ct;contact time;1;m;.0001;100;3;1;float
# added from csecho.acq
tau;relax. delay;10;u;.1;1000000;2;1;float
pw90X;90 pulse;8;u;.1;10000;2;1;float
tau1;2nd delay;10;u;.1;1000000;2;1;float
# end additions from csecho.acq
rd;receiver delay;10;u;3;100;2;1;float
dw;dwell;50;u;.2;1000;3;1;float
```

```
ad;acq delay;35;u;1;1000;2;1;float
sw;spectrum width;20;kHz;1;5001;3;1;float
pd;pulse delay;1;s;.01;6500;3;1;float
#
# Pulse/Receiver attributes
#
aH;H rf ampl;0.0;-;0.0;1.0;4;1;float
aXcp;X cp ampl start;0.1;-;0.0;1.0;4;1;float
aHcp;H CP ampl;0.0;-;0.0;1.0;4;1;float
aXcpmod;X cp ampl change;0.0;-;0.0;1.0;4;1;float
aHdec;H dec. ampl;0.0;-;0.0;1.0;4;1;float
scX;X scalar;0.1;-;0.001;1.0;4;1;float
scH;H scalar;0.1;-;0.001;1.0;4;1;float
aqtm;acq time;12.801;m;.001;1000;3;1;float
#
# Other variable, e.g., al, loop counters
#
al;acq length;1024;-;4;65536;0;1;long
rb;receiver bandwidth;500;khz;1;2000;1;1;float
dp;dummy pulses;0;-;0;1000;0;1;long
rg;receiver gain;100;-;1;1000;2;1;float
txduty1;trans duty;0.01;-;0.0;0.2;3;1;float
temp;Set Temp. (C);0;-;-1000;250;2;1;float;acc_array
time1d;1D time (min);1;-;0.000005;999999999;3;0;float
speed;spin rate;-1;kHz;-1000;50;3;1;float;acc_array
#
# si_name;long name;value;units;min;max;decimal pnts;user level;data type
```

REFERENCES

REFERENCES

1. Davis, J.H., *The Description Of Membrane Lipid Conformation, Order And Dynamics By H-2-NMR.* Biochimica Et Biophysica Acta, 1983. **737**(1): p. 117-171.

2. Brown, M.F. and G.D. Williams, *Membrane NMR - A Dynamic Research Area.* Journal of Biochemical and Biophysical Methods, 1985. **11**(2-3): p. 71-81.

3. Burnett, L.J. and B.H. Muller, *Deuteron Quadrupole Coupling Constants In 3 Solid Deuterated Paraffin Hydrocarbons-C2D6, C4D10, C6D14.* Journal of Chemical Physics, 1971. **55**(12): p. 5829-&.

4. Seelig, J., *Deuterium Magnetic-Resonance - Theory And Application To Lipid-Membranes.* Quarterly Reviews of Biophysics, 1977. **10**(3): p. 353-418.

5. Wildman, K.A.H., D.K. Lee, and A. Ramamoorthy, *Mechanism of lipid bilayer disruption by the human antimicrobial peptide, LL-37.* Biochemistry, 2003. **42**(21): p. 6545-6558.

6. Brown, M.F., *Modern Magnetic Resonance*. 2006.

7. Bloom, M., E. Evans, and O.G. Mouritsen, *Physical-Properties Of The Fluid Lipid-Bilayer Component Of Cell-Membranes - A Perspective.* Quarterly Reviews of Biophysics, 1991. **24**(3): p. 293-397.

8. Hemminga, M.A. and T.W. Poile, *Biological Applications Of Solid-State NMR*. Dynamic Properties of Biomolecular Assemblies, ed. S.E. Harding and A.J. Rowe. Vol. 74. 1989, Cambridge: Royal Soc Chemistry. 74-89.

9. McCabe, M.A. and S.R. Wassall, *Fast-Fourier-Transform Depaking.* Journal of Magnetic Resonance Series B, 1995. **106**(1): p. 80-82.

10. Duer, M.J., *Introduction to Solid State NMR*. 2008: Blackwell.

11. Gabrys, C.M., et al., *Nuclear Magnetic Resonance Evidence For Retention Of A Lamellar Membrane Phase With Curvature In The Presence Of Large Quantities Of The Hiv Fusion Peptide.* Biochimica Et Biophysica Acta-Biomembranes, 2010. **1798**(2): p. 194-201.

12. Bienvenue, A., et al., *Evidence For Protein-Associated Lipids From Deuterium Nuclear Magnetic-Resonance Studies Of Rhodopsin-Dimyristoylphosphatidylcholine Recombinants.* Journal of Biological Chemistry, 1982. **257**(6): p. 3032-3038.

13. Paddy, M.R., et al., *Dynamical And Temperature-Dependent Effects Of Lipid-Protein Interactions - Application Of Deuterium Nuclear Magnetic-Resonance And Electron-*

Paramagnetic Resonance Spectroscopy To The Same Reconstitutions Of Cytochrome-C-Oxidase. Biochemistry, 1981. **20**(11): p. 3152-3162.

14. Jacobs, R.E. and S.H. White, *Lipid Bilayer Perturbations Induced By Simple Hydrophobic Peptides.* Biochemistry, 1987. **26**(19): p. 6127-6134.

15. Ketchem, R.R., W. Hu, and T.A. Cross, *High-Resolution Conformation Of Gramicidin-A In A Lipid Bilayer By Solid-State NMR.* Science, 1993. **261**(5127): p. 1457-1460.

16. Moltke, S., et al., *Chromophore Orientation In Bacteriorhodopsin Determined From The Angular Dependence Of Deuterium Nuclear Magnetic Resonance Spectra Of Oriented Purple Membranes.* Biochemistry, 1998. **37**(34): p. 11821-11835.

17. Stockton, G.W., et al., *Molecular-Motion And Order In Single-Bilayer Vesicles And Multilamellar Dispersions Of Egg Lecithin And Lecithin-Cholesterol Mixtures - Deuterium Nuclear Magnetic-Resonance Study Of Specifically Labeled Lipids.* Biochemistry, 1976. **15**(5): p. 954-966.

18. Schmidt-Rohr, K.a.S., H.W. , *Multidimensional Solid State NMR and Polymers*. 2005.

19. Harris, R.K., *Nuclear Magnetic Resonance Spectroscopy*. 1986.

20. Bloom, M. and E. Sternin, *Transverse Nuclear-Spin Relaxation In Phospholipid-Bilayer Membranes.* Biochemistry, 1987. **26**(8): p. 2101-2105.

21. Oldfield, E., et al., *Spectroscopic Studies Of Specifically Deuterium Labeled Membrane Systems - Nuclear Magnetic-Resonance Investigation Of Effects Of Cholesterol In Model Systems.* Biochemistry, 1978. **17**(14): p. 2727-2740.

Chapter 6

Summary and Future work

Over the last ~ 4 years I have been working on three projects:

(1) Determining the structure of both the 20- and the 23- residue HAfp in membranes, and correlating the structural features with the functional studies,

(2) Development of a new NMR method to study the motions of lipids adjacent to the peptide,

(3) Determining the structure of HAfp mutant Gly-1Glu.

6.1 Summary

The structures of the 20- and 23- residue peptides were determined using ^{13}C-^{15}N REDOR. In detergents, the 20- residue peptide predominantly adopts open structure[1] and the 23- residue peptide predominantly adopts closed structure.[2]Both HAfp variants catalyze fusion but very different catalytic mechanisms were proposed based on the open and closed structures in detergent. My project was motivated by the lack of data about the interhelical HAfp geometry in membrane. I measured via SSNMR the distribution of Phe-9^{15}N to Gly-16^{13}CO and Met-17^{15}N to Ala-5^{13}CO distances in membrane where these nuclei are respectively in the N- and C-helices of HAfp. The solid-state NMR data revealed that in membrane, there are populations of both the previously-observed closed structure as well as a newly-observed semiclosed structure. [3]Our work shows that the structure of the HAfp is different in membranes and detergents which suggestthat the structure of HAfp is sensitive to the curvature of the substrate. Besides in membrane, the structure of HAfp (1) is independent of the length of the peptide; the 23- residue peptide favors the formation of closed structure, and (2) has a moderate dependence on the pH; larger semiclosed fraction at lower pH.The structure-function correlation was probed using vesicle fusion assays. Using the experimentally-determined fractions of closed and semiclosed

structures, the hydrophobic surface area of each peptide was determined. The hydrophobic surface area was correlatedto the extent of vesicle fusion. This suggests that the hydrophobic interaction between HAfp and the membrane is an important factor in HAfp-catalyzed fusion.[4]

My second major project was to understand the changes in the structures and motions that are induced by the fusion peptides. The changes in the lipid membranes induced by the HAfp and HIV-fusion peptide (HFP) were studied using ^{2}H NMR. The ^{2}H solid echo results suggests that the more fusogenic peptides, HFP and HAfp-pH 5, lower the phase transition temperature of the lipid whereas the less fusogenic peptide HAfp-pH 7 increases the phase transition temperature of the lipid. The fusogenic peptides, HAfp-pH 5 and HFP, induce fusion by disrupting the acyl chain packing. The effect of the acyl chain disruption is greater in the lower part of the lipid chain (C7 – C14) which is consistent with the deeper insertion of the peptides in membranes. In contrast, HAfp-pH 7 increases the ordering of the membrane and do not disrupt acyl chain packing. The local motion of the lipids adjacent to the peptides was probed by a newly developed NMR method. The new method is called cross polarization with solid echo (cpquecho).In the conventional solid echo experiment we are observing signal from all the ^{2}Hs that are present in the sample. As a result, the ^{2}H NMR data is the sum over all the lipid molecules. On the other hand, in the cpquecho experiment we will observe the signal from the lipid molecules that are next to the peptide. The shape of the ^{2}H NMR spectra obtained from the solid echo is very different from the ^{2}H NMR spectra obtained from the cpquecho experiment which suggests that the observed signal arises from a subset of ^{2}Hs adjacent to the peptide.The splitting between the horns in the cpquecho spectra suggested that the more fusogenic peptides are inserted deeply in the membranes compared to the less fusogenic peptide. Additionally, from our T_2 measurements we saw the greatest effect of the peptide on the lipids only at the gel phase

of the lipid. After the addition of the peptide, the T_2's of the lipid containing more fusogenic peptide are shorter than the pure lipid and the HAfp-pH 7/DMPC-d54 sample. This result suggests that the more fusogenic peptides induce large amplitude slow motions.

6.2 Future work

For future work, it will be interesting to study the membrane locations of HAfp. The residue specific insertion depth can be probed by the ^{13}C -^{2}H REDOR using selectively labeled per-deuterated lipids and ^{13}C isotopic labeling at different positions of the peptide. In this way one can get the exact membrane location in membranes. The next interesting project is to study the structure of HAfp in different lipid composition because the structure of a peptide also varies with lipid composition. All the experiments were done in DTPC and DTPG lipid in 4:1 mole ratio. PC is a neutrally charged lipid and forms bilayers with zero curvature. It will be interesting to study the structure of HAfp in lipids that forms intrinsically positively curved membranes. This is because earlier solution NMR showed the formation of open structure of HAfp in micelles. This "open" conformation of the HAfp was thought to be very important in the fusion process. However, we never observed any open structures in membranes. One possible reason for this observation is the curvature of the membranes and micelles. Micelles have positive curvature whereas the membranes that we are using have zero curvature. Therefore, it will be interesting to study the HAfp structure as a function of lipid composition and membrane curvature.

6.3 Studies of the dynamics of HAfp and HFP

To study the local dynamics of the lipid in presence of fusion peptides, we used the newly developed NMR method called as "cpquecho". In my research, the lipid-peptide samples were made withDMPC-D54 lipid.DMPC-D54 has five ^{1}Hs that cannot be removed. It will be interesting to run the ^{2}H NMR experiments in a lipid that has no ^{1}Hs and the only ^{1}Hs are the ^{1}Hs present in the peptide. In the present study, I have only measured the T_2's of the lipid with and without peptide. It will be really interesting to study the T_1's of the peptide with and without the peptide because the T_1 processes reflect the fast motions. One particularly interesting study will be to incorporate the cholesterol in the lipid dynamics study. In case of HAfp, the presence of cholesterol increases the extent of vesicle fusion (own unpublished data). Therefore, it will be interesting to study the dynamics of the lipid bilayer changes in presence of both cholesterol and HAfp that leads to higher lipid mixing.

6.4 Mutational studies of HAfp

The sequence of HAfp is highly conserved, 18 out of 23 residues are highly conserved across most of the subtypes of influenza. Mutation of the conserved residues will make HAfp ineffective in the fusion process. It will be interesting to study the structures of the HAfp mutants that make HAfp fusion ineffective. Besides the amino terminus of the peptide is also high fusion inactive. For example, mutation of Gly to Val, Glu or deletion of the first residue has a negative effect on fusion. Therefore, studying the structure of the fusion inactive form will allow us to understand the structural changes essential/undergone by the HAfp to fuse with the host cell membrane. Currently I am working on the HAfp-Gly1Glu mutation. The preliminary results suggest that the secondary structure of HAfp-Gly1Glu mutant is different from the wild type HAfp. Apart from the structural studies, peptide/lipid interactions of the mutant HAfps can also

be studied. In this case, we will get some information about how the peptide interacts with the membranes or the insertion depth of the peptide in the membranes- this can be studied by ^{13}C-^{2}H REDOR or the ^{13}C-^{31}P REDOR.

APPENDIX

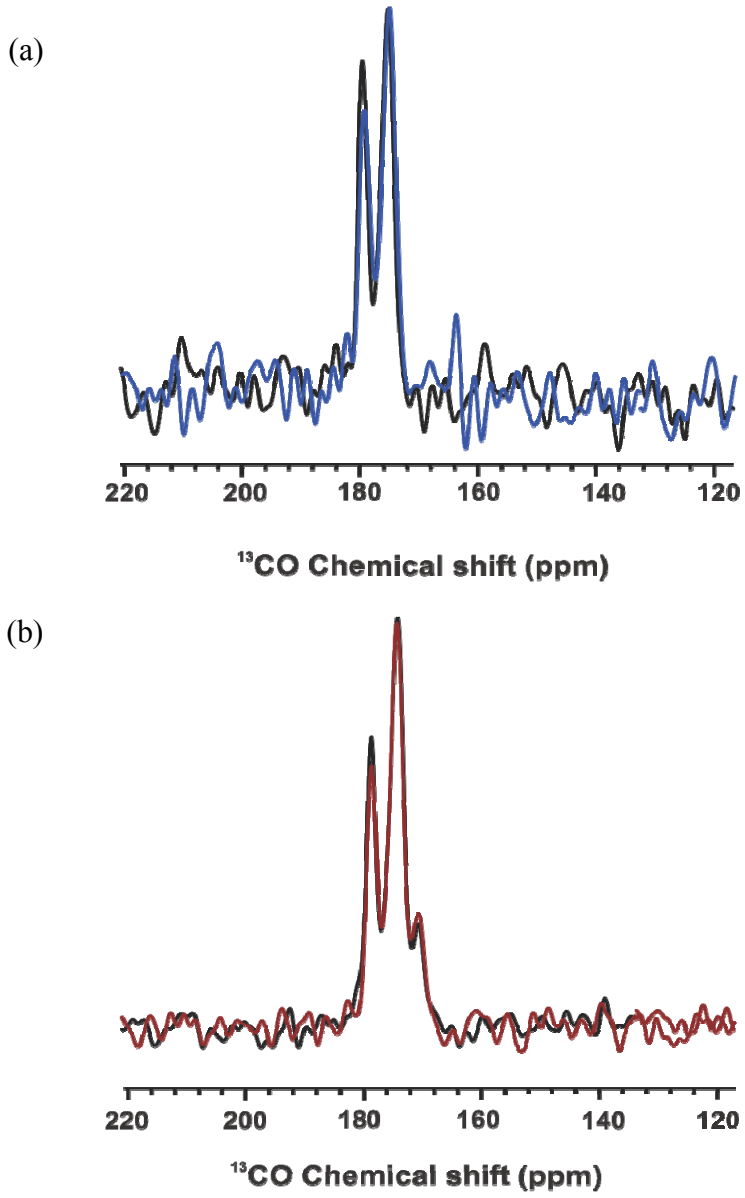

Figure F1. ^{13}C detect ^{15}N dephased REDOR S_0 (black) and S_1 (colored) spectra of HA1fp23 G1E mutant at (a) pH 5 and (b) pH 7 at 40 ms dephasing time. Each spectrum is sum of ~ 60000 scans and processed with 100 Hz line broadening and polynomial baseline correction. The chemical shift of the higher ppm ^{13}CO Ala peak is 179.8 ppm and 175.4 ppm. 179.8 ppm corresponds to α-helical structure whereas the 175.4 ppm corresponds to a coil structure.

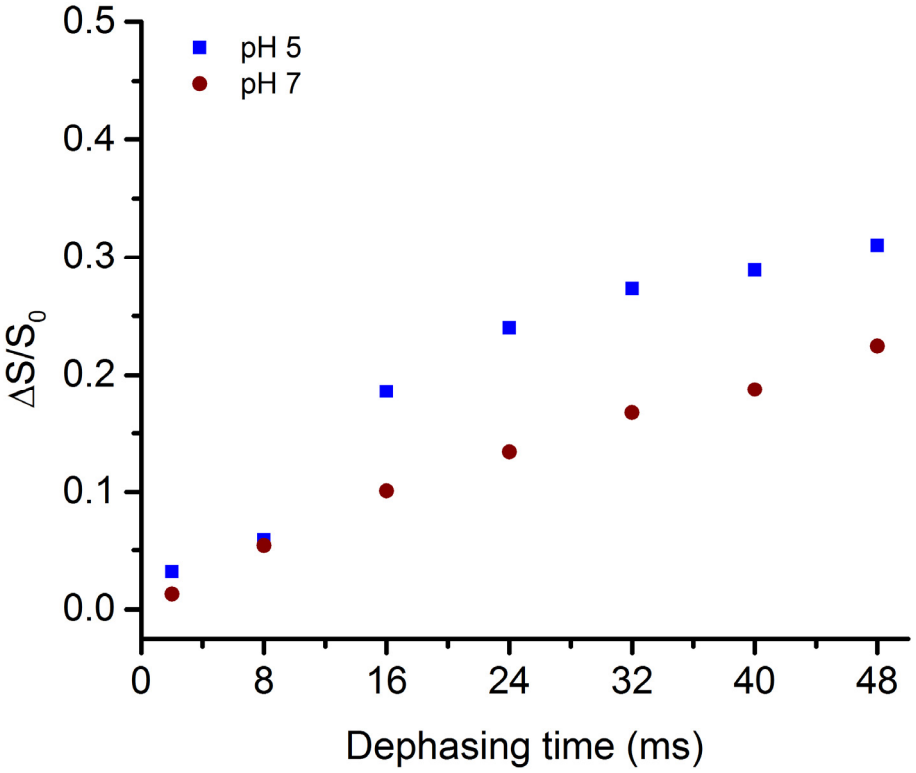

Figure F2. ^{13}CO – ^{15}N ($\Delta S/S_0$) REDOR experimental buildups at pH 5 and pH 7. The typical uncertainties are 0.04. Only the dephasing for the α-peak is plotted.

REFERENCES

REFERENCES

1. Han, X., et al., *Membrane structure and fusion-triggering conformational change of the fusion domain from influenza hemagglutinin.* Nature Structural Biology, 2001. **8**(8): p. 715-720.

2. Lorieau, J.L., J.M. Louis, and A. Bax, *The complete influenza hemagglutinin fusion domain adopts a tight helical hairpin arrangement at the lipid:water interface.* Proceedings of the National Academy of Sciences of the United States of America, 2010. **107**(25): p. 11341-11346.

3. Ghosh, U., L. Xie, and D.P. Weliky, *Detection of closed influenza virus hemagglutinin fusion peptide structures in membranes by backbone (CO)-C-13-N-15 rotational-echo double-resonance solid-state NMR.* Journal of Biomolecular Nmr, 2013. **55**(2): p. 139-146.

4. Ghosh, U., et al., *Closed and Semiclosed Interhelical Structures in Membrane vs Closed and Open Structures in Detergent for the Influenza Virus Hemagglutinin Fusion Peptide and Correlation of Hydrophobic Surface Area with Fusion Catalysis.* Journal of the American Chemical Society, 2015. **137**(24): p. 7548-7551.